VOLUME 16 \ ISSUE 1 \ APRIL 2021

MSURJ

MCGILL SCIENCE UNDERGRADUATE RESEARCH JOURNAL

ON THE COVER

Severe acute respiratory syndrome coronavirus 2 (SARS-CoV-2) is the causative agent of the COVID-19. On page 61, Zhang et al. designed 192 small interfering RNAs (siRNA) that target conserved sequences in the SARS-CoV-2 genome. siRNA therapies have been promising in preventing viral infections.

The digital painting on the cover depicts how SARS-CoV-2, a positive-sense RNA virus recognizable by its spike protein, enters the host cell by fusing its viral envelope with the phospholipid bilayer.

MCGILL SCIENCE
UNDERGRADUATE
RESEARCH JOURNAL

BOARD 2020-2021

805 Sherbrooke St. West, Room 1B22
Montreal, Quebec, H3A 2K6 Canada
Phone: (514) 398-6979
Fax: (514) 398-6766
Email: msurj.sus@mail.mcgill.ca
Website: msurj.com

TABLE OF CONTENTS

7 Foreword

9 Acknowledgements

RESEARCH ARTICLES

12 Eco-Audit of MOFs as H_2 Storage for Vehicle Applications, Using Novel Refueling Model
Elias Andraos et al.

19 Imagine All the People: Investigating People's Perceptual Biasesas they Pertain to Age, Race, and Gender
Marion Audet

25 An in-Silico Molecular Dynamical Investigation of the 7,8-dihydro-8-oxoguanine Mutation in dsDNA using Metadynamics
Ilya Dementyev et al.

31 Effects of Adolescent Cannabinoid Administration in Miceon Behavioural Inhibitionand Susceptibility to Stress During Adulthood
Armaan Fallahi et al.

38 Automated Ultrasonic Vocalization Analysis: Training and Testing VocalMat on Rat-based Dataset
Samir Gouin

43 What is the Best Music for Neurofeedback Training? Exploration into musical attributes that contribute to success in music neurofeedback
Lyla Hawari et al.

50 Convective Rolls in a Stratified Fluid
Katherine Simzer et al.

57 Hochschild Cohomology of the Cohomology Algebra of Closed Orientable Three-Manifolds
Qiu Shi Wang

61 Design and Evaluation of Small Interfering RNAs for the Treatment of Severe Acute Respiratory Syndrome-Coronavirus-2
William Zhang et al.

REVIEW ARTICLES

67 The Role of Stress in the Spread of Transposable Elements
Oscar Dumoulin

74 The EPR Paradox, Einstein-Rosen Bridges and Teleportation
Florian Seefeld

82 Comparitive Analysis of Delivery Methods for Stem Cell Therapy in Liver Diseases
Celia Zhu

SCICOMM CASE COMPETITION SYMPOSIUM

88 Changing Climate Change: Examining efficacy of community based initiatives and micro-scale climate action
Maya Willard-Stepan et al.

FOREWORD

Dear Reader,

Every scientific progress is built upon countless challenges and failures. In the 1960s, an undergraduate student named Martin Chalfie faced a series of failed research experiments that almost convinced him against pursuing a scientific career. Luckily, he persevered and eventually went on to receive the 2008 Nobel Prize in Chemistry.

Reflected in Volume 16 is the same resilience that motivated Martin Chalfie to continue his pursuit of new discoveries. In the following pages, we showcase the research conducted by young, aspiring scientists who have confronted new obstacles in this unprecedented year. As we all navigate the ongoing pandemic, our editorial board is inspired by their persistence, adaptability, and diligence.

This issue contains 13 research and review articles spanning a wide range of disciplines, from quantum theory to chemistry to social psychology. Behind each article is hours of unspoken dedication and uncertainty. By presenting their findings, we hope that the 16th McGill Science Undergraduate Research Journal reflects the authors' passion and aptitude for research.

On behalf of our entire editorial board, thank you.

Michael Agaby & Jacqueline Yao
Editors-in-Chief

ACKNOWLEDGEMENTS

The McGill Science Undergraduate Research Journal (MSURJ) would like to thank its many contributors, without whom the ongoing success of the journal would not be possible.

We thank Dean Bruce Lennox for supporting our work in engaging undergraduate students in scientific research. We thank the librarians of McGill University for their guidance and for helping MSURJ explore the Open Journal System (OJS) platform. In particular, we would like to thank Jennifer Innes and Michael Miller who have been paramount in the transition to OJS. Lastly, we are grateful to those in the McGill community who have given their time and spoken at the various events held by MSURJ this year.

We thank all of our financial supporters in the McGill community for their generosity:

Science Undergraduate Society of McGill (SUS)
Faculty of Medicine
Biology Department
Physiology Department
Biochemistry Undergraduate Society
Pharmacology Department

Finally, we are grateful towards the peer reviewers, many of whom have no affiliation to McGill University, who took the time to review our submissions and to the authors who submitted their work. The journal is only made possible thanks to their time, expertise, and dedication.

Submitted: 01/12/2021

Research Article

[1]Department of Chemistry, McGill University, Montreal, QC, Canada
[2]Berufskolleg Hilden des Kreises Mettmann, Am Holterhöfchen 34, 40724 Hilden, Germany

Keywords

Metal-organic framework, Ni-MOF-74, hydrogen storage, fuel cell vehicles, vehicular hydrogen storage, exergy

Email Correspondence

elias.andraos@mail.mcgill.ca

Elias Andraos[1], Guido Merino[1], Maximilian Ritter[2]

Eco-Audit of MOFs as H_2 Storage Materials for Vehicle Applications, Using Novel Refueling Model

Abstract

Metal-organic frameworks (MOFs) are a heavily researched candidate for fuel-cell electric vehicle (FCEV) hydrogen storage. However, little analysis has been done on the environmental impact of potential MOF vehicles compared to established alternative vehicles, such as compressed hydrogen or battery-electric vehicles. In this work, a preliminary eco-audit was conducted for a FCEV using an MOF hydrogen storage system based the best current MOF Ni_2(*m*-dobdc) (Ni-MOF-74). (1) Cost and environmental impact analyses were performed for both the production and use phases of an MOF-FCEV. The cost and environmental impact of MOF production was compared to that of Lithium Nickel Manganese Cobalt Oxide (LiNMCO) batteries, the current state-of-the-art for BEVs. (2) Environmental impact was assessed using embodied energy estimates based on reported values for LiNMCO BEVs. These highlighted MOF vehicles as a competitor to current renewable energy vehicle technologies. For the use phase, a hydrogen refueling station that produces hydrogen onsite by proton exchange membrane (PEM) electrolysis from grid electricity was compared to an equivalent population of battery electric vehicles (BEVs) charged at distributed recharging stations. FCEVs using the proposed refueling model were able to compete with BEVs both in terms of electricity CO_2 footprint and cost in the simulated solar-dominated Californian grid, but not in the hydro- and nuclear-heavy Ontario grid.

Introduction

Hydrogen has received much attention as a renewable vehicle fuel due to its high specific energy and potentially low footprint of production. (3) The main challenge facing its application as a vehicle fuel is its low volumetric density. Current applications use either heavily compressed (350-700 bar) or cryogenic hydrogen, both of which come with a heavy energy penalty. (4) Even the theoretical minimum thermodynamic values for intense compression or liquefaction are a significant fraction of the specific energy of hydrogen, making possible alternatives to simple physical storage systems attractive. Chemical approaches to increase the energy density of hydrogen broadly fall into 4 categories: hydrogenation of organic molecules, synthesis of hydrogen-rich small molecules, metal hydrides, or adsorption. (5) Adsorption-based storage systems, as depicted in Figure 1, rely on the adsorption-desorption equilibrium to lower the gaseous pressure of H_2. In a material with a high surface area and a low skeletal volume, this can increase the possible volumetric density of the gas compared to empty space at the same pressure. Current candidates for adsorption-based hydrogen systems for fuel cell electric vehicles (FCEV) include graphene, multi-walled carbon nanotubes (MWCNTs), and metal-organic frameworks (MOFs). (6)

MOFs

MOFs have been examined as a hydrogen storage solution since the discovery of hydrogen physisorption in MOF-5 in 2003. (7) MOFs are excellent candidates for hydrogen storage by physisorption as they have exceptionally high specific surface areas (up to 2900 m^2/g, compared to 805 m^2/g for MWCNTs). (8) For on-board storage, the volumetric capacity is of greater concern than the gravimetric capacity, but the densities of MOFs and other adsorptive media are similar enough to make the surface area per weight a reasonable proxy. Additionally, MOFs are more thermally stable than carbon nanotubes and other high-surface area materials. (6)

MOFs are a class of material which form highly organized one-, two- or most commonly three-dimensional structures comprised of metal ions or clusters coordinated to organic ligands. MOFs are extremely porous due to the coordination geometry around the metal and the shape of the organic linker. The high variability in the cluster or linkage selection for MOF synthesis allows for the control of its characteristics, such as the quantity of available adsorption sites. (9) These properties make MOFs an attractive candidate for hydrogen storage via adsorption. Fine control over energies of adsorption and desorption is needed to provide both high H_2 bonding at high pressures as well as fast H_2 release at low pressures. (10) Additionally, the wide range of combinations of potential metals and organic ligands allows for a variety of methods for synthesis, making scale-up for industrial production easier.

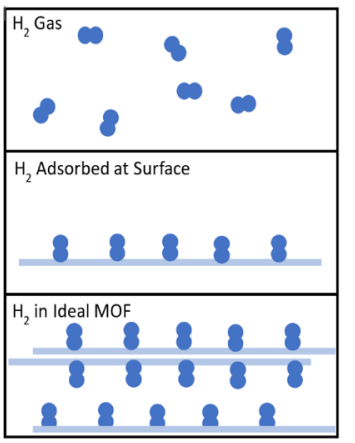

Figure 1. Schematic showing principle behind adsorptive H_2 storage. While it is counterintuitive that more H_2 can be fit into a space also containing an MOF, the lowering of pressure through adsorption allows a significant increase in g H_2/L.

Although MOFs have not yet been commercialized for vehicular gas storage, MOFs are available for other commercial uses and research is being devoted to minimizing the environmental impact of MOF synthesis. Other than solvothermal synthesis in an organic solvent, MOFs have been pre

pared by aqueous synthesis (11) and by mechanochemical methods such as liquid-assisted grinding. (12) Although MOFs with high gravimetric capacities have not yet been produced with the latter method, recent advances have been made, such as the use of salt additives to enhance mechanosynthesis. (12) We assume that it will be a comparable method to the current solvothermal synthesis approach and can thus be considered a feasible synthesis method for this preliminary analysis. Current state-of-the-art MOFs achieve gravimetric capacities of up to 10 wt.% and volumetric capacities of up to 40 gH_2/L, at a pressure swing from 5 to 100 bar and a temperature of 77 K. (8)

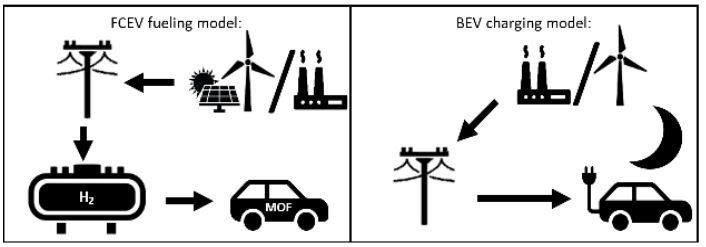

Figure 2. Proposed MOF-FCEV refueling model compared to model of current BEV charging. The low pressure required for MOF-FCEVs compared to traditional FCEVs means that no significant compressionis required between bulk storage and vehicle refueling. This allows complete flexibility in terms of electricity usage times, unlike conventional high-pressure FCEV refueling which requires significant compression shortly before refueling.

Proposed Refueling Model

Due to the thermodynamic efficiency limits of hydrogen production by electrolysis and hydrogen oxidation by fuel cells, even an ideal hydrogen storage solution will not rival the cycle efficiency of a battery system. (13) An advantage of using hydrogen that may make up for this is that it can be stored between its production by electrolysis and used in vehicles, compared to BEVs, which must draw electricity from the grid while charging. Many current electrical grids have a significant share of renewable energy sources but rely on non-renewable energy, instead of energy storage, for times when renewable energy cannot meet demand. In such grids, CO_2 footprint and cost of electricity will vary significantly over timescales as short as hours. Drawing energy from the grid at a time when it is produced with a low carbon footprint before storing this energy may lead to a lower footprint even if more electricity is used overall. Considering that most battery electric vehicles are charged overnight due to long charging time, (14) grids with an abundance of solar energy during the day may be an ideal target for such a FCEV refueling model.

Using MOF vehicle hydrogen storage is crucial to this model, as the lower operational pressures lower the energy requirements of hydrogen preparation. Additionally, current state-of-the-art refueling stations (for 350-700 bar vehicles) keep the majority of their hydrogen at a lower pressure in storage tanks before compressing it into short-term buffer tanks for use, (15) which must draw electricity at the time of demand instead of being able to wait for ideal conditions.

Methods

Production Model

The production cost of a fuel cell electric vehicle with MOFs as hydrogen storage (MOF-FCEV) was estimated by the sum of literature and estimated production costs for the separate vehicle components constituting an MOF-FCEV. The production cost of the MOF material needed was modeled for the best current MOF (1) Ni_2(*m*-dobdc) (Figure 3) by calculating the factor relating the literature values for Mg_2(dobdc) (Mg-MOF-74) MOF cost (16) to the Mg_2(*m*-dobdc) cost (17) and applying it to the Ni_2(dobdc) cost. (16) This calculation was done considering two different synthesis methods for the MOF: liquid assisted grinding (LAG) and solvothermal. The total weight of MOF needed to adsorb the assumed 5.6 kg of H_2 for a full vehicle tank was determined by the reported 2.2 wt % hydrogen storage capacity of Ni_2(*m*-dobdc). (16) The cost of a storage system using MOFs as hydrogen storage was previously modeled. (18) To incorporate the cost of the MOF material estimated in this report to the production cost of the storage system, the price for the material was replaced by the calculated production cost of the required Ni_2(*m*-dobdc) to yield the total storage system cost. The hydrogen storage system must be attached to a fuel cell to complete the power supply system of the MOF-FCEV. In this case, a proton exchange membrane (PEM) fuel cell of 80 kW for light duty vehicles was assumed to be the fuel cell of choice as this technology is currently used for on-road light-duty vehicles and is considered by literature to estimate future fuel cell system production and manufacturing costs. (19) To complete the total production cost of a MOF-FCEV, an additional cost of $22,352 (CAD) was assumed for other auto parts (including heating, ventilation, braking system, etc) and mark-up percentages for the power supply production, marketing, warranty and profit costs taken from literature. (19) The calculated cost for the MOF-FCEV was compared to the production cost of a current LiNMCO battery electric vehicle of same power as the MOF-FCEV fuel cell based on costs calculated by Berckmans et al. (Table 1), which include profit margins of production. (20) Furthermore, the MOF-FCEV was compared to a FCEV for which the total cost was calculated following the same assumptions as the MOF-FCEV, where the cost of the MOF storage system was replaced with that for a type 4 compressed hydrogen storage system. The compressed hydrogen storage system is used by the literature for cost projections of future light-duty fuel cell vehicles. (18)

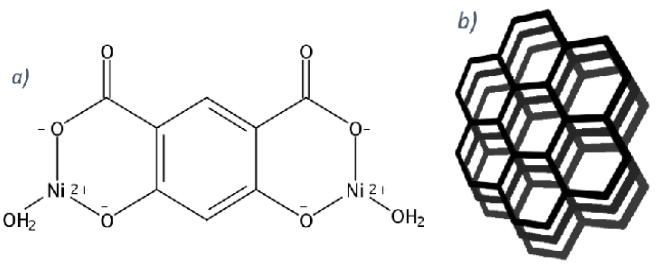

Figure 3. a) Nickel metal clusters coordinated to the organic linker (H_4(m-dobdc)) which constitute the Ni-MOF-74. The clusters are coordinated in three directions to form b) hexagonal sheets that stack vertically with noncovalent interactions.

	Value	Unit
Production rate for vehicle components	500 000	Systems/year
PEM Fuel cell efficiency(19)	0.6	kWh/kWh
Electric vehicle efficiency(19)	0.3	kWh/km
PEM Fuel Cell cost rate for 80 kW low duty vehicle(17)	45	$USD/kW
mark up factor for power supply production(17)	1.17	
mark up factor for Marketing /warranty and profit(17)	1.29	
Lithium ion BEV cost of production (from NMC BEV)(18)	466	$/kWh

Table 1. Key assumed values used for the calculation of the total cost of production of the various power supplies for electric vehicles.

To assess the energetic impact of MOF-FCEV production, an estimation on the total embodied energy of production of a MOF-FCEV power supply (i.e: the MOF storage system and the PEM fuel cell) was conducted. The embodied energy of production for the MOF material was determined by exergy approximation, using literature values for the MOF embodied energy to attempt an estimate of the embodied energy for the specific best current MOF Ni_2(*m*-dobdc). (21)

Exergy estimates the energy needed to produce a material by considering the maximum amount of work required to produce it as the minimum amount of work required to produce the material. (22) In other words, it

assumes ideal values for the energy usage in production of a material. Furthermore, exergy calculations for materials assumes the exergy lost during a reaction to be equivalent to Gibbs energy of formation. The calculation needed to determine the total exergy of a material therefore involves summing the exergies of the elements it is comprised of and the Gibbs energy of formation, as seen in Equation 1. (22)

$$b_{cd} = b_c + b_d + \Delta G_{f,cd}$$

Equation 1. Exergy calculation for a material, where b is the exergy value, delta G is the Gibbs energy of formation, and 'c' and 'd' are the elements reacting to produce material 'cd'.

To use exergy as an approximation, the exergy of the same reference MOF used in the cost analysis (Mg-MOF-74) was calculated from literature values (22,23) and related to its literature embodied energy (21) by calculating a correlation factor. We assumed that the synthesis methods for Mg-MOF-74 and Ni-MOF-74 were identical to offer an adequate comparison between embodied energies and exergies of material production. The calculated factor was applied to the exergy value calculated for Ni_2(*m*-dobdc) to obtain an estimated embodied energy of production. To calculate the total embodied energy of the power supply for a MOF-FCEV, the storage system required for MOF was assumed to be comparable to a Type 3 (350 bar) compressed hydrogen storage system. It was compared to a Type 3 system, which includes the fewest undesired components for a hypothetical MOF-FCEV storage system compared to other compressed hydrogen systems. Additionally, the embodied energy required to manufacture the storage system per weight was readily available in literature (see Table 2), which was used to calculate the embodied energy of its production. Furthermore, the embodied energy for production of the PEM fuel cell in the power supply system of the MOF-FCEV was calculated from 'case 3 of production' literature values (see Table 2), which assumes a mix in electricity grid composition going towards production of the PEM fuel cell and 75% recycling of the platinum group metals used in production. (24)

This estimated total embodied energy of production was compared to that of a FCEV power supply made with the same PEM fuel cell as the MOF-FCEV power supply but with a type 4 (700 bar) compressed hydrogen storage system. As previously mentioned, this is the hydrogen storage system used by most literature for cost projections of future light-duty fuel cell vehicles, for which embodied energy values can be seen in Table 2. The MOF-FCEV power supply was also compared to a LiNMCO BEV battery, for which the total embodied energy was calculated using the average embodied energy of manufacturing (Table 2).

	Value	Units
Embodied energy for storage system (Type 3) production(25)	0.138	MJ/kg
Embodied Energy for a Type 4 (700 bar) hydrogen storage tank(25)	16.2	MJ/tank
case 3 estimated PEM embodied energy(24)	744	MJ/kW
LCO embodied energy(26)	320	MJ/kW
Li ion Battery production embodied energy (average)(27)	2318	MJ/kWh
Literature MOF Embodied energy(20)	91300	MJ/ton

Table 2. Key assumed values used for the calculation of the total embodied energy of various power supplies for electric vehicles.

Use Model

As shown in Figure 2, the model used is a refueling station that produces H_2 onsite by electrolysis during peak renewables capacity. H_2 is stored at 100 bar in traditional storage, until it is cooled to 198 K shortly before being filled into vehicle MOF tanks. On-site electrolysis capacity was modelled to be between 1500 and 2000 kW, falling well within a reasonable cost range for a refueling station (using an estimate of $323/kW for mass-produced PEM electrolyzers.) (27) Energy for hydrogen compression and cooling was calculated using tabulated values (28) that assume ideal gas behavior of H_2. Calculated values were compared to values from literature (4) to confirm that this assumption is reasonable over the range of conditions of operation (Table 1). H_2 demand for vehicle refueling was modelled after USA gas station demand data from Nexant Inc. 2008, (29) as reported in Grouset et al. 2018. (30) Battery vehicle charging demand was modelled after Fig 11. from Schey et al. 2012 (digitized using ImageJ). (14) Station tank capacity was modelled after gas station underground tank sizes ranging from 12000-24000 gallons. (31)

Quantity	Value	Unit
Ideal Energy of Isentropic Compression to 700 bar[1]	2.38	kWh/kgH_2
Real Energy of Compression to 700 bar[1]	2.72 - 7.42	kWh/kgH_2
Ideal Energy of H_2 Liquefaction[1]	3.9	kWh/kgH_2
Ideal Energy of Isothermal Compression to 700 bar[2]	2.25	kWh/kgH_2
Ideal Energy of Isothermal Compression to 100 bar[2]	1.58	kWh/kgH_2
Compressor Pump Efficiency[1]	92	%
Ideal Energy of Isobaric Cooling from 300 to 200 K [2]	0.41	kWh/kgH_2
Total Energy needed for H_2 Preparation before FCEV fueling[2]	2.13	kWh/kgH_2

Table 3. Thermodynamic Calculations for Preparation of H_2 before FCEV fueling. 1) From Gardiner 2009 2) Own calculations, assuming ideal gas. All compression calculations assume H_2 source at 1 bar.

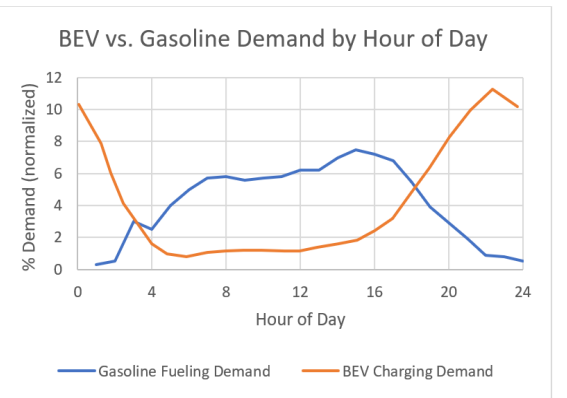

Figure 4. Demand models for gasoline refueling (29,30) and BEV charging. (14)

CO_2 footprint and cost of electricity use were compared using best-case and worst-case numbers for different electricity sources. (32) The compilation of these numbers was provided as class material by Prof. McCalla, and a copy of the table with individual sources can be found in the Supporting Information. CO_2 footprint per kWh was calculated according to Equation 2. Cost per kWh was calculated using estimates for delivered cost of individual electricity types, as actual pricing schemes varied between Ontario and California, and varied by type of consumer.

$$Total CO_2 intensity\left(\frac{kg}{kWh}\right) = CO_2 int.fuel\left(\frac{kg}{kWh}\right) + \frac{CO_2 int.construction\left(\frac{kg}{kW}\right)}{plantlifespan(h)*capacityfactor}$$

Equation 2. Total CO_2 intensity as calculated from values in Information Pack.

Geothermal energy was excluded as no estimate for delivered cost was present in the data set. Because hourly averages of the power grid composition lack information about intermittent power sources such as wind (see Figure 4), the model calculated the energy used hour-by-hour over one year using data from 2019 from Ontario and California. (33,34) California is a prime example of an electrical grid with a large percentage of renewables without adequate grid storage, resulting in a large difference in CO_2 footprint across the day. Ontario was chosen as a reference for a more diverse grid, with significant contribution from low-impact nuclear and hydro sources (see SI for raw grid composition data).

The model used to represent the optimization of electricity use by the refueling station was relatively simple. Electricity was drawn from the grid to produce hydrogen if the hourly carbon footprint was lower than the

average of the twelve hours before and after. While a real refueling station would not have exact grid composition data available for the future, weather forecasts provide a decent estimate of the amount of wind and solar energy that will be available within 12 hours. Additionally, electricity would be used at suboptimal hours (i.e. when the footprint of energy production is higher) if the station tank reached a minimum threshold. Better performance could be achieved with larger electrolyzer capacity used over a shorter time every day, but this cost-benefit analysis is outside of the scope of this project. Optimization of cost was also considered but losses in carbon footprint made this option unattractive (see model in SI).

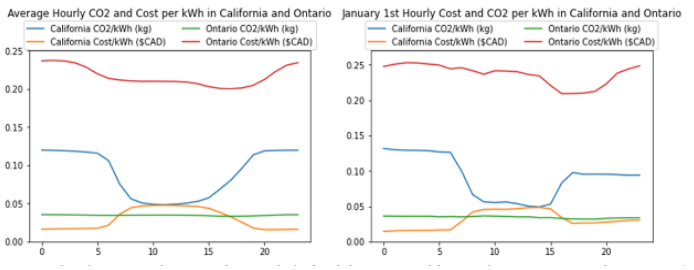

Figure 5. Plots showing CO_2 footprint and cost per kWh of grid electricity in California and Ontario, a) averaged over 2019 and b) for January 1st. Other days showed even larger difference (see SI for raw hourly grid data), but Jan. 1st is shown for transparency. Differences show that simply considering hourly averages is too reductive, as renewable energy sources are not regular, especially in the case of wind energy in Ontario.

Results - Eco-Audit

Production – Cost & Embodied Energy comparison

Based on our assumptions, the results show the financial advantage of producing a MOF-FCEVs. As seen in Figure 6, the total cost of production for an electric vehicle using the best current MOF as hydrogen storage is lower than that for a LiNMCO battery electric vehicle but remains higher than the production cost of a fuel cell electric vehicle with a compressed hydrogen storage system. However, the development of an MOF volumetric hydrogen capacity could lower those costs as it would reduce the amount of tank mass needed and thus offer a competitive alternative to compressed hydrogen.

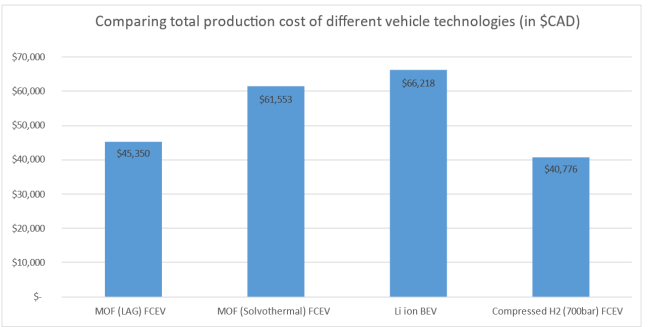

Figure 6. Comparison of the resulting total cost (in $CAD) of vehicle production for different power supply methods and synthesis methods of MOF material.

The total cost of a MOF-FCEV also depends on the synthesis method employed. The most widely used to date for MOF synthesis in MOF research and development is solvothermal synthesis. As seen from Figure 6, the cost of MOF material production increases by roughly $15,000 (CAD) because the synthesis requires expensive organic solvents to dissolve the materials. By modifying the synthesis method to liquid assisted grinding, it was found in literature and demonstrated below that the cost of production greatly lowers because little to no organic solvent is used. (16) Since the development of alternative methods of synthesis promise lower costs in the future, this further confirms the potential of MOF hydrogen storage systems as a competitor to compressed hydrogen fuel cell vehicles.

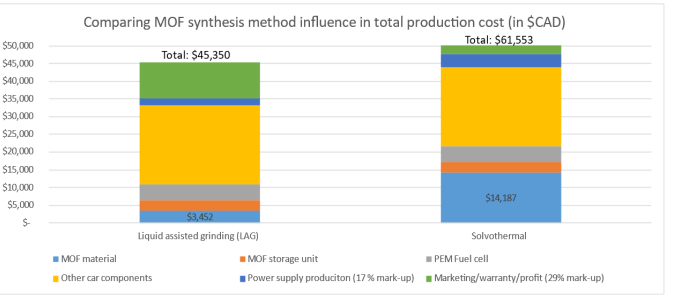

Figure 7. Comparison of the total production costs for two different synthesis methods of the MOF.

The estimated embodied energy of 76 MJ/kg for the $Ni_2(m\text{-dobdc})$ MOF was calculated using the literature embodied energy of 100 MJ/kg for Mg-MOF-74. It was compared to other power supply technologies for electric vehicles to assess the relative environmental impact. As seen in Figure 8, the MOF storage system has a roughly three times lower embodied energy than that of a LiNMCO battery for a battery electric vehicle. Furthermore, the lower embodied energy of Ni-MOF-74 compared to Mg-MOF-74 demonstrates the previously mentioned possibility of developing new MOFs with lower environmental impacts.

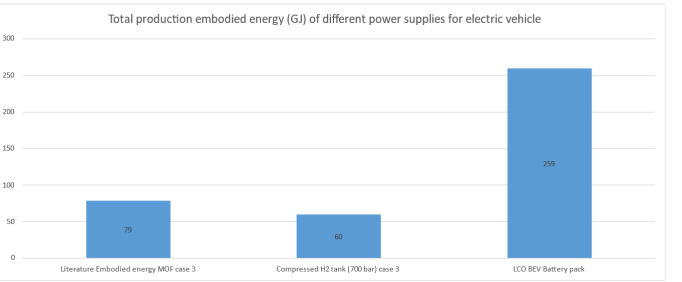

Figure 8. Comparison of the total embodied energy of production of electric vehicles with different power supplies, where the embodied energy for material production for the MOF case was from literature and case 3 denotes the conditions of PEM FC production previously stated.

Like the cost of production results, there is still some modification and optimization needed towards the MOF storage production in order to appropriately compete with current technology. As seen from Figure 9, the MOF material contributes to ~24% of the total embodied energy of production (19 GJ of the total 79 GJ). Therefore, the development of an MOF that would reduce the total mass of the MOF material needed as well as offer a more energy conservative and sustainable synthesis method and increase its viability as an alternative hydrogen storage system for electric vehicles.

Use Phase

The results of refueling model described in the Methods section above are shown in Figure 9. In the solar-dominated Californian grid, MOF-FCEVs can achieve similar carbon footprint values to BEVs, albeit at higher cost (discussed in Limitations below). In Ontario, the fluctuation of renewables, mainly wind, is not enough to make up for the lower efficiency of FCEVs, as shown by both carbon footprint and price.

Based on the cost estimate to produce an MOF-FCEV compared to a BEV and the estimated cost per kilometer driven, we calculated a break-even

point of 960,000-740,000 km in California or 310,000 to 150,000 km in Ontario for the LAG-MOF vehicle compared to the BEV vehicle. No lifespan data is available for MOFs for hydrogen storage, but the break-even point for California is well outside of the lifespan of a battery or fuel-cell, Meanwhile, the break-even point for Ontario is approximately equal to or just beyond the lifespan of a battery for a BEV.

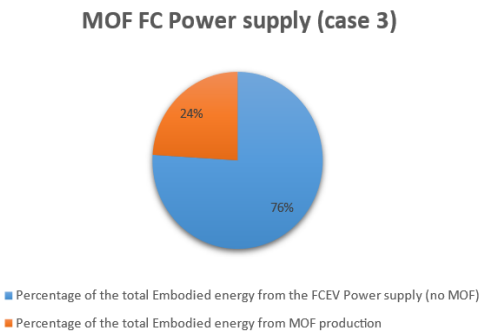

Figure 9. Percentage contribution to the total embodied energy of the fuel cell vehicle power supply by the MOF material.

Comparing the environmental impacts of both the production and use of an MOF-FCEV with a BEV would require additional information, as embodied energy does not translate directly to greenhouse gas emissions. However, based on these separate comparisons of embodied energy of production and CO_2 footprint of use, it is safe to say that MOFs are roughly comparable to BEVs in both production and use phases in terms of cost

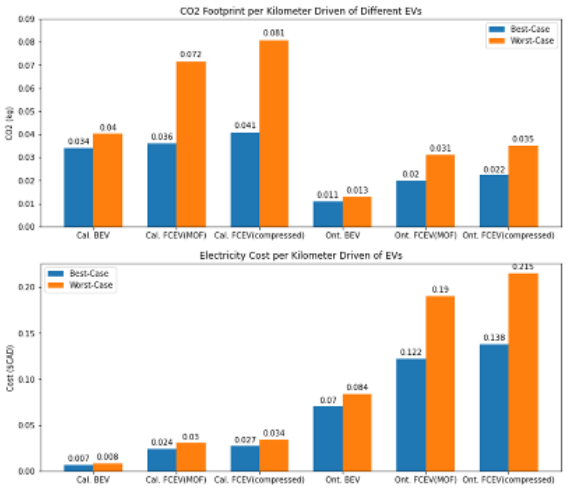

Figure 10. Results of refueling model. FCEV using 700 bar compressed system was added forcomparison, by scaling MOF-FCEV values by factor shown in Table 3. Compressed-H2 FCEV values arelikely underestimated due to the model being tailored towards MOF-FCEVs.

and environmental footprint.

Conclusions

Potential

We believe our estimates and preliminary calculations show that MOF hydrogen storage systems have the potential to compete with battery systems such as the state-of-the-art LiNMCO battery packs for vehicle energy storage, both in terms of CO_2 footprint and cost. Despite the rough estimates made due to lack of data, our modelling approach can be easily refined when more data becomes available. The MOF considered for this model, Ni_2(*m*-dobdc), is an already synthesized material, and other MOFs that may be better suited for H_2 storage have already been identified in theoretical work. (8)

One technology that may also greatly improve the competitiveness of MOF-FCEVs is high-pressure electrolysis, which might be able to produce hydrogen at pressures high enough for direct use, which eliminates the need for energy-costly compression. (35) MOF-FCEVs might benefit more from this technology than other FCEVs due to lower pressure requirements.

Limitations

As stated previously, multiple values were estimated due to a lack of available data. For the production phase calculations, the exergy-based estimation of the embodied energy of a MOF-FCEV will need to be investigated further before drawing any conclusive statements. The refueling model proposed in the use phase will also need a more thorough proof of concept and experimental verification. However, we do believe that these estimates are enough to show that MOF-FCEVs are a viable alternative to current BEVs. Of course, battery technologies other than LiNMCO batteries are currently used and are being developed for use in EVs, and these may compare more favourably to MOF-FCEVs.

It should be noted that two limitations in this study present a disadvantage to MOF-FCEV. First, the data set used for CO_2 footprint and delivered cost of various energy sources is slightly outdated because newer comparable numbers could not be found for all types of energy production considered. This caused an overestimation of footprint and cost of some technologies, particularly of solar energy, which disadvantaged the FCEV in our model.

Second, the difference in vehicle space and weight requirements were not considered even though they are significant. Despite the mass density of only 2.2% H_2 in the MOF, the total mass needed for hydrogen storage ranges from 175 to 205 kg, while the BEV requires between 365 and 475 kg of batteries. The volume occupied by the energy storage is also markedly better for the MOF-FCEV, with under 0.2 m^3 needed compared to 0.2 to 0.45 m^3 for a BEV. While neither of these values for the MOF-FCEV include the fuel cell, the difference is large enough to show the advantage of an MOF hydrogen storage system over batteries for vehicle design. Despite these differences, both types of vehicles were modelled as having an efficiency of 0.3 kWh/km. (3) Accounting for this difference may significantly improve the results of the MOF-FCEV.

As mentioned above, no degradation data or estimates are available for MOF hydrogen storage systems, so the fuel cell was taken to be the limiting factor in terms of vehicle lifespan. Vehicle maintenance was also not considered. No end-of-life recovery was considered. Li-ion battery recycling is challenging but under development, while no data on MOF recycling was found.

Outlook

As stated above, we believe our work provides a "back of the envelope" estimate showing that MOF hydrogen storage materials have the potential to compete with other forms of power supplies for electric vehicles. This is not news to any of the researchers working in the MOF gas storage field. However, we believe that the value of this work is to provide a simple set of assumptions and calculations, any of which may be challenged, to stimulate further discussion of real-world applications. We provide sources for all our assumptions and calculations should any reader be interested in performing a similar analysis for a different set of materials or environments. We look forward to more data becoming available about the application of MOFs as vehicular hydrogen storage and we hope that this work can provide a starting point for more refined calculations.

Acknowledgements

This project was started as part of the CHEM 429: *Chemistry of Energy, Storage and Utilization* course. The authors thank Dr. Eric McCalla for his guidance and support throughout the completion of the research.

Software Used

Calculations and Figures: Microsoft Excel, Jupyter Notebook
Code and raw data available at https://github.com/EA-chem/MOF-FCEV/tree/original/Github%20version
Image digitization: ImageJ

Image Credits

Figure 2: Own composition from built-in Word icons, Electricity Pole and Power plant from Andrejs Kirma from the Noun Project (Creative Commons License)

References

1. Kapelewski MT, Runčevski T, Tarver JD, Jiang HZH, Hurst KE, Parilla PA, et al. Record High Hydrogen Storage Capacity in the Metal–Organic Framework Ni_2(*m*-dobdc) at Near-Ambient Temperatures. Chem Mater. 2018 Nov 27;30(22):8179–89.

2. Xu C, Dai Q, Gaines L, Hu M, Tukker A, Steubing B. Future material demand for automotive lithium-based batteries. Commun Mater. 2020 Dec 9;1(1):1–10.

3. Mazloomi K, Gomes C. Hydrogen as an energy carrier: Prospects and challenges. Renew Sustain Energy Rev. 2012 Jun 1;16(5):3024–33.

4. Gardiner M. Energy requirements for hydrogen gas compression and liquefaction as related to vehicle storage needs. US Department of Energy; 2009.

5. Hydrogen Storage [Internet]. Energy.gov. [cited 2020 Nov 24]. Available from: https://www.energy.gov/eere/fuelcells/hydrogen-storage

6. Gangu KK, Maddila S, Mukkamala SB, Jonnalagadda SB. Characteristics of MOF, MWCNT and graphene containing materials for hydrogen storage: A review. J Energy Chem. 2019 Mar 1;30:132–44.

7. Rosi NL, Eckert J, Eddaoudi M, Vodak DT, Kim J, O'Keeffe M, et al. Hydrogen Storage in Microporous Metal-Organic Frameworks. Science. 2003 May 16;300(5622):1127–9.

8. Ahmed A, Seth S, Purewal J, Wong-Foy AG, Veenstra M, Matzger AJ, et al. Exceptional hydrogen storage achieved by screening nearly half a million metal-organic frameworks. Nat Commun. 2019 Apr 5;10(1):1568.

9. Gangu KK, Maddila S, Mukkamala SB, Jonnalagadda SB. A review on contemporary Metal–Organic Framework materials. Inorganica Chim Acta. 2016 May 1;446:61–74.

10. Langmi HW, Ren J, Musyoka NM. 7 - Metal–organic frameworks for hydrogen storage. In: Gupta RB, Basile A, Veziroğlu TN, editors. Compendium of Hydrogen Energy [Internet]. Woodhead Publishing; 2016 [cited 2020 Sep 10]. p. 163–88. (Woodhead Publishing Series in Energy). Available from: http://www.sciencedirect.com/science/article/pii/B9781782423621000079

11. DeSantis D, Mason JA, James BD, Houchins C, Long JR, Veenstra M. Techno-economic Analysis of Metal–Organic Frameworks for Hydrogen and Natural Gas Storage. Energy Fuels. 2017 Feb 16;31(2):2024–32.

12. Friščić T, Reid DG, Halasz I, Stein RS, Dinnebier RE, Duer MJ. Ion- and Liquid-Assisted Grinding: Improved Mechanochemical Synthesis of Metal–Organic Frameworks Reveals Salt Inclusion and Anion Templating. Angew Chem Int Ed. 2010 Jan 18;49(4):712–5.

13. Haseli Y. Maximum conversion efficiency of hydrogen fuel cells. Int J Hydrog Energy. 2018 May 3;43(18):9015–21.

14. Schey S, Scoffield D, Smart J. A First Look at the Impact of Electric Vehicle Charging on the Electric Grid in The EV Project. World Electr Veh J. 2012 Sep;5(3):667–78.

15. Reddi K, Elgowainy A, Rustagi N, Gupta E. Two-tier pressure consolidation operation method for hydrogen refueling station cost reduction. Int J Hydrog Energy. 2018 Feb 1;43(5):2919–29.

16. DeSantis D, Mason JA, James BD, Houchins C, Long JR, Veenstra M. Techno-economic Analysis of Metal–Organic Frameworks for Hydrogen and Natural Gas Storage. Energy Fuels. 2017 Feb 16;31(2):2024–32.

17. Houchins C, James B. Hydrogen Storage System Cost Analysis: Summary of FY 2017 Activities Sponsorship and Acknowledgements. 2017.

18. James BD, Houchins C, Huya-Kouadio JM, DeSantis DA. Final Report: Hydrogen Storage System Cost Analysis [Internet]. Strategic Analysis Inc., Arlington, VA (United States); 2016 Sep [cited 2020 Nov 23]. Report No.: DOE-SA-0005253. Available from: https://www.osti.gov/biblio/1343975

19. James BD, Huya-Kouadio JM, Houchins C, DeSantis DA. V.E.5 Fuel Cell Vehicle Cost Analysis. Strateg Anal. 2017;6.

20. Berckmans G, Messagie M, Smekens J, Omar N, Vanhaverbeke L, Van Mierlo J. Cost Projection of State of the Art Lithium-Ion Batteries for Electric Vehicles Up to 2030. Energies. 2017 Sep;10(9):1314.

21. Sathre R, Masanet E. Prospective life-cycle modeling of a carbon capture and storage system using metal–organic frameworks for CO_2 capture. RSC Adv. 2013 Mar 18;3(15):4964–75.

22. De Meester B, Dewulf J, Janssens A, Van Langenhove H. An Improved Calculation of the Exergy of Natural Resources for Exergetic Life Cycle Assessment (ELCA). Environ Sci Technol. 2006 Nov 1;40(21):6844–51.

23. Jain A, Ong SP, Hautier G, Chen W, Richards WD, Dacek S, et al. Commentary: The Materials Project: A materials genome approach to accelerating materials innovation. APL Mater. 2013 Jul 1;1(1):011002.

24. Pehnt M. Life-cycle assessment of fuel cell stacks. Int J Hydrog Energy. 2001 Jan 1;26(1):91–101.

25. Evangelisti S, Tagliaferri C, Brett DJL, Lettieri P. Life cycle assessment of a polymer electrolyte membrane fuel cell system for passenger vehicles. J Clean Prod. 2017 Jan 20;142:4339–55.

26. Ellingsen LA-W, Majeau-Bettez G, Singh B, Srivastava AK, Valøen LO, Strømman AH. Life Cycle Assessment of a Lithium-Ion Battery Vehicle Pack. J Ind Ecol. 2014;18(1):113–24.

27. Shiva Kumar S, Himabindu V. Hydrogen production by PEM water electrolysis – A review. Mater Sci Energy Technol. 2019 Dec 1;2(3):442–54.

28. McCarty RD, Roder HM, Hord J, Center for Chemical Engineering (U.S.), United States. Selected properties of hydrogen (engineering design data) [Internet]. Washington, D.C.: U.S. Dept. of Commerce, National Bureau of Standards : For sale by the Supt. of Docs., U.S. G.P.O.; 1981 [cited 2020 Nov 7]. 523 p. in various pagings. (NBS monograph ;168). Available from: https://catalog.hathitrust.org/Record/000939076

29. Nexant I. H2A Hydrogen Delivery Infrastructure Analysis Models and Conventional Pathway Options Analysis Results. 2008;

207–70. Available from: http://www.sciencedirect.com/science/article/pii/B9780128111970000063

31. How much gas does a tanker truck hold? [Internet]. Transcourt Inc. 2018 [cited 2020 Nov 23]. Available from: http://transcourt.com/blog/how-much-gas-does-a-tanker-truck-hold/

32. McCalla E. L7-information-pack - Fall 2020 - CHEM-429-001 - Chem of Energy, Storage & Util [Internet]. 2020 [cited 2020 Oct 11]. Available from: https://mycourses2.mcgill.ca/d2l/le/content/462835/viewContent/5227868/View

33. Ontario Independent Electricity System Operator. Generator Output by Fuel Type Hourly Report [Internet]. 2020. Available from: https://www.ieso.ca/Power-Data/Data-Directory

34. California Independent System Operator. Daily Renewables Output Data [Internet]. 2019 [cited 2020 Nov 14]. Available from: http://content.caiso.com/green/renewrpt/20181231_DailyRenewablesWatch.txt

35. Marangio F, Santarelli M, Calì M. Theoretical model and experimental analysis of a high pressure PEM water electrolyser for hydrogen production. Int J Hydrog Energy. 2009 Feb 1;34(3):1143–58.

Submitted: 11/24/20

Research Article

[1]Department of Pyschology, McGill University, Montreal, QC, Canada

Keywords

Face perception, biases, age, gender, race

Email Correspondence

marion.audet@mail.mcgill.ca

Marion Audet[1]

Imagine All the People: Investigating People's Perceptual Biases as They Pertain to Age, Race, and Gender

Abstract

Typically, perceptual biases are studied by investigating how people respond to written scenarios, without considering the mental representations people form while reading these descriptions. This paper provides a novel approach to face perception research by looking at people's mental representations of strangers and aims to determine whether current ways of classifying people into definite race, age, and gender categories were accurate or needed to be rethought. Specifically, participants digitally reproduced the faces they imagined while reading different scenarios where strangers were described only by race, age, and gender (N = 76). Subsequently, a different set of participants rated these faces on various traits (N = 1024). In the first part of the study, participants created 9 faces from written descriptions of strangers, the last of which included information about criminal history. In the second part, participants rated these faces on dimensions of attractiveness, trustworthiness, intelligence, and physical strength for faces in the non-crime condition, and on dimensions of threat, criminality, and attractiveness for the crime condition. Linear regression models showed that age, race, and gender had various effects on scores on different dimensions, as well as on within-group variance. For instance, older faces were awarded lower attractiveness ratings than younger faces overall, an effect which was also moderated by race, with older age being less predictive of attractiveness ratings for Black faces. Furthermore, there was significantly less variability in attractiveness ratings for Black faces than White faces. Overall, this study revealed that stereotypes do not always adhere to clear-cut categories of race, age, and gender, suggesting that they may be applied somewhat dimensionally rather than categorically.

Introduction

The recent social media phenomenon of blackfishing, or trying to "pass for" a Black person in order to profit of off an identity and/or culture that is not your own, evokes the idea that identity, even racial identity, can be performed. (1) In other words, people can pretend to be something they are not by darkening their skin tone, but also by changing the way they speak, dress, or act. Therefore, blackfishing seems to be one of the most recent manifestations of Goffman's Self in Everyday Life, and the idea that rather than simply extending our private self into the social realm we create and perform a public identity: the social self. (2) Appearance (physical traits, clothing, make-up, etc.) plays a crucial part in determining how we are seen by others, and we know from previous research that faces inspire social judgments of dominance, attractiveness, and trustworthiness. (3) Of course, the face is also a crucial sign of race, age, and gender, and can be used to make inferences about one's culture and life experience.

Stereotyping In-person Perception

Although people can make judgments of race, gender and age in a controlled and reflective manner, these judgments tend to occur quickly in social situations. In these instances, people rely on more automatic mental operations to formulate an impression. People may also have a sense of belonging toward certain groups, and the ways in which they perceive themselves within social categories may in turn impact how they view other people. (4)

Social identity theory argues that people organize their thoughts about others by classifying individuals into categories according to how well they fit within specific social groups, such as that of "woman" or "student". (5) According to dual process theory, these stereotypes can be the product of conscious reflections, but can also be implicitly held, as shown by the Implicit Association Test. (6)

Physical characteristics may also influence people's opinions of others through automatic bottom-up processes, and although people have been found to make fast and accurate judgments of attractiveness, trustworthiness, and dominance, (7) attributions can become stereotyped by over-reliance on such patterns. Additionally, face perception may involve top-down processes that depend on the characteristics of both the perceiver (context, mood, arousal, personality, etc.) and the target (context, affect, appearance, etc.), as well as interactions between the two. (8) Therefore, face perception interacts with a perceiver's beliefs about race, age, and gender to generate judgments and categorizations of others. (9) In this way, a person's race, age and gender stereotypes may affect how they perceive and imagine strangers' faces. Accordingly, a review of the literature on race (in this case focusing on Black people versus White people), age and gender stereotypes is imposed before establishing new lines of inquiries.

Racism Against Black People

In a study on implicit stereotypes about race, people showed an implicit Black-ape mental association when given the opportunity to associate pictures of apes with pictures of Black versus White faces. These findings helped explain the higher likelihood for Black defendants to be described by the media in ape-like terms, which correlated with the likelihood that they would be executed at the outcome of their trials. (10) Relatedly, the weapon bias has consistently demonstrated a propensity for participants to mistake an object for a weapon more often when in the hands of a Black man compared to a White man (11); the same was true even for young Black boys, (12) and to a lesser degree, for women and young girls. (13) Furthermore, there is a perceptual bias of Black men as being more formidable (taller, heavier, more muscular, and stronger) and more capable to harm than non-Black men that relates to how prototypical the target is. (14) Indeed, Afrocentric facial features are a significant within-race predictor of prison sentence length, as well as a between-race predictor to the extent that White inmates with more Black-typical features than average were given longer sentences than equivalently Afrocentric Black prisoners convicted for similar crimes. (15) Taken together, these findings suggest that we see Black people as threatening, especially black men. Consequently, we might expect that the more Afrotypical a person's features, the more they will be perceived and judged according to specific racial stereotypes. Darkness of the skin, maleness, facial prominence of the lips and nose, and physical cues such as tallness and muscularity may then

define the prototypical Black person in people's imagination, and lead to increased stereotyping and assessment of threat.

Ageism

Ageism is the phenomenon by which older people are perceived by their younger counterparts as "senile, rigid and old fashioned in morality and skills", creating a disconnect between the two groups. This detachment on the part of the younger generation results in the subsequent neglect of the old. (16 p894) According to the terror management theory, negative attitudes may serve to position old people as an outgroup, protecting younger people from the shock of their own mortality through emotional distancing. (17) According to the stereotype content model, old age most frequently elicits high warmth and low competence judgments, and evokes feelings of pity in others, a finding which has been replicated across cultures, including in collectivist samples. (18) Research on impression formation has given us a few insights into face perception of older targets, who are rated as less attractive, likeable, energetic and growth-oriented than younger faces. (19)

Sexism

Gender stereotypes are linked to sex-differentiated behaviours that give rise to specific gender roles, which in turn perpetuate the status quo and reinforce those same stereotypes. (20) These gender stereotypes may even have an impact on the way women perceive themselves. For instance, the more women felt different from the typical person who studies in a STEM field, the less confident they were in their ability to excel in that field. (21)

Facial characteristics may also contribute to differences in perception of men and women. The more gender-extreme a person's facial features (more masculine men, more feminine women), the faster people could classify them into the appropriate sex category. (22) In the same study, attractiveness was found to be almost identical to femininity for women, while masculinity did not equal being attractive for men. It may be that perception of men and women operates according to different mechanisms, or even different criteria. Prescriptive and descriptive gender stereotypes are associated with a multitude of sex-typed interests, behaviours and personality traits. However, in old age, stereotypes get less precise, and mostly have to do with women being communal. (23)

Intersectional Stereotyping

Research by Kang and Bodenhausen (24) has focused on investigating people's preconceived ideas about different social groups when confronted to individuals with conflicting (ex. biracial, transgender) or intersecting identities (gender and race, ex. a black woman)—what Kimberle Crenshaw (25) described as the co-existence of multiple social identities within a single person. When signals are ambiguous, impression formation can be challenging: depending on how identity-forming labels such as socio-economic status, race, gender and age combine, they may lead to very different outcomes, for instance the classification of a person of ambiguous race as Black or White depending on perceived social status. (26) The recurrent neglect of some social subgroups can also be examined through the lens of intersectionality. With racial stereotypes being typically male-oriented, and gender stereotypes being especially focused on White women, women of color may be left aside. (27) Research in person perception has shown that Black people are rated as more masculine than White people, leading to higher ratings of attractiveness for Black men but lower ones for Black women, compared to their White counterparts. (28) These findings provide some evidence for the idea that race, age, and gender stereotypes may not be as generalizable as previously thought.

How do we Imagine Others?

While people may use stereotypes in social interactions, drawing on an array of sensory and contextual cues to inform this process, whether such categorical thinking occurs outside of the social realm is less understood. Specifically, how stereotypes manifest in one's imagination is still unclear. For example, it remains to be explored how people form mental representations of faces when they are given only limited information about a stranger's race, age, and gender, and are subsequently asked to imagine, then reproduce this face.

Psychological research in social perception often neglects the visual component of real-world interactions, substituting facial and bodily cues with written descriptions. (9, p.247) We now know that faces influence our impressions of others in numerous and complex ways, but the types of inferences resulting from this process are still unclear.

Current Study

The current study was two-part, looking first at how people mentally represent strangers of different races, ages and genders, and then at how people judge members of various social groups on the basis of facial characteristics. Part 1 was completed with the use of FaceGen, a software that is easy to navigate for first-time users and allows them to manipulate facial features in order to recreate on the computer the face they imagined. People were asked to create eight faces at the intersection of three social categories: age (young versus old), race (Black person versus White person) and gender (male versus female). Participants were also asked to create a final face of a male ex-prisoner who varied by race (White person versus Black person; between-subjects). In part 2, online participants rated the faces from part 1, allowing the collection and aggregation of ratings on different traits.

Across age, it was hypothesized that the older the face, the more stereotypical it would be. In line with intersectionality research, it was thought that women would be rated as less intelligent than men, with Black women being rated as the least intelligent; furthermore, it was predicted that men would be rated as more physically strong than women, with White women being rated as the least physically strong. For the crime condition, it was anticipated that Black ex-prisoners would be rated as more likely to commit a crime, and as more threatening than White ex-prisoners. Lastly, attractiveness ratings were expected to vary across race, and across condition (crime vs non-crime).

Methods

Materials

FaceGen software. FaceGen is a flexible and user-friendly program that allows people to create a face by changing its dimensions using both general (e.g., older/younger or masculine/feminine) and specific commands (i.e., wider/narrower nose, thicker/thinner lips).

Attitudes Toward Blacks. (29) This scale uses 20 items to assess White people's feelings about Black people.

Ambivalent Sexism Inventory. (30) This scale uses 6 items of hostile sexism and 6 items of benevolent sexism to measure sexist attitudes.

Ambivalent Ageism Inventory. (31) This scale is constituted of 13 items measuring both hostile and benevolent forms of ageism

Participants

For part 1, 76 participants were recruited through the McGill psychology participant pool. For part 2, 1024 participants were recruited online through Mechanical Turk and paid $0.50 to complete the survey.

Procedure, Part 1

Participants were seated at a computer, where they were asked to read and sign a consent form. Subsequently, the research assistant running

the session explained the study procedure briefly and oriented participants to the FaceGen software. Participants were then asked to first read a short description of a stranger, and then imagine the face of the stranger in the scenario with their eyes closed. 4 minutes were allowed for participants to reproduce the imaginary stranger's face on the computer using the FaceGen software. The first 8 scenarios were given to participants in a randomized, within-subject design. The last scenario was randomized between two alternatives in a between-subject design, with participants receiving either the Black male ex-criminal scenario or the White male ex-criminal scenario (Fig. S1).

Participants were then asked to complete the attitude questionnaires. Once they were done, they were debriefed about the study verbally and in written form. Each session lasted an hour and participants were awarded 1% in course credit.

Procedure, Part 2

Participants clicked on a link to access the online survey, where they were asked to rate faces generated through FaceGen by participants in part 1. The race-by-gender-by-age faces were assessed on intelligence, physical strength, attractiveness and trustworthiness. The Black and White ex-criminals' faces were rated on dimensions of attractiveness, threat, and likelihood to commit a crime. Finally, participants provided their age and gender.

Results

Data analysis was conducted separately for the non-crime and crime conditions, with 572 and 73 faces, respectively.

Mean Ratings by Social Category

Mixed effects linear regression models for the non-crime condition included race, age, and gender as potential predictors of participant ratings on the dimensions of intelligence, trustworthiness, physical strength and attractiveness. These predictors were nested within participants. Analysis revealed several significant main effects, as well as a few interaction effects.

Attractiveness (Fig. S2, Table S1). Older faces were awarded lower ratings than younger faces. This effect was moderated by race, with older age being less predictive for Black faces.

Intelligence (Fig. S3, Table S2). A marginal effect of racist beliefs on ratings of intelligence was found; more racist beliefs predicted lower scores for Black faces. An effect of age was also found, with older faces receiving lower intelligence scores than young faces.

Physical strength (Fig. S4, Table S3). Gender and race both independently predicted judgments of physical strength, with higher scores for male and Black faces. However, the gender effect was less predictive for old versus young faces, and the effect of race was larger for female faces. These findings support the initial hypothesis that men would be rated as stronger than women, and White women would be rated as least physically strong. The finding that older faces are less susceptible to gender effects feeds into the hypothesis that old faces are stereotyped more often than young ones. Given these effects, additional analysis to include participants' beliefs about race and gender were entered into the model. No mediating effect of such beliefs was found on ratings of strength. Therefore, gender and race effects do not appear to be driven by prejudicial attitudes.

Trustworthiness (Fig. S5, Table S4). Interestingly, the same pattern of results as that for attractiveness was found for trustworthiness, including the moderating effect of race. Old faces were rated as less trustworthy than young ones, but less so for Black faces. Given the redundancy of the age effect for attractiveness, intelligence and trustworthiness ratings, a secondary analysis was run to control for the effect of age on intelligence and attractiveness. Most of the effect of age on trustworthiness could be accounted for by these two other variables. In other words, ratings of intelligence and attractiveness mediated the relationship between old age and ratings of trustworthiness. Furthermore, females were rated as more trustworthy than males on average, which is concurrent with research on agency and communality. (23)

Overall, the lower ratings given to old faces on most dimensions revealed a pattern of more negative attitudes toward the aging population but were not unexpected given the literature on the subject. Results on physical strength are also worth mentioning, as they point to the relevance of intersectionality in psychological research.

Variance in Face Ratings by Social Category

In order to answer our hypotheses concerning tendencies to stereotype groups as homogenous, the variance between the ratings of faces within the same age, gender, and race group was analysed.

Attractiveness (Fig. S6, Table S5). There was significantly less variability in the attractiveness ratings of Black faces. Ratings also varied less for old faces than they did for young ones, feeding into the narrative that older people are generally perceived as a homogenous group.

Intelligence (Fig. S7, Table S6). Contrary to ratings of attractiveness, those for intelligence were actually found to vary more for old versus young faces. Notably, this effect was marginally weaker for Black faces.

Physical strength (Fig. S8, Table S7). There was a main effect of race on ratings of physical strength, with less variance for Black faces, but this was moderated by gender, so that this effect was found for female faces, but not male ones.

Trustworthiness (Fig. S9, Table S8). There was a marginal effect of race on ratings of trustworthiness, resulting in less variance for ratings of Black faces compared to White faces; this effect seemed to be moderated by age, with old Black faces varying less than young ones. Overall, these findings seem to point toward a general trend of stereotyping Black faces more than White faces. There was also a significant effect of gender on variance of trustworthiness ratings, but it was moderated by age and race. Ratings were more similar for young White male faces than they were for young White female faces.

Overall findings. Black faces were significantly more likely to be rated uniformly. Globally, Black faces being rated more similarly than White ones is relevant as it pertains to stereotyping in general. However, the fact that this effect is sometimes moderated by age or gender suggests that stereotyping may not affect all members of the same group equally.

Ratings of Ex-Criminal Faces

For the crime condition, a simple linear regression was run on participants' ratings according to race. Contrary to expectations, race did not seem to have an influence on outcomes related to criminality.

There was no difference in the estimated likelihood of committing a crime between White and Black faces, b=0.02, t(0.50), p=0.616, 95% CI [-0.06, 0.10]. Similarly, race did not have an effect on perceived threat, b=0.09, t(0.57), p=0.571, 95% CI [-0.24, 0.43]. To confirm the results, the analysis was run again, this time including racist beliefs and afro-typicality of the facial features. Neither had an effect on ratings of threat, which was somewhat surprising considering the literature on Afrocentrism and on racial disparities within the criminal system.

However, there was a marginal effect of race on attractiveness, b=-0.21, t(-1.71), p=0.093, 95% CI [-0.45, 0.04], with White faces rated as marginally less attractive than Black faces. Once again, this was regardless of racist beliefs or facial Afrocentrism. Interestingly, we found a main effect of race on shape gender, b=-0.88, t(-3.24), p=0.002, 95% CI[-1.43, -0.34] such that white faces were significantly more male-shaped than Black ones. One explanation for the co-occurrence of these two results may relate to studies which have found an association between femininity and attractiveness, and the lack thereof for masculinity. These effects were somewhat surprising, especially considering the effect of race on dimensions evaluated for the non-crime condition. A reasonable hypothesis would be that the information about crime took primacy over racial cues when participants were asked to imagine these faces.

Discussion

Overall, these findings support the idea that certain groups of people are more likely than others to be stereotyped or judged negatively. Although this is not surprising in the least, outcomes show more complex patterns of stereotyping than would be expected according to traditional views. By evaluating participants' stereotypes from the faces they created, this study examined biases in people's mental representations, rather than their ratings of real faces. Indeed, participants in part 2 were evaluating figments of other people's imagination, which were created according to Part 1 participants' beliefs about various social groups. In this sense, the stereotypes that emerged should be approached as mostly driven by perceiver characteristics. The purpose of taking this perspective is accentuating the role of the perceiver in relation to that of the target in social impression formation. Neglecting perceiver characteristics is a mistake because it leads to over-generalizations in the types of stereotypes we expect from specific agents.

Old faces were consistently perceived in a less flattering light than young faces, even for trustworthiness. On this point, results were somewhat surprising. As the stereotype content model suggests, judgments of competence are expected to be low, but ratings of warmth should be rather high. However, trustworthiness ratings were actually lower for old faces. This might be explained by the lower ratings of attractiveness and intelligence for old faces. The discrepancy between the literature and the findings may be explained by the way people interpreted "trustworthiness", for instance as something more akin to competence than to warmth. The effect of gender on perceived strength was also weaker for old faces, which is consistent with research on the discarding of people as they get older, making them more likely to be rated in a uniform way.

Despite overall lower intelligence ratings, there was significant variance in the scores given to old people, which may be attributed to the subtypes that can be found within the main category "old". (32) Depending on people's specific schemas of old people, they may think of them as being full of wisdom, or conversely, may believe that they are completely out of touch with today's reality.

Black men and women were equally likely to be rated at less intelligent than White men and women. This ties into the concept of interactions between target and perceiver characteristics (8) as people's personal beliefs about Blackness influenced how they rated Black faces relative to White ones. Furthermore, Black faces were less susceptible to the effects of age on ratings of attractiveness and trustworthiness, meaning old and young Black faces were rated similarly. Looking at variance specifically, Black faces were rated more similarly on attractiveness, a trend that could also be observed for old Black faces on trustworthiness, and female Black faces on physical strength. Together, these findings may be interpreted as evidence for the increased stereotyping of Black people compared to White people. The results mentioned above are also significant as they relate to intersectionality. Although ratings of physical strength varied less for Black people, the effect was moderated by gender, meaning that only Black female faces were rated more similarly. This may be interpreted as an instance of Black women being perceived differently than men, or White women. Feelings of trust regarding old Black men in particular were also significantly uniform, pointing to the idea that this group may possess certain unique characteristics.

Interestingly, ratings of young white males varied significantly less than young white females. Considering the pattern of ratings for this group (stronger, more intelligent, more attractive, less trustworthy), they seem to be perceived overall as competent, and agentic. It is worth considering whether this ensemble of traits may be uniquely associated with this group in people's collective imaginary. Furthermore, it is interesting to reflect upon the comparison of young white males to young white females in the context of stereotypes about gender. Indeed, a pattern of constant comparison between maleness and femaleness was observed in the literature search on gender stereotypes, and although sex-typed stereotyping tends to seem restrictive for women, perhaps as these results suggest, they are also very much so for men.

Despite the effects of race on ratings of non-criminals, and expectations regarding the crime condition, race did not impact opinions about threat, nor criminality. One explanation for this finding is that while making the faces, participants focused on the information about crime more than any other cue, creating faces that are similarly threatening and evocative of criminal tendencies regardless of race. This would also explain the findings on attractiveness ratings. While no main effect of race was found for ratings of attractiveness in the non-crime condition, White faces in the crime conditions were rated as marginally less attractive. This once again points to the idea that faces of criminals were created somewhat differently than other faces. Coincidentally, White criminals also had more masculine features than did Black ones, suggesting that gender shape may have been the variable most affected by this condition. However, understanding the reason why White and Black men were differently impacted by this variable would require further investigation.

Limitations

Exploring people's mental representations of strangers is a novel method of studying stereotyping in person perception, and as such, results should be interpreted with caution. The use of computer-generated faces presents the advantage of giving people complete freedom in creating faces, while being a fairly easy tool to use. However, real-world interactions are filled with extra-facial cues that inform people's judgments about others, which were not present in this study. These results should therefore be considered as preliminary, and as an encouragement for others to explore this novel perspective further. Additionally, cognitive processes do not always translate into specific behaviours, and unconscious biases of our imagination may not reflect conscious beliefs either. It is thus impossible to elaborate on the potential impact of people's mental representations on the way they interact with others in daily life. Lastly, cross-level interactions between variables of interest and people's attitudes about gender, race, and age were based on a much smaller sample size and might not have allowed for sufficient statistical power. Consequently, although truly significant effects of people's beliefs on participants' ratings were not found, it is possible that the sample size was simply too small to detect an effect.

Conclusion

It appears that the faces people imagine when reading about different groups of strangers are not as similar as they would be if they depended solely on stereotypical categories of race, age and gender. Instead, people's mental representations of unknown others seem to be intersectional in nature, varying depending on the ways in which perceiver and target characteristics combine. Intersectionality was even present in specific age, race and gender categories, with different levels of variability pointing to the existence of various subgroups within the main cluster. This study demonstrates the importance of individuality in the process of stereotyping in face perception and takes a stance toward increased inclusion of intersectional theory and knowledge of the variability in age, race and gender stereotypes in the conceptualization of psychological research.

References

1. Virk K, McGregor N. Blackfishing: The women accused of pretending to be black [internet]. [place unknown]: BBC News; 2018 [cited 2020 Jan 25]. Available from: https://www.bbc.com/news/newsbeat-46427180
2. Burns T. Erving Goffman. London, New York: Routledge; 1992. 386 p.

3. Todorov A, Mende-Siedlecki P, Dotsch R. Social Judgments from Faces. Curr Opin in Neurobiol [internet]. 2013 [updated 2020; cited 2020 Feb 22]; 23(3): 373-380. Available from: https://www.sciencedirect.com/science/article/pii/S0959438813000147?via%3Dihub doi: 10.1016/j.conb.2012.12.010

4. Welder DA, Shapiro P. Facilitation of outgroup stereotypes by enhanced ingroup identity. J Exp Soc Psychol [internet]. 1991 [cited 2020 Feb 13]; 27(5): 431-452. Available from: https://www.sciencedirect.com/science/article/pii/002210319190002N?via%3Dihub doi: 10.1016/0022-1031(91)90002-N

5. Ashforth BE, Mael F. Social Identity theory and the organization. Acad Manage Rev [internet]. 1989 [cited 2020 Jan 29]; 14(1), 20-39. Available from: https://www.jstor.org/stable/258189

6. Nosek BA, Greenwald AG, Banaji MR. Understanding and using the implicit association test: II. Method variables and construct validity. Pers Soc Psychol Bull [internet]. 2005 [cited 2020 Mar 05]; 31(2), 166-180. Available from: https://journals.sagepub.com/doi/10.1177/0146167204271418 doi 10.1177/0146167204271418
7. Hugenberg K, Wilson JP. Faces are central to social cognition. In Carlston DE, editor. The Oxford Handbook of Social Cognition. Oxford library of psychology: Oxford University Press; 2013. 167-193 p.

8. Hehman E, Stolier RM, Freeman JB, Flake JK, Xie SY. Toward a comprehensive model of face impressions: What we know, what we do not, and paths forward. Soc Personal Psychol compass [internet]. 2019 [cited 2020 Feb 12]; 13(2). Available from: https://onlinelibrary.wiley.com/doi/abs/10.1111/spc3.12431 doi: 10.1111/spc3.12431

9. Freeman JB, Ambady N. A dynamic interactive theory of person construal. Psychol Rev [internet]. 2011 [cited 2020 Feb 12]; 118(2), 247-279. Available from: https://doi.apa.org/doiLanding?doi=10.1037%2Fa0022327 doi: 10.1037/a0022327

10. Goff PA, Elberhardt JL, Williams MJ, Jackson MC. Not yet human: Implicit knowledge, historical dehumanization, and contemporary consequences. J Pers Soc Psychol [internet]. 2008 [cited 2020 Mar 05]; 94(2), 292-306. Available from: https://doi.apa.org/doiLanding?doi=10.1037%2F0022-3514.94.2.292 doi: 10.1037/0022-3514.94.2.292

11. Payne K. Weapon bias: Split second decisions and unintended stereotyping. Curr Dir Psychol Sci [internet]. 2006 [cited 2020 Feb 07]; 15(6), 287-291. Available from: https://journals.sagepub.com/doi/10.1111/j.1467-8721.2006.00454.x doi: 10.1111/j.1467-8721.2006.00454.x

12. Todd AR, Thiem KC, Neel R. Does seeing faces of young Black boys facilitate the identification of threatening stimuli? Psychol Sci [internet]. 2016 [cited 2020 Mar 05]; 27(3), 384-393. Available from: https://journals.sagepub.com/doi/10.1177/0956797615624492 doi: 10.1177/0956797615624492

13. Thiem KC, Neel R, Simpson AJ, Todd, AR. Are Black women and girls associated with danger? Implicit racial bias at the intersection of target age and gender. Pers Soc Psychol Bull [internet]. 2019 [cited 2020 Mar 06]; 45(10), 1427-1439. Available from: https://journals.sagepub.com/doi/10.1177/0146167219829182 doi 10.1177/0146167219829182

14. Wilson JP, Hugenberg K, Rule NO. Racial bias in judgments of physical size and formidability: From size to threat. J Pers Soc Psychol [internet]. 2017 [cited 2020 Mar 05]; 113(1), 59-80. Available from: https://doi.apa.org/doiLanding?doi=10.1037%2Fpspi0000092 doi: 10.1037/pspi0000092

15. Blair IV, Judd CM, Chapleau KM. The influence of Afrocentric facial features in criminal sentencing. Psychol Sci [internet]. 2004 [cited 2020 Mar 06]; 15(10), 674-679. Available from : https://journals.sagepub.com/doi/abs/10.1111/j.0956-7976.2004.00739.x doi: 10.1111/j.0956-7976.2004.00739.x

16. Butler RN. Psychiatry and the elderly: An overview. The American Journal of Psychiatry [internet]. 1975 [cited 2020 Feb 16]; 132(9), 893-900. Available from: https://ajp.psychiatryonline.org/doi/abs/10.1176/ajp.132.9.893doi: 10.1176/ajp.132.9.893

17. Martens A, Goldenberg JL, Greenberg J. A terror management perspective on ageism. J Soc Issues [internet]. 2005 [cited 2020 Feb 20]; 61(2), 223-239. Available from: https://spssi.onlinelibrary.wiley.com/doi/abs/10.1111/j.1540-4560.2005.00403.x doi: 10.1111/j.1540-4560.2005.00403.x

18. Cuddy AJC, Norton MI, Fiske ST. This old stereotype: The pervasiveness and persistence of the elderly stereotype. J Soc Issues [internet]. 2005 [cited 2020 Mar 05]; 61(2), 267-285. Available from: https://spssi.onlinelibrary.wiley.com/doi/abs/10.1111/j.1540-4560.2005.00405.x doi: 10.1111/j.1540-4560.2005.00405.x

19. Ebner NC. Age of face matters: Age-group differences in ratings of young and old faces. Behav Res Methods [internet]. 2008 [cited 2020 Feb 07]; 40(1), 130-136. Available from: https://link.springer.com/article/10.3758/BRM.40.1.130 doi: 10.3758/BRM.40.1.130

20. Wood W, Eagly AH. Cross-cultural analysis of the behavior of women and men: Implications for the origins of sex differences. Psychol bull [internet]. 2002 [cited 2020 Feb 05]; 128(5), 699-727. Available from: https://doi.apa.org/doiLanding?doi=10.1037%2F0033-2909.128.5.699 doi: 10.1037/0033-2909.128.5.699

21. Cheryan S, Siy JO, Vichayapai M, Drury BJ, Kim S. Do female and male role models who embody STEM stereotypes hinder women's anticipated success in STEM? Soc Psychol Personal Sci [internet]. 2011 [cited 2020 Feb 05]; 2(6), 656-664. Available from: https://journals.sagepub.com/doi/10.1177/1948550611405218 doi: https://doi.org/10.1177/1948550611405218

22. O'Toole AJ, Deffenbacher KA, Valentin D, McKee K, Huff D, Abdi H. The perception of face gender: The role of stimulus structure in recognition and classification. Mem Cogn [internet]. 1998 [cited 2020 Feb 07]; 26(1), 146-160. Available from: https://link.springer.com/article/10.3758%2FBF03211378 doi: 10.3758/BF03211378

23. Koenig, AM. Comparing prescriptive and descriptive gender stereotypes about children, adults, and the elderly. Front Psychol [internet]. 2018 [cited Jan 27]; 9(article 1086). Available from: https://www.frontiersin.org/articles/10.3389/fpsyg.2018.01086/full doi: 10.3389/fpsyg.2018.01086

24. Kang SK, Bodenhausen GV. Multiple identities in social perception and interaction: Challenges and opportunities. Annu Rev Psychol [internet]. 2015 [cited 2020 Jan 15]; 66(1), 547-574. Available from: https://www.annualreviews.org/doi/10.1146/annurev-psych-010814-015025 doi: 10.1146/annurev-psych-010814-015025

25. Crenshaw K. Demarginalizing the intersection of race and sex: A Black feminist critique of antidiscrimination doctrine, feminist theory and antiracist politics Univ Chic Leg Forum [internet]. 1989 [cited 2020 Jan 15]; 1989(1):139-167. Available from: https://chicagounbound.uchicago.edu/uclf/vol1989/iss1/8

26. Freeman BJ, Penner AM, Saperstein A, Scheutz M, Ambady N. Looking the part: Social status cues shape race perception. PLoS One [internet]. 2011 [cited 2020 Feb 17]; 6(9), e25107. Available from: https://journals.plos.org/plosone/article?id=10.1371/journal.pone.0025107 doi: 10.1371/journal.pone.0025107

27. Purdie-Greenaway V, Eibach R. Intersectional invisibility: The distinctive advantages and disadvantages of multiple subordinate-group identities. Sex Roles [internet]. 2008 [cited Jan 05]; 59(5), 377-291. Available from: https://link.springer.com/article/10.1007%2Fs11199-008-9424-4

doi: 10.1007/s11199-008-9424-4

28. Goff PA, Thomas MA, Jackson MC. "Ain't I a woman?": Towards an intersectional approach to person perception and group-based harms. Sex Roles [internet]. 2008 [cited 2020 Feb 04]; 59(5-6), 392-403. Available

from: https://link.springer.com/article/10.1007%2Fs11199-008-9505-4 doi: 10.1007/s11199-008-9505-4

29. Brigham JC. College students' racial attitudes. J Appl Soc Psychol [internet]. 1993 [cited 2020 Jan 29]; 23(23), 1933-1967. Available from: https://onlinelibrary.wiley.com/doi/abs/10.1111/j.1559-1816.1993.tb01074.x doi: 10.1111/j.1559-1816.1993.tb01074.x

30. Rollero C, Glick P, Tartaglia S. Psychometric properties of short versions of the ambivalent sexism inventory and ambivalence toward men inventory. TPM Test Psychom Methodol Appl Psychol [internet]. 2014 [cited 2020 Mar 05]; 21(2), 149-159. Available from: https://www.tpmap.org/psychometric-properties-of-short-versions-of-the-ambivalent-sexism-inventory-and-ambivalence-toward-men-inventory/ doi: 10.4473/TPM21.2.3

31. Cary AL, Chasteen AL, Remedios J. The Ambivalent Ageism Scale: Developing and Validating a Scale to Measure Benevolent and Hostile Ageism. Gerontologist [internet]. 2017 [cited 2020 Jan 29]; 57(2), e27-e36. Available from: https://academic.oup.com/gerontologist/article/57/2/e27/2632136 doi: 10.1093/geront/gnw118

32. Brewer MB, Dull V, Lui L. (1981). Perceptions of the elderly: Stereotypes as prototypes. J Personal Soc Psychol [internet]. 1981 [cited 2020 Feb 04]; 41(4), 656-670. Available from: https://content.apa.org/record/1982-09795-001 doi: 10.1037/0022-3514.41.4.656

Submitted: 01/14/21

Research Article

[1]Deparment of Chemistry, McGill University, Montreal, QC, Canada

Keywords

Hoogsteen, Watson-Crick, Metadynamics, Oxoguanine, GROMACS

Email Correspondence

ilya.dementyev@mail.mcgill.ca

Ilya Dementyev[1], Ashkan Karimi[1]

A Molecular Dynamical Investigation of the 7,8-dihydro-8-oxoguanine Mutation in dsDNA

Abstract

Background: The oxidization of a Guanine (G) base pair to 7,8-dihydro-8-oxoguanine (OG) is one of the most common DNA mutations. OG mutations can undergo a regular Watson-Crick base-pairing, or a reverse Hoogsteen (HG) base-pairing, especially in OG:A mismatches. While the causes of these mutations are well-understood, the kinetic and energetic characteristics of this new pseudo-base have never been fully investigated, especially at temperatures around biological function (17-37°C).

Methods: We created a simulation to derive the Free Energy Surface (FES) of OG:C and OG:A Hoogsteen to Watson-Crick base-pair (bp) transitions under multiple temperatures, relative to 2 collective geometric variables: the dihedral Chi and the pseudo-dihedral CPD angle. To make the simulation, we used the relatively recent Metadynamics algorithms in conjunction with GROMACS 2020.2.

Results: The lowest free energy increased linearly with increasing temperatures (17-37°C). Major Chi and CPD rotations at these minima varied heavily for 27°C and 32°C (the largest was seen in the former), but stayed relatively similar for other temperatures, indicating a highly sensitive relationship to temperature, likely due to DNA flexibility, quantum mechanical (QM) effects, and hydrogen bonding. Free energies had a weak negative linear relationship, and free energy hypersurfaces were given for studied temperatures of 17-37°C. Human body temperature (37°C) results were also included and explained. The simulations showed why OG:A Hoogsteen bps often occur in organisms and are energetically preferable to standard Watson-Crick. OG:C HG base pairings are determined to likely be not as common as OG:A HG.

Limitations: Future investigations must focus on discovering rate constants of these base-pairs, as time constraints did not permit them to be done here, as well as more QM-focused simulations.

Introduction

Genetic information storage in DNA, encoded by base-pair sequences of Adenine, Guanine, Cytosine, and Thymine, is extremely sensitive to change. Cancer and other genetic diseases, such as Sickle-cell Anemia, are all caused by mutations in this polymer, leading to a change in function due to information distortion. The conversion of a Guanine (G) base pair to 7,8-dihydro-8-oxoguanine (OG) via oxidation (1) is among the most common and biologically relevant DNA mutations. This mutation is caused by the oxidation of guanine, by a reactive oxygen species (ROS), for instance with HOOO, O2-, and OH. (2) While these mutations and the mechanism of their formation is well-studied, dynamical characteristics of the new pseudo-base have not been fully investigated. HG pairing is also a required characteristic for proper DNA strand replication. (3) Hence, HG is necessary for some genomic loci, but is detrimental in others.

The 8-oxoguanine-Cytosine (G:C) base pair, mutated from the standard G:C base pair, is the mutation that will be covered, as well as OG:A (mutated from G:A). Upon mutating, OG is capable of forming not only a Watson-Crick base-pair, but also the less-common Hoogsteen base-pair after propeller rotation (when one base (OG) turns using its glycosidic bond with respect to the other (C or A)). It is the DNA bending local to the mutation, caused by this glycosidic bond rotation, which causes the human OGG1 enzyme to identify and repair the mismatch. (4) Therefore, understanding the kinetic details would help scientists develop better diagnostic tools and treatments for cancer, especially at the human body temperature (approximately 37°C). (5)

The software PLUMED was used in conjunction with GROMACS. For PLUMED, GROMACS v. 2019.6 was used (6) (later releases not yet supported for PLUMED). For non-Metadynamics simulations, GROMACS v. 2020.2 was used (29)—a software for molecular dynamics (MD) simulations. Metadynamics is a computational method where one is able to sample conformations with high-energy barriers for any molecular process (from a geometric transition to a chemical reaction) that are normally not reached with regular non-biased methods. Metadynamics is especially useful to study the energetics of conformational changes, as more than one collective variable (CV) can be used to study the energy. CVs are differentiable functions of vectors of 3N atomic cartesian coordinates, (7) which may be anything from dihedral angle torsion, to the centre-of-mass distance between 2 nucleotides. (8) CVs were chosen at the researcher's discretion and are constrained only by the software's capabilities. The most important CVs that were used for this project were the Chi dihedral and CPD pseudo-dihedral angles defined by Pak et. al.—the outlined boxes represent the centre of mass of atoms within the box (Fig. 1B). (9)

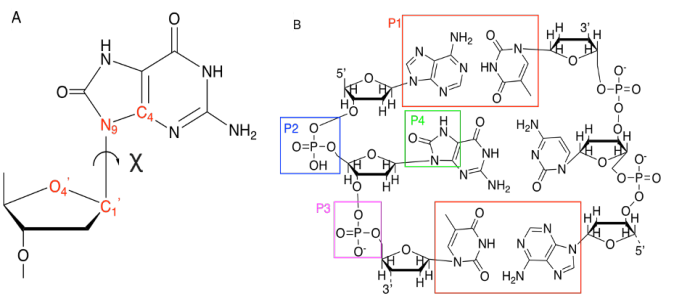

Figure 1. A. The definition of the glycosidic dihedral angle, chi. B. The definition of the pseudo-dihedral angle CPD. Both modified diagrams from Pak et. al. to fit this paper's context. (6)

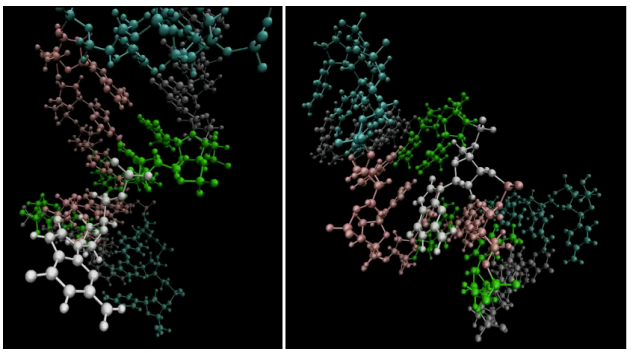

Figure 2. (left to right) A. A nitrogenous base flipped out of the helix. B. The nitrogenous base engaging in Hoogsteen base pairing.

Contrary to older energetic sampling methods, no "a priori knowledge of the [energy] landscape is required" (8) for accurate sampling with Metadynamics. The only requirement is to have a sufficiently long simulation that will allow the sampling to explore every niche of the energy surface. According to Pak et. al., 20 ns is sufficient, (9) although 500 ns was used to ensure convergence specific for the outlined systems. This was decided based on simulations performed from 50 to 200 ns. Metadynamics is inherently parallelizable, allowing GPU acceleration to speed up the sampling. (8) Specifically, Well-tempered Metadynamics was used, in which a biased sampling filled up a region, and became progressively less biased the "higher" it sampled, ensuring a relevant description of the potential landscape. Energetics plays an important role as seen in its direct mathematical relationship to probability (10):

$$\lim_{t\to\infty} P(s,t) \propto e^{\frac{-F(s)}{T+\Delta T}} \quad (1)$$

Where P(s, t) is the probability of the system having CV "s" at time "t", e is Euler's number, F(s) is the Free Energy, T is the absolute temperature (17-37°C), and ΔT is the raised temperature, defined as such (10):

$$\Delta T = T(\gamma - 1) \quad (2)$$

Where γ is the bias factor (γ = 15). (9) Hence, the lower a conformation's free energy, the higher the likelihood of that conformation existing at any time, which is relevant when predicting the equilibrium rate constants for the WC to HG transition. A system's free energy is defined as:

$$\Delta G = \Delta G° + k_B T \ln Q \quad (3)$$
$$\Delta G = \Delta H - T\Delta S \quad (4)$$

Where ΔG° is the Gibbs free energy (GFE) at SATP, k_B is Boltzmann's constant, T is the absolute Kelvin temperature, Q is the reaction quotient, ΔH is enthalpy, and ΔS is entropy. At equilibrium, Q = K, whose formula is expressed as:

$$K = \frac{k_{WC\to HG}}{k_{HG\to WC}} \quad (5)$$

Because of DNA's complex chemistry, some genomic loci will have different energies than others. (11) Propeller rotation does not happen in a regular simulation because of the high energy barrier between WC and HG conformations. For instance, one calculated value of kWC->HG = 16.7 s^{-1} showed that the HG conformation occurs infrequently. (12) Although the nucleotides used by Alvey et. al. differ from the ones we studied, around the same values for the OG:A and OG:C were expected. The forward rate constant for OG:A may be slightly greater than OG:C, due to OG:A being the preferred mismatch. To analyze the error, block sampling was used. Sometimes, CVs were correlated, as can be displayed by the autocorrelation function (13):

$$R(\tau) = \frac{(X_t - <X>)(X_{t+\tau} - <X>)}{\sigma^2} \quad (6)$$

Where X is a variable, <X> is the variable's average, σ^2 is the variance, t is time, and τ is the time lag. Between 2 variables, if the function is 1 at x = 0, and 0 elsewhere, the variables are perfectly independent. Within these simulations, CVs had non-zero values at x ≠ 0, displaying correlation. This implies that the central limit theorem does not hold, and taking the variance of all the values is not enough for calculating error bars as it underestimates such errors. (14) However, block sampling circumvents this issue by taking averages of groups of data ("blocks"), giving an accurate value for the error while taking correlation into account:

$$\sigma^2 = \frac{1}{N_b - 1}\sum_{i=1}^{N_b}(s_i' - < S >)^2 = 1 \quad (7)$$

Where N_b is the number of blocks, s_i' the block's average, and <S> is the average of all blocks summed together.

Methods

System Preparation

The system designed was an NPT canonical ensemble. PDB files for the B-DNA were made on Avogadro (15) and edited using Notepad++. (16) The charge entries for 8-oxo-guanine in residuetypes.dat were taken from Miller et. al (17) to ensure a charge close to zero (-0.0001 < Qsys < 0.0001). (18) The Particle-Mesh Ewald (PME) algorithm was used for long-range interactions, which introduced new species into the system if the net charge was non-zero. (18) Miller's data did not include the sugar, but the charge became an integer once the partial charges for the deoxyribose were included (Appendix I). The resonance structures shown in Fig. 2A demonstrate that the base's 5-membered ring is planar. For the simulated system, the most recent and reliable AMBER-OL15 force field used (19) was available on GROMACS' user-generated site. The SPCE model of water was used for solvation. (20) VMD software was used for the modelling to check every GROMACS output file. (21) To neutralize the system, the 5.69 nm cubic unit cell was programmed to contain 0.2 M NaCl. This salt was chosen per the supervisors' advice since they designed probes to analyze Hoogsteen base-pairings in NaCl solution. A Van-der-Waals cut-off was used for short-range atomic interactions. (22) The algorithms used for the barostat and thermostat were Parrinello-Rahman and Nose-Hoover respectively. (23, 24) These algorithms were chosen based on accuracy. Results would have been different if different parameters were used. The dsDNA used was an 11-nucleotide sequence (11-mer) recommended by Mr. Karimi, shown below:

5'-GGGTT(OG)ATGGG-3'
3'-CCCAA(T/A)TACCC-5'

The 3 GC pairs at each end increased the structural stability of the strand by decreasing fraying. An 11-mer was chosen since an 11-nucleotide strand is the minimum length required to be stable over long simulation periods, as suggested by Mr. Karimi.

The simulation process was divided into 5 sections: System Design and Preparation (including solvation and addition of ions), Energy Minimization, NVT Equilibration, NPT Equilibration, and the canonical production MD. (25) NVT was done first as it is less calculation-dense and avoids the travelling of the dsDNA molecule between unit cells. NPT then equilibrates for pressure and prepares the system for NPT-style Production MD, more accurate to real-life experiments. The equilibration took no longer than an hour, with a time step of 1 fs. The simulations ran on the Cedar cluster located in Vancouver, CA. To speed up the simulation, the Nvidia P100 GPU was used to perform CUDA acceleration, an optimization method used for parallelizing heavy computational tasks. (26) Metady

namics was used to analyze the kinetics of OG propeller rotation. Since a larger time-length gives more accurate results, (8) 500 ns simulations were conducted on OG:C and OG:A base pairs.

All MD parameter and topology files were displayed in the supporting information. The following summarization steps were modified from Dr. Lemkul's tutorials on GROMACS. (30) The following steps assume that GROMACS and PLUMED were already installed, and that the topology file was saved after every step.

System Design

To begin the simulation, the pre-edited .pdb file was converted into a GROMACS file. AMBER99-sb-il and SPCE were chosen for the force field and water model respectively. Now that the file was created, the system shape was defined to be a cubic unit cell of side length 5.69 nm. This number was taken from Pak et al., (9) who had previously done calculations for 8-oxoguanine in a different dsDNA system. The dimension was also chosen due to it tightly fitting around the dsDNA, while also maintaining enough space so that the dsDNA did not immediately leave the unit cell.

Solvation

Now that the system was constructed, it needed to be solvated with water, with the gmx solvate command. Several other commands were used that chose the spc216.gro GROMACS water model file corresponding to SPCE.

Addition of Ions

To add ions, the grompp command was used to prepare the file (ions.mdp must be created beforehand; see Supporting Information). This created a .tpr (portable binary run input) file, which contains coordinate, trajectory, and parameter information about the system. (29) Then, the actual ion generation was performed using the gmx genion command. When prompted, "SOL" was chosen, which would correspond to a number—the same process as choosing the force field. This replaced some solvent molecules with ions.

Energy Minimization

Energy minimization was performed using the "grompp" command, which outputted file_em.tpr, used for energy minimization. It used the steepest-descent minimization algorithm to adequately minimize the system's energy. Graphs made from the descent simulation showed convergence. A conjugate gradient method would have also increased the speed of the initial convergence, but at the time of creating the simulation, we had not received help from supervisors with regards to minimization algorithms, and were not aware of this method. Hence, a good quantity of information was found by searching through past online MD tutorials, none of which made mention of the conjugate gradient method.

The simulation ran using the gmx mdrun command. The important file was "file_em.tpr" as that gave the specificity to the MD simulation type that ran with mdrun. Using "-v" (verbose), every step of the process was listed out. This simulation took no longer than 30 minutes. The output file was "file_em.edr". To analyze the results, we used the gmx energy command. Any analysis that was listed by GROMACS was able to be performed in this step. The most important would be the potential energy. Its graph appears as exponential decay for most systems. The graph was acquired by typing "xmgrace analysis.xvg" into the terminal (assuming xmgrace is installed), and the results were displayed.

NVT Equilibration

The first step of the 2-step equilibration was performed using gmx grompp, which was a similar process to the previous step, outputting the file "file_nvt.edr". The second simulation was performed using the same gmx mdrun code syntax. Again, this did not take more than an hour. The file was analyzed using the same command, "gmx energy".

NPT Equilibration

The second step was done with gmx grompp with the file_nvt.gro file as the checkpoint and the gmx mdrun command as usual:

gmx grompp -f file_npt.mdp -c file_nvt.gro -r file_nvt.gro -t file_nvt.cpt -p topol.top -o file_npt.tpr

The "-t" command included the checkpoint file (file_nvt.cpt) that contained the required variables needed for the equilibration to continue from the previous one. The results were again analyzed using "gmx energy", and the "xmgrace" software.

Production MD

The final simulation was longer than the previous 3, because they always ran for at least 1 ns, corresponding to a 500,000 time-step simulation (the previous ones had 50,000). Nevertheless, the syntax was very similar to the NPT equilibration step, except the file_npt.gro and file_npt.cpt files were used as checkpoint files. The final step was done using the gmx mdrun and -plumed command, with "plumed.dat" written in text after the latter command. The production MD was NPT, to ensure that the GFE was being calculated (10)

Post-Production Analysis

There were a lot of possible analyses that could be done after the final MD was finished. However, correcting for periodicity is good for all analyses. The studied solute would sometimes cross the boundary between system boxes (i.e. unit cells). To avoid re-analysing that periodicity, the "trjconv" command was used as per GROMACS guidelines. Now, any type of analysis could've been performed using analytical commands found in the GROMACS handbook. (29)

Metadynamics – PLUMED Analysis

For correct PLUMED utilization, the steps were completed until NPT Equilibration. Then, the template file "plumed.dat" (Supporting Info) generated necessary variables. Chi, CPD, bias-factors, and sigma values were found in published papers related to the system investigated. (9) For OG-related simulations with dsDNA, only atom index editing was necessary. Chi and CPD values were cross-referenced with the most recent coordinate (.gro) file to ensure that the correct atoms are used. Finally, the simulation ran with the mdrun and -plumed commands. When the simulation finished, dihedral angles (and their energy) were extracted using plumed sum_hills, which generated a file called "fes.dat" which was then converted to Excel format and plotted.

Error Analysis

Error analysis was performed using simulation post-analysis. To do this, the PLUMED "driver" function was used. However, before any inputs were given for the function, we created a mass-charge (mc) file for the driver to use. To do this, the most recent .gro file was taken (usually the NPT one) and analyzed via gmx editconf. This created the necessary .pdb file that was used with the "plumed driver" utility and plumed.dat. This gave COLVAR_ERR, which would then be used to extract the error biases for each data point (the hashtags in the beginning denote sentences that should not be written into the terminal). The following code is modified from https://www.plumed.org/doc-v2.5/user-doc/html/trieste-4.html:

```
# find maximum value of bias
bmax=`awk 'BEGIN{max=0.}{if($1!="#!" && $4>max)max=$4} END{print max}' COLVAR_ERR`
```

 # print phi values and weights
awk '{if($1!="#!") print $2,exp(($4-bmax)/kbt)}' kbt=2.494339 bmax=$bmax COLVAR_ERR > chi.weight

This created an error file for the Chi variable (chi.weight). This file was then processed using a python script to get the results for each block size:

for i in `seq 1 10 x`; do python3 do_block_fes.py chi.weight 1 -3.141593 3.018393 51 2.494339 $i; done

Variable "x" was chosen for the length of the simulation, as it can vary. This printed out one data file for each block size containing the error value. To collect the data into one text file, the following input was given:

for i in `seq 1 10 x`; do a=`awk '{tot+=$3}END{print tot/NR}' fes.$i.dat`; echo $i $a; done > err.blocks

This outputs an Excel-compatible ".blocks" file. The same steps can be repeated for as many CVs as necessary. The error for a specific temperature was given as the average between the corresponding Chi and CPD errors.

Results

All data was analysed and visualized using the Python Pandas package in Spyder 4.0 and Matplotlib.

In Fig. 3, OG:A energetics have a much smaller range, indicating more stability. This was expected, as OG tends to get mismatched more with A during replication. Both energies have a positive correlation, as expected, with high R-squared values. However, while the R-squared value was relatively strong, neither lines will likely give an accurate description of the process' enthalpy and entropy, due to the non-Boltzmann interactions that took place. (12)

Lastly, for both base-pairs, Chi was determined to change in a polynomial fashion across the temperature scale chosen. The curves bore a resemblance to sinusoidal functions, but such a relation can only be confirmed from multiple analyses of each temperature. All Chi and CPD values had an error of ± 0.0561 rad (= ± 3.2°).

Discussion and Conclusion

Firstly, the "blue" area for all simulations had the largest area at the highest temperature, due to an increase in area with an increase in temperature (Fig. 3 – Only OG:A bp is shown). This makes sense, as each increase in temperature steadily approached DNA's melting point. It also confirms that HG base-pairing is more preferential (on average) in OG:A as opposed to OG:C bp, evidenced by the larger frequency of blue areas in $-\pi/2 = -90° < \text{Chi} < \pi/2 = 90°$.

Next, all of the minimum FE angles lied within the HG range, indicating that both systems were relatively more stable in that state rather than a WC one. However, the absolute transition energy was quite small, indicating a weakly spontaneous rotation can occur, except for OG:A 27°C (Fig. 3). Furthermore, OG:C showed an almost-constant angle for the most stable WC angle, which interestingly lies exactly on the upper angle bound for HG to WC transition. Lastly, the rotational energy for the more stable OG:A bp at $T_{\text{human body}} = 37°C$ (310 K) (Fig. 4 and 5) showed an almost double increase relative to the OG:C transition, implying that they were likely more common and more relevant to biological effects of HG bp. Smaller error within OG:A points implies a greater stability of that conformation relative to OG:C.

For OG:C, although the general positive trend was expected, the low strength of it was not (Fig. 5 – Only OG:A bp is shown). This was very likely due to the non-Boltzmann effects on the system, such as quantum mechanical (QM) effects that were not taken into consideration for the interest of fast time and data processing. QM effects of the glycosidic and CPD angles potentially contributed to the discrepancy. Simulations in the future should focus on finding them.

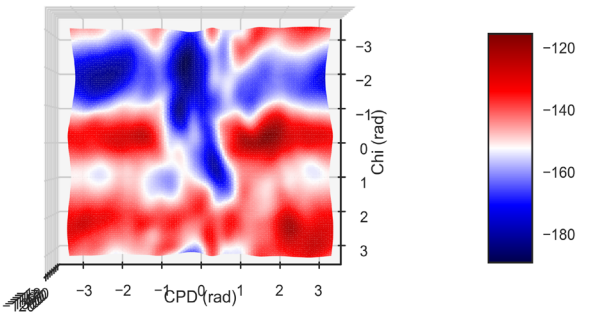

Figure 3. A. The Gibbs FES (in kJ/mol) of OG:A at 27°C

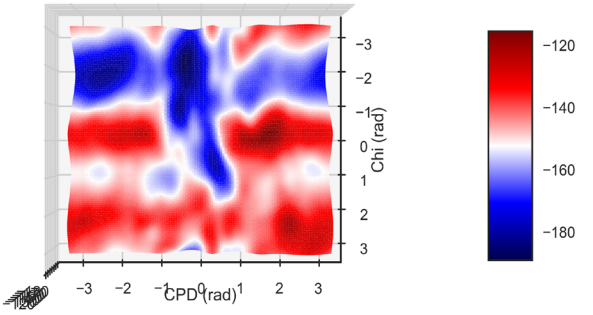

Figure 4. A. The Gibbs FES (in kJ/mol) of OG:A at 37°C

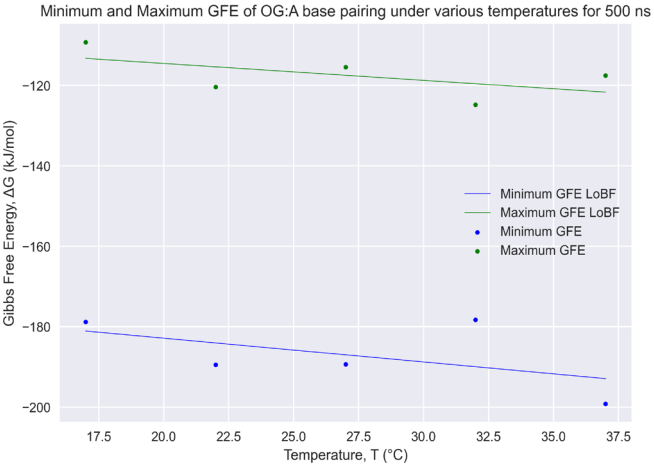

Figure 5. The minimum and maximum GFE of OG:A base pairing under various temperatures for 500 ns, with their corresponding lines of best fit (LoBF). The R-squared values for the maximum and minimum lines are 0.57 and 0.53 respectively. This shows decent correlation with the minimum GFE from standard thermodynamic principles. Error bars are too small to be significant in visual format.

In Fig. 5, most of the data trends were expected. The relatively high R-squared of the minimum value indicates that the MD was partially successful in replicating the results without QM assistance. However, while the R-squared value was relatively strong, neither lines will likely give an accurate description of the process' enthalpy and entropy, due to the

non-Boltzmann interactions that took place. (12) In Fig. 6, it is interesting that the major rotations from WC to Hoogsteen occur between 300-305 K (27-32°C), just before reaching the original position at the human body temperature of 310 K (37°C). This suggests a very sensitive relationship between the stability of the Hoogsteen conformation to temperature, within just a few degrees Celsius, which is the same as the CPD angle, although the latter shows less dramatic changes between temperatures. It is likely that at these temperatures, the dihedral angle rotations would occur the most frequently, but this can only be confirmed through more Metadynamics studies of this temperature range. More data points at or above the minimum GFE could have been sampled to create a better representation of the angle. However, assuming that the sampling of the minimum GFE is sufficient, one reason for this phenomenon could be the DNA's intrinsic flexibility providing more support for the Chi angle to turn. At lower temperatures, the DNA may not be as flexible, but at higher temperatures, the flexibility could cause the CPD angle to change significantly, indirectly affecting Chi. This would not explain the regular Chi at 310 K (37°C) though.

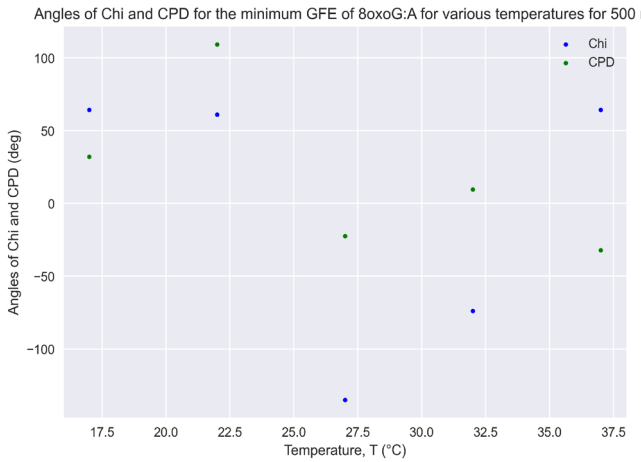

Figure 6. Chi and CPD angles for minimum GFE of OG:A for various temperatures for 500 ns.

Lastly, since the rotations of Chi in both base pairs are periodic for the temperature scales chosen, it is likely that a sinusoidal function (or some form of a Taylor approximation) can represent it well (Fig. 6 – only OG:A is shown). However, the CPD angle's deviation from a sinusoid in OG:C implies backbone contributions to base-pair flipping are more complex than trigonometric expressions, and potentially better represented with polynomials, which is why they were fitted and analyzed as such. Again, QM likely played a large role in influencing this data that Classical MD could not account for. The maximum errors listed were all smaller than k_BT, further supporting that the simulations converged well. Error graphs also showed excellent convergence too, with very small error. Future simulations should focus on confirming the near-sinusoidal relationship between temperature and Chi rotation, as well as finding ways to incorporate a more QM-leaning analysis for the sake of improved accuracy, as simulation technology advances to the point where such is possible.

Acknowledgements

This research was enabled in part by support provided by WestGrid (www.westgrid.ca), ACENET (www.ace-net.ca) and Compute Canada (www.computecanada.ca). This work was carried out using the open-source, community-developed PLUMED library,(27) version 2.5.4.(28). According to supervisors, the author is the first person in McGill Chemistry to perform MD simulation research, so some of the techniques/algorithms chosen may not be up-to-standard with the latest research due to lack of guidance. For access to more figures, they can be provided free-of-charge by contacting the author at ilya.dementyev@mail.mcgill.ca.

References

1. Pinak M. CHAPTER 10 - Enzymatic recognition of radiation-produced oxidative DNA lesion. Molecular dynamics approach. In: Starikov EB, Lewis JP, Tanaka S, editors. Modern Methods for Theoretical Physical Chemistry of Biopolymers. Amsterdam: Elsevier Science; 2006. p. 191-210.

2. Bruskov VI, Malakhova LV, Masalimov ZK, Chernikov AV. Heat-induced formation of reactive oxygen species and 8-oxoguanine, a biomarker of damage to DNA. Nucleic Acids Res. 2002;30(6):1354-63.

3. Johnson RE, Prakash L, Prakash S. Biochemical evidence for the requirement of Hoogsteen base pairing for replication by human DNA polymerase ι. Proceedings of the National Academy of Sciences of the United States of America. 2005;102(30):10466.

4. Hashiguchi K, Stuart JA, de Souza-Pinto NC, Bohr VA. The C-terminal alphaO helix of human Ogg1 is essential for 8-oxoguanine DNA glycosylase activity: the mitochondrial beta-Ogg1 lacks this domain and does not have glycosylase activity. Nucleic Acids Res. 2004;32(18):5596-608.

5. Obermeyer Z, Samra JK, Mullainathan S. Individual differences in normal body temperature: longitudinal big data analysis of patient records. BMJ. 2017;359:j5468.

6. Berendsen HJC, van der Spoel D, van Drunen R. GROMACS: A message-passing parallel molecular dynamics implementation. Computer Physics Communications. 1995;91(1):43-56.

7. Fiorin G, Klein ML, Hénin J. Using collective variables to drive molecular dynamics simulations. Molecular Physics. 2013;111(22-23):3345-62.

8. Barducci A, Bonomi M, Parrinello M. Metadynamics. Wiley Interdiscip Rev: Comput Mol Sci. 2011;1(5):826-43.

9. Yang C, Kim E, Pak Y. Free energy landscape and transition pathways from Watson–Crick to Hoogsteen base pairing in free duplex DNA. Nucleic Acids Res. 2015;43(16):7769-78.

10. Barducci A, Bussi G, Parrinello M. Well-Tempered Metadynamics: A Smoothly Converging and Tunable Free-Energy Method. Physical Review Letters. 2008;100(2):020603.

11. Khandelwal G, Lee RA, Jayaram B, Beveridge DL. A statistical thermodynamic model for investigating the stability of DNA sequences from oligonucleotides to genomes. Biophys J. 2014;106(11):2465-73.

12. Alvey HS, Gottardo FL, Nikolova EN, Al-Hashimi HM. Widespread transient Hoogsteen base pairs in canonical duplex DNA with variable energetics. Nat Commun. 2014;5:4786.

13. Nounou MN, Bakshi BR. Chapter 5 - Multiscale Methods for Denoising and Compression. In: Walczak B, editor. Data Handling in Science and Technology. 22: Elsevier; 2000. p. 119-50.

14. Ross SM. Chapter 7 - Distributions of Sampling Statistics. In: Ross SM, editor. Introductory Statistics (Fourth Edition). Oxford: Academic Press; 2017. p. 297-328.

15. Hanwell MD, Curtis DE, Lonie DC, Vandermeersch T, Zurek E, Hutchison GR. Avogadro: an advanced semantic chemical editor, visualization, and analysis platform. Journal of Cheminformatics. 2012;4(1):17.

16. Berman H, Henrick K, Nakamura H. Announcing the worldwide Protein Data Bank. Nature Structural & Molecular Biology. 2003;10(12):980-.

17. Miller JH, Fan-Chiang C-CP, Straatsma TP, Kennedy MA. 8-Oxoguanine Enhances Bending of DNA that Favors Binding to Glycosylases. Journal of the American Chemical Society. 2003;125(20):6331-6.

18. Hub JS, de Groot BL, Grubmüller H, Groenhof G. Quantifying Artifacts in Ewald Simulations of Inhomogeneous Systems with a Net Charge.

Journal of Chemical Theory and Computation. 2014;10(1):381-90.

19. Zgarbová M, Šponer J, Otyepka M, Cheatham TE, Galindo-Murillo R, Jurečka P. Refinement of the Sugar–Phosphate Backbone Torsion Beta for AMBER Force Fields Improves the Description of Z- and B-DNA. Journal of Chemical Theory and Computation. 2015;11(12):5723-36.

20. Berendsen HJC, Grigera JR, Straatsma TP. The missing term in effective pair potentials. The Journal of Physical Chemistry. 1987;91(24):6269-71.

21. Humphrey W, Dalke A, Schulten K. VMD: Visual molecular dynamics. Journal of Molecular Graphics. 1996;14(1):33-8.

22. De Leeuw SW, Perram JW, Smith ER. Simulation of electrostatic systems in periodic boundary conditions. I. Lattice sums and dielectric constants. Proc R Soc London, Ser A. 1980;373(1752):27-56.

23. Hoover W. Canonical Dynamics: Equilibrium Phase-Space Distributions. Phys Rev A: At, Mol, Opt Phys. 1985;31:1695.

24. Parrinello M, Rahman A. Polymorphic transitions in single crystals: A new molecular dynamics method. J Appl Phys. 1981;52(12):7182-90.

25. Zheng L, Alhossary AA, Kwoh C-K, Mu Y. Molecular Dynamics and Simulation. In: Ranganathan S, Gribskov M, Nakai K, Schönbach C, editors. Encyclopedia of Bioinformatics and Computational Biology. Oxford: Academic Press; 2019. p. 550-66.

26. Hwu W, Rodrigues C, Ryoo S, Stratton J. Compute Unified Device Architecture Application Suitability. Computing in Science & Engineering. 2009;11(3):16-26.

27. Bonomi M, Bussi G, Camilloni C, Tribello GA, Banáš P, Barducci A, et al. Promoting transparency and reproducibility in enhanced molecular simulations. Nature Methods. 2019;16(8):670-3.

28. Tribello GA, Bonomi M, Branduardi D, Camilloni C, Bussi G. PLUMED 2: New feathers for an old bird. Computer Physics Communications. 2014;185(2):604-13.

29. Lindahl, Abraham, Hess, & van der Spoel. (2020, January 1). GROMACS 2020 Manual (Version 2020). Zenodo. http://doi.org/10.5281/zenodo.3562512

30. Lemkul J. From Proteins to Perturbed Hamiltonians: A Suite of Tutorials for the GROMACS-2018 Molecular Simulation Package [Article v1.0]. Living Journal of Computational Molecular Science. 2018;1.

Submitted: 01/11/2021

Research Article

[1]Faculty of Science, McGill University, Montreal, QC, Canada
[2]Department of Psychiatry, McGill University, Montreal, QC, Canada
[3]Douglas Mental Health University Institute, Montreal, QC, Canada

Keywords

Psychopharmacology, adolescence, cannabinoids, depression, impulsivity

Email Correspondence

armaan.fallahi@mail.mcgill.ca

Armaan Fallahi[1], Giovanni Hernandez[2,3], Jose-Maria Restrepo Lozano[2,3], Cecilia Flores[2,3]

Effects of adolescent cannabinoid administration in mice on behavioural inhibition and susceptibility to stress during adulthood

Abstract

Background: Cannabis is one of the most frequently used substances by adolescents. Early exposure to psychoactive compounds has been shown to alter normal brain development and has consequences for psychiatric illness and behaviour in adulthood. In this study, we explored the effects of adolescent synthetic cannabinoid exposure on susceptibility to stress in adulthood, in addition to changes in impulsive behaviour.

Methods: Chronic treatment with synthetic cannabinoid WIN55,212-2 (WIN) at various doses in adolescent mice was followed by the chronic social defeat stress paradigm in adulthood to assay changes in susceptibility to stress. We then employed the operant Go/No-Go task to investigate changes in impulsivity.

Results: No changes in susceptibility to stress were identified ($\chi 2(3)=0.585$, $p=0.900$). Strikingly, we demonstrated a dose dependent decrease in impulsivity of adolescent WIN-treated subjects as measured using the Go/No-Go task ($F(3, 20)=5.743$, $p=0.0053$).

Limitations: The main limitation of our findings is the small sample size, particularly for assaying changes in susceptibility to stress using the chronic social defeat stress paradigm. Furthermore, the single housing of animals and suboptimal performance of controls may have affected our findings in the Go/No-Go task.

Conclusion: Overall, this study presents a novel behavioural finding consequent to adolescent exposure to cannabinoids. Further research into the long-term effects of cannabinoid use in adolescence is needed, especially in light of its prevalent use and legalization in Canada.

Background

Cannabis is a psychoactive compound which has been legalized for recreational use in Canada. (1) Considering the subsequent increase in cannabis usage rates among adolescents (2), it is important to consider the consequences of exposure to cannabinoids during this critical period. (3–7) Neurobiological changes that occur during adolescence critically influence the development of healthy behaviours and psychiatric health. (8,9) Evidence from humans and animal models suggests that adolescent usage of drugs of abuse has lasting impacts on the development of the brain such as notable changes in cognitive features and increased susceptibility to stress in adulthood. (3,4,10,11)

There are many studies which address the consequences of adolescent cannabis use on a population level as they relate to neuropsychiatric illness. A large Swedish conscript registry study identified baseline cannabis use as a prominent risk factor for any psychotic symptom, rigorously demonstrating the population level association of cannabis with psychotic illness. (6,12–14) On the spectrum of stress-related disorders, Gobbi et al.'s 2019 systematic review and meta-analysis showed an association between cannabis use in adolescence and development of depression or suicidality in young adulthood. (11) Smolkina et al. in 2017 applied modelling to twin-registry studies including subjective reports, and even suggested a causal association between cannabis use disorder and major depressive disorder. (15) These studies demonstrate the importance of investigating the mechanisms behind how cannabis affects the developing brain. Findings from these studies may inform public health dissemination surrounding cannabis use in adolescence.

The endocannabinoid system is known to be involved in many aspects of neurodevelopment, including normal formation of synapses and plasticity. (16) Cannabis is more complex than other drugs of abuse with respect to its cognitive effects and the number of molecular pathways it modulates (16,17). Δ^9-Tetrahydrocannabinol (THC), the psychoactive component of cannabis, interacts with the endocannabinoid system in ways. It is challenging to determine whether THC administration will be excitatory or inhibitory at a neuronal level; factors such as local receptor density and temporal dynamics mediate the efficiency and valence of THC-mediated neurotransmission. (16) Since THC is a partial agonist of Cannabinoid receptor type 1 (CB1R) and Cannabinoid receptor type 2 (CB2R), in the present study we use the synthetic cannabinoid WIN55,212-2 (WIN), an agonist of CB1Rs, to isolate the effects of exogenous agonism of the endocannabinoid system. WIN has been used in numerous studies for its exceedingly high binding affinity for the CB1R when compared with that of THC. The endocannabinoid system modulates the development of the prefrontal cortex, known to be a major center for cognitive development during adolescence. (18) Consequently, studying the effect of agonism at CB1Rs during adolescence may shine light on persisting behavioural changes into adulthood.

Through human neuroimaging studies, cannabis use in adolescence has been shown to cause functional differences in the prefrontal cortex. Some studies suggest chronic cannabis users have decreased gray matter in the hippocampus and increased amygdalar volume, in addition to aberrant signalling in the nucleus accumbens, amygdala, and the prefrontal cortex. (19,20) These systems are strongly involved in memory, emotional regulation, and cognitive behaviours. Further, Miller et al. demonstrated that chronic adolescent administration of THC altered morphology of and transcriptional trajectories in cortical neurons. (21) Because insult to the endocannabinoid system is expected to alter prefrontal cortex development, this study examined a cognitive function associated with this area. Behavioural inhibition and impulsivity are known to be associated with the medial and dorsolateral prefrontal cortices. (22,23) The prefrontal cor

tex forms circuits with the posterior parietal cortex and supplementary motor areas to direct these behaviours, whose transmission is dominated by glutamatergic and dopaminergic inputs. (22)

There are a handful of studies which address similar behavioural questions. These studies use comparable tests of impulsivity and behavioural inhibition, such as the impulsive choice in a delayed reward paradigm, reversal learning, or response inhibition in a stop-signal paradigm. (24,25) Pattij et al. were interested in the acute effects of WIN on impulsive behaviour in decision making paradigms and found that they did not differ from controls. (25) In a paradigm very similar to our own, Johnson et al. chronically treated adolescent and adult rats with WIN and tested them on a battery of cue reversal-based tasks in adulthood. They found that adult, but not adolescent, experimental subjects had impaired behavioural inhibition. (24) Despite these results, we are interested in assaying this behaviour in a different behavioural paradigm.

In two parts, this study examines how adolescent synthetic cannabinoid exposure affects both susceptibility to stress and impulsive behaviour in a murine model. Given the demonstrated cortical changes in response to cannabinoid exposure, we hypothesized that exogenous modulation of the endocannabinoid system in adolescence could be associated with altered susceptibility to stress and behavioural inhibition in adulthood. We employed a chronic social-defeat stress model in mice to evaluate differential susceptibility to stress. In addition, the operant Go/No-Go paradigm was used to investigate changes in impulsivity across WIN treatment groups. This study is especially relevant since cannabis use is prevalent in adolescents.

Methods

Study Overview

A between-subjects design consisting of treatment with WIN, exposure to Chronic Social Defeat Stress (CSDS), and testing in Go/No-Go was used to address the hypotheses posited. The experimental strategy is detailed in Fig. 1. Fig. 2 describes the subjects of the study and their allocation to experimental groups. Only animals who did not undergo CSDS were tested in the Go/No-Go paradigm.

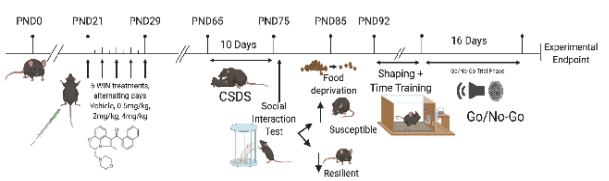

Figure 1. Timeline and schematic of study conducted. WIN55-212,2 treatment in adolescence, defeat paradigm and behavioural assessments, and Go/No-Go tasks.

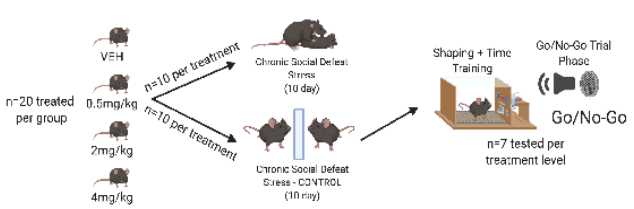

Figure 2. Subjects of the study, and their random allocation to experimental groups. 20 subjects treated with Vehicle, 0.5mg/kg, 2mg/kg, or 4mg/kg. 10 from each treatment group allocated to defeat or no-defeat, and 7 no-defeat subjects allocated to Go/No-Go tasks.

Ethical Considerations and Animal Information

The study was performed in accordance with the guidelines of the Canadian Council of Animal Care and approved by the McGill University and Douglas Hospital Animal Care Committee under Animal Use Protocol #5084. All mice used as subjects were obtained from Charles River Canada and were maintained on a 12 h light-dark cycle (lights on 8h00) with ad libitum access to food and water at all stages except during weight restriction for Go/No-Go.

Design and Subjects

The study included four groups: three treatment groups with 0.5 mg/kg, 2 mg/kg, and 4 mg/kg of WIN, and a vehicle (VEH) control. Twenty male C57BL/6 mice were treated per group (n = 20) and housed in groups of four. Subsequently, ten animals were randomly assigned to the defeat or non-defeat condition (n = 10). From the non-defeat condition, seven subjects from each of the four groups were randomly selected to perform the Go/No-Go task (n = 7). (Fig. 2) After the chronic social defeat stress paradigm, animals were singly housed until study completion. In sum, the study consisted of eighty mice. Deaths and exclusions from results are justified in Appendix 1.

WIN Treatment

Dosages used in this study include 0.5 mg/kg, 2 mg/kg, and 4 mg/kg of WIN. WIN was solubilized in 18:1:1 0.9% saline:cremophor:ethanol. Early adolescent mice were treated with saline or WIN via intraperitoneal injections from postnatal day (PND) 21 to PND29 between 12h00-13h00. Consistent with our previous experiments, groups received doses every other day in the same timeframe while alternating injection side for a total of five doses. Mice were returned to their cages upon drug administration. Although no rigid margins exist for this critical developmental period, the literature suggests that the period between weaning and PND32 comprise early adolescence due to distinct neurobehavioural traits exhibited. (9,26–28)

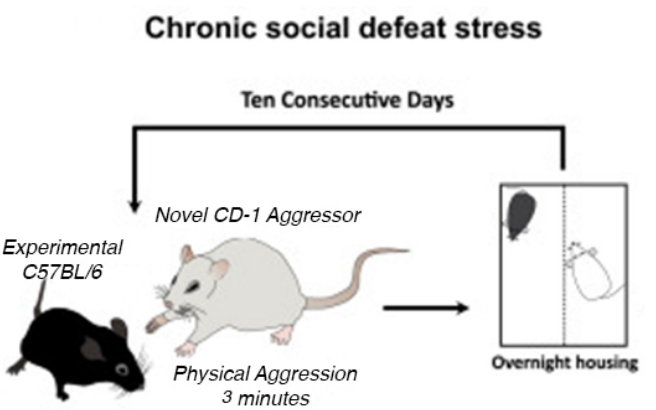

Figure 3. Flow of the CSDS model. Figure adapted from Torres-Berrió et al. 2019. C57BL/6 mice are subject to physical aggression from a novel CD1 aggressor mouse for 10 consecutive days. Overnight, they are housed with their aggressor from the preceding day with sensory but no physical contact.

Chronic Social Defeat Stress (CSDS)

The CSDS paradigm is a reliable method to produce stress-related phenotypes in mice and is widely used in mouse studies of susceptibility to stress. (29,30) The protocol was performed as in (30–32) and consisted of 10 daily sessions in which adult (PND65) subjects were exposed to 3 minutes of physical aggression by a novel aggressive CD-1 mouse, followed by overnight housing of the subject and the aggressor as shown in Fig. 3. The mice were separated by a perforated cage partition which allows for sustained

Control C57BL/6 mice were housed with a different control mouse every day, and no physical contact was permitted. Twenty-four hours after the final CSDS session, subjects were assessed on the social interaction test to determine whether the paradigm produced stress-related phenotypes.

Social Interaction Test (SIT)

To classify whether a subject was susceptible to stress, we assessed social preference using the social interaction test. The SIT was conducted as in. (30) In the first part of this test, subjects explore an open-field arena (42cm x 42cm) in the absence of a CD-1 mouse for 2.5 minutes. The second part involves a novel CD-1 mouse contained within a mesh cage in the same arena for 2.5 minutes. The social interaction ratio (SIR) is calculated by dividing time spent in the interaction zone with/without CD-1. The corner time ratio (CTR) is similarly calculated for time spent in corners. A subject is classified as susceptible if they spent less (SIR<1, CTR>1) or resilient if they spent more time socializing (SIR>1, CTR<1) compared to baseline (ratio = 1). (32)

Go/No-Go

Cognitive changes were assessed using a Go/No-Go task, as performed in previous studies. (27,33–35) Seven subjects from each treatment level (taken from controls in CSDS) were used in the Go/No-Go experiment to assess behavioural inhibition and impulsivity. Briefly, mice were food restricted for the duration of the behavioural testing, such that they maintained 85% of initial free-feeding weight. The task took place in operant behavioural boxes (Med Associates, Inc., St. Albans, Vermont). The boxes contained a house light, two illuminated nose poke holes, an adjustable tone generator, and a pellet dispenser. Chocolate-flavored dustless precision pellets (BioServ, Inc., Flemington, New Jersey) were used as the operant reinforcer. The experimental procedure consisted of three stages: conditioned reinforcement training, reaction time training, and the Go/No-Go task. Animals were subjected to one training or testing session per day, at approximately the same time daily.

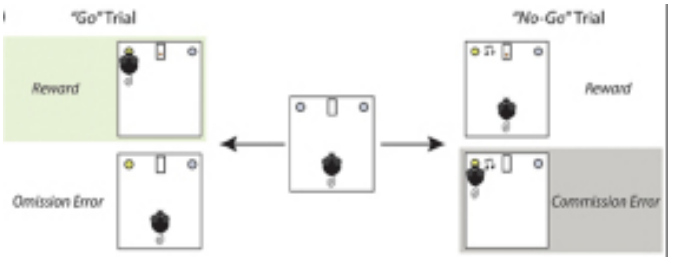

Figure 4. Coding of behaviours in the trial phase of Go/No-Go. Figure adapted from Cuesta and Restrepo-Lozano et al. 2019. Correct responses on the Go-trial are coded as hit, whereas lack of response to cue coded as an omission error. On No-Go-trials, abstention of behaviour results in reward, whereas response results in a commission error.

The subject is driven by hunger to pay attention and drive an association between cue-light and pellet reward. Once the task is learned by the subject, it is taught to respond quickly by shortening the window of successful response to the cue. Following successful completion of both training stages, mice underwent 16 sessions of the Go/No-Go task. Although 10 sessions were planned, the trial was extended to 16 days to assess behavioural differences. This task requires mice to respond to a "go" cue, identical to the cue they were trained on, or to inhibit their response to this cue when it is simultaneously presented with an auditory "no-go" cue (85dB tone). In the go trials, mice had 3 seconds to respond to the cue to receive a reward. This was coded as a "hit" in our analyses. In the no-go trials, the paired tone with the light cue signals the mouse to withhold from responding. If mice responded during the no-go trial, an inter-trial-interval is initiated, and no reward is dispensed. This counted as a "commission error" in the analyses. If mice withheld their response to the light cue on a no-go trial, a reward was dispensed. Within each session, the number of go and no-go trials is given an approximately 1:1 ratio and presented in a randomized order. Each session is 30 minutes in duration and consists of 30-50 of both go and no-go trials. Graphical description of behavioural coding for analysis is described in Fig. 4.

Data Analyses

Analyses were conducted by experimenters blinded to subject identity and treatment group. Preliminary data processing was conducted using Microsoft Excel. Visualisation and figure preparation were performed using Graphpad Prism 8.1. Sigmoidal curve fitting and associated statistical testing for Go/No-Go results were performed using OriginLab.

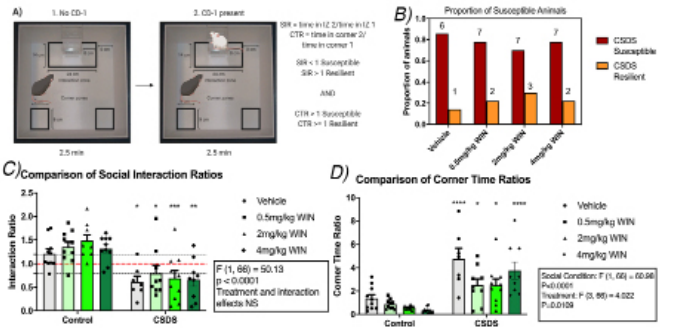

Figure 5. Susceptibility results from Social Interaction Test. A) Graphical description of the social interaction test. In brief, subject spends time exploring the arena, then, explores the arena with a CD-1 present. B) Proportion of susceptible and resilient animals by treatment group. C) SIR plotted for treatment groups compared by CSDS condition. D) CTR plotted for treatment groups plotted by CSDS condition. Mean +/- SEM. p-values: *<0.05, **<0.01, *** <0.001, ****<0.0001.

Results

Susceptibility to Stress

To address whether mice treated with WIN in adolescence were susceptible to stress, we compared the proportion of susceptible animals from each treatment level. The sample proportions of susceptible animals were roughly equal, failing to reject the null hypothesis (23=0.585, p=0.900). Graphical representation is found in Fig. 5B.

Social Interaction Test

To investigate the effect of WIN treatment level and the effect of CSDS on social interaction in the subjects, Two-Way ANOVAs were conducted. Treatment group (level of WIN) and CSDS condition were used as the factors, and SIR and CTR were the dependent variables. CSDS indeed produced a stress-susceptible phenotype by decreased interaction time and increased time spent in the corners for all treatment groups. (Fig. 5C-D) The significant difference and independence of samples indicated in the ANOVA allowed for Sidak's post-hoc comparisons, which validated the production of stress-susceptible phenotypes using the CSDS model.

Go/No-Go

Fig. 4 graphically depicts how a subjects' actions are coded in the trial phase of Go/No-Go. The assumption for assessing behavioural inhibition on this task is that sustained commission errors indicate increased impulsivity or decreased behavioural inhibition. The data is modeled in a few

ways to glean such information. In addition to plotting proportional commission errors over time, we use a pooled efficiency formula, an index of successful learning, to identify the proportion of trials (go or no-go) where the mouse performs correctly. Pooled efficiency is calculated by taking the mean of proportional hits and correct omissions on no-go. Another way to analyze such results is to iteratively fit sigmoidal curves for each subject on their proportional commission errors and determine an equation that best reflects each experimental group. This method is advantageous, as identifying M50 (day at which they reach 50% of their total learning) allows for comparison on relative inhibitory learning rates. It also provides a lower asymptote to their learning, which stands proxy for the level of total motor inhibition.

Go/No-Go – Commission

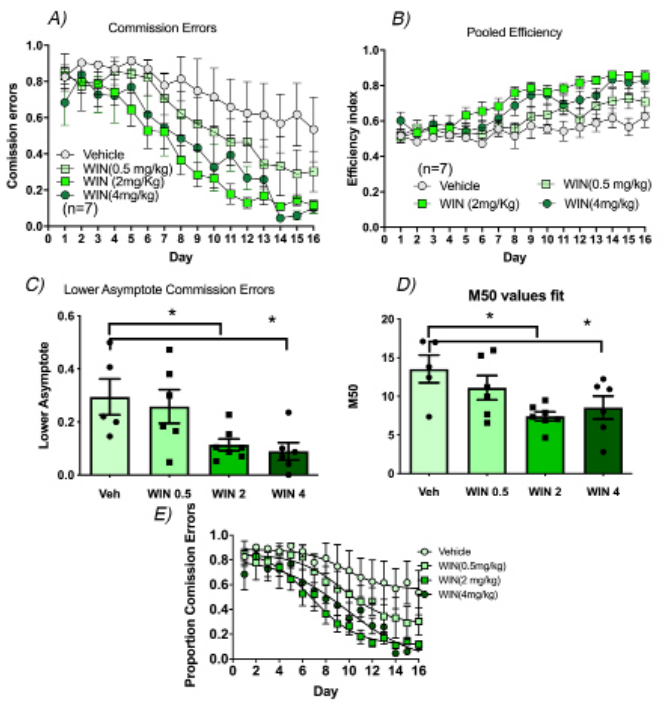

Figure 6. Summary of Go/No-Go results over 16 day trial period. A) Proportional commission error over time. B) Pooled efficiency over time. C) Sigmoidal curve fitting to commission errors. D) M50 group comparison. E) Lower asymptote group comparison. Mean +/- SEM. p-value * <0.05

In plotting commission errors over time, a Two-Way Repeated Measures ANOVA identifies the effect of treatment, days learning, as well as any potential interaction effect. Summary of the F-tests conducted are found in Table 1. There were main effects for both time F(15, 300)=33.34, p<0.0001 and WIN treatment F(3, 20)=3.843, p=0.0254; however, no statistical interaction effect was found F(45, 300)=1.286, p=0.1147. Treatment with 2 mg/kg and 4 mg/kg of WIN significantly decrease commission rates, whereas 0.5 mg/kg treated animals do not differ from vehicle control. Proportional commission errors resultantly suggest improved behavioural inhibition at high WIN doses during adolescence. Proportional commission errors for all groups are plotted in Fig. 6A, and significance for each treatment level in Supplementary Fig.1. There is no difference in proportion of omission errors across treatment groups.

Go/No-Go – Pooled Efficiency

Statistical analysis of the Pooled Efficiency measure is identical to that for proportional commission. Summary of F-tests conducted are found in Table 1. There were main effects for time F(15, 300)=24.12, p<0.0001 and WIN treatment F(3, 20)=5.743, p=0.0053, as well as a statistical interaction effect observed (indicating presence of an extraneous variable) F(45, 300)=1.882, p=0.0011. Like the report of commission errors, 2 mg/kg and 4 mg/kg WIN-treated animals outperformed vehicle controls, and this effect was more pronounced for the 2 mg/kg group. Pooled Efficiency for all groups is plotted in Fig. 6B.

Go/No-Go – Curve Fitting

Fig. 6C depicts the sigmoidal curves describing proportional commission errors. This mathematical model allows for the analysis of new parameters on behaviourally relevant dimensions. With smaller M50 values indicating more rapid inhibitory learning, a One-Way ANOVA revealed statistically different learning rates described in Supplementary 2. Tukey's HSD post-hoc comparison of these independent observations echoed previous findings; WIN 2 mg/kg and 4 mg/kg groups learned significantly faster in comparison to the vehicle group. When applying similar analyses to the lower asymptote, increased motor inhibition was observed in the high dose WIN groups. These parameters are depicted graphically in Fig. 6D and E, respectively. Statistics for M50 and lower asymptote can be found in Supplementary Material 2.

Commission Two-Way RM ANOVA

Source of Variation	P value	P value summary	Significant?	F (DFn, DFd)	P value
Time x Drug	0.1147	ns	No	F (45, 300) = 1.286	P=0.1147
Time	<0.0001	****	Yes	F (15, 300) = 33.34	P<0.0001
Drug	0.0254	*	Yes	F (3, 20) = 3.843	P=0.0254
Subject	<0.0001	****	Yes	F (20, 300) = 16.51	P<0.0001

Pooled Efficiency Two-Way RM ANOVA

Source of Variation	P value	P value summary	Significant?	F (DFn, DFd)	P value
Time x Treatment	0.0011	**	Yes	F (45, 300) = 1.882	P=0.0011
Time	<0.0001	****	Yes	F (15, 300) = 24.12	P<0.0001
Treatment	0.0053	**	Yes	F (3, 20) = 5.743	P=0.0053
Subject	<0.0001	****	Yes	F (20, 300) = 13.26	P<0.0001

Table 1. Two-Way Repeated Measures (RM) ANOVA summaries with significance for proportional commission error (top) and pooled efficiency metric (bottom).

Discussion

Long-term effects of cannabinoid administration during adolescence remain poorly understood. (24) This study explores two hypotheses pertaining to adolescent mice treated with WIN55,212-2 during adolescence. The first component used the Chronic Social Defeat Stress model to determine whether adolescent cannabinoid exposure altered susceptibility to stress as adults. The second considered alterations in impulsive behaviour in these animals as adults using the Go/No-Go operant conditioning task. By identifying behavioural correlates of exogenous modulation of the endocannabinoid system during a critical period of development, we may begin to ask more refined questions to identify underlying mechanisms of such alterations.

Since there were only 10 subjects in each treatment group exposed to CSDS, we cannot suggest an increase in susceptibility to stress as adults

in animals exposed to WIN during adolescence. The CSDS model is a validated and reliable method to produce stress-related phenotypes in wild-type mice. (30,32) With less than 10 animals in most treatment groups, a susceptibility rate of approximately 75% was globally observed. Despite finding no significant differences in susceptibility to stress which may indicate lack of effect, we cannot conclude that adolescent cannabinoid exposure does not change susceptibility to stress in adulthood. Notably, chronic low-doses of THC in adolescent but not adult rodents have been shown to produce depressive-like phenotypes. (36) There is compelling evidence, however, that WIN-treated animals showed greater levels of behavioural inhibition, as they demonstrated decreased impulsivity on the Go/No-Go task. High dose (WIN 2 mg/kg, 4 mg/kg) subjects learned to suppress previously conditioned behaviours remarkably quickly in comparison to both vehicle and low dose (WIN 0.5 mg/kg) animals in our sample. An alternative consideration is that the vehicle group in the study was particularly slow in this task. These findings diverge from what was previously identified in acute WIN and THC exposure, as well as adolescent WIN exposure. Neither chronic nor acute exposure to WIN have been shown to change impulsivity in rodents. (24,25) The endocannabinoid system contributes to the maturation of the prefrontal cortex; its modulation during adolescence has consequences that persist later in life. Future studies should aim to replicate these results and subsequently investigate underlying mechanisms associated with changes in impulsivity. Approaches such as stereology may be used to quantify morphological changes in dendritic architecture in regions of the prefrontal cortex, and functional calcium imaging studies may glean information on aberrant processing in this region.

The strength of this study is also its greatest limitation. By taking a broad scope and simultaneously investigating two separate lines of inquiry, simplicity in design as well as sample sizes were lost. These limitations need to be considered in the conclusions that can be drawn from either component of the study. Although this study may suggest that adolescent exposure to WIN does not alter susceptibility to stress, determining susceptibility to social defeat stress requires samples much larger than 10 per group for high sensitivity, particularly if susceptibility is not substantially altered. Upon replication of this study, changes to the experimental design should be considered, such as the use of two treatment groups and conducting a power calculation for sample sizes to detect changes in susceptibility with sufficient confidence and effect size. The consideration of sample size with the Go/No-Go task may be less problematic given that the variability for most groups is low. The more pertinent limitation on this behavioural task is the fact that animals were singly housed for approximately 3 weeks before Go/No-Go began. Social isolation is a known stressor for mice and may have posed an interaction effect with the behaviour we are interested in. (37,38) Finally, when comparing the vehicle controls in the study with controls from other studies, they appear to learn at a relatively slower rate. This may explain the astonishing comparisons drawn; replication studies are duly needed. Despite these limitations, the dose response effect of the drug is hard to ignore and warrants further investigation.

This finding contributes to the body of literature examining cognitive alterations in adulthood in response to early exposure to cannabinoids. These behavioural findings are novel and warrant further exploration of its validity and mechanisms. It would be quite interesting to repeat this experiment with THC for comparison and ecological validity. This would allow for mechanistic comparison of the effect of these drugs and reflect consumption of cannabis in a more accurate way. Reflecting on what Go/No-Go measures and the circuits associated with behavioural inhibition, it is worth considering the best approach to identifying the locus of initiating a go vs no-go response. (39) Perhaps an in-vivo experimental approach, such as calcium imaging or neural telemetry may be apt for characterising the cortical organisation which gives rise to this inhibitory behaviour, in addition to its alterations from cannabinoid exposure.

In summary, this study provides preliminary evidence for a dose-dependent increase in behavioural inhibition as measured by the Go/No-Go task in adult animals treated in adolescence with WIN. There were some key limitations in the study design and small sample sizes. We did not find evidence of altered susceptibility to stress in these animals. However, we report a decrease in impulsive behaviour in adolescent WIN-treated adults. Further studies and replication are needed to make meaningful conclusions. Research on the effects of cannabinoids in adolescence is especially important given its prevalence in society and association with mental health issues. Deepening our understanding of how drugs affect the developing brain is imperative in a time when evidence-based information on youth cannabis use is incomplete.

Acknowledgements

Author AF was a research student in NSCI396. We give particular thanks to the Flores research team for their support during the duration of the experiments. Philip Vasilev contributed to SIT recording set-up, and Dominique Nouel in the coordination of research activities. Figure 3 was originally prepared by Carlos Torres-Berrío. Figures 1 and 2 were created on biorender.com.

References

1. Canada H. Bill C-45, the Cannabis Act, passed in Senate. Canada.ca. 2019.

2. Health Canada. Canadian Tobacco, Alcohol and Drugs (CTADS) Survey: 2017 detailed tables - Canada.ca [Internet]. Canada.ca. 2017 [cited 2019 Nov 25]. Available from: https://www.canada.ca/en/health-canada/services/canadian-tobacco-alcohol-drugs-survey/2017-summary/2017-detailed-tables.html#t16

3. Volkow ND, Baler RD, Compton WM, Weiss SRB. Adverse health effects of marijuana use. N Engl J Med [Internet]. 2014 Jun 5 [cited 2019 Nov 25];370(23):2219–27. Available from: http://www.ncbi.nlm.nih.gov/pubmed/24897085

4. Volkow ND, Swanson JM, Evins AE, DeLisi LE, Meier MH, Gonzalez R, et al. Effects of Cannabis Use on Human Behavior, Including Cognition, Motivation, and Psychosis: A Review. JAMA Psychiatry [Internet]. 2016 Mar 1 [cited 2019 Nov 25];73(3):292. Available from: http://archpsyc.jamanetwork.com/article.aspx?doi=10.1001/jamapsychiatry.2015.3278

5. Fergusson DM, Boden JM, Horwood LJ. Psychosocial sequelae of cannabis use and implications for policy: findings from the Christchurch Health and Development Study. Soc Psychiatry Psychiatr Epidemiol [Internet]. 2015 Sep 26 [cited 2019 Nov 25];50(9):1317–26. Available from: http://link.springer.com/10.1007/s00127-015-1070-x

6. Camchong J, Lim KO, Kumra S. Adverse Effects of Cannabis on Adolescent Brain Development: A Longitudinal Study. Cereb Cortex [Internet]. 2017 [cited 2019 Nov 19];27(3):1922–30. Available from: http://www.ncbi.nlm.nih.gov/pubmed/26912785

7. Lubman DI, Cheetham A, Yücel M. Cannabis and adolescent brain development. Pharmacol Ther [Internet]. 2015 Apr 1 [cited 2019 Nov 19];148:1–16. Available from: https://www.sciencedirect.com/science/article/pii/S0163725814002095?via%3Dihub

8. Spear LP. Adolescent neurodevelopment. J Adolesc Health [Internet]. 2013 Feb [cited 2019 Nov 19];52(2 Suppl 2):S7-13. Available from: http://www.ncbi.nlm.nih.gov/pubmed/23332574

9. Spear LP. The adolescent brain and age-related behavioral manifestations. Neurosci Biobehav Rev [Internet]. 2000 Jun 1 [cited 2019 Nov 24];24(4):417–63. Available from: https://www.sciencedirect.com/science/article/pii/S0149763400000142?via%3Dihub

10. Simpson AK, Magid V. Cannabis Use Disorder in Adolescence. Child Adolesc Psychiatr Clin N Am [Internet]. 2016 Jul 1 [cited 2019 Nov 25];25(3):431–43. Available from: https://www.sciencedirect.com/science/article/pii/S105649931630030X?via%3Dihub

11. Gobbi G, Atkin T, Zytynski T, Wang S, Askari S, Boruff J, et al. Association of Cannabis Use in Adolescence and Risk of Depression, Anxiety, and Suicidality in Young Adulthood. JAMA Psychiatry [Internet]. 2019 Apr 1 [cited 2019 Jul 22];76(4):426. Available from: http://archpsyc.jamanetwork.com/article.aspx?doi=10.1001/jamapsychiatry.2018.4500

12. French L, Gray C, Leonard G, Perron M, Pike GB, Richer L, et al. Early Cannabis Use, Polygenic Risk Score for Schizophrenia and Brain Maturation in Adolescence. JAMA psychiatry [Internet]. 2015 Oct [cited 2019 Nov 19];72(10):1002–11. Available from: http://www.ncbi.nlm.nih.gov/pubmed/26308966

13. van Os J, Bak M, Hanssen M, Bijl R V., de Graaf R, Verdoux H. Cannabis Use and Psychosis: A Longitudinal Population-based Study. Am J Epidemiol [Internet]. 2002 Aug 15 [cited 2019 Nov 25];156(4):319–27. Available from: https://academic.oup.com/aje/article-lookup/doi/10.1093/aje/kwf043

14. Andréasson S, Allebeck P, Engström A, Rydberg U. Cannabis and schizophrenia. A longitudinal study of Swedish conscripts. Lancet (London, England). 1987 Dec;2(8574):1483–6.

15. Smolkina M, Morley KI, Rijsdijk F, Agrawal A, Bergin JE, Nelson EC, et al. Cannabis and Depression: A Twin Model Approach to Co-morbidity. Behav Genet [Internet]. 2017 [cited 2019 Nov 25];47(4):394–404. Available from: http://www.ncbi.nlm.nih.gov/pubmed/28466235

16. Busquets-Garcia A, Bains J, Marsicano G. CB(1) Receptor Signaling in the Brain: Extracting Specificity from Ubiquity. Neuropsychopharmacology [Internet]. 2017/09/01. 2018;43(1):4–20. Available from: https://www.ncbi.nlm.nih.gov/pubmed/28862250

17. Wyrofsky RR, Reyes BAS, Zhang X-Y, Bhatnagar S, Kirby LG, Van Bockstaele EJ. Endocannabinoids, stress signaling, and the locus coeruleus-norepinephrine system. Neurobiol Stress [Internet]. 2019 Nov [cited 2019 Nov 25];11:100176. Available from: http://www.ncbi.nlm.nih.gov/pubmed/31236436

18. Klugmann M, Goepfrich A, Friemel CM, Schneider M. AAV-Mediated Overexpression of the CB1 Receptor in the mPFC of Adult Rats Alters Cognitive Flexibility, Social Behavior, and Emotional Reactivity. Front Behav Neurosci [Internet]. 2011;5:37. Available from: https://www.ncbi.nlm.nih.gov/pubmed/21808613

19. Lorenzetti V, Solowij N, Yücel M. The Role of Cannabinoids in Neuroanatomic Alterations in Cannabis Users. Biol Psychiatry [Internet]. 2016 Apr 1 [cited 2019 Nov 26];79(7):e17–31. Available from: https://www.sciencedirect.com/science/article/pii/S0006322315009907?via%3Dihub

20. Bloomfield MAP, Hindocha C, Green SF, Wall MB, Lees R, Petrilli K, et al. The neuropsychopharmacology of cannabis: A review of human imaging studies. Pharmacol Ther [Internet]. 2019 [cited 2019 Nov 26];195:132–61. Available from: http://www.ncbi.nlm.nih.gov/pubmed/30347211

21. Miller ML, Chadwick B, Dickstein DL, Purushothaman I, Egervari G, Rahman T, et al. Adolescent exposure to Δ 9 -tetrahydrocannabinol alters the transcriptional trajectory and dendritic architecture of prefrontal pyramidal neurons. Mol Psychiatry [Internet]. 2019 Apr 1 [cited 2020 Nov 23];24(4):588–600. Available from: https://pubmed.ncbi.nlm.nih.gov/30283037/

22. Bari A, Robbins TW. Inhibition and impulsivity: Behavioral and neural basis of response control. Vol. 108, Progress in Neurobiology. Pergamon; 2013. p. 44–79.

23. Sakagami M, Pan X, Uttl B. Behavioral inhibition and prefrontal cortex in decision-making. Neural Networks. 2006 Oct 1;19(8):1255–65.

24. Johnson KR, Boomhower SR, Newland MC. Behavioral effects of chronic WIN 55,212-2 administration during adolescence and adulthood in mice. Exp Clin Psychopharmacol [Internet]. 2019/05/24. 2019;27(4):348–58. Available from: https://www.ncbi.nlm.nih.gov/pubmed/31120283

25. Pattij T, Janssen MCW, Schepers I, González-Cuevas G, de Vries TJ, Schoffelmeer ANM. Effects of the cannabinoid CB1 receptor antagonist rimonabant on distinct measures of impulsive behavior in rats. Psychopharmacology (Berl) [Internet]. 2007 Jul [cited 2019 Nov 28];193(1):85–96. Available from: http://www.ncbi.nlm.nih.gov/pubmed/17387457

26. Dutta S, Sengupta P. Men and mice: Relating their ages. Life Sci [Internet]. 2016 May 1 [cited 2019 Dec 2];152:244–8. Available from: https://www.sciencedirect.com/science/article/abs/pii/S0024320515300527?via%3Dihub

27. Cuesta S, Restrepo-Lozano JM, Popescu C, He S, Reynolds LM, Israel S, et al. DCC-related developmental effects of abused- versus therapeutic-like amphetamine doses in adolescence. Addict Biol [Internet]. 2019 Jun 13 [cited 2019 Nov 24];e12791. Available from: https://onlinelibrary.wiley.com/doi/abs/10.1111/adb.12791

28. Schneider M. Adolescence as a vulnerable period to alter rodent behavior. Cell Tissue Res [Internet]. 2013 Oct 22 [cited 2019 Nov 24];354(1):99–106. Available from: http://link.springer.com/10.1007/s00441-013-1581-2

29. Torres-Berrío A, Nouel D, Cuesta S, Parise EM, Restrepo-Lozano JM, Larochelle P, et al. MiR-218: a molecular switch and potential biomarker of susceptibility to stress. Mol Psychiatry [Internet]. 2019 Apr 12 [cited 2019 Jul 8];1. Available from: http://www.nature.com/articles/s41380-019-0421-5

30. Golden SA, Covington HE, Berton O, Russo SJ, Russo SJ. A standardized protocol for repeated social defeat stress in mice. Nat Protoc [Internet]. 2011 Jul 21 [cited 2019 Nov 25];6(8):1183–91. Available from: http://www.ncbi.nlm.nih.gov/pubmed/21799487

31. Torres-Berrío A, Lopez JP, Bagot RC, Nouel D, Dal Bo G, Cuesta S, et al. DCC Confers Susceptibility to Depression-like Behaviors in Humans and Mice and Is Regulated by miR-218. Biol Psychiatry [Internet]. 2017 [cited 2019 Nov 25];81(4):306–15. Available from: http://www.ncbi.nlm.nih.gov/pubmed/27773352

32. Krishnan V, Han M-H, Graham DL, Berton O, Renthal W, Russo SJ, et al. Molecular Adaptations Underlying Susceptibility and Resistance to Social Defeat in Brain Reward Regions. Cell [Internet]. 2007 Oct 19 [cited 2019 Nov 25];131(2):391–404. Available from: https://www.sciencedirect.com/science/article/pii/S0092867407012068?via%3Dihub

33. Cuesta S, Restrepo-Lozano JM, Silvestrin S, Nouel D, Torres-Berrío A, Reynolds LM, et al. Non-Contingent Exposure to Amphetamine in Adolescence Recruits miR-218 to Regulate Dcc Expression in the VTA. Neuropsychopharmacology [Internet]. 2018 [cited 2019 Jul 22];43(4):900–11. Available from: http://www.ncbi.nlm.nih.gov/pubmed/29154364

34. Reynolds LM, Pokinko M, Torres-Berrío A, Cuesta S, Lambert LC, Del Cid Pellitero E, et al. DCC Receptors Drive Prefrontal Cortex Maturation by Determining Dopamine Axon Targeting in Adolescence. Biol Psychiatry [Internet]. 2018 Jan 15 [cited 2019 Nov 24];83(2):181–92. Available from: http://www.ncbi.nlm.nih.gov/pubmed/28720317

35. Reynolds LM, Yetnikoff L, Pokinko M, Wodzinski M, Epelbaum JG, Lambert LC, et al. Early Adolescence is a Critical Period for the Maturation of Inhibitory Behavior. Cereb Cortex [Internet]. 2019 Aug 14 [cited 2019 Nov 24];29(9):3676–86. Available from: https://academic.oup.com/cercor/article/29/9/3676/5122728

36. De Gregorio D, Dean Conway J, Canul M-L, Posa L, Bambico FR, Gobbi G. Effects of Chronic Exposure to Low-Dose delta-9-Tetrahydrocannabinol in Adolescence and Adulthood on Serotonin/Norepinephrine Neurotransmission and Emotional Behavior. Int J Neuropsychopharmacol [Internet]. 2020 Dec 17 [cited 2021 Mar 1];23(11):751–61. Available from: https://academic.oup.com/ijnp/article/23/11/751/5877833

37. Morgan M, Einon D. Incentive motivation and behavioral inhibition in socially-isolated rats. Physiol Behav. 1975 Oct 1;15(4):405–9.

38. Mumtaz F, Khan MI, Zubair M, Dehpour AR. Neurobiology and consequences of social isolation stress in animal model—A comprehensive review. Biomed Pharmacother [Internet]. 2018 Sep 1 [cited 2019 Dec 3];105:1205–22. Available from: https://www.sciencedirect.com/science/article/abs/pii/S0753332217371226

39. Smith JL, Jamadar S, Provost AL, Michie PT. Motor and non-motor inhibition in the Go/NoGo task: An ERP and fMRI study. Int J Psychophysiol [Internet]. 2013 Mar 1 [cited 2019 Nov 25];87(3):244–53. Available from: https://www.sciencedirect.com/science/article/abs/pii/S0167876012005508?dgcid=raven_sd_recommender_email

Submitted: 01/22/21

Research Article

[1]Faculty of Science, McGill University, Montreal, QC, Canada

Keywords

Pharmacology, ultrasonic vocalization, convolutional neural network, rat, call classification

Email Correspondence

samir.gouin@mail.mcgill.ca

Samir Gouin[1]

Automated ultrasonic vocalization analysis: Training and testing VocalMat on a rat-based dataset

Abstract

Background: Ultrasonic vocalizations (USVs) offer another way to study the behaviour of rodents in addition to commonly used visual methods. USV subtypes have been associated with behaviour such as the concurrence of 22-kHz calls and signs of distress (defensive behaviour). (1,2) However, the categories used to analyze USVs are a source of contention, most notably with 50-kHz calls, and may even be arbitrary altogether. (3) To facilitate subtyping calls, VocalMat has been developed for USV identification and classification, and it has shown an accuracy of greater than 98% for mice USV detection and 86% for mice USV classification. (4) In this project, we have constructed a rat-based dataset of USVs and then used it to train the VocalMat program to assess automated USV classification.

Methods: Avisoft-SASLab Pro was used to manually classify USVs from 216 audio files. The sorted USVs were then used to train VocalMat's classification program.

Results: Our results show overall accuracies greater than 90% with the highest in the trill and flat categories (97.2% and 91.0%). We experimented with the number of USV categories and found high accuracies when grouping spectrographically similar calls, which are flat calls with up and down ramp calls (96.9%) and trill calls with trill jump and flat-trill calls (98.7%).

Limitations: There are large variations in the number of calls per category in our dataset. More data is needed to fill these gaps and provide more training samples for infrequent calls.

Conclusions: By creating a database of rat USVs and then using it to train VocalMat, we have shown the potential of its adaption to a rat vocal repertoire. Going forward, we hope to test more variations of USV categories on machine learning programs to establish a robust approach to classifying USVs.

Introduction

Ultrasonic vocalizations (USVs) offer perspective into the social and emotional states of rodents. (5) Rodent USVs are composed of syllables collectively ranging from 20-110 kHz, a range higher than human perception. USVs have distinctive acoustic features including frequency, duration, and pitch. The analysis of these acoustic features and spectrographic shapes allows USVs to be categorized into subtypes. USVs have been associated with behaviour, such as the concurrence of 22-kHz calls and signs of distress, (2) and are thought to play an important role in affective signaling, social communication, and thermoregulation. (5) USV analysis can be used to study the effects of drugs on rodents by monitoring changes in calling during experiments, making it an important tool in pharmacology research. (6-8)

Laboratory rats make three broad types of calls: pup calls, 22-kHz calls, and highly heterogenous 50-kHz calls. The 22-kHz and 50-kHz labels are approximations, as in reality the frequencies of these calls vary from 18-32 kHz and 35-72 kHz respectively. (9) There appear to be spectral graphic similarities between mice and rat USVs. However, mice lack 22-kHz and trill call equivalents. (5) Moreover, there are spectral differences between rat and mice USVs, such as shorter short calls and greater modulation of frequency in upward ramp and downward ramp calls in mice. (4, 10) The categories used to analyze USVs are a source of contention, most notably with 50-kHz calls, and may even be arbitrary altogether. (3) Regardless, USV analysis has value as a non-invasive method to monitor changes in rodent behaviour.

Categorization schemes for rat 50-kHz USVs have evolved and increased in complexity. Initially, calls were categorized in only two groups, frequency-modulated and flat calls. (11, 12) They were subsequently categorized in three/four groups, (13, 14) and currently, in 14 groups (Fig. 1). (1)
At present, most groups studying rat USVs use software called Avisoft-SASLab Pro developed by Avisoft Bioacoustics. Avisoft software is commonly used to record USVs, analyze spectrograms, and categorize calls. Post-recording, the sound files can be preprocessed in Avisoft-SASLab Pro through contrast adjustment and noise reduction. Subsequently, USVs can be identified and manually classified by subtype. Avisoft-SASLab Pro also includes an automatic call selection option. However, this approach is unreliable and requires frequent manual configuration. When analyzing

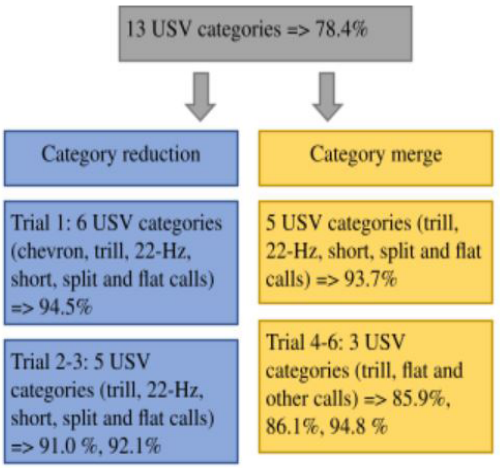

Figure 1. A graphical representation of the two approaches tested, category reduction (removing USC categories) and category merge (combining USV categories), and the overall accuracies of each trial.

hundreds of calls, manual processing is both time-consuming and prone to error. In addition, some USVs may be difficult to readily classify, which highlights the need for more robust classification procedures.

In the field of USV analysis, convolutional neural networks (CNN), a machine learning approach that leverages computer vision, have been increasingly used to identify and classify USVs. Programs such as DeepSqueak and VocalMat have shown high accuracies of USV identification and classification in mice. (15, 4) Furthermore, these programs have implemented adaptive methods to reduce noise and heighten the clarity of USV spectrograms. Notably, machine learning approaches can be trained on different datasets. This increases a program's flexibility for use in different experiments.

Although these new programs are promising, they have been developed largely or exclusively to recognize mouse USVs. VocalMat has not been established for use with rat USVs. This motivated us to develop a rat dataset, train VocalMat with it, and evaluate its performance on rat USV classification. By extending a program developed for use in mice to classify rat calls, we aim to advance automated USV analysis.

Review of Automated USV Analysis Approaches

Many programs have been used for automating rodent USV analysis, including MUPET, (16) A-MUD, (17) WAAVES, (18) XBAT, (19) DeepSqueak, (15) and VocalMat. (4) Since many of these programs do not employ machine learning, they lack the necessary flexibility to deal with different datasets that each contain a variety of USV categories. As a result, these programs, in addition to the other non-machine learning approaches, would need to be tailored to specific testing conditions. Most recently, DeepSqueak and VocalMat have been developed to use machine learning in the identification and classification of mouse calls.

DeepSqueak is a MATLAB package that couples an object detection network with a region proposal network[1] (R-CNN). DeepSqueak detects USVs by analyzing USV length, frequency range, and a classification confidence parameter. The classification confidence parameter is based on the probability that the region of interest contains a call or background noise. The calls can be discriminated from background noise (denoised) automatically to reduce the number of false positives. Thresholds for tonality, or the amount of energy focused at a single frequency, are applied to further reduce silence and noise, and subsequently, optimize the clarity and detection of USVs. The authors showed that high levels USV detection were maintained despite the addition of white noise or natural noise.

Supervised or unsupervised training methods can be used in DeepSqueak to classify USVs based on contour extraction of their spectrographic shapes. When employing supervised[2] training, Coffey et al. used five categories (split, inverted U, short rise, wave and step) to sort ~56,000 mouse USVs and train the classification CNN. For unsupervised training, the contours were automatically clustered by shape, duration and frequency. Individual USVs were subsequently sorted by their degree of similarity to the clusters. When optimized, 20 clusters were found to be most effective[3]. Therefore, DeepSqueak recognized 20 potential categories of mouse USVs with unsupervised training. (15)

VocalMat, developed by the Dietrich lab (Yale School of Medicine), is a MATLAB package that employs image-processing and differential geometry[4] approaches to analyze USVs. (4) In contrast to DeepSqueak, VocalMat identifies calls based on intensity thresholds calculated for each recorded segment. Sound recordings are converted to gray-scale spectrograms in which brighter pixels represent high-intensity values, and contrast enhancement is used to emphasize the USVs against background noise. Noise is further reduced via a local median filter based on the ratio of the median intensity of pixels in the detected USV candidates versus the background. Several morphological operations and the removal of small noise artifacts (≤ 60 pixels) enhance the clarity of USVs. The remaining USV candidates are classified into subtypes. In developing VocalMat, the Dietrich lab used transfer learning from AlexNet[5], pretrained on the ImageNet dataset, to train the CNN on prelabeled data (supervised learning method). They trained their program on images of individual calls extracted from spectrograms rather than trained on acoustic datafiles. They used 12,954 mice USVs across 12 categories: chevron, reverse chevron, down-frequency modulation, up-frequency modulation, flat, short, complex, step up, step down, two steps, multiple steps and noise.

When testing VocalMat and DeepSqueak, which were trained on a mouse datasets, on rat calls, there was poor performance (<50% accuracy). To test the efficacy of a CNN approach to USV classification, we modified VocalMat and trained it on a rat USV dataset. To date, no other labs have developed automated USV analysis programs specific to rats. VocalMat was selected over DeepSqueak due to its higher detection rate of mouse calls: 91.7% compared to 78.0%. (4) VocalMat classified USVs in 12 categories of mouse calls at an overall accuracy of 86.0%. (4) Additionally, VocalMat allows for efficient adaption of the program to different datasets as it uses transfer learning rather than training a network from scratch[6].

Methods

USV Categories

The USVs were classified according to the following categories (1):

USV	Description
Complex	Contain two or more directional changes in frequency of at least 3 kHz each
Upward Ramp	Monotonically increasing in frequency, with a mean slope not less than 0.2 kHz/ms
Downward Ramp	Monotonically decreasing in frequency, with a mean negative slope not less than 0.2 kHz/ms
Flat	Near-constant frequency greater than 30 kHz with a mean slope between -0.2 and 0.2 kHz/ms
Short	Duration less than 12 ms
Split	Middle component "jumps" to a lower frequency and contains a harmonic
Step-Up	Instantaneous frequency change to a higher frequency
Step-Down	Instantaneous frequency change to a lower frequency
Multi-Step	Two or more instantaneous frequency changes
Trill	Rapid frequency oscillations with a period of approximately 15 ms (either sinusoidal or appearing as repeated "inverted- U's")
Flat-Trill Combination	A trill that is flanked on one or both sides by a monotonic portion that is no less than 10 ms
Trill with Jumps	A trill that contains one or more higher-frequency components
Chevron	A monotonic increase followed by a monotonic frequency decrease, each of at least 5 kHz
Composite	Calls (other than flat/trill combinations) that comprise two or more categories
Unclear	Unclassifiable
Miscellaneous	Calls that are clear but do not fit into any of the above call categories
22- kHz	Near-constant frequency calls between 20 and 25 kHz

[1] A method used to predict the regions of objects and reduce the time of detection
[2] The use of a prelabelled dataset
[3] Based on the elbow method - the inflection point at which the introduction of new clusters produced diminishing improvement on error reduction
[4] Used to fine-tune CNNs with image features such as curvature
[5] A large CNN used for object recognition
[6] A computationally intensive process that could last days-weeks with negligible performance differences

Animals

Eight adult male Long-Evans rats (290-344 g, weighed at the start of USV recordings) were housed in a reverse cycle room (2 per cage). Food and water were accessible ad libitum outside of testing sessions, and the home cages were maintained by the animal facility of McGill University. All procedures were approved by the McGill Animal Care Committee in accordance with the guidelines of the Canadian Council on Animal Care.

Recording Sessions

The rats were recorded in a plexiglass chamber (29.5 cm high × 57.6 cm wide × 53.5 cm deep, ENV-007CT, Med Associates, St. Albans, VT). The chambers contained bedding that was changed between recording sessions and were encased in sound-reduction acoustic foam (Primacoustic, Port Coquitlam, British Columbia). USVs were recorded with a CM16 (Avisoft Bioacoustics, Berlin Germany) microphone angled towards the center of the box with the Avisoft Bioacoustics RECORDER software (version 4.2.29). Recording sessions were conducted on alternating days. During each recording session (20 min), four rats, each with their own chamber and microphone, were recorded as they naturally vocalized. Recording was started before the rats were placed in the chambers. A total of 216 audio (WAV) files were obtained.

Dataset

Spectrograms were generated from the audio files using a fast Fourier transform (FTT) length of 512 points and an overlap of 75% (FlatTop window, 100% frame size). The USVs had been previously manually identified and classified using Avisoft-SASLab Pro by another lab member (Adithi Sundarakrishnan) who provided the audio files used in this project. The next challenge was to export the classified USVs in separate image files with a standardized time and frequency axis. To this end, we adjusted the export parameters of the batch progress function with Raimund Specht (Berlin-based Avisoft Bioacoustics developer) and implemented new features that allowed the export of USVs into image (PNG) files organized by their classification. To standardize the time axis, we added margins to the USVs by inserting random background sections of the spectrograms. Following this procedure for 216 audio files, we obtained a total of 19,769 USVs[7].

VocalMat

The next step was to train VocalMat's USV classification program[8] on the rat dataset of images. Each training trial was independent of the others. We implemented a custom reader to standardize image size (227 x 227) and convert grayscale images to RGB for use with VocalMat.

```
function data = customreader(filename)
onState = warning('off', 'backtrace');
c = onCleanup(@() warning(onState));
data=imread(filename);
data = imresize(data, [227 227]);
data=data(:,:,min(1:3,end));
end
```

The classification CNN was trained using the Dietrich Lab recommended settings: a batch size of M=128 images and a maximum epoch number of 100. 33 epochs was the highest quantity used in our training. A stochastic gradient descent with momentum (0.9) at a learning rate of $\alpha = 10\text{-}4$ and weight decay $\lambda = 10\text{-}4$ was used to optimize training parameters. As this process is stochastic, the results from training a dataset differed between trials. Thus, we trained similar categories multiple times to compare results. In addition, we varied the number of categories to avoid overfitting[9] on our relatively small dataset. Specifically, we reduced the number of categories to lower the complexity, or number of parameters used for classification. The classification was trained on 90% of the inputted images and the accuracy, defined as the rate at which the automated classification matches the manual one, was assessed on the validation set (10%).

Results

We experimented with removing and merging categories of USVs used to train VocalMat (Fig. 1). The latter approach was used when USV subtypes shared stereotypical features such as trill jump and flat-trill USVs. Notably, removing categories would limit the pipeline's usefulness and merging categories would require manual categorization to distinguish the USVs within the merged category. When balancing the complexity of the model, or the number of categories with the degree of accuracy of specific USV subtypes, we prioritized high accuracy over including many categories. This would be of use when quantifying specific USV subtypes over recording sessions, rather than the prevalence of all USV subtypes over recording sessions.

Training with Original Categories

We trained the program to recognize all the categories of USVs described by Wright et al. (2010) with two exceptions: complex and composite calls were excluded as there were insufficient images available for training purposes. We obtained an overall accuracy of 78.4%. An accuracy higher than 85% was obtained for 22-kHz calls and for 50-kHz call types, i.e. trill (91.2%), short (93.3%), split (86.7%) and flat (87.1%). Based on these results, we reduced the USV categories from the initial 13 to 6 to omit the categories with the lowest accuracies, with the exception of chevron calls (Fig. 2a: Trial 1). We kept the chevron category because it had high accuracies when VocalMat was trained on the mouse dataset. The accuracy improved to 94.5%. All categories had an accuracy over 90.0% except for the classification of chevron calls (75.8%). Subsequently, we discarded the least accurate category, chevron calls, with its samples, and trained the program two times, now with only five categories: trill, 22-kHz, short, split and flat (Figure 2a: Trials 2 & 3). Trills, splits and flats showed the most consistent results. The overall accuracies were 91.0% and 92.1%, slightly below the previously obtained 94.5%.

Training with Merged Categories

To reduce potential overfitting, we next experimented with combining spectrographically similar USVs into categories. We merged the trill, flat-trill and trill jump calls (n=7724 calls), the split calls with the multi-step calls (n=899 calls), and the up ramp, down ramp and flat calls (n=5808 calls). The combined trill group resulted in an accuracy of 93.7%, lower than the mean of trills alone (~ 97%). The split calls combined with the multi-step calls had a lower accuracy of 53.3%. Notably, the multi-step

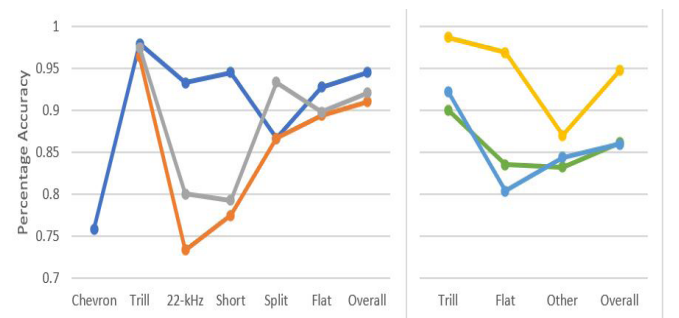

Figure 2a The performance of classification training when grouping the images in chevron, trill, 22-kHz, short, split and flat categories across three trials (blue, grey and orange). Figure 2b. The performance of classification training when grouping the images in trill, flat and other categories across three trials (yellow, blue and green).

[7] Please contact the author for access to the dataset
[8] Available at https://github.com/ahof1704/VocalMat.git
[9] This occurs when the model is too closely fitted to the training data and cannot be generalized and successfully used on different data
[10] A lack of capturing characteristic features, often the result of biased or limited data

calls have a much smaller training set and are thus susceptible to underfitting[10]. The flat calls combined with up and down ramp calls showed an accuracy of 93.8%, comparable to a mean accuracy of 92.0% of flats alone. Every region of a spectrogram that VocalMat identifies as salient (i.e. pinpointed by high-intensity pixels) must be classified in a category. Consequently, the authors included a "noise" category. Similarly, we implemented a three-way classification consisting of an "other" group, in addition to the trill and flat groups (the two most prevalent USVs). This gave us a better indication of how VocalMat would perform when analyzing highly variable noise artifacts and audio files, which are replete with individual calls that bear similarity to multiple categories and cannot be readily classified. We trained the program three times with different combinations of the flat and trill calls. In the first instance, we assessed trill (n=6330 calls) and flat calls (n=5103 calls) alone with the "other" category (n=7625 calls) and obtained a total accuracy of 85.9% (Fig. 2b: Trial 4). We then grouped the trill category with the trill jump and flat-trill categories (n=7724 calls) and retrained VocalMat. The accuracy of the combined trill category decreased from 92.2% to 90.0%, but the overall accuracy showed a negligible change of 85.9% to 86.1% (Fig. 2b: Trial 5). We observed the strongest performance when grouping the trill category with the trill jump and flat-trill categories (n=7724 calls), and the flat USVs with the up ramp and down ramp categories (n=5808 calls). Compared to the other two trials, the performance was higher in all groups and the overall result was 94.8% accuracy (Fig. 2b: Trial 6).

Discussion

Our results show high overall accuracy with a 6-category classification scheme of chevron, trill 22-Hz, short split and flat calls (94.5%, Trial 1) and with 3 merged categories (94.8%, Trial 6) as reductions from the initial 13 categories. These results are the first foray into adjusting VocalMat for rat, rather than mouse, USV classification. These 2 categorization approaches could be used depending on the degree of complexity required; the former is best suited for experiments evaluating multiple USV subtypes and the latter is best for focused analysis of specific subtypes.

As predicted, omitting certain call subtypes and merging other call subtypes to form larger categories had an effect on training accuracy. Counterintuitively, removing the most inaccurate USV category of chevron calls with its accompanying samples did not increase overall accuracy (Fig. 2a). This may be the result of decreased variance in the dataset. Merging categories also led to a decrease in accuracy except flat calls with up and down ramp calls (96.9%, Fig. 2b) and trill calls with trill jump and flat-trill calls (98.7%, Fig. 2b). Merging multiple USV subtypes that may not look alike within a category was expected to increase intra-category variability and decrease the accuracy of categorization. This approach is sufficient for experiments focused on trill and flat calls but will require adaptation for other common call subtypes. Further manual processing will be required to classify USVs within merged categories, such as discriminating between trill, trill jump and flat-trill calls. As VocalMat relies on a stochastic training process, more trials are required to compare the accuracies of different USV group combinations and determine the highest potential accuracies of each combination of categories, in addition to testing calls that are unable to be categorized.

While not a direct correlation, the USV categories with the most images, trill and flat calls, retained relatively consistent accuracies across the training trials and notably, the highest average accuracies (97.2% and 91.0%, Fig. 2a). These calls have relatively simple spectrographic shapes in comparison to the other call categories. As a result, the dataset for these categories may have less variability, leading to more consistent categorization. Our dataset is a reflection of the actual USV prevalence by category; notably, trills and flat calls each represent on average about 30% of all 50-kHz calls. In addition, there are large variations in the number of calls per category. More data is needed to fill these gaps and provide additional training samples for infrequent calls. Specifically, a large dataset comprising calls from male and female rats at different ages will be critical to capture variations within USV categories, (20, 21) as individual rats differ in terms of which USV subtype they most commonly emit. (1) Through following the procedure outlined in this paper, it is possible to construct and grow databases for use with machine learning programs.

In summary, we have adapted VocalMat for use in adult rats and have shown that it can classify 50-kHz calls with a high degree of accuracy. These results show promise and the established procedure will help build upon these results. By experimenting with other datasets, we hope to further test VocalMat and improve USV call classification.

Acknowledgements

I thank my supervisor, Dr. Paul Clarke, for his insightful feedback and continual guidance and Adithi Sundarakrishnan for her generous support. This work was partially funded by an NSERC undergraduate student research award. The author declares no conflict of interest.

References

1. Wright JM, Gourdon JC, Clarke PBS. Identification of multiple call categories within the rich repertoire of adult rat 50-kHz ultrasonic vocalizations: effects of amphetamine and social context. Psychopharmacology. 2010;211(1):1-13.

2. Litvin Y, Blanchard DC, Blanchard RJ. Rat 22kHz ultrasonic vocalizations as alarm cries. Behavioural Brain Research. 2007;182(2):166-72.

3. Goffinet J, Mooney R, Pearson J. Inferring low-dimensional latent descriptions of animal vocalizations. bioRxiv. 2019:811661.

4. Fonseca AHO, Santana GM, Bampi S, Dietrich MO. Analysis of Ultrasonic Vocalizations from Mice Using Computer Vision and Machine Learning. bioRxiv. 2020:2020.05.20.105023.

5. Clarke PB WJ. Rodent ultrasonic vocalizations. In: Stolerman I, editor. I.P. Encyclopedia of Psychopharmacology: Springer-Verlag Berlin Heidelberg; 2015. p. 1918.

6. Simola N, Granon S. Ultrasonic vocalizations as a tool in studying emotional states in rodent models of social behavior and brain disease. Neuropharmacology. 2019;159:107420.

7. Simola N. Rat Ultrasonic Vocalizations and Behavioral Neuropharmacology: From the Screening of Drugs to the Study of Disease. Curr Neuropharmacol. 2015;13(2):164-79.

8. Brudzynski SM. Pharmacology of Ultrasonic Vocalizations in adult Rats: Significance, Call Classification and Neural Substrate. Current neuropharmacology. 2015;13(2):180-92.

9. Boulanger-Bertolus J, Rincón-Cortés M, Sullivan RM, Mouly A-M. Understanding pup affective state through ethologically significant ultrasonic vocalization frequency. Scientific reports. 2017;7(1):13483-.

10. Scattoni ML, Ricceri L, Crawley JN. Unusual repertoire of vocalizations in adult BTBR T+tf/J mice during three types of social encounters. Genes, Brain and Behavior. 2011;10(1):44-56.

11. Burgdorf J, Wood PL, Kroes RA, Moskal JR, Panksepp J. Neurobiology of 50-kHz ultrasonic vocalizations in rats: Electrode mapping, lesion, and pharmacology studies. Behavioural Brain Research. 2007;182(2):274-83.

12. Ahrens AM, Ma ST, Maier EY, Duvauchelle CL, Schallert T. Repeated intravenous amphetamine exposure: rapid and persistent sensitization of 50-kHz ultrasonic trill calls in rats. Behavioural brain research. 2009;197(1):205-9.

13. Kaltwasser M-T. Acoustic signaling in the black rat (Rattus rattus). Journal of Comparative Psychology. 1990;104(3):227-32.

14. Vivian JA, Miczek KA. Morphine attenuates ultrasonic vocalization during agonistic encounters in adult male rats. Psychopharmacology (Berl). 1993;111(3):367-75.

15. Coffey KR, Marx RG, Neumaier JF. DeepSqueak: a deep learning-based system for detection and analysis of ultrasonic vocalizations. Neuropsychopharmacology. 2019;44(5):859-68.

16. Van Segbroeck M, Knoll AT, Levitt P, Narayanan S. MUPET—Mouse Ultrasonic Profile ExTraction: A Signal Processing Tool for Rapid and Unsupervised Analysis of Ultrasonic Vocalizations. Neuron. 2017;94(3):465-85.e5.

17. Zala S, Nicolakis D, Noll A, Balazs P, Penn D. Automatic mouse ultrasound detector (A-MUD): A new tool for processing rodent vocalizations. PLOS ONE. 2017;12:e0181200.

18. Reno JM, Marker B, Cormack LK, Schallert T, Duvauchelle CL. Automating ultrasonic vocalization analyses: The WAAVES program. Journal of Neuroscience Methods. 2013;219(1):155-61.

19. Barker DJ, Herrera C, West MO. Automated detection of 50-kHz ultrasonic vocalizations using template matching in XBAT. Journal of Neuroscience Methods. 2014;236:68-75.

20. Mittal N, Thakore N, Bell RL, Maddox WT, Schallert T, Duvauchelle CL. Sex-specific ultrasonic vocalization patterns and alcohol consumption in high alcohol-drinking (HAD-1) rats. Physiology & Behavior. 2019;203:81-90.

21. Wöhr M, Schwarting RKW. Affective communication in rodents: ultrasonic vocalizations as a tool for research on emotion and motivation. Cell and Tissue Research. 2013;354(1):81-97

Submitted: 12/10/20

Research Article

[1]Faculty of Science, McGill University, Montreal, QC, Canada
[2]Department of Psychology, McGill University, Montreal, QC, Canada
[3]Department of Neurology and Neurosurgery, McGill University, Montreal, QC, Canada

Email Correspondence

lyla.hawari@mail.mcgill.ca

Lyla Hawari[1], Neomi Singer[2], Arielle Rabinowitz[3], Robert Zatorre[2]

What is the Best Music for Neurofeedback Training?

Exploration into musical attributes that contribute to success in music neurofeedback

Abstract

The nucleus accumbens (NAc) is widely known for its role in reward seeking behavior which is heavily reliant on dopamine signaling. Dopamine plays an important role in reward seeking behavior and motivation and its dysregulation is shown to cause symptoms of depression such as apathy, a lack of motivation, and anhedonia, a loss of pleasure. Studying the NAc, specifically the ventral striatum in this case, is critical in understanding the underlying mechanisms of this dysregulation. Music neurofeedback is a biofeedback technique that provides feedback on brain activity through the audio quality of the music, with lower quality sounding more muffled. This study uses this technique to train participants to increase the activity of their ventral striatum in an attempt to upregulate the activity of the reward system.

This paper aims to investigate what the most effective music choices are in terms of genre, key, valence (positive or negative emotions) and energy (pertaining to levels of arousal) to maximize the improvement on neurofeedback training. These musical attributes were identified by the Spotify "Organize Your Music" categorization tool. Participants underwent six EEG music neurofeedback training sessions with individually tailored pleasurable music as the source of feedback. The participants either received real feedback in the neurofeedback group (NF) or sham feedback in the control group. The results of this study showed that neurofeedback performance was negatively correlated with valence whereby songs that led to the greatest performance, measured as increase in ventral striatum activity from baseline, were those low in valence. Participants that had the greatest improvement in their neurofeedback training selected songs that were in a minor key and belonged to the pop genre. Although this study is based on a small sample, it takes the first step towards the overarching goal of using music to manage dysregulation in the reward system.

Introduction

Music is a pleasurable stimulus that transcends age, gender and cultural differences. Previous studies have shown that listening to music activates many brain areas including the auditory cortex, amygdala and most notably the NAc. (14) The NAc regulates the release of dopamine and plays a crucial role in reward processing of both natural rewards like food as well as drugs, which has been studied previously in animals (Britt et al, 2012). The involvement of the NAc in music listening underscores the music-derived pleasure whereby the amount of enjoyment a participant experienced from listening to a certain song can be predicted by the increase in connectivity between the auditory cortex and the nucleus accumbens. (14) Reward system dysregulation has been heavily investigated in psychiatry. Anhedonia, the lack of pleasure, is a main symptom of depression as classified by the DSM V in 2013.

Studies have attributed this decreased feeling of pleasure to reduced activity in the NAc in response to reward. (13) Studies by Barch and colleagues in 2011 showed that this dysregulation in the reward system can start as early as three years of age for children with or at risk of depression as determined by parent reports and behavioral tests. Knowing that depression is a leading cause of disability worldwide (WHO, 2018) finding ways to alleviate it is crucial. This led to the search for techniques to upregulate the reward system in hopes of reducing the severity of anhedonia and apathy symptoms. (16)

In the past, techniques that aim to stimulate brain areas were not very convenient such as deep brain stimulation which is very invasive. (8) Therefore, a need for a non-invasive, volitional technique came about. Neurofeedback is a biofeedback technique that provides continuous neural feedback to the participant to help them regulate the activity of certain brain regions. Previous studies using visual imagery have confirmed that neurofeedback can be successful in training participants to upregulate the reward system. (7; 17). Combining these findings with our knowledge of the pleasurable nature of music, music neurofeedback can be utilized for this purpose in the form of music quality; clearer quality indicating greater activity in the region of interest. This paper uses EEG music neurofeedback as opposed to fMRI based on findings from Keynan and colleagues in 2016 that suggest that mesolimbic brain activity can be reliably recorded using EEG by establishing an electronic fingerprint (EFP) for the region of interest.

As music is such a complex stimulus, it is critical to identify the musical features that may be associated with neurofeedback success. When classifying music in the affective/emotional domain, the literature tends to follow a circumplex model of two attributes, valence and arousal (11), suggesting that happier, exciting music has positive valence and high arousal whereas sad, calm music has a negative valence and low arousal. Studies have found that participants that experienced musical chills, a physiological response related to feeling of pleasure from music (1), reported the song to have been both happy and sad (9) leaving a valence assignment to be desired.

The paper showed that compared to the physiological tears group, the chills group scored higher on measures of arousal and rated their self-selected music as significantly happier. (9) Extrapolating these results to musical attributes, this would suggest that higher valence, higher arousal music is associated with chills, an indication of pleasure from music. Two other musical attributes, key and energy were analyzed to extend the exploration beyond the typical model of valence and arousal.

This paper aims to answer the question of what musical attributes are associated with the greatest improvement in neurofeedback training. Based on the previous literature, we would predict that songs with higher valence and energy levels should yield the greatest improvement in neurofeedback performance.

Methods

Participants

10 control and 10 test subjects ages 18-35 were recruited (9 male, 11 female, mean age = 21.1, standard deviation = 2.8). Eligibility criteria included no known medical diagnoses, including neurological or psychiatric disorders, hearing impairments. All participants were fluent English speakers. Participants provided written informed consent prior to experiment and were monetarily compensated upon finishing the experiment. All procedures were run in accordance with the Montreal Neurological Institute's research ethics office (REB) guidelines.

Two participants were excluded from the analysis: one participant was excluded from all analyses pertaining to performance because their first three sessions were sham (control) sessions although they were assigned to the test group. Another participant was excluded from all analyses pertaining to music because their songs could not be found by the Spotify organization tool. Two participants had one session each excluded when calculating their average improvement in maximal performances due to technical issues pertaining to those sessions.

EEG Recording

EEG measurements were acquired during the six music neurofeedback training sessions using a BrainAmp EEG amplifier. EEG activity was recorded from a 14 electrode channels EEG cap. The EEG was sampled at a rate of 250Hz and recorded from the following 14 channels: FP1, FP2, C4, F7, F8, T7, T8, P8, Fz, Cz, Pz, TP9, TP10, ECG. The data was recorded using the Brain Vision Recorder software (BrainProducts, GmbH, Germanny).

Music Neurofeedback Task

Participants completed six training sessions lasting 1.5-2 hours, over the course of two to three weeks. Each session consisted of a global baseline run, five training cycles and a transfer run (same instructions as the training cycle but without music/feedback). All runs required the participant to sit still with their eyes closed with earphones in while wearing an EEG cap. Each participant was asked to provide their top 10 favorite songs to be used during the neurofeedback training sessions.

The neurofeedback was produced using the NFM software, an in-house Graphical User Interface, which was implemented with the OpenViBE software for brain computer interface. For the global baseline period, the participant was asked to clear their mind so that their baseline neural activity level could be measured. The training cycles involved listening to music and were split up into a passive listening and training phase, lasting 2.5 and 2 minutes, respectively.

During the listening phase the music quality was extremely poor while during the training phase, the participant received continuous neurofeedback reflected in the music quality which was manipulated using filtering. Worse quality equated to lower neural activity in the electrical fingerprint (EFP) of the NAc and more frequency bands filtered. During the listening phase, the participant was simply prompted to passively listen to the music whereas during the training phase they were asked to regulate their brain activity using a suggested strategy (see below) or one of their choosing. Between every training cycle, the experimenter asked the participant questions regarding their general mood, how well they thought they did on a scale of 1-7, and what their chosen strategy was. In addition, they were shown a graph of the neural activity of the particular cycle which was indicative of performance. The participant was requested to adapt their strategies according to the feedback presented in order to determine the most effective one for them. Control participants underwent the exact same procedure except they received sham feedback which came from a different participant.

Strategies

The participant was prompted to explore the following four strategies throughout the training sessions and to evaluate their effectiveness in increasing neural activity and improving the quality of the music during the training phase:

1. *Imagination*: imagination centered around the song/piece or artist, usually involving a concert or imagination of the artists performing. Included imagination of singing or dancing along to the song.

2. *Memory*: recollection of happy memories. The memories did not have to be connected to the song at all but in some cases may be.

3. *Visual imagery*: imagination involving any visual images not directly related to the song or artists of the song/piece.

4. *Motor imagery*: imagination that involved motor movements specifically pertaining to playing instruments (typically related to the song/piece)

Data Analysis

Neurofeedback analysis:
Performance for every cycle was calculated by subtracting the average EFP at baseline from the average EFP during neurofeedback training. Improvement in maximal performance was calculated by subtracting the performance of the best cycle of the first session from the performance of the best cycle of each of the other sessions. These five values of improvement of maximal performance were then averaged to get one numeric measure of performance which is the average improvement in maximal performance with a greater value indicating better performance. Throughout the rest of the paper, the average improvement in maximal performance will simply be referred to as performance. Subgroups of good and bad performances in test and control groups were assigned using a median split whereby participants with performance greater than the median of the test group (median = 0.058) were categorized in the "good performer" category and those below the median belonged to the "bad performer" category.

Music analysis:
All information regarding the musical attributes of the songs were retrieved from a Spotify tool called "Organize Your Music" (http://organizeyourmusic.playlistmachinery.com/). The information used came from the measures of: valence, energy and genre. This Spotify tool operates according to algorithms that have been explained in depth by Jedmar et al (2015) which included analyzing lyrical and audio features extracted using the online music intelligence platform The Echo Nest and weighting them through statistical analyses. Information regarding song key was retrieved from https://tunebat.com/Analyzer. Analyses were run using attributes of all the NF songs as well as the song of the cycle that had the best performance overall, which will be referred to as the "best song" hereafter. This was done to observe any possible discrepancies between the general trends of the chosen songs as compared to the song with the best performance.

Statistics

To analyze the difference in performance between the control and test groups, a paired samples t-test was conducted using the coupling of neurofeedback received since every control participant received sham feedback from a specific NF participant. One-Way ANOVAS were conducted across groups for comparisons of song valence, % major and energy levels and Tukey's HSD post hoc comparisons were run when appropriate. A Shapiro-Wilks test was used to establish that the data was normally distributed. A Pearson correlation was used to assess the association between song valence and energy with performance. Correlations were collapsed across groups to compare the music attributes to performance regardless of the accuracy of neurofeedback received. Separate correlations were run exclusively for the NF group. Error bars on the graphs represent +/- standard error of the mean (SEM). The significance level

was set to $p < 0.05$.

Results

Neurofeedback Performance

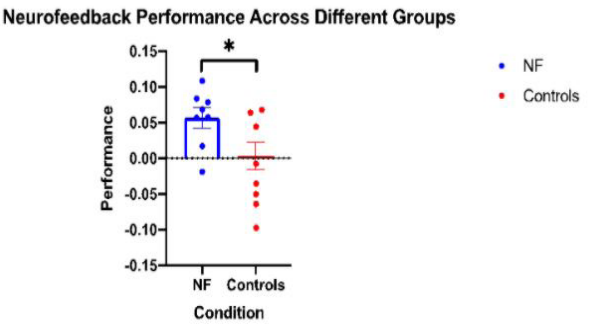

Figure 1. Neurofeedback performance across groups. (a) Difference in performance between control and NF groups. Error bars represent +/- SEM. Scattered data points represent individual performances. * indicates $p < 0.05$.

A paired samples t-test was conducted to analyze the data from neurofeedback performance across the control and NF groups (fig. 1). There was a significant difference in means of neurofeedback performance between groups ($t(7) = 3.692$, $p<0.05$) suggesting that the NF group neurofeedback performed significantly better than the control group.

Valence

A one-way ANOVA was conducted to analyze the average valence of the neurofeedback training songs across the four subgroups (fig. 2a), which was not significant ($p > 0.05$). This indicates that there was no significant difference between the mean of average valences of the training songs across the groups, thus confirming that the observed group effects of training cannot be explained by a mere difference in the valence of the musical selection. A Pearson correlation was conducted for average valence of training songs vs performance across all groups (fig. 2b) which was also not significant ($p>0.05$).

A one-way ANOVA was also conducted to analyze the data from the valence of the "best" song across the four subgroups (fig. 2c). The differences in means of best song valence across the four groups was not significant ($p > 0.05$). This indicates that there was no significant difference between the mean valence of best song across the groups. A Pearson correlation was conducted for valence of best song vs performance across all groups (fig. 2d). There was a significant negative correlation ($R= -0.468$, $p<0.05$) indicating that performance improved as valence of the best song decreased across the entire sample.

Neurofeedback Performance

A one-way ANOVA was conducted to analyze the average energy level of the neurofeedback training songs across the four subgroups (fig. 3a). The differences in means of average training song energy across the four groups was not significant ($p > 0.05$) indicating that there was no significant difference between the mean of average energy of the training songs across the groups. A Pearson correlation was conducted for average energy of training songs vs performance across all groups (fig. 3b). There was a small positive correlation ($r = 0.2061$) however it was not significant ($p>0.05$).

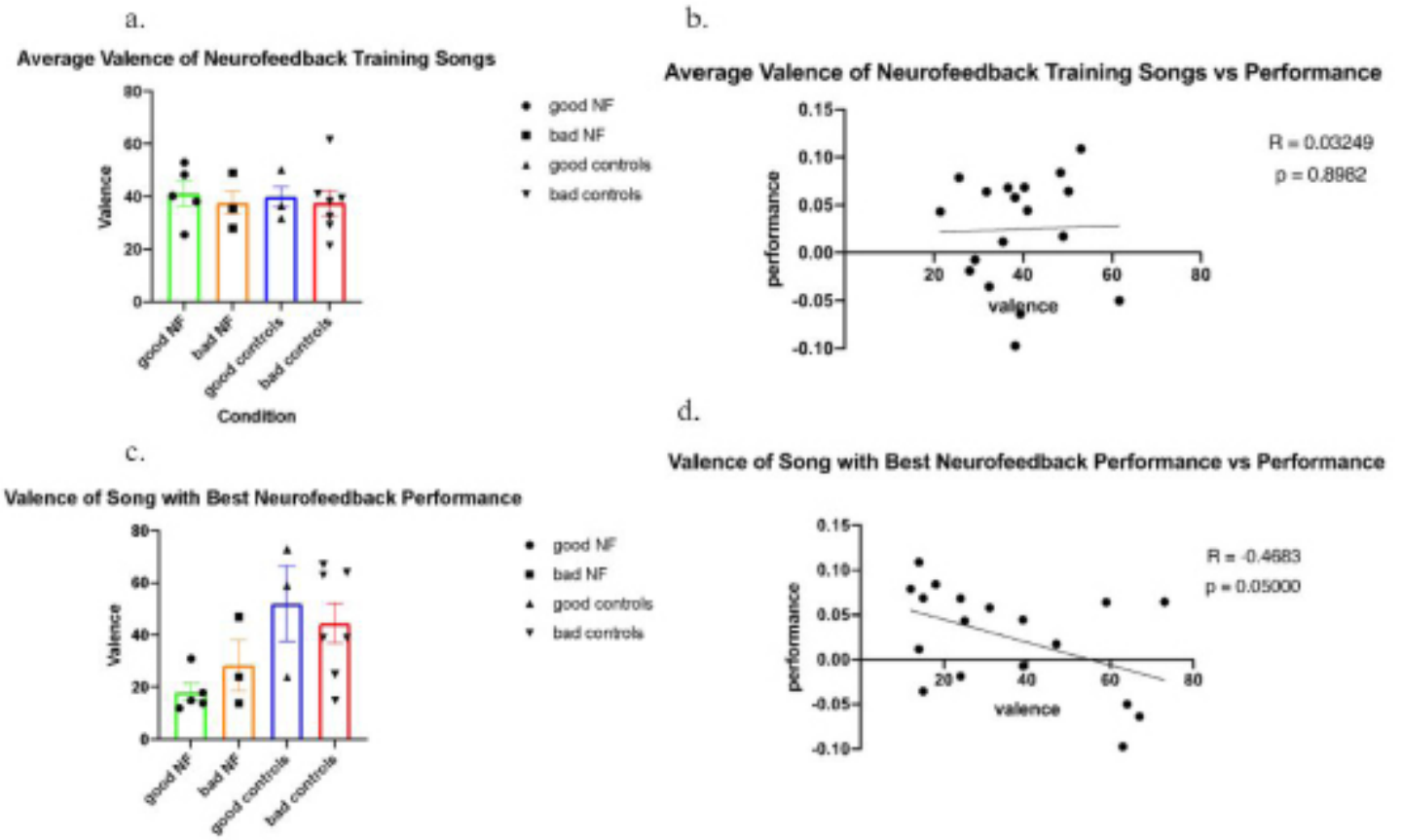

Figure 2. Song valence across subgroups. (a) Average valence of training songs across the four subgroups. (b) Correlation of the average valence of training songs with performance across all subgroups. (c) Valence of the best song across the four subgroups. (d) Correlation of the best song valence against performance across all subgroups. Error bars represent +/- SEM. Scattered data points represent individual performances. * indicates $p < 0.05$.

A one-way ANOVA was also conducted to analyze the data from the valence of the "best" song across the four subgroups (fig. 2c). The differences in means of best song valence across the four groups was not significant ($p > 0.05$). This indicates that there was no significant difference between the mean valence of best song across the groups. A Pearson correlation was conducted for valence of best song vs performance across all groups (fig. 2d). There was a significant negative correlation ($R= -0.468$, $p<0.05$) indicating that performance improved as valence of the best song decreased across the entire sample.

Energy

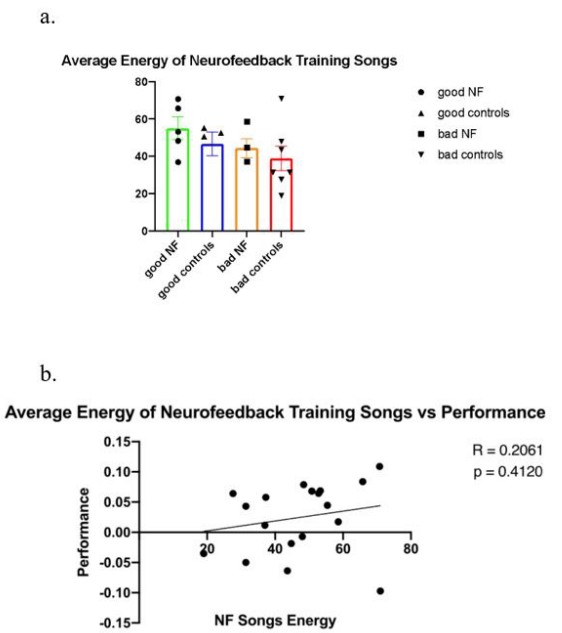

Figure 3. Song energy across subgroups. (a) Average energy of training songs across the four subgroups. (b) Correlation of the average energy of training songs with performance across all subgroups. (c) Energy of the best song across the four subgroups. (d) Correlation of the best song energy against performance across all subgroups. Error bars represent +/- SEM. Scattered data points represent individual performances. * indicates $p < 0.05$.

A one-way ANOVA was conducted to analyze the average energy level of the neurofeedback training songs across the four subgroups (fig. 3a). The differences in means of average training song energy across the four groups was not significant ($p > 0.05$) indicating that there was no significant difference between the mean of average energy of the training songs across the groups. A Pearson correlation was conducted for average energy of training songs vs performance across all groups (fig. 3b). There was a small positive correlation ($r = 0.2061$) however it was not significant ($p>0.05$).A one-way ANOVA was conducted to analyze the data from the energy of the best song across the four subgroups (fig. 3c). The differences in means of best song energy across the four groups was not significant ($p > 0.05$). This indicates that there was no significant difference between the mean energy of best song across the groups. A second order polynomial was fit to the distribution of best song song vs performance across all groups (fig. 3d). A nonlinear regression analysis was conducted yielding ($R2 =0.3295$, $F(1,15) = 6.859$, $p = 0.0194$) which suggests that the second order polynomial was a good model for the distribution of best song energy across performance levels and 33% of the variation in performance can be attributed to the energy level of the best song.

NF Group Correlations:

Four Pearson correlations were run for valence and performance and energy and performance specifically for the NF group (fig. 4a-d). All four correlations were not significant. That being said, a trend of positive correlation was found for average energy against performance ($r =0.59$, $p =0.12$) and average valence against performance ($r =0.44$, $p =0.27$). A negative correlation was found between the valence of the best song and performance ($r = -0.44$, $p = 0.27$).

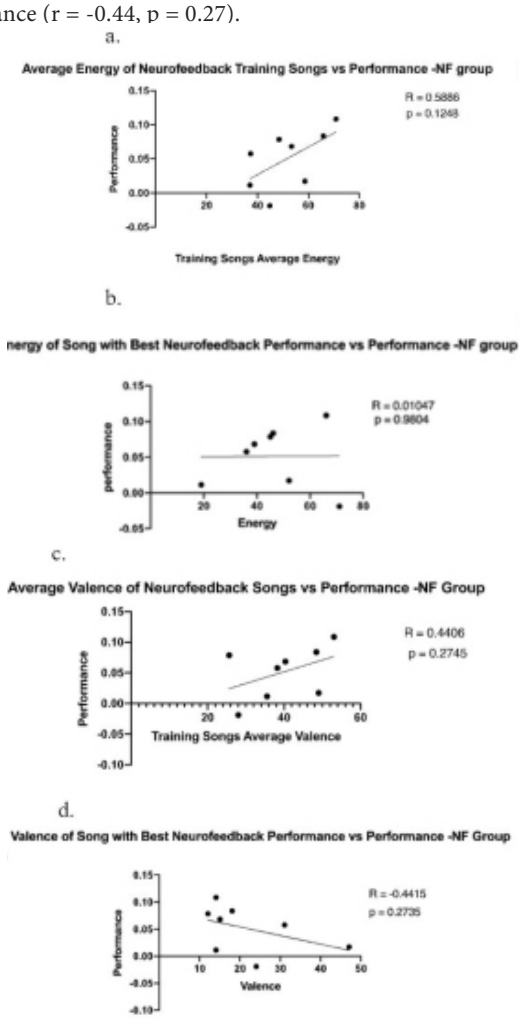

Figure 4. Energy and valence correlations exclusively for the NF groups. (a) Correlation of average energy of training songs vs performance. (b) Correlation of best song energy vs performance. (c) Correlation of average valence of training songs vs performance. (d) Correlation of best song valence vs performance. Error bars represent +/- SEM. Scattered data points represent individual performances. * indicates $p < 0.05$.

Genre and Key Breakdown

The pie charts (fig. 5a-h) show that the most common genre for the best song across all four subgroups is pop and that the most common key for all the subgroups except the bad controls is minor.

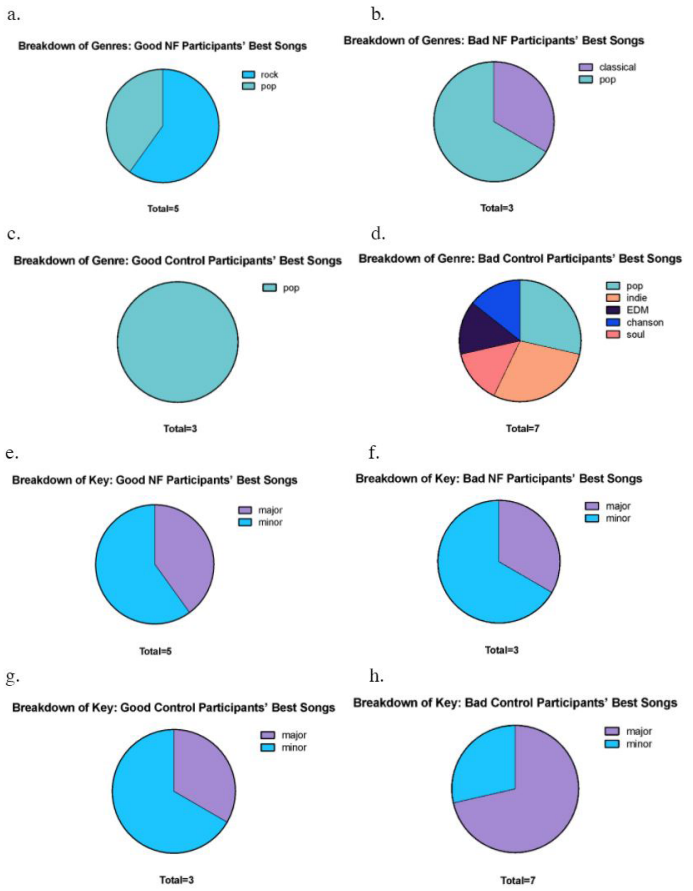

Figure 5. Genre and key of best song breakdown across the four subgroups. (a) Best song genres of good NF group. (b) Best song genres of bad NF group. (c) Best song genres of good control group. (d) Best song genres of bad control group. (e) Best song key of good NF group. (f) Best song key of bad NF group. (g) Best song key of good control group. (h) Best song key of bad control group.

Strategies of Best Cycle Breakdown

The pie charts (fig. 6a-d) show that the most common strategy used during the best cycle is memory across all four subgroups.

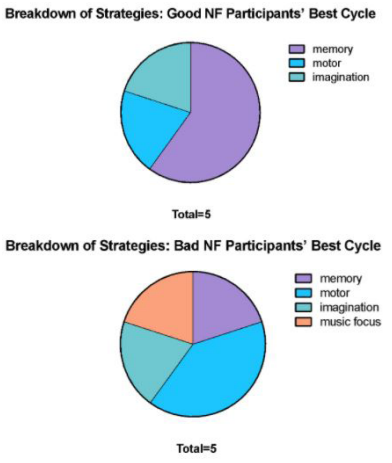

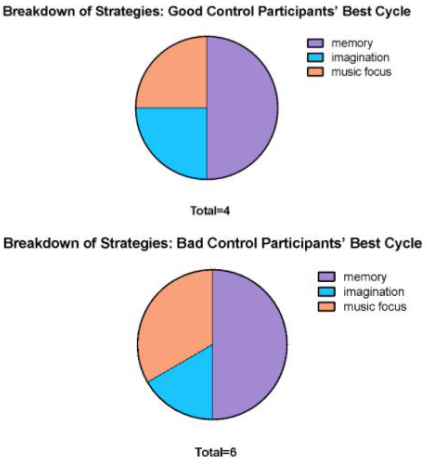

Figure 6| Best cycle strategy breakdown across the four subgroups. (a) Best cycle strategies of good NF group. (b) Best cycle strategies of bad NF group. (c) Best cycle strategies of good control group. (d) Best cycle strategies of bad control group.

Discussion

This paper aimed to investigate what music attributes were linked to best music neurofeedback performance. The musical attributes investigated were: valence, energy (arousal), key and genre. Participants were split into NF and control groups. Results compared groups and subgroups as well as collapsing the data across the entire sample and observing trends. We hypothesized that songs with higher valence and energy levels would be associated with the greatest improvement in neurofeedback performance. However, our data showed that songs with lower valence, medium energy levels, minor keys and within the pop genre were related to neurofeedback success.

Valence and Performance link: best song valence negatively correlated with performance

The valence of songs was extracted using the Spotify organizational tool as an indication of how happy or sad the song felt. Following work from previous studies, we hypothesized that songs with a more positive valence would be correlated with greater performance (9) however our data does not support this. Valence was correlated against performance in two ways. The first was the average valence of the songs used during the neurofeedback training. The second was the valence of the song of the cycle with the best neurofeedback performance. Average valence did not show significant correlation across the entire sample, nor within the NF group. For the NF group, although insignificant, here seemed to be a trend for the NF group whereby greater average valence was linked with greater performance. These results suggest that on average, music that subjects find pleasurable is highly variable in terms of valence which aligns with research regarding participants finding their own self-selected music pleasurable. (1)

The valence of best song showed a more interesting result. Across the entire sample, a strong negative correlation was found between best song valence and performance ($r = -0.468$, $p = 0.05$). This correlation maintained in the correlation of the NF group only however it was not significant ($r = -0.44$, $p > 0.05$). This finding suggests that songs with a negative valence are linked to increased performance regardless of whether the neurofeedback received is accurate (NF group), or not (control group). Studies have found that music can induce a sad affective state depending on the personality of listeners (18) however, people continue to listen to, and in fact enjoy sad music. (19) A systematic review suggests that sad music is found pleasurable "when it is perceived as non-threatening, aesthetically pleasing and produces psychological benefits such as mood

regulation." (12) These studies may help explain why participants seemed to have increased pleasure levels with the more negative valence songs, contrary to what had been hypothesized.

Energy and Performance link: medium energy for best song optimizes performance

The energy of songs was extracted using the Spotify organizational tool as an indication of arousal levels. We hypothesized that songs with higher energy levels would correlate with greater performance based on literature that suggested participants who experienced musical chills rated their songs as high in arousal (9) however our findings do not fully support this. The average energy of neurofeedback training songs did not correlate significantly with performance across the entire sample or across the NF group alone. However, there seemed to be a trend that was more defined in the NF group correlation, whereby a greater average energy score correlated with greater performance ($r = 0.59$, $p = 0.12$). Once again this is probably due to the large variation in energy levels in song preferences even within the same participant. The energy of the best song across the sample seemed to follow an inverted u-shape curve when correlated against performance and fit nicely to a second order polynomial function ($F(1,15) = 6.859$, $p = 0.0194$). This finding suggests that songs with the best performance fell in a medium energy score of around 50. A possible explanation for this could be that songs that had high energy levels were overpowering the participant's focus which led to decreased performance. In 2010, Sandstrom & Russo showed that higher arousal music was not as effective at helping a participant recover from an acute stressor so perhaps the same logic applies here, however more extensive research is needed to properly assess and understand this relationship.

Genre and Key Breakdown: successful participants selected minor songs and pop genre

Genre and key breakdowns provide more insight into the stimuli being used during the NF training sessions, particularly during a participant's best cycle. It was hypothesized that happier, higher energy songs would be linked to greater performance. Often, happy songs are characterized by a major key whereas more sad songs are characterized by a minor key. (2) So according to the hypothesis, we expected to see a greater number of major songs in the best song category which pertained to increased neurofeedback performance. However, consistent with the rest of our findings, the majority of the best songs had a minor key, which links back to the concept of sad songs generally being in a minor key. This data serves as a confirmation of the valence classification from the Spotify tool against the more traditional approach of categorizing music whereby major and minor keys were used to classify positive and negative valences respectively. (2)

The genre breakdown showed that the most common genre in the best song category across the entire sample was pop, however, this alone does not explain much. Possibly due to our age demographics, pop was the most selected genre across all song selections for the sample, so conclusions from the genre breakdown alone are not reliable. Having the genre information available may shed some light in later stages of the research when investigating interaction effects between genre, energy and valence for example. The strategy breakdown was also included for the same reason. Although the most common strategy for the best cycles was memory, it was also the most frequently chosen strategy overall, so conclusions regarding that cannot be drawn yet and require more extensive research.

Limitations of study

The biggest limitation of this study is the small sample size (N=20 although some participants were excluded in certain analyses) which leads to a decrease in statistical power. As such, we are less likely to detect effects if they are indeed evident. This small sample size also leads to an inability to generalize our findings past our sample, especially considering that it comes from a biased undergraduate sample. Nevertheless, this paper provides a necessary first step into the investigation of aspects of music that lead to greater improvement in music neurofeedback training but more research is required to solidify these findings and generalize them beyond the sample.

Another limitation of this study comes from the subgroup split design. In order to classify participants into better and worse performing groups, they were split using the median of NF participants. This allowed for a clearer definition of what "good" performance was regardless of whether it was in the control group or NF group. However, due to the control group split being dependent on the NF median, subgroup comparisons (for example good NF vs good controls) could not be reliably conducted. In future studies, splitting the groups according to each of their own medians instead would allow for these subgroup comparisons.

An additional limitation was regarding the variability of the music. The fact that measures of average valence and average energy both did not vary significantly with performance implies that the large variation in energy and valence across the sample was too heterogeneous to establish a clear correlation. This could be corrected for by using experimenter-selected music instead of participants to self-select their own music however that would compromise the increased pleasure that comes specifically from one's own music. Another aspect of variability that was not controlled for in this design was personality. Studies have shown that enjoyment of different types of music varies with personality traits. (19) In future studies therefore, it would be worth trying to focus on individuals that score high on a certain personality trait such as withdrawal (10) for example to reduce this variation. Finally, it is important to acknowledge that the statistical analyses conducted were correlational and causation cannot be implied from these findings as a result and it could be that there is an interaction effect between valence and energy, or other variables that contribute to neurofeedback performance.

Future Experiments

A finding that prompted future investigation ideas was that the significant correlations in best song energy and valence levels that were found were across the entire sample. This suggested that the effects of valence and energy on performance were evident regardless of whether or not the feedback the participant received was accurate. This motivates the question of whether highly pleasurable music can be just as effective at upregulating the NAc activity as neurofeedback. According to our findings, to answer this question, music that exhibits medium energy levels and low valence levels should be used.

Additionally, an expansion that was touched upon the discussion above was the need to separate the effects of energy and valence on performance. A suggestion for doing so would be to give participants music with a constant energy level and varying valences and vice versa to establish a more concrete effect of each by reducing the possible interaction. Additionally, an interaction effect could be investigated by giving participants music high in valence and arousal, low in valence and arousal or high in one and low in another and observe the effects that has on performance.

Further expansions from our data could include a more extensive analysis of genre and key. This could be executed by assigning participants music of a specific genre or key and observing its effect on their performance. This data could also be triangulated with the valence and energy data to try and establish a specific sub-genre that might be most effective at enhancing neurofeedback performance.

Finally, a component that this paper briefly touched upon is the use of

mental strategies during the music neurofeedback training. In order to study strategies according to their effectiveness, independently of their frequency, success using a strategy should be characterized by dividing the number of best cycles using that strategy by the number of total cycles the participant used the strategy. This gives us a measure of percent success rate. This would mitigate the effect of having the most frequent strategy also be the one used on the most successful trials which was observed in our data. Additionally, a strategy-music interaction study can be proposed. This study would look at whether certain strategies are coupled with songs of a particular valence or energy. Within our discussions between training cycles, some participants mentioned that they have specific strategies for specific songs which would motivate this suggested interaction study. Overall, this paper is meant to be seen as a stepping stone in the much larger realm of investigating the effects of different aspects of music on neurofeedback training.

References

1. Blood, A. J., & Zatorre, R. J. (2001). Intensely pleasurable responses to music correlate with activity in brain regions implicated in reward and emotion. Proceedings of the National Academy of Sciences, 98(20), 11818–11823. doi: 10.1073/pnas.191355898

2. Hunter, P. G., Schellenberg, E. G., & Schimmack, U. (2010). Feelings and perceptions of happiness and sadness induced by music: Similarities, differences, and mixed emotions. Psychology of Aesthetics, Creativity, and the Arts, 4(1), 47–56. doi: 10.1037/a0016873

3. Huron, D. (2011). Why is Sad Music Pleasurable? A Possible Role for Prolactin. Musicae Scientiae, 15(2), 146–158. doi: 10.1177/1029864911015002O2

4. Jamdar, A., Abraham, J., Khanna, K., & Dubey, R. (2015). Emotion analysis of songs based on lyrical and audio features. International Journal of Artificial Intelligence & Applications, 6(3), 35-50. doi:10.5121/ijaia.2015.6304

5. Keynan, J. N., Meir-Hasson, Y., Gilam, G., Cohen, A., Jackont, G., Kinreich, S., … Hendler, T. (2016). Limbic Activity Modulation Guided by Functional Magnetic Resonance Imaging–Inspired Electroencephalography Improves Implicit Emotion Regulation. Biological Psychiatry, 80(6), 490–496. doi: 10.1016/j.biopsych.2015.12.024

6. Keynan, J. N., Cohen, A., Jackont, G., Green, N., Goldway, N., Davidov, A., … Hendler, T. (2018). Electrical fingerprint of the amygdala guides neurofeedback training for stress resilience. Nature Human Behaviour, 3(1), 63–73. doi: 10.1038/s41562-018-0484-3

7. Macinnes, J. J., Dickerson, K. C., Chen, N.-K., & Adcock, R. A. (2016). Cognitive Neurostimulation: Learning to Volitionally Sustain Ventral Tegmental Area Activation. Neuron, 89(6), 1331–1342. doi: 10.1016/j.neuron.2016.02.002

8. Mayberg, H. (2008). Deep brain stimulation for treatment-resistant depression. Journal of Affective Disorders, 107. doi: 10.1016/j.jad.2007.12.153

9. Mori, K., & Iwanaga, M. (2017). Two types of peak emotional responses to music: The psychophysiology of chills and tears. Scientific Reports, 7(1). doi: 10.1038/srep46063

10. Raymond, J., Varney, C., Parkinson, L. A., & Gruzelier, J. H. (2005). The effects of alpha/theta neurofeedback on personality and mood. Cognitive Brain Research, 23(2-3), 287–292. doi: 10.1016/j.cogbrainres.2004.10.023

11. Russell, J. A. (1980). A circumplex model of affect. Journal of Personality and Social Psychology, 39(6), 1161–1178. doi: 10.1037/h0077714

12. Sachs, M. E., Damasio, A., & Habibi, A. (2015). The pleasures of sad music: a systematic review. Frontiers in Human Neuroscience, 9. doi: 10.3389/fnhum.2015.00404

13. Salamone, J. (1997). Behavioral functions of nucleus accumbens dopamine: Empirical and conceptual problems with the anhedonia hypothesis. Neuroscience & Biobehavioral Reviews, 21(3), 341–359. doi: 10.1016/s0149-7634(96)00017-6

14. Salimpoor, V. N., Bosch, I. V. D., Kovacevic, N., Mcintosh, A. R., Dagher, A., & Zatorre, R. J. (2013). Interactions Between the Nucleus Accumbens and Auditory Cortices Predict Music Reward Value. Science, 340(6129), 216–219. doi: 10.1126/science.1231059

15. Sandstrom, G. M., & Russo, F. A. (2010). Music Hath Charms: The Effects of Valence and Arousal on Recovery Following an Acute Stressor. Music and Medicine, 2(3), 137–143. doi: 10.1177/1943862110371486

16. Schlaepfer, T. E., Cohen, M. X., Frick, C., Kosel, M., Brodesser, D., Axmacher, N., … Sturm, V. (2007). Deep Brain Stimulation to Reward Circuitry Alleviates Anhedonia in Refractory Major Depression. Neuropsychopharmacology, 33(2), 368–377. doi: 10.1038/sj.npp.1301408

17. Sulzer, J., Sitaram, R., Blefari, M. L., Kollias, S., Birbaumer, N., Stephan, K. E., … Gassert, R. (2013). Neurofeedback-mediated self-regulation of the dopaminergic midbrain. NeuroImage, 75, 176. doi: 10.1016/j.neuroimage.2013.02.041

18. Vuoskoski, J. K., & Eerola, T. (2012). Can sad music really make you sad? Indirect measures of affective states induced by music and autobiographical memories. Psychology of Aesthetics, Creativity, and the Arts, 6(3), 204–213. doi: 10.1037/a0026937

19. Vuoskoski, J. K., Thompson, W. F., McIlwain, D., & Eerola, T. (2012). Who Enjoys Listening to Sad Music and Why? Music Perception: An Interdisciplinary Journal, 29(3), 311–317. doi: 10.1525/mp.2012.29.3.311

20. Y. Renard, F. Lotte, G. Gibert, M. Congedo, E. Maby, V. Delannoy, O. Bertrand, A. Lécuyer, "OpenViBE: An Open-Source Software Platform to Design, Test and Use Brain-Computer Interfaces in Real and Virtual Environments", Presence: teleoperators and virtual environments, vol. 19, no 1, 2010

Submitted: 01/15/21

Research Article

[1]Department of Atmospheric and Oceanic Sciences, McGill University, Montreal, QC, Canada
[2]Faculty of Science, University of Ontario Institute of Technology

Keywords

Rayleigh-Bénard problem, onset of convection, compressible fluid, numerical linear stability analysis.

Email Correspondence

katherine.simzer@mail.mcgill.ca

Katherine J. Simzer[1], Gregory M. Lewis[2]

Convective Rolls in a Compressible Fluid

Abstract

Rayleigh-Bénard convection occurs between two horizontally infinite plates when the lower plate is heated with respect to the upper one. The temperature gradient between the two plates causes convective rolls to form as the warmer fluid below becomes more buoyant than the cooler fluid above it. The standard (classical) analysis uses the Boussinesq approximation, which neglects the variations of fluid density except in relation to buoyancy forces. This approximation is not accurate for some real-world applications. This project is inspired by the atmosphere, so we will consider the onset of convection in a vertically stratified layer of fluid which we model using the anelastic equations. The standard analysis is presented in many textbooks and is used as a comparison to the analysis for the compressible fluid presented here. Using linear stability analysis, we compute the critical temperature differences required to induce convection. It is not possible to find analytical solutions, and therefore, numerical methods implemented in Python using LAPACK subroutines are used. Results of the critical Rayleigh number at the half-height of the fluid for a range of plate separation distances are computed. For all the cases that are considered, the solution for the compressible problem follows the standard solution for plate separation distances smaller than some viscosity-dependent value that increases with the viscosity of the fluid. For larger *d*, it is observed that the stratification inhibits the onset of convection. Our solution is far more idealized than any actual convection happening in the atmosphere. However, it does demonstrate, in this context, the limits of the Boussinesq approximation.

Introduction

Rayleigh-Bénard convection occurs in a fluid confined between two horizontally infinite plates when the lower plate is heated with respect to the upper one. When the temperature difference between the two plates is sufficiently large, the fluid begins to flow, as the warmer fluid below becomes more buoyant than the cooler fluid above it. This problem was first studied by Lord Rayleigh, in the context of an approximately incompressible fluid. (1,2) The onset of convection leads to the formation of patterns in the fluid. As the temperature difference between the plates is increased further past the critical value required to support fluid flow, the pattern seen in the fluid becomes increasingly more complicated. (3-5) This paper will consider the simplest pattern that is known to occur near the onset of convection, which consists of straight, parallel convection rolls; (5,6) see Fig. 1. This work is inspired by convection in the atmosphere, and, thus, will investigate the onset of these rolls in a compressible, vertically-stratified fluid which we model using the anelastic equations, which have been used extensively to model convection in the atmosphere. (7,8) Natural convective patterns in the atmosphere tend to vary greatly in time and across the horizontal plane, but they do keep a similar vertical structure to these idealized convective rolls. (5)

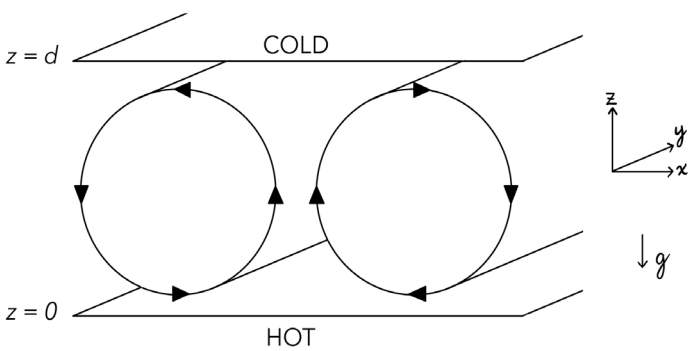

Figure 1. Thermal convective rolls between two infinite plates of different temperatures. Reproduced following Acheson (1990). (18)

The standard classical analysis of Rayleigh-Bénard convection uses the Boussinesq approximation, (9) in which variations in the density of the fluid are only accounted for in the buoyancy term, and thus the fluid is consider to be incompressible. This approximation requires low Mach-number and neglects acoustic frequencies. Work has been done to study the validity of the Boussinesq approximation in a compressible fluid in the context of the onset of convection, (10) which shows that it is only valid when the vertical dimension of the fluid is much less than any scale height. This implies that, in this context, the Boussinesq approximation will not hold at the spatial scales of the atmosphere.

Jeffreys (1930) found that instability in a compressible fluid arises only once the temperature gradient exceeds the adiabatic one. (11) They propose that the excess temperature gradient could be found by the same formula which gives the gradient needed for instability in a Boussinesq fluid. However, they conclude that this can only be applied directly when density does not vary greatly in the system. Spiegel (1965) verified Jeffreys' claim by performing a perturbation expansion in terms of layer thickness. (12) Non-Boussinesq convection with no-slip top and bottom boundaries has been studied by Tilgner (2011), using parameter values fitting the terrestrial troposphere. (13) They conclude that data collapse is obtained when an effective density given by the geometric mean of the maximum and minimum densities in the convecting layer is introduced to the scaling laws.

Other studies have looked at the anelastic approximation for a compressible fluid. This approximation was first proposed by Ogura and Charney (1960), (14) who implemented the anelastic approximation by filtering out the sound waves from the adiabatic motions of an inviscid fluid. (15) Further analysis of anelastic convection by a one-parameter expansion was done by Gough (1969), showing that molecular and radiative transport processes are approximately static on a convective timescale in the atmosphere. (15) In both papers, the range of the temperature is assumed to be close to the minimum required to produce the onset of convection. In the context of stellar convection, Spiegel (1965) studied the onset of convection in a polytropic atmosphere using a perturbation expansion in terms of layer thickness. (12)

There have been further studies of non-Boussinesq fluids in a variety of other contexts as well. Burnishev, Segre, and Steinberg (2010) looked at heat transport in turbulent convection of SF_6 near its gas-liquid critical point, and found that there is a symmetrical vertical dependence of the main physical properties such that the temperature in the midplane of the cell stays equal to the average value, despite the variations in fluid properties across the cell height. (16) Ahlers et al. (2007) experimentally measured and then calculated the non-Boussinesq effects of strongly turbulent

convection in ethane gas, finding a decrease of the central temperature compared to the mean of the top- and bottom-plate temperatures in the Boussinesq case. For the case of a numerical simulation of a perfect gas contained in a rigid box, Robinson and Chan (2004) found that a strong enough stratification caused changes in the observed bifurcation, where the signs of the thermal perturbations became antisymmetric about the roll center instead of symmetric as seen without the stratification. (17)

This paper will present an analysis of the onset of convection in a compressible fluid and compare the results with those for a fluid that follows the Boussinesq approximation shown in, for example, Acheson (1990) (18) and Kundu and Cohen (2002). (19) In this context, we seek a quantitative measure for the spatial scale at which the Boussinesq approximation breaks down for the parameter values relevant to the Earth's atmosphere, and we seek to determine how this value changes when the viscosity of the fluid is changed.

Model

We consider the problem of the onset of motion in a layer of fluid contained between two infinite horizontal plates, where the plates are separated by a distance d, the lower plate is held at a temperature T_l, and the upper plate is held at $T_l - \Delta T$. We model the flow of the fluid with the 3-D Navier-Stokes equations together with the thermodynamic energy equation for dry air and the mass continuity equation. (20) We assume that the equation of state of the fluid is given by the ideal gas law. In an isothermal atmosphere in hydrostatic balance, the hydrostatic pressure p_0 and density ρ_0 vary only with height z and are given explicitly by

$$p_0 = p_{00}e^{-z/H}, \qquad \rho_0 = \rho_{00}e^{-z/H}$$

where $H = R_*T_0/g$ is a scale height, R_* is the ideal gas constant, g is the gravitational constant, T_0 is a constant reference temperature defined as $p_0/(R_*\rho_0)$, and $p_{00} = p_0(z = 0)$ and $\rho_{00} = \rho_0(z = 0)$ are a reference pressure and density, respectively. We make the assumption that the density and pressure exhibit only small deviations from these profiles, which is a reasonable approximation for the atmosphere. (20) In particular, elastic variations in the flow, such as sound waves, are filtered. The resulting equations are generally referred to as the anelastic equations. We therefore write the pressure $p = p_0+p'$, density $\rho = \rho_0+\rho'$, and absolute temperature $T = T_0+T'$ of the fluid, where

$$\left|\frac{p'}{p_0}\right| \ll 1, \qquad \left|\frac{\rho'}{\rho_0}\right| \ll 1, \qquad \left|\frac{T'}{T_0}\right| \ll 1.$$

In addition, we make the assumption that the deviations from the static vertical profile satisfy

$$\left|\frac{\rho'}{\rho_0}\right| \approx -\left|\frac{T'}{T_0}\right|$$

which is expected to be a good approximation when the distance d between the plates is small relative to the scale height H. With these approximations, we can eliminate the density deviation ρ', and the momentum equation becomes

$$\rho_0 \frac{D\vec{u}}{Dt} = 2\rho_0\vec{\Omega} \times \vec{u} - \nabla p' - \frac{\rho_0}{T_0}\vec{g}T' + \mu\nabla^2\vec{u} \tag{1}$$

the thermodynamic equation becomes

$$\rho_0 c_V \frac{DT'}{Dt} = -\rho_0 g w + k\nabla^2 T' + Q \tag{2}$$

and the continuity equation becomes

$$\nabla \cdot (\rho_0\vec{u}) = \nabla \cdot \vec{u} - \frac{w}{H} = 0 \tag{3}$$

where $\vec{u} = (u, v, w)$ is the fluid velocity vector in a Cartesian coordinate system (x, y, z) rotating at rate $\vec{\Omega}$, $\vec{g} = -g$,

$$\frac{D}{Dt} = \frac{\partial}{\partial t} + \vec{u} \cdot \nabla, \quad \nabla = \hat{x}\frac{\partial}{\partial x} + \hat{y}\frac{\partial}{\partial y} + \hat{z}\frac{\partial}{\partial z},$$

the Laplacian $\nabla^2 = \nabla \cdot \nabla$, μ is the dynamic viscosity or alternatively an Eddy viscosity coeicient, k is the thermal conductivity, c_V is the specific heat at constant volume, and Q is the heating rate due to, for example, radiant and latent heat. We have assumed that the dynamic viscosity μ and the thermal conductivity k are constant.

For the boundary conditions, we assume no-slip at both plates. That is, the fluid will have zero velocity relative to the boundary. The temperature at the upper and lower plate is fixed at the prescribed values.

Equations 1–3 define a closed system for the fluid velocity $\vec{u}$, temperature deviation T', and pressure deviation p'. Similar equations appear in Spiegel (1965), (12) except that equations 1–3 use a simpler form of the viscosity and relation between the temperature and density deviations. We follow Spiegel (1965) and choose to work with the equations in dimensional form, because non-dimensionalization does not simplify the analysis. (12) In particular, in this context, the Rayleigh number depends on height z. However, to facilitate comparison with the classical results, we will present our results in terms of the Rayleigh number R_h at the centre height between the plates

$$R_h = \frac{gc_p\left(\frac{\Delta T}{d} - \frac{g}{c_p}\right)d^4\rho_{00}^2}{T_0 k\mu}e^{-\frac{d}{h}} \tag{4}$$

as in Spiegel (1965), where c_p is the specific heat at constant pressure (12). This is similar to the standard definition of the Rayleigh number except that it includes the vertical variation in the basic density profile, and the difference $\Delta T/d - g/c_p$ of the imposed temperature gradient and the adiabatic lapse rate replaces the temperature gradient alone. The latter emphasizes that the imposed temperature gradient must overcome the adiabatic lapse rate before instability can set in.

In this paper, we consider a non-rotating system and we assume that there is no source of heating other than the plates. That is, we take $\vec{\Omega} = 0$ and $Q = 0$. The effects of these choices on the dynamics will be considered in subsequent investigations.

Analysis

In the absence of motion, an analytical solution can be found in which the temperature has a linear dependence on z, where z has bounds from $z = 0$ to $z = d$. This solution is the conduction solution $T' = T_{cd}$, where

$$T_{cd} = \Delta T\left(\frac{-z}{d} + \frac{1}{2}\right)$$

and we have chosen $T_l = T_0 + \Delta T/2$. It is convenient to write $T' = T'' + T_{cd}$, in which case the thermodynamic equation becomes

$$\rho_0 c_V \frac{DT''}{Dt} = -\rho_0\left(g - \frac{c_V\Delta T}{d}\right)w + k\nabla^2 T'' \tag{5}$$

with corresponding boundary conditions $T''(z = 0) = T''(z = d) = 0$. Written as such, $T'' = 0$, $w = 0$ is the solution of Eq. 5, which corresponds to the conduction solution.

For sufficiently low values of ΔT, the conduction solution is stable. We expect the onset of convection to occur at the value of ΔT for which the conduction solution becomes unstable to some small perturbation. In particular, we seek the parameter value $\Delta T = \Delta T_c$ for which perturbations decay for $\Delta T < \Delta T_c$, and for which at least one form of perturbation grows for $\Delta T > \Delta T_c$. Because we consider only small perturbations, we can determine their dynamics from the linearization about the conduction solution.

We will restrict our attention to the case where the solutions at onset correspond to convective rolls (Fig. 1), where the flow consists of spatially

periodic pairs of counter-rotating cylindrical cells. As such, we consider only perturbations of this form. In this case, by orienting the y-axis along the lengthwise direction of the rolls, we can assume that $v = 0$ and that the solutions do not depend on y. We can, therefore, use a modified stream function, ψ, which ensures the continuity equation 3 is implicitly satisfied. In particular, we choose $\psi = \psi(x, z, t)$ such that

$$u = \frac{1}{\rho_0}\frac{\partial \Psi}{\partial z}, \qquad w = -\frac{1}{\rho_0}\frac{\partial \Psi}{\partial z} \tag{6}$$

If we take the curl of the linearized momentum equation 1, we can eliminate the pressure, and obtain

$$\frac{\partial}{\partial t}(\nabla \times \rho_0 \vec{u}) = -\frac{\rho_0}{T_0}\nabla T'' \times \vec{g} + \mu \nabla^2 (\nabla \times \vec{u}) \tag{7}$$

We can determine the evolution of ψ from the y-component of Eq. 7

$$\frac{\partial}{\partial t}\nabla^2 \Psi = -\frac{\rho_0 g}{T_0}\frac{\partial T''}{\partial x} + \mu \nabla^2 \left(\frac{1}{H\rho_0}\frac{\partial \Psi}{\partial z} + \frac{1}{\rho_0}\nabla^2 \Psi\right) \tag{8}$$

where we have eliminated u and w using Eq. 6. This equation together with the linearization of Eq. 5 defines a closed system that describes the evolution of the perturbations ψ, T'' when these are small. The corresponding boundary conditions are

$$\Psi = 0, \qquad \frac{\partial \Psi}{\partial z} = 0, \qquad T'' = 0, \qquad \text{at } z = 0, d$$

The second boundary condition on ψ ensures that the horizontal velocity u vanishes on the boundaries. In order to ensure that the vertical velocity w vanishes, we only require that ψ is constant on the boundaries. If this constant were different on the top and bottom boundaries, then there would be a net (average) flow in the x-direction, which is not expected due to the symmetry of the problem. We can, therefore, take $\psi = 0$ on both boundaries, because ψ is only determined up to an additive constant.

Because the convective rolls are spatially-periodic in the horizontal for some unknown period, we seek separable solutions of the form

$$\Psi = e^{\lambda t}\hat{\Psi}(z)e^{iax}, \qquad T'' = e^{\lambda t}\hat{T}(z)e^{iax} \tag{9}$$

where $2\pi/a$ is the horizontal spatial wavelength of the solution and, therefore, π/a gives the horizontal extent of each roll. Substitution of Eq. 9 into the linearized equations results in a (generalized) linear differential eigenvalue problem for the eigenvalues λ

$$\lambda A U = L U \tag{10}$$

where A and L are linear ordinary differential operators and $U = U(z) = \left[\hat{\Psi}, \hat{T}\right]$. In particular, the operators A and L involve up to fourth-order derivatives with respect to z; they will also depend on a and ΔT.

If for a given ΔT, all eigenvalues corresponding to all a have a negative real part, all small perturbations of the form of Eq. 9 will decay, and the conduction solution will be asymptotically stable. If any eigenvalue corresponding to any value of a has positive real part, the associated perturbations will grow, and the conduction solution is unstable. Therefore, if, for each a, we find the ΔT at which a single eigenvalue has zero real part, while all other eigenvalues have negative real part, then onset of convection will occur at the minimum such value of ΔT. That is, at the critical temperature difference ΔT_c a single eigenvalue for $a = a_c$ will have zero real part and all other eigenvalues associated with all other values of a will have negative real part.

This process is not able to determine the full form of the solution for $\Delta T > \Delta T_c$ because it is not able to determine the possible variations that may occur in the y-direction. In particular, in the classical Rayleigh-Bénard convection, close to onset, both rolls and hexagonal cells can be observed. (18) Thus, it is expected that our analysis will only determine the critical ΔT_c and the preferred horizontal spatial scale $a = a_c$ of the solution. The eigenvalue problem (Eq. 10) cannot be solved analytically, and therefore we use second-order centred finite differences to discretize in the z-direction on a uniform grid. Upon discretization, the problem is reduced to a matrix eigenvalue problem. The solution process is implemented in Python using LAPACK subroutines from the SciPy linear algebra module, which is expected to be accurate to round-o error. For all calculations, we discretize the vertical using $N = 100$ uniformly-spaced grid points; some of the computations are verified by also using $N = 50$ and $N = 200$ grid points.

Table 1 lists the values of the parameters used in the solution.

Variable	Value
g	9.81 [m s^{-1}]
c_v	716 [J kg^{-1} K^{-1}]
k	0.0227 [W m^{-1} K^{-1}]
ρ_0	1.412 [kg m^{-3}]
H	7310 [m]
T_0	250 [K]
R_*	287.058 [J kg^{-3} K^{-3}]

Table 1. Values of parameters used.

Results

For each value of the plate separation distance d that we consider, we seek the minimum value of the temperature difference ΔT for which the conduction state is neutrally stable. That is, we seek the critical temperature difference ΔT_c for which a single eigenvalue associated with wave number $a = a_c$ has zero real part while all other eigenvalues associated with all other values of a have negative real part. The eigenvalues are determined from Eq. 10, from which the evolution of perturbations from the conduction solution of the form of Eq. 9, can be determined. If we increment through a range of values of the wave number a, and for each a, we find the critical temperature difference associated with that specific wave number, then ΔT_c and a_c can be found where this critical temperature difference as a function of the wave number a achieves its minimum. Fig. 2 is an example of a plot of the Rayleigh number at half-height (see Eq. 4) calculated using the critical temperature difference as a function of wave number for plate separation $d = 0.1$m, for which $R_h = 2390.77$ and $a_c = 31\text{m}^{-1}$. In this case, and in all others that we consider, it is found that the critical eigenvalue is real, i.e. it is equal to zero.

The overall minimum critical temperature distance ΔT_c and its corresponding value of a_c are calculated for different plate separation distances d, with the corresponding Rayleigh number calculated at half-height. Fig. 3a highlights the relationship between d and R_h; for these calculations, the dynamic viscosity $\mu = 15.98 \times 10^{-3}$kg m^{-1} s^{-1}, and values for the other parameters are listed in Table 1. Two different trends can be seen, with lines of best fit that intersect where $d = 1.28$m. Spiegel (1965) found that in the limit of very small layer thickness the problem of convective stability is exactly represented by the Boussinesq equations as modified by Jeffreys (1930). (11, 12) This is what we see for values of d less than 1.28m, where the Rayleigh number at the half-height for the onset of convection is approximately constant with d. For values of d greater than 1.28m, the Rayleigh number at half-height increases for increasing d. Specifically, the

slope of the line of best fit on the log-log plot for $d > 1.28$m is 3.97, which implies the approximate relation $R_h \propto d^4$. The extra data points around the point of intersection of the two lines of best fit in Fig. 3a allow us to see that the transition between the two relationships is smooth.

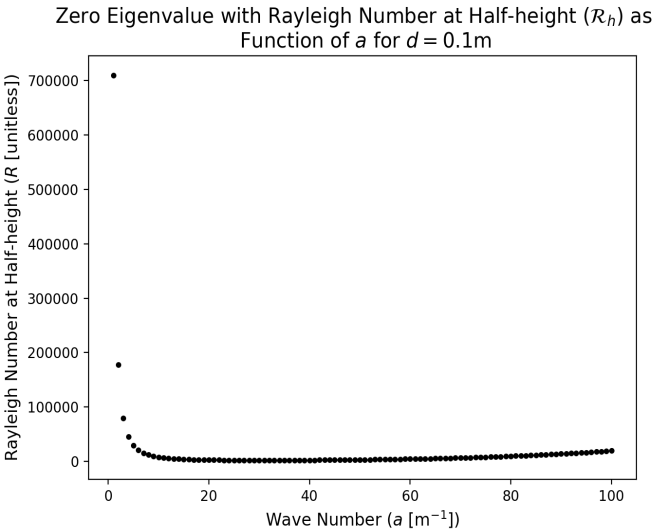

Figure 2. Zero eigenvalue plot produced for μ = 15.98 × 10−3 [kg m^{-1}s^{-1}] for d = 0.1m.

Fig. 3b shows the relationship between the wave number a and the plate separation distance d. Except for the largest value of d, this relationship is linear with slope -1.00 and intercept 3.10 on this log-log plot, implying that $a_c \approx 3.1/d$, approximately. The points where $d = 5000$m and $d = 10000$m do not fit well to the line of best fit, with corresponding values of a being smaller than expected; we have not included these points in the best fit calculation.

In the classical case addressed by Rayleigh (1916) (see Acheson (1990)), where it is assumed that the fluid is modelled well by the Boussinesq approximation and stress-free boundary conditions are used, (1, 18) the relationship between the critical wave number a_c and plate separation distance d is given by the expression

$$a_c = \frac{\pi}{\sqrt{2}d} \tag{11}$$

with corresponding critical Rayleigh number given by

$$R_c = \frac{agc_p\rho_0^2\Delta T_c d^3}{\mu k} = \frac{27\pi^4}{4} \tag{12}$$

where α is the coefficient of thermal expansion, and ρ_0 is constant. When more realistic boundary conditions are employed, the corresponding critical values are $a_c \approx 3.1/d$ and $R_c \approx 1708$ (see Kundu and Cohen (2002)). (19) We employ the more realistic boundary conditions, and therefore we expect our results to compare more closely to these.

In these classical problems, the critical Rayleigh number is independent of plate separation distance d. However, it is clear from Fig. 3a that this is not the case for a compressible fluid. At small d, the critical Rayleigh number at half-height is approximately constant with d. However, for $d > 1$m, the critical Rayleigh number at half-height grows with d; in particular, there is a $R_h \propto d^4$ relationship. The Rayleigh number at half-height approaches the standard Rayleigh number when d is small, and therefore it may be expected that the critical value for small d in the compressible case should approach that of the classical case. However, even in the limit as d goes to zero, the Boussinesq equations are only completely recovered from our anelastic equations when c_p is replaced with c_v (see Spiegel and Veronis (1960)). (10) If we do this, we recover the classical $R_c = 1708$ result for the smallest values of d, as expected, which provides some validation for our numerical results, as well. Although a discrepancy is observed in the critical Rayleigh number at half-height, the relationship between the critical wave number a_c and plate separation distance d for the compressible and Boussinesq cases only differ at the largest d. In particular, both cases exhibit an $a_c \approx 3.1/d$ relationship, except for the two largest values of plate separation distances where $d = 5000$m and $d = 10000$m, at which the compressible case deviates.

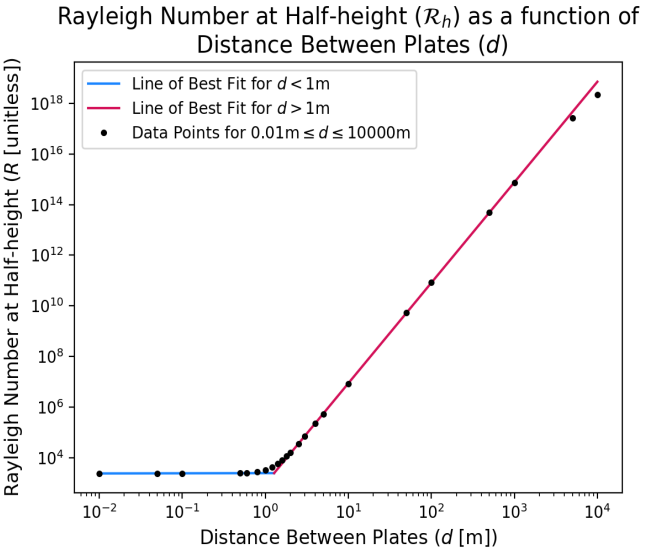

A. The two lines of best fit intersect at the point where $d = 1.28$m and $R_h = 2446.27$. Their slopes are 0.006 for $d < 1.28$m and 3.97 for $d > 1.28$m.

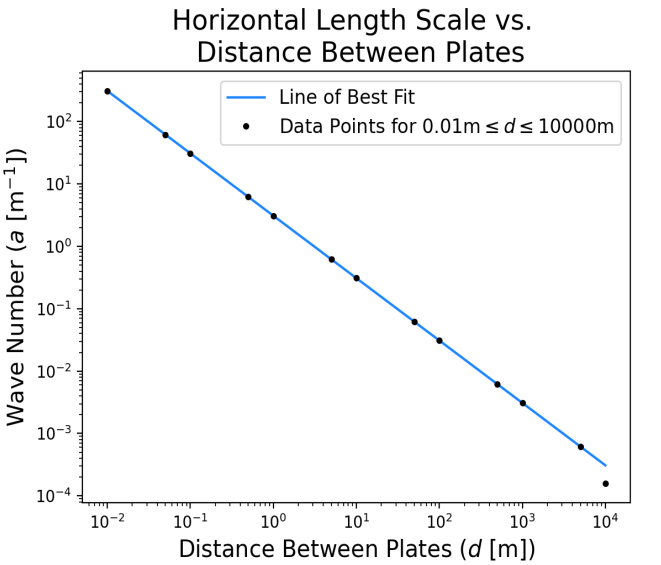

B. Comparing the horizontal length scale of the disturbance for different distances between the plates. The slope of the line of best fit is -1.00.

Figure 3. Graphs produced for $\mu = 15.98 \times 10^{-3}$ [kg m^{-1} s^{-1}].

These results have been verified by repeating the calculations with $N = 50$ and $N = 200$ grid points. Most values of ΔT_c have a percentage change much less than 1%, with only $d = 0.01$m having a larger change for $N =$

200. For values of a, most have no change with the exception of the largest d for d = 5000m and d = 10000m. This could explain the deviations in the results for large d in the graph of a vs. d. The reason for this is likely because at the small scales of a when d is large, there are only very small changes in R_h when trying to obtain the minimum, so the error in finding the true minimum a_c is higher.

Effects of Viscosity

The plots shown in Fig. 3 are recreated for a larger and smaller value of the dynamic viscosity μ. The viscosities we use differ greatly from the viscosity of dry air at atmospheric pressure since μ can alternatively be interpreted as an eddy viscosity coefficient. The value of the eddy viscosity coefficient depends on the flow rather than the physical properties of the fluid (Holton 2004), (20) so changes in the eddy viscosity may reflect changes in the smaller scale fluctuations within the fluid. As previously, the values for all the other parameters are taken to be those listed in Table 1; see Fig. 4 and Fig. 5. All of the plots have the same general trends, except with significant differences in the points of intersection of the lines of best fit, which are listed in Table 2. These points of intersection signify where compressible and Boussinesq fluids begin to differ, where the value of R_h begins to increase significantly. The data shows that the higher the viscosity of the fluid is, the larger the value of d and the smaller the value of a will be for the Rayleigh number to start increasing, and vice versa. The plots for each value of viscosity can be seen together in Fig. 4. Despite the differing viscosities, the data points and fit for values of $d \leq$ 1m are very similar (at the scale at which the points are plotted). The different viscosities show a significant difference for high values of d, where the results of the compressible solution deviate from the trend of the Boussinesq solution and the viscosity of the fluid has an effect.

Viscosity [kg m^{-1} s^{-1})]	d vs. $\mathcal{R}_h$	a vs. $\mathcal{R}_h$
15.98×10^{-1}	d_m = 3.87m	a_m = 0.77m^{-1}
	$\mathcal{R}_h$ = 2393.51	$\mathcal{R}_h$ = 2393.81
15.98×10^{-3}	d_m = 1.28m	a_m = 2.41m^{-1}
	$\mathcal{R}_h$ = 2446.27	$\mathcal{R}_h$ = 2446.37
15.98×10^{-6}	d_m = 0.23m	a_m = 13.53m^{-1}
	$\mathcal{R}_h$ = 2477.35	$\mathcal{R}_h$ = 2477.35

Table 2. Location of the point of intersection (d_m, a_m) for the lines of best fit for three values of viscosity μ.

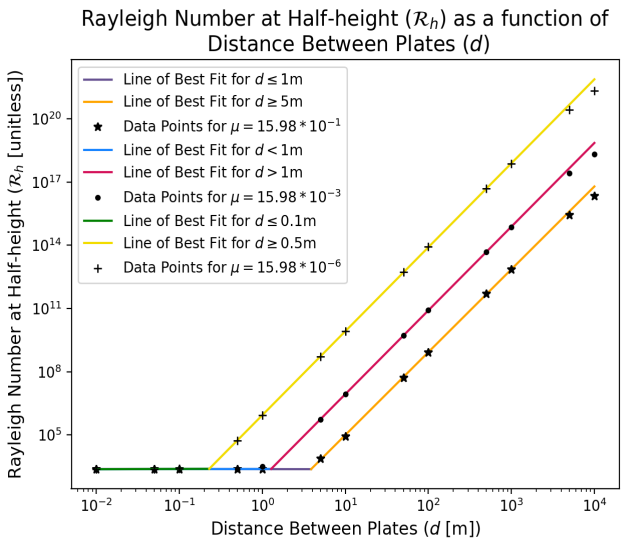

Figure 4. Plot of the relationship between R_h and d for three different values of viscosity. The points of intersection for each are detailed in Table 2.

Comparing the relationship between the critical wave number a_c and the plate separation distance d for the higher and lower viscosity in Fig. 5, we can see that the lower viscosity diverges from the linear relationship at a lower d, when d = 5000m, and that the deviation is more pronounced. The opposite is true for the higher viscosity, where the linear relationship is closely maintained for d = 10000m. The reasoning for this is likely the same as described before, due to the fact that it is difficult to get an exact minimum value of a because they are so small for large values of d. With the smallest value of viscosity this is the most pronounced because the change in the value of R_h at small d is the smallest. For many of the smaller values of d, their corresponding values of a are very similar despite the differences in viscosity.

Discussion and Conclusion

For all the cases that we consider, the compressible solution follows the Boussinesq solution for a small plate separation distance d. This is because for smaller values of d there is less difference in the density of the fluid from the bottom to the top of the layer. This difference in density increases as d increases and the stratification becomes more pronounced, which causes the Rayleigh number R_h to increase as the stratification plays a more important role in convection. Jeffreys (1930) proposed that, for instability to set in, the temperature gradient across the layer of fluid must first overcome the stability due to stratification of the fluid. (11) That is, it must exceed the adiabatic lapse rate. The d^4 dependence, observed in Fig 4 for large d, supports this, as it implies that the imposed temperature gradient is small compared to the adiabatic lapse rate. To investigate this further, we plot the critical temperature gradient ($\Delta T_c/d$) as a function of the distance d between the plates, and compare this to the adiabatic lapse rate; see Fig. 6. It can be seen that, for all three viscosities, the critical temperature gradient between the plates needed to induce convection is greater than the dry adiabatic lapse rate. This difference is even greater for smaller values of d. For higher values of d, the critical temperature gradient for all viscosities converges to the same constant value that is greater than the dry adiabatic lapse rate. In particular, for 50m $\leq d \leq$ 10000m, the difference between the data and the dry adiabatic lapse rate is 3.95×10^{-3} [K/m] for all viscosities.

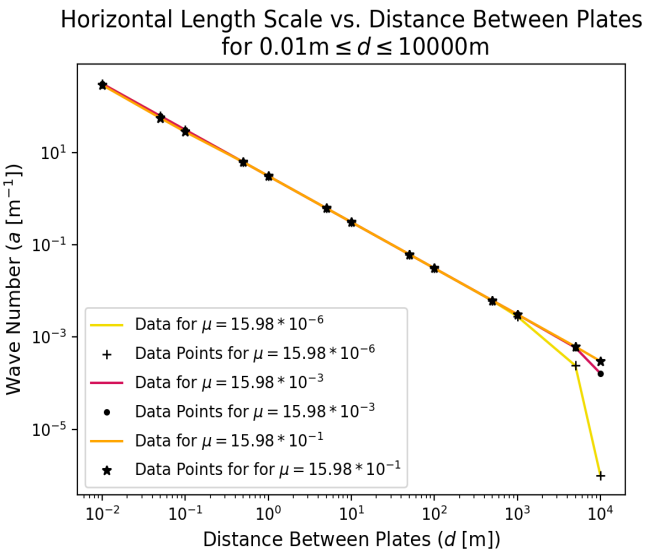

Figure 5. Plot of the relationship between a and d for three different values of viscosity.

We found that the range of plate separation distance d over which the Boussinesq assumption is applicable to the compressible case depends on the viscosity of the fluid. In particular, there is some clearly-defined viscosity-dependent value of d, which we have determined quantitatively, at which the compressible solution deviates from the Boussinesq solution. This value of d is larger for a more viscous fluid. It is interesting that this deviation comes at scales as small as 1m, although it is not unexpected, based solely on the requirement that the imposed temperature gradient

must overcome the adiabatic lapse rate. It should be noted that these results do not imply that the anelastic equations must be employed at all scales greater than 1m. In particular, in a stably stratified layer vertical motion is inhibited, and in the limit as w goes to zero, we recover an incompressible fluid (see Eq. 3), in which the effects of gravity are not important. Thus, it is only important to consider the anelastic equations in cases when there is significant vertical motion.

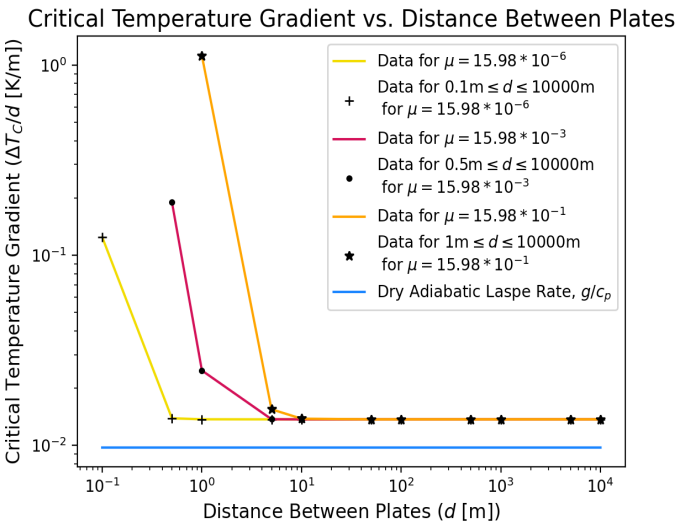

Figure 6. The relationship between $\Delta T_c/d$ and d is shown for three different values of viscosity.

Another deviation between the compressible and Boussinesq cases occurs in the $a_c = 3.1/d$ relation at large plate separation distance d. For the lowest viscosity, the deviation is orders of magnitude for $d = 10000$m; the corresponding horizontal wave length of the convection rolls in the compressible fluid is of the order of 1000km. This result, however, must be taken with caution, as should all results at the largest plate separation distances, because the assumptions of our model are only valid when the plate separation is small relative to the scale height. For the parameters that we considered, this scale height is of the order of 7km, which means that we cannot be sure of our results for the largest d that we considered. In addition, we also observed larger changes in the computed values when performing the computations on a finer grid. It is for this reason that the two largest values of d are not included in the calculation of the intersections for Fig. 3a and Fig. 4, so we can maintain confidence in the results of the change in the behaviour.

Near the onset of convection, the structure of the convective rolls can often be approximately determined by the eigenfunction (i.e. the perturbation) corresponding to the zero eigenvalue. Furthermore, because the eigenvalue is real, we would expect the flow to be steady. We do not prove these here, because the proof would have to take into consideration the nonlinear terms in the governing equations. Thus, the form of the convective rolls is determined by the value of the critical wave number a for a given d, and the vertical part of the eigenfunction $U = \left[\hat{\Psi}(z), \hat{T}(z)\right]$ (see Eq. 9 and Eq. 10). Fig. 7 shows a contour plot of an example of the temperature portion of the eigenfunction for $d = 1000$m; the corresponding plots for all other plate separation distances d have similar form. The real part of the eigenfunction is plotted; the imaginary part is the same, but with a shifted spatial phase. The horizontal structure of the rolls is periodic with period $2\pi/a_c$, and the vertical structure is symmetric about the mid-plane, with a maximum occurring at the mid-plane. This follows with the expected straight, parallel convection rolls that occur near the onset of convection. (5, 6) The vertical cross section through height, which is not shown here, also matches what was found in Spiegel (1965). (12)

In this paper, we have studied the onset of convection in a compressible fluid contained between two infinite horizontal plates. We use a model that is inspired by the parameters found for the Earth's atmosphere. However, in order to simplify the analysis, we consider an isothermal atmosphere and we incorporate an assumption that restricts its applicability to plate separations that are less than the troposphere's height. These assumptions are sufficient to explore the region in which the solutions of the Boussinesq equations begin to differ from those of the anelastic equations. Future work will investigate the eects of relaxing these assumptions and will also include exploring the effects of a rotating system ($\vec{\Omega} \neq 0$) or one with internal sources of heat ($Q \neq 0$).

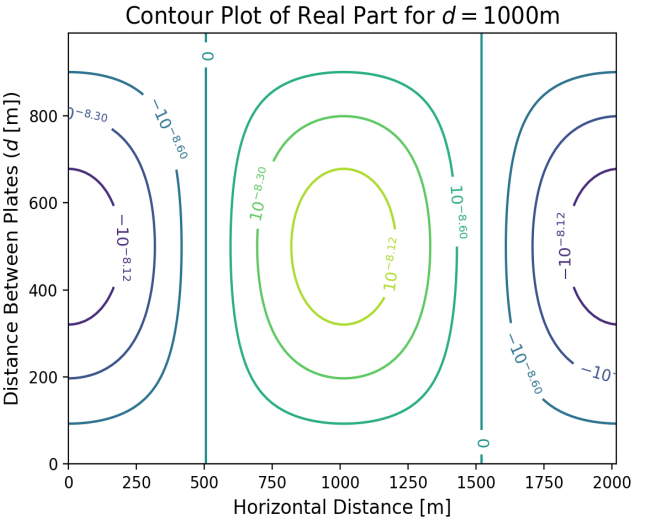

Figure 7. Contour plot of the real part of the temperature perturbation corresponding to the critical eigenvalue, produced for $\mu = 15.98 \times 10^{-3}$ [kg m^{-1} s^{-1}] for d = 1000m. The level heights for each contour line are labelled.

Acknowledgements

G.M. Lewis would like to acknowledge support from the Natural Sciences and Engineering Research Council of Canada (NSERC). The authors would also like to thank the reviewers for their comments, which provided insight to improve this work.

References

1. Rayleigh, L. 1916. "LIX. On convection currents in a horizontal layer of fluid, when the higher temperature is on the under side." The London, Edinburgh, and Dublin Philosophical Magazine and Journal of Science 32 (192): 529–546. https://doi.org/10.1080/14786441608635602.

2. Chitre, S. M., and M. H. Gokhale. 1973. "Convective instability in a compressible atmosphere." Solar Phys. 30:309–318. https://doi.org/10.1007/BF00152662.

3. Busse, F. H. 1978. "Non-linear properties of thermal convection." Reports on Progress in Physics 41, no. 12 (December): 1929–1967. https://doi.org/10.1088/0034-4885/41/12/003. https://doi.org/10.1088/0034-4885/41/12/003.

4. Busse, F. H. 1989. Fundamentals of thermal convection. In Mantle Convection: Plate Tectonics and Global Dynamics, edited by W. Peltier. 23–95. Montreux: Gordon / Breach.

5. Bodenschatz, E., W. Pesch, and G. Ahlers. 2000. "Recent Developments in Rayleigh-Bénard Convection." Annual Review of Fluid Mechanics 32 (1): 709–778. https://doi.org/10.1146/annurev.fluid.32.1.709.

6. Schlüter, A., D. Lortz, and F. Busse. 1965. "On the stability of steady

finite amplitude convection." Journal of Fluid Mechanics 23 (1): 129–144. https://doi.org/10.1017/S0022112065001271.

7. Kurowski, M. J., W. W. Grabowski, and P. K. Smolarkiewicz. 2014. "Anelastic and Compressible Simulation of Moist Deep Convection." Journal of the Atmospheric Sciences (Boston MA, USA) 71, no. 10 (October): 3767–3787. https://doi.org/10.1175/JAS-D-14-0017.1.

8. Lipps, F. B. 1990. "On the Anelastic Approximation for Deep Convection." Journal of Atmospheric Sciences 47, no. 14 (July): 1794–1798. https://doi.org/10.1175/1520-0469(1990)047<1794:OTAAFD>2.0.CO;2.

9. Boussinesq, J. 1903. Théorie analytique de la chaleur. Vol. 2. Paris: Gauthier-Villars.

10. Spiegel, E. A., and G. Veronis. 1960. "On the Boussinesq Approximation for a Compressible Fluid." Astrophysical Journal 131:442–447.

11. Jeffreys, H. 1930. "The Instability of a Compressible Fluid heated below." Mathematical Proceedings of the Cambridge Philosophical Society 26 (2): 170–172. https://doi.org/10.1017/S0305004100015413.

12. Spiegel, E. A. 1965. "Convective Instability in a Compressible Atmosphere. I." 141 (April): 1068–1090. https://doi.org/10.1086/148197.

13. Tilgner, A. 2011. "Convection in an ideal gas at high Rayleigh numbers." Phys. Rev. E 84 (2): 026323. https://doi.org/10.1103/PhysRevE.84.026323.
14. Ogura, Y., and J. G. Charney. 1960. "A numerical model of thermal convection in the atmosphere." Proc. Internat. Symposium on Numerical Weather Prediction, 431–452.

15. Gough, D. O. 1969. "The Anelastic Approximation for Thermal Convection." Journal of Atmospheric Sciences (Boston MA, USA) 26, no. 3 (May): 448–456. https://doi.org/10.1175/1520-0469(1969)026<0448:TAAFTC>2.0.CO;2.

16. Burnishev, Y., E. Segre, and V. Steinberg. 2010. "Strong symmetrical non-Oberbeck–Boussinesq turbulent convection and the role of compressibility." Physics of Fluids 22 (3): 035108. https://doi.org/10.1063/1.3358462. https://doi.org/10.1063/1.3358462.

17. Robinson, F., and K. Chan. 2004. "Non-Boussinesq simulations of Rayleigh–Bénard convection in a perfect gas." Physics of Fluids 16 (5): 1321–1333. https://doi.org/10.1063/1.1689350. https://doi.org/10.1063/1.1689350.

18. Acheson, D. J. 1990. Elementary Fluid Dynamics. Oxford: Clarendon Press.

19. Kundu, P., and I. Cohen. 2002. Fluid Mechanics. 2nd ed. San Diego, CA: Academic Press.

20. Holton, J. R. 2004. An Introduction to Dynamic Meteorology. Burlington, MA: Elsevier Academic Press.

Submitted: 12/12/20

Research Article

Department of Physics, McGill University, Montreal QC H3A 2T8, Canada

Keywords

Hochschild cohomology, Frobenius algebras, 3-manifolds, cohomology algebra

Email Correspondence

qiu.s.wang@mail.mcgill.ca

Qiu Shi Wang[1]

Hochschild Cohomology of the Cohomology Algebra of Closed Orientable Three-Manifolds

Abstract

Let $\mathbb{F}$ be a field of characteristic other than 2. We show that the zeroth Hochschild cohomology vector space $HH^0(A)$ of a degree 3 graded commutative Frobenius $\mathbb{F}$-algebra $A = \oplus_i A^i$, where we will always assume $A^0 \cong \mathbb{F}$, is isomorphic to the direct sum of the degree $0, 2$ and 3 graded components and the kernel of a certain natural evaluation map $\iota_\mu : A^1 \to \Lambda^2(A^1)$. In particular, this holds for $A = H^*(M; \mathbb{F})$ the cohomology algebra of a closed orientable 3-manifold M.

In Theorem A of [1], Charette proves the vanishing of a certain discriminant Δ associated to a closed orientable 3-manifold L with vanishing cup product 3-form. It turns out that if we could show that $HH^{2,-2}(A) = 0$ for $A = H^*(L; \mathbb{C})$, we would have found a more elementary proof of this part of Charette's theorem. We show that for any $\beta \geq 3$, the degree 3 graded commutative Frobenius algebra A with $\mu_A = 0$ and $\dim(A^1) = \beta$ satisfies $HH^{2,-2}(A) \neq 0$. Thus Charette's theorem is not simplified.

1 Introduction

Overview of the problems

We first introduce the problem without defining the mathematical objects involved. The definitions will be provided in further sections of the text, with references.

To any $\mathbb{F}$-algebra A we can associate the Hochschild cohomology $HH^*(A; A)$. If A is a graded algebra, then it also has a bigraded version $HH^{*,*}(A; A)$ defined in (2.4). In this text we will always use coefficients in A, so we omit it and write $HH^*(A)$ and $HH^{*,*}(A)$.

The cohomology algebra of a closed orientable 3-manifold is a degree 3 graded commutative Frobenius algebra with zeroth graded component of dimension 1. As we are interested in characterizing the cohomology algebra of such manifolds, we restrict our study to the above-mentioned type of algebra.

We are interested in answering the following two questions:

- **Question 1:** Let A be a degree 3 graded commutative Frobenius algebra with $A^0 \cong \mathbb{F}$. Can we compute $HH^*(A)$ and $HH^{*,*}(A)$ in terms of its 3-form μ_A and $\dim(A^2)$?
- **Question 2:** In particular, if $\mu_A = 0$, is $HH^{2,-2}(A)$ necessarily zero?

Main results

We give a limited partial answer to Question 1. As the computational complexity of calculating $HH^n(A)$ is of $O(e^n)$, brute force calculation using a computer is infeasible. However, we can still characterize $HH^0(A)$. Define the 3-form of A to be the map $\mu_A : A^1 \times A^1 \times A^1 \to \mathbb{F}$ by $\mu_A(x, y, z) = \sigma(xy, z)$ where σ is the Frobenius form of A. Define the map $\iota_\mu : A^1 \to \Lambda^2(A^1)$ by $\iota_\mu(x) = \mu_A(x, \cdot, \cdot)$. Then our first main result is:

Theorem 1. *Let $\mathbb{F}$ be a field of characteristic other than 2 and let A be a graded commutative Frobenius $\mathbb{F}$-algebra of degree 3, with graded components A^0, A^1, A^2 and A^3 such that $A^0 \cong \mathbb{F}$. Then*

$$HH^0(A) \cong A^0 \oplus \ker(\iota_\mu) \oplus A^2 \oplus A^3 \cong \mathbb{F}^{2+\dim A^2} \oplus \ker(\iota_\mu).$$

Note that $\dim(A^1) = \dim(A^2)$. Our second main result answers Question 2 in the negative.

Theorem 2. *Let $\mathbb{F}$ be a field of characteristic other than 2 and let $\beta \geq 3$ be an integer. Then the unique degree 3 graded commutative Frobenius algebra $A = \oplus_i A^i$ with $A^0 \cong \mathbb{F}$ such that $\dim_{\mathbb{F}}(A^1) = \beta$ and $\mu_A = 0$ satisfies*

$$HH^{2,-2}(A) \neq 0.$$

Motivation and significance

Recall that for any closed orientable 3-manifold M, we have $H^3(M; \mathbb{F}) \cong \mathbb{F}$ by Poincaré duality. We can define an antisymmetric 3-form using the cup product:

$$\mu_M : H^1(M; \mathbb{F}) \times H^1(M; \mathbb{F}) \times H^1(M; \mathbb{F}) \to H^3(M; \mathbb{F}) \cong \mathbb{F}.$$

Together with Poincaré duality, μ_M uniquely determines the cohomology algebra $H^*(M; \mathbb{F}) \equiv A$, a degree 3 graded commutative Frobenius algebra with 3-form $\mu_A = \mu_M$. Thus, Theorem 1 provides a characterization of the zeroth Hochschild cohomology of the cohomology $\mathbb{F}$-algebra of a closed orientable 3-manifold in terms of its cup product 3-form μ_M.

Another motivation for our work on degree 3 graded commutative Frobenius algebras is the following result due to Sullivan:

Theorem 3 (Sullivan [2])**.** *Let μ be an integral antisymmetric 3-form on a free abelian group H of finite rank. Then there exists a closed orientable 3-manifold M such that μ is the cup product 3-form of M and $H^1(M; \mathbb{Z}) = H$.*

However, Sullivan's theorem is not necessarily true for an arbitrary 3-form on a finite-dimensional $\mathbb{F}$-vector space, and thus not every Frobenius algebra we consider may be realized by a manifold.

In Theorem A of [1], Charette proves the vanishing of a discriminant Δ associated to a closed orientable Lagrangian 3-manifold L with vanishing

cup product 3-form μ_L by using holomorphic curve techniques. It turns out that Δ is the discriminant of a quadratic form in the image of a map $\Theta : HH^{2,-2}(H^*(L;\mathbb{C})) \to Q^2(H^1(L;\mathbb{C});\mathbb{C})$ from $HH^{2,-2}$ to the space of complex valued quadratic forms on the first cohomology group of L. Then, one can ask if there is a more elementary proof that Δ vanishes, for example by showing that $HH^{2,-2} = 0$ for any L with $\mu_L = 0$. This is precisely Question 1, to which Theorem 2 answers in the negative. Thus Charette's proof is not simplified. More details can be found in section 2.5.

2 Background

2.1 Graded commutative Frobenius algebras

Let $\mathbb{F}$ be a field. We recall the following definitions.

An $\mathbb{F}$-algebra A is said to be graded if it can be decomposed into a direct sum $A = \oplus_{n=0}^{\infty} A^n$ such that $A^p A^q \subset A^{p+q}$. The highest n for which $A^n \neq 0$, if it exists, is the degree of the graded algebra. An algebra is said to be graded commutative if it is graded and also, for $x_p \in A^p$ and $x_q \in A^q$, we have

$$x_p x_q = (-1)^{pq} x_q x_p. \tag{2.1}$$

We define a graded commutative Frobenius algebra as an associative finite-dimensional unital graded commutative algebra $A = \oplus_{i=0}^{n} A^i$ equipped with a nondegenerate bilinear form $\sigma : A \times A \to \mathbb{F}$ satisfying $\sigma(xy, z) = \sigma(x, yz)$ for all $x, y, z \in A$. We require σ, the Frobenius form of A, to be consistent with the grading of A in the sense that $\sigma|_{A^i \times A^j}$ is the zero map whenever $i + j \neq n$. Note that the unit of the algebra is in A^0.

Throughout this article we will only consider degree n graded commutative Frobenius algebras $A = \oplus_{p=0}^{n} A^p$ such that $A^0 \cong \mathbb{F}$. For $n = 3$, we define the 3-form of A to be the map $\mu_A : A^1 \times A^1 \times A^1 \to \mathbb{F}$ sending (x, y, z) to $\sigma(xy, z)$. The proof of a version of the following useful proposition can be found in [3, Section 10.2].

Proposition 1. *Given a basis $\{x_1, \cdots, x_b\}$ for A^p, there is a basis $\{\overline{x_1}, \cdots, \overline{x_b}\}$ for A^{n-p} dual to it in the sense that $\sigma(x_i, \overline{x_j}) = \delta_{ij}$.*

2.2 Cohomology algebra of closed orientable 3-manifolds

The following results from elementary homology theory can be found in any introductory textbook in algebraic topology, notably [4] and [5]. They show that Theorems 1 and 2 apply to cohomology algebras of closed orientable 3-manifolds.

For an abelian coefficient group G, the singular cohomology functors H^i : **Top** $\to$ **Ab** take a topological space X to its cohomology groups $H^i(X; G)$. By Poincaré duality, we know that for a closed orientable 3-manifold M and $\mathbb{F}$ a coefficients field, $H^0(M;\mathbb{F}) \cong H^3(M;\mathbb{F}) \cong \mathbb{F}$ and $H^1(M;\mathbb{F}) \cong H^2(M;\mathbb{F}) \cong \mathbb{F}^\beta$, where β is the first Betti number of M. We have $H^i(M;\mathbb{F}) = 0$ for $i < 0$ or $i \geq 4$. The vector space $H^*(M;\mathbb{F}) = \bigoplus_i H^i(M;\mathbb{F})$, together with the cup product $\smile$: $H^i(M;\mathbb{F}) \times H^j(M;\mathbb{F}) \to H^{i+j}(M;\mathbb{F})$, forms the cohomology algebra of M with coefficients in $\mathbb{F}$. The cup product is graded commutative, that is, for $x_p \in H^p(M;\mathbb{F})$ and $x_q \in H^q(M;\mathbb{F})$, it satisfies (2.1).

Choose an orientation for M and let $[M] \in H_n(M;\mathbb{F})$ be the corresponding fundamental class. We will need the following consequence of Poincaré duality:

Theorem 4. *For a field $\mathbb{F}$ and M^n a closed and orientable manifold, the map*

$$\varphi : H^p(M;\mathbb{F}) \to \mathrm{Hom}_{\mathbb{F}}(H^{n-p}(M;\mathbb{F}), \mathbb{F})$$

taking $\alpha \mapsto \overline{\alpha}$ where $\overline{\alpha}(x) = (\alpha \smile x)([M])$, is an isomorphism. Equivalently, there is a nondegenerate pairing

$$H^p(M;\mathbb{F}) \times H^{n-p}(M;\mathbb{F}) \xrightarrow{\langle\ ,\ \rangle} \mathbb{F}$$

sending $(a, b) \mapsto \varphi(a)(b) = (a \smile b)([M])$. Therefore, the algebra $H^*(M;\mathbb{F})$ is a degree n graded commutative Frobenius algebra with Frobenius form $\sigma(a, b) = \langle a, b\rangle$.

Now let $n = 3$. If we choose the basis $\{e\}$ of $H^3(M;\mathbb{F})$ such that $e([M]) = 1 \in \mathbb{F}$, we get that $x_i \smile \overline{x_j} = \delta_{ij} e$ for x_i and $\overline{x_j}$ from Proposition 1. The latter Proposition notably implies that any nonzero element $x \in A^1$ has a dual $x^* \in A^2$ such that $xx^* = e$.

We define the multilinear map $\mu_M : A^1 \times A^1 \times A^1 \to \mathbb{F}$ by $\mu_M(x, y, z) = (x \smile y \smile z)([M])$. Then, (2.1) for $i = j = 1$ gives us that μ_M is an alternating 3-form. In the above basis, if $x \smile y \smile z = \eta e$, then $\mu_M(x, y, z) = \eta$.

Proposition 2. *The 3-form μ_M and Poincaré duality determine the cup product $A^1 \times A^1 \to A^2$.*

Proof. Take $n = 3$ and $p = 2$ in Theorem 4. To each $\alpha, \beta \in A^1$ corresponds an element of $\mathrm{Hom}_{\mathbb{F}}(A^1, \mathbb{F})$ defined by sending $x \mapsto \mu(\alpha, \beta, x)$. Thus $\alpha \smile \beta \in A^2$ is $\varphi^{-1}(\mu(\alpha, \beta, \cdot))$. ∎

In the basis for A^1 of Proposition 1 (for $n = 3$ and $p = 1$), an arbitrary 3-form can be written as, for scalars $a_{ijk} \in \mathbb{F}$,

$$\mu = \sum_{i<j<k} a_{ijk} dx^i \wedge dx^j \wedge dx^k. \tag{2.2}$$

In the above basis, we have the formula $x_i \smile x_j = \sum_k a_{ijk} \overline{x_k} \in A^2$, justified by Proposition 2.2.

Define the evaluation map $\iota_\mu : A^1 \to \Lambda^2(A^1)$ by $\iota_\mu(x) = \mu(x, \cdot, \cdot)$.

Example 1. The 3-torus $T = S^1 \times S^1 \times S^1$ has first Betti number 3 and three-form $\mu_T = dx^1 \wedge dx^2 \wedge dx^3$. Its cohomology algebra is then the exterior algebra $\Lambda^3(\mathbb{F})$, and as a result $\ker(\iota_\mu) = \{0\}$.

Example 2. Let $M = \#^\beta(S^1 \times S^2)$, the connected sum of β copies of $S^1 \times S^2$. The Künneth formula, which can be found in [5, Section 3.2] for example, gives us an isomorphism $H^*(S^1 \times S^2;\mathbb{F}) \cong H^*(S^1;\mathbb{F}) \otimes H^*(S^2;\mathbb{F})$. This gives us $H^1(S^1 \times S^2;\mathbb{F}) \cong H^2(S^1 \times S^2;\mathbb{F}) \cong \mathbb{F}$. Suppose a generates H^1 and b generates H^2. Then $a \smile b$ generates H^3. It is standard to show that taking the connected sum preserves the cup product structure on each copy of $S^1 \times S^2$ and sets cup products of cohomology classes from different copies to 0; see for example [4, Chapter VI, Section 9]. This results in the cup product on $H^1(M;\mathbb{F}) \cong \mathbb{F}^\beta$ being trivial, giving $\mu_M = 0$ and thus $\iota_\mu = 0$ and $\ker(\iota_\mu) = A^1$.

2.3 Hochschild cohomology

For a field $\mathbb{F}$, Hochschild cohomology associates a sequence of $\mathbb{F}$-vector spaces $HH^i(A)$ to an $\mathbb{F}$-algebra A. In Hochschild's original paper [6], the Hochschild chain complex of A with coefficients in A are defined as

$$CC^k(A) = \mathrm{Hom}_{\mathbb{F}}(A^{\otimes k}, A)$$

where $A^{\otimes k}$ is the tensor product of A with itself k times and $A^{\otimes 0} = \mathbb{F}$. They are equipped with the differential $d : CC^k(A) \to CC^{k+1}(A)$ defined by the following formula, for $f \in CC^k(A)$:

$$\begin{aligned} df(a_1 \otimes \cdots \otimes a_{k+1}) &= a_1 f(a_2 \otimes \cdots \otimes a_{k+1}) \\ &+ \sum_{i=1}^{k} (-1)^i f(a_1 \otimes \cdots \otimes a_i a_{i+1} \otimes \cdots \otimes a_{k+1}) \\ &+ (-1)^{k+1} f(a_1 \otimes \cdots \otimes a_k) a_{k+1}. \end{aligned} \tag{2.3}$$

For the $k = 0$ case, we have $df(a_1) = a_1 f(1) - f(1) a_1$.

The proof of the following proposition is a tedious calculation that will be omitted. It can be found in [6].

Proposition 3. $d^2 = 0$.

Thus we can define the *n-th Hochschild cohomology of A* (with coefficients in A) as

$$HH^n(A) = \frac{\ker(d : CC^n(A) \to CC^{n+1}(A))}{\mathrm{im}(d : CC^{n-1}(A) \to CC^n(A))}.$$

Note that for $n \leq -1$, $HH^n(A) = 0$.

2.4 Bigraded Hochschild cohomology

Let $A = \oplus_i A^i$ be a graded algebra. A standard procedure, described in for example [7, Section 5.4], is incorporating the grading of A into its Hochschild cohomology by defining the bigraded Hochschild complex $CC^{n,r}(A) = \mathrm{Hom}^r_{\mathbb{F}}(A^{\otimes n}, A) \subset CC^n(A)$. Here $\mathrm{Hom}^r_{\mathbb{F}}(A^{\otimes n}, A)$ is the set of all maps $f \in \mathrm{Hom}_{\mathbb{F}}(A^{\otimes n}, A)$ such that

$$|f(a_1 \otimes \cdots \otimes a_n)| = \sum_{i=1}^{n} |a_i| + r.$$

We can verify that $d(CC^{n,r}(A)) \subset CC^{n+1,r}$, that is, the differential d preserves the grading. Thus we can define $HH^{*,r}(A)$, the bigraded Hochschild cohomology of degree r, by

$$HH^{n,r}(A) = \frac{\ker(d : CC^{n,r} \to CC^{n+1,r})}{\mathrm{im}(d : CC^{n-1,r} \to CC^{n,r})}. \tag{2.4}$$

2.5 Quadratic forms

Let $A = H^*(L; \mathbb{C})$ be the cohomology algebra of a closed orientable 3-manifold L. Biran and Cornea [8, Section 5.3] define a map $\Theta : HH^{2,-2}(A) \to Q^2(A^1; \mathbb{C})$ to the space of quadratic forms on A^1 as follows. Consider an element $f \in CC^{2,-2}(A)$, and restrict it to a map $f : A^1 \otimes A^1 \to A^{1+1-2} \cong \mathbb{F}$. Define $\Theta(f) \in Q^2(A^1; \mathbb{C})$ to be the quadratic form $\Theta(f)(x) = f(x \otimes x)$. The proof of the following can be found in [8, Section 5.3.1].

Proposition 4. *The map Θ is well defined on cohomology classes in $HH^{2,-2}(A)$.*

Proof. It is sufficient to show that $\Theta = 0$ on coboundaries. Let $f \in CC^{2,-2}(A)$ be a coboundary $f = dg$. Let $x \in A^1$. Then $\Theta(f)(x) = f(x \otimes x) = dg(x \otimes x) = xg(x) - g(x \cdot x) + g(x)x$. But $x \cdot x = 0$ by (2.1) and $|g(x)| = |x| - 2 = -1$ since $g \in CC^{1,-2}(A)$. Therefore $\Theta(dg)(x) = 0$. ∎

The discriminant Δ that Charette considers in [1] is $\Delta(\psi)$ for a quadratic form $\psi \in \mathrm{im}\,\Theta$. Thus, if $HH^{2,-2}(A) = 0$, then $\mathrm{im}(\Theta) = 0$ and as a result $\Delta = 0$.

3 Zeroth Hochschild cohomology

The following is a standard result that can be found in [9, Section 9.1] for example.

Proposition 5. $HH^0(A) \cong Z(A)$, *the center of the algebra A.*

Let $A = \oplus_i A^i$ be a graded commutative Frobenius algebra of degree 3. For $a \in A^i$, we write its degree $|a| = i$.

By (2.1), we know that A^0 and A^2 are in $Z(A)$. In fact, $A^3 \subset Z(A)$ as well because the only nontrivial cup product with elements of A^3 is a commutative one with A^0. We have a lemma:

Lemma 1. *$x \in A^1$ is in $Z(A)$ if and only if $xyz = 0$ for all $y, z \in A^1$.*

Proof. Let $x \in A^1$ be in $Z(A)$. Then, for any $y \in A^1$, we have $xy = yx = -xy$ by graded commutativity. Then $2xy = 0$, which implies that $xy = 0$ since $\mathrm{char}(\mathbb{F}) \neq 2$. Therefore $xyz = 0$ for all $y, z \in A^1$.

Let $x \in A^1$ such that $xyz = 0$ for all y, z. Suppose that there exists y such that $xy \neq 0$. Then, as previously mentioned, by Proposition 1, we can choose $z \in A^1$ dual to xy in the sense that $xyz = e$. This contradicts the hypothesis that $xyz = 0$ for all y, z, so we must have $xy = 0$ for all $y \in A^1$. Therefore $xy = yx = 0$ for all $y \in A^1$ and $x \in Z(A)$. ∎

Proof of Theorem 1. Suppose that $x \in A^1$ is in $Z(A)$. Then, by Lemma 1, $xyz = 0$ for all $y, z \in A^1$. Then $\iota_\mu(x)(y, z) = \mu_A(x, y, z) = \sigma(x, yz) = \sigma(1, xyz) = \sigma(1, 0) = 0$ for all y, z and thus $\iota_\mu(x) = 0$.

Conversely, suppose that $\iota_\mu(x) = 0$. Then $\mu_A(x, y, z) = \sigma(x, yz) = \sigma(1, xyz) = 0$ for all $y, z \in A^1$. By the nondegeneracy of σ on $A^0 \times A^3$ and the fact that $A^3 \cong \mathbb{F}$, we must have $xyz = 0$ for all $y, z \in A^1$, so that $x \in Z(A)$ by Lemma 1.

Therefore, by Proposition 5, we have $HH^0(A) \cong A^0 \oplus \ker(\iota_\mu) \oplus A^2 \oplus A^3$. Note that $A^0 \cong A^3 \cong \mathbb{F}$, so that by counting dimensions, we get $HH^0(A) \cong \mathbb{F}^{2+\dim A^2} \oplus \ker(\iota_\mu)$. ∎

4 Bigraded Hochschild cohomology of an algebra with trivial 3-form

Proof of Theorem 2. We choose the same bases for the algebra A as in Proposition 1 and (2.2). That is, we choose a basis $\{x_1, \cdots, x_\beta\}$ for A^1 and a basis $\{\overline{x_1}, \cdots, \overline{x_\beta}\}$ for A^2 such that $x_i\overline{x_j} = \delta_{ij}e$, where e is a generator of A^3.

All products commute since the only noncommutative product in A is $A^1 \times A^1 \to A^2$, which vanishes for $\mu = 0$. The product $A^0 \times A^i \to A^i$ is scalar multiplication, the product $A^1 \times A^2 \to A^3$ is, in the chosen basis, characterized by the relation $x_i\overline{x_j} = \delta_{ij}e$, and all other products $A^i \times A^j$ vanish.

We give a basis for $CC^{1,-2}(A) = \mathrm{Hom}^{-2}_{\mathbb{F}}(A, A)$. Define f_p with $f_p(\overline{x_i}) = \delta_{ip}1 \in A^0$ and $f_p(e) = 0$, define g_p with $g_p(\overline{x_i}) = 0$ and $g_p(e) = x_p$. We see that $\{f_1, \ldots, f_\beta, g_1, \ldots, g_\beta\}$ is a basis for $CC^{1,-2}(A)$.

We now describe the image of $d : CC^{1,-2} \to CC^{2,-2}$ (which is injective, giving $HH^{1,-2}(A) = 0$, but we don't need that fact). We have the differential $df(a_1 \otimes a_2) = a_1 f(a_2) - f(a_1 a_2) + f(a_1)a_2$. By linearity it suffices to consider a_i to be basis elements of A. Since $df(a_1 \otimes a_2) = df(a_2 \otimes a_1)$ by the fact that A is commutative, it suffices to consider half the cases.

df_p is nonzero only when either a_1 or a_2 is $\overline{x_p}$ and neither is 1. For suppose without loss of generality that $a_1 = 1$. Then $df(1 \otimes a_2) = f(a_2) - f(a_2) + f(1)a_2 = 0$. Then, suppose $a_1, a_2 \in A^2$. Then $df(a_1 \otimes a_2) = -f(a_1 a_2) = 0$ by the fact that the product $A^1 \times A^1$ is trivial since $\mu = 0$. The only nonzero values df_p can take in $A^0 \cup A^1$ are, up to multiplication by a scalar,

$$df_p(x_i \otimes \overline{x_p}) = x_i. \tag{4.1}$$

We move on to $dg_p(x_i \otimes \overline{x_j})$. The only nonzero values in $A^0 \cup A^1$, up to a scalar factor are

$$dg_p(x_i \otimes \overline{x_i}) = -x_p. \tag{4.2}$$

Equations (4.1) and (4.2) imply that for every $h = \sum_m (\alpha_m f_m + \gamma_m g_m) \in$

$CC^{1,-2}$, if i, j, k are distinct, we have

$$dh(x_i \otimes \overline{x_j})\overline{x_k} = \sum_m \alpha_m df_m(x_i \otimes \overline{x_j})\overline{x_k} + \gamma_m dg_m(x_i \otimes \overline{x_j})\overline{x_k} = 0. \quad (4.3)$$

Assuming that $\dim(A^1) \geq 3$, we define $\varphi \in CC^{2,-2}(A)$ as follows:

$$\varphi(x_1 \otimes \overline{x_2}) = x_3, \varphi(x_1 \otimes \overline{x_3}) = x_2 \text{ and } \varphi(\overline{x_2} \otimes \overline{x_3}) = \overline{x_1}.$$

Set φ to be symmetric, that is, such that $\varphi(a_1 \otimes a_2) = \varphi(a_2 \otimes a_1)$, and set φ to zero on every other generator of $A \otimes A$. Clearly $\varphi \notin d(CC^{1,-2})$ by (4.3).

We show that $d\varphi = 0$ for all a_1, a_2, a_3 using the differential formula of (2.3):

$$d\varphi(a_1 \otimes a_2 \otimes a_3) = a_1\varphi(a_2 \otimes a_3) - \varphi(a_1a_2 \otimes a_3) + \varphi(a_1 \otimes a_2a_3) - \varphi(a_1 \otimes a_2)a_3. \quad (4.4)$$

It is sufficient to only check for a_i basis elements of A by linearity. Furthermore, we only need to check one of $d\varphi(a_3 \otimes a_2 \otimes a_1) = 0$ and $d\varphi(a_1 \otimes a_2 \otimes a_3) = 0$ since φ is symmetric.

It is clear that if any one of a_1, a_2 or a_3 is 1, then $d\varphi = 0$ because at least two terms of (4.4) cancel out and $\varphi(1 \otimes a_i) = 0$ by the definition of φ. It is also clear that $d\varphi(a_1 \otimes e \otimes a_3) = 0$ since we defined φ such that $\varphi(a_i \otimes e) = 0$. We calculate

$$d\varphi(a_1 \otimes a_2 \otimes e) = -\varphi(a_1 \otimes a_2)e$$

which can only be nonzero when $\varphi(a_1 \otimes a_2) \neq 0$ in A^0, which never occurs since φ was defined to be zero on all generators $a_1 \otimes a_2$ such that $|a_1| + |a_2| = 2$. Therefore, if any one of a_1, a_2, a_3 is e, $df = 0$. For this reason, from this point on we take $a_i \in A^1 \cup A^2$.

We have

$$d\varphi(a_1 \otimes x_j \otimes a_3) = a_1\varphi(x_j \otimes a_3) - \varphi(a_1 \otimes x_j)a_3.$$

If either of a_1 or a_3 is in A^1, this expression is 0 because $\varphi(x_i \otimes x_j) = 0$, $\varphi(1 \otimes x_i) = 0$, and $\mu_A = 0$. We compute

$$d\varphi(x_i \otimes \overline{x_j} \otimes x_k) = x_i\varphi(\overline{x_j} \otimes x_k) - \varphi(x_i \otimes \overline{x_j})x_k = 0$$

by the fact that the product $A^1 \times A^1 \to A^2$ is trivial since $\mu = 0$. We have $d\varphi(\overline{x_i} \otimes \overline{x_j} \otimes \overline{x_k}) \in A^4 = 0$. Therefore, we have two last cases to check:

$$d\varphi(\overline{x_i} \otimes x_j \otimes \overline{x_k}) = \overline{x_i}\varphi(x_j \otimes \overline{x_k}) - \varphi(\overline{x_i} \otimes x_j)\overline{x_k} = 0, \quad (4.5)$$

$$d\varphi(x_i \otimes \overline{x_j} \otimes \overline{x_k}) = x_i\varphi(\overline{x_j} \otimes \overline{x_k}) - \varphi(x_i \otimes \overline{x_j})\overline{x_k} = 0. \quad (4.6)$$

Both (4.5) and (4.6) are true if i, j, k are ≥ 4. Note that only one of the cases (i, j, k) and (k, j, i) needs to be checked. By (4.6) and by the way φ was defined, it is sufficient to check the cases in which i, j, k are distinct. Checking by hand over $(i, j, k) = \{(1, 2, 3), (2, 1, 3), (1, 3, 2)\}$ we see that both equations are always satisfied.

Thus, $\varphi \in \ker(d : CC^{2,-2} \to CC^{3,-2})$ but $\varphi \notin d(CC^{1,-2})$ and as a result $HH^{2,-2}(A) \neq 0$. ■

Acknowledgments

I would like to thank my mentor and supervisor Dr. François Charette of Marianopolis College for providing teaching and guidance for the completion of this project. The project was funded by Dr. Charette's grant #271306 from the *Fonds de recherche du Québec - Nature et technologies (FRQNT)*.

I also thank the anonymous referees who provided detailed comments and criticism, which helped improve the structure and content of this article.

References

1. Charette F. On the cohomology ring of narrow Lagrangian 3-manifolds, quantum Reidemeister torsion, and the Laudau-Ginzburg superpotential. Arxiv. [Preprint] 2016. Available from https://arxiv.org/abs/1603.05586.
2. Sullivan D. On the intersection ring of compact three manifolds. Topology. 1975;14(3):275-277.
3. Hoffman K, Kunze R. Linear Algebra. Englewood Cliffs: Prentice-Hall; 1971. 407p.
4. Bredon G. Topology and Geometry. New York: Springer-Verlag; 1993. 557 p.
5. Hatcher A. Algebraic Topology. Cambridge: Cambridge University Press; 2001. 551 p.
6. Hochschild G. On the cohomology groups of an associative algebra. Annals of Mathematics. 1945;46(1):58-67.
7. Witherspoon, S. J. Hochschild Cohomology for Algebras. Providence: American Mathematical Society; 2019. 251p.
8. Biran P, Cornea O. Lagrangian topology and enumerative geometry. Geometry & Topology. 2012;16(2):963-1052.
9. Weibel C. A. An introduction to homological algebra. Cambridge: Cambridge University Press; 1994. 450 p.

Submitted: 01/22/21

Research Article

[1]Virus-Cell Interactions Laboratory, Lady Davis Institute for Medical Research, Montreal, QC, Canada
[2]Department of Microbiology and Immunology, McGill University, Montreal, QC, Canada
[3]Division of Experimental Medicine & Division of Infectious Diseases, Department of Medicine, McGill University, Montreal, QC, Canada

Keywords

COVID-19, SARS-CoV-2, siRNA, sequence conservation, GFP constructs

Email Correspondence

william.zhang@mail.mcgill.ca

William J. Zhang[1,2], Aïcha Daher[1], Anne Gatignol[1-3], Robert J. Scarborough[1,2]

Design and evaluation of small interfering RNAs for the treatment of Severe Acute Respiratory Syndrome-Coronavirus-2

Abstract

SARS-CoV-2 is the virus responsible for the COVID-19 pandemic. As the 2019 coronavirus disease continues to spread, it will be useful to have as many effective treatment options as possible. This research has the potential to create a siRNA treatment that is safe, effective, and practical in design and administration; 192 siRNAs were designed to target conserved regions of the SARS-CoV-2 genome. The first aim of this study is to confirm, via sequence analysis, that these target sites have remained highly conserved over the course of the pandemic. Multiple sequence alignments were generated for the first half of 30,312 full SARS-CoV-2 genomes, which were averaged and compared with the Wuhan-Hu-1 reference genome. Most target sites maintained a very high level of conservation, suggesting that potential repressor siRNAs could be effective in a majority of infected individuals. To evaluate the efficacy of the 192 test siRNAs, we cloned sections of the SARS-CoV-2 RNA genome into GFP fusion genes. Some of these constructs were transfected in different conditions to set up a screening assay based on GFP expression. Preliminary data on the setup of this GFP reporter assay show that the M, N, E, ORF8, and ORF10 constructs produced a good GFP signal, whereas the S, F1, F2 and F3 constructs did not produce a sufficiently strong GFP signal to detect above background. In a preliminary experiment, we evaluated siRNAs targeting the M, N, and E open reading frames and found some to be efficacious. Future directions for this project include generating alignments of the second half of the SARS-CoV-2 genome for a complete sequence conservation estimate, and cell metabolism assays for supplementing visual observations of siRNA toxicity, optimization of GFP readout, and screening of all designed siRNAs.

Introduction

Coronavirus disease 2019 (COVID-19) is an infectious disease caused by a newly discovered strain of coronavirus: severe acute respiratory syndrome coronavirus-2 (SARS-CoV-2). SARS-CoV-2 is unlike common human coronaviruses (e.g., 229E alpha coronavirus, OC43 beta coronavirus) which cause the common cold. (1) However, SARS-CoV-2 is genetically related to SARS-CoV, the virus behind the first threat of a coronavirus pandemic in 2003. (2) Coronaviruses are transmitted when individuals are in close proximity. When people are within approximately 6 feet, respiratory droplets produced by an infected individual (e.g., through coughing, sneezing, talking) can be inhaled into the nose, mouth, airways, and lungs of an uninfected individual. This is believed to be the major way the virus spreads. (3)

Coronaviruses are enveloped, non-segmented, and positive-sensed double-stranded RNA (dsRNA) viruses. They are the largest group of viruses in the *Nidovirales* order, of the family *Coronaviridae*, and can be classified into four genera: *Alphacoronavirus*, *Betacoronavirus*, *Gammacoronavirus*, and *Deltacoronavirus*. (4) Coronaviruses possess large RNA genomes whose sizes range from approximately 26 to 33 kilobases (kb) and include a variable number (from 6 to 11) of open reading frames (ORFs). (5) The coronaviral genome encodes four major structural proteins: the spike surface glycoprotein (S), small envelope protein (E), matrix protein (M), and nucleocapsid protein (N). (4) The spike protein plays an essential role in binding angiotensin-converting enzyme 2 (ACE2) or CD209L receptors on the host cell and determines host tropism. (6, 7)

Our research aims to use RNA interference (RNAi) as a tool to combat the spread of COVID-19. Also known as Post-Transcriptional Gene Silencing (PTGS), RNAi is a conserved biological pathway among eukaryotes. This mechanism involves small RNAs (fewer than 30 bases long) with characteristic two-nucleotide 3' overhangs which allow them to be recognized by RNAi enzymatic machinery. (8) In some organisms, RNAi is triggered by double-stranded RNAs (dsRNA) of viral origin that lead to homology-dependent targeting of the foreign RNAs. In mammalian cells, the RNAi pathway is primarily responsible for the regulation of genes by microRNAs (miRNAs), which direct the RNAi machinery to repress the translation of several target genes. RNAi is also used to target specific genes for degradation by introducing artificially designed, 19-nucleotide short interfering RNAs (siRNAs) into mammalian cells. siRNAs are typically made to resemble the cleavage products of double stranded RNA by the RNase III endonuclease Dicer. (9) Once introduced into a cell, siRNAs are loaded into the RNA-induced silencing complex (RISC). (10) The argonaute-2 (Ago-2) protein uses its endonuclease activity to cleave and release the siRNA "passenger" strand, activating the RISC. The remaining single-stranded "guide" RNA molecule allows target specificity by intermolecular base pairing, resulting in the cleavage of the target RNA by Ago2. (11) siRNAs represent promising drugs against viral infections as they can be rapidly designed and manufactured and lyophilized for long-term storage and transport. (12) Lastly, siRNAs are attractive drug candidates against SARS-CoV-2 because their delivery into lungs by intranasal administration has been proven effective in clinical studies for other respiratory viruses, such as RSV. (13) siRNAs were also effective in monkeys infected with SARS-CoV. (14)

The threat on global health posed by SARS-CoV-2 highlights the need to develop of a multitude of treatments. Given that RNA interference could be used as a novel COVID-19 therapy, our first step was to find conserved target sites in the SARS-CoV-2 genome suitable for small interfering RNAs (siRNAs) through genetic sequence analysis. The design of siRNAs involves identifying targets in viral genomes that are conserved across all circulating strains of the virus-of-interest, as siRNA activity is dependent on accurate base pairing with the target sequence in the given virus. One way to identify conserved target sites is to generate sequence alignments of all available CoV-2 genomes and calculate the percent conservation of each possible 19-base siRNA target. This approach has been previously optimized for the design of clinically relevant ribozymes targeting HIV RNA.

(15) In the current literature, few studies focus specifically on siRNAs' efficacy against coronaviruses by targeting subgenomic RNAs (sgRNAs) as opposed to target the open reading frame 1 (ORF1). Hence, in this study, we designed and evaluated the efficiency of novel siRNAs targeting different regions of SARS-CoV-2. Specifically, our study aims to determine siRNA target sites within the SARS-CoV-2 ORF1a, ORF1b, and eight sgRNAs via sequence conservation and evolutionary conservation. We hypothesize that targeting accessible and conserved sites within the SARS-CoV-2 genome will identify efficacious siRNAs against COVID-19.

Methods

SARS-CoV-2 Sequence Conservation Estimates

The sequence alignment tool on NCBI Virus was used to generate sequence FASTA alignments containing all complete SARS-CoV-2 genome sequences (30,312 at the time of analysis). The accession number for the reference strain is NC_045512.1. FASTA files were imported into Jalview alignment editor (version 2.11.1.3), which was used to calculate the conservation percentage for each nucleotide within the selected target site (expressed as the percentage of sequences containing the consensus nucleotide at each position). A histogram representing the percent (%) of conservation for each nucleotide in the alignment with reference to the consensus nucleotide was then generated. This annotation was exported as a CSV (Spreadsheet), saved as a .txt extension, and imported as a comma delimited file into Microsoft Excel. The data was transposed from rows into columns, and the average conservation was characterized.

Cell Culture

HEK293T cells and VeroE6 (ATCC) cells were maintained in DMEM with high glucose (HyClone) supplemented with 10% fetal bovine serum (FBS) (HyClone), 50 U/mL penicillin, and 50 µg/mL streptomycin (Life Technologies).

Cell Plating and Transfections

For transfections of GFP expression plasmids, a master mix was created using 1 uL TransIT-LT1 DNA Transfection Reagent (Mirus Bio), diluted in 39 uL opti-MEM. The mix was added to DNA at different amounts, and this mixture rested for 15 minutes and was added over top of pre-plated cells at 1.40 × 105 cells/mL at a volume of 100 µL per well in a black-bottom 96-well plate. Clear-bottom plates were used for microscopy. Reverse transfection with non-targeting siRNAs and targeting siRNAs were also performed with 4 µL of 5 µm siRNA in 16 µL OptiMEM was added to 60 wells of a black-bottom plate. A master mix was made using 0.3 µL of RNAi MAX transfection reagent and 19.7 µL OPTI-MEM, and 20 µL was added to the siRNA dilutions. Cells were seeded after 15 minutes at 1.40 × 105 cells/mL 24 h prior to DNA transfection at a volume of 100 µL per well. After 24 h, GFP transfections were performed as above. The 36 border wells of the plate were seeded with 100 µL PBS. Plates were read 48 h after GFP transfection on a BioTek Instruments Synergy 4 Multi-Detection Microplate Reader. Fluorometer readings were detected at an excitation of 485 nm and an emission of 515 nm.

Results

Design of siRNAs targeting SARS-CoV-2 RNA and construction of GFP reporter constructs

In these experiments, we aimed to identify siRNAs targeting SARS-CoV-2 RNA which could potently inhibit viral replication. We designed siRNAs against conserved regions of the SARS-CoV-2 genome, and reporter constructs linking different regions of the RNA genome to GFP reporter sequences were produced. To confirm that the identified siRNA target sites remained conserved as the pandemic progresses, all available and complete SARS-CoV-2 sequences (collected between January 12, 2020 to October 23, 2020) were subject to multiple sequence alignment using NCBI Virus and analysed for nucleotide conservation with Jalview. Microsoft Excel was used to calculate sequence homology for the first half of the SARS-CoV-2 genome. The selected siRNA target sites are illustrated in Fig. 1.

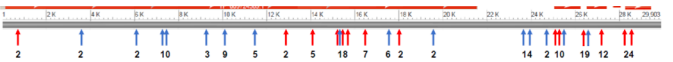

Figure 1. Target sites for siRNAs identified by sequence conservation and RNA structure analysis. The number of siRNAs identified for each target region are illustrated under the SARS-CoV-2 genome. The different open reading frames (in red) of the genome are shown, over the full-length RNA (in grey). Red arrows indicate regions that are highly conserved across SARS-CoV-2 genomes and related coronaviruses (40 siRNAs). Blue arrows indicate regions that are conserved across SARS-CoV-2 genomes and are predicted to be unstructured (56 siRNAs). 96 siRNAs were also designed by Thermo Fisher (target sites not shown).

Every site we selected is highly conserved across SARS-CoV-2 genomes, but those indicated with a red arrow in Fig. 1 are also highly conserved in various related coronaviruses infecting bats and humans. These target sites might be important for several coronaviruses and are less likely to mutate. The target sites indicated by blue arrows in Fig 1. are predicted to be unstructured, though still highly conserved across SARS-CoV-2 genomes. We chose 96 target sites (number of wells in a 96-well plate), of which 40 target areas are indicated by red arrows and 56 target regions are indicated by blue arrows (Fig. 1). These target sites were selected by eliminating siRNAs having target sites with partial homology to the human transcriptome (one of the potential off-target effects of siRNA) using GGGenome, a web-based application which helps identify targeting mismatches in the human transcriptome.(16) An i-Score (inhibitory-Score) was also used to predict which siRNAs would be highly active based on their RNA sequences (e.g., thermostability of siRNA duplex, presence of G/C nucleotides and A/T stretches on the antisense strand). The i-Score was generated from a web-based siRNA-designing algorithm created through observation of siRNAs in HEK293 cells.(17) Another 96 siRNAs were designed by Thermo Fisher to make up a total of 192 test siRNAs.

Available complete SARS-CoV-2 sequences show high percentage conservation as compared to various candidate siRNA sequences

After we determined the SARS-CoV-2 sequence homology at the nucleotide level, the average percent nucleotide identity between the first half of all available NCBI SARS-CoV-2 genomes and the SARS-CoV-2 consensus sequence was compared with the 19-nucleotide siRNA target sites identified from the first half of the genome. We did this to confirm that the siRNA target sites we selected are conserved as the pandemic progresses. So far, all siRNA target sites evaluated have remained highly conserved. As an example, the conservation at the nucleotide level of three siRNA target sites within the RNA coding for the nsp2, proteinase, and RDRP proteins located in ORF1 are shown (Fig. 2). A 19-nucleotide sequence that has not remained conserved is also shown as an example of what would be a poor siRNA target site.

Fluorescence readouts from GFP transfections show greater detection in HEK293T cells than in VeroE6 cells

Given the putative conserved regions that will be targeted for siRNA silencing, the next step was to develop a method to test if the siRNAs are effective at marking the SARS-CoV-2 gene target for degradation. We chose green fluorescent protein (GFP) to report the efficacy of the targeted degradation because of its simple tracking method. If a given siRNA is effective, it will decrease GFP fluorescence. In other words, the designed siRNAs should target the SARS-CoV-2 RNA that is also linked to the GFP RNA. As such, when the SARS-CoV-2 RNA is degraded, the GFP RNA

will also be destroyed, and the GFP will not be expressed. GFP fluorescence readouts can thus be used as a measure of siRNA efficacy in targeting chosen RNA segments of SARS-CoV-2. We divided the SARS-CoV-2 genome into seven fragment templates (using fragments obtained from Xie and colleagues), from which primers were designed to place them in frame ahead of the GFP sequence.(18) Each of the subgenomic open reading frames (S, 3a, E, M, 6, 7ab, 8, N) and the large ORF1ab (which was divided into five fragments; F1–F5) was inserted. Relative fluorescent units (RFUs) for serial dilutions of the majority sgRNAs in VeroE6 cells remained lower than those seen in HEK293T cells. Transfection into VeroE6 cells (Fig. 3) exhibited low detectable GFP fluorescence signal, with 3,611 RFU detected at 250 ng of transfected DNA, and 3,603 RFU detected at 125 ng for the empty construct. In contrast, 10,606 RFU was detected at 250 ng and 6,203 RFU was detected at 125 ng for the empty construct, in HEK293T cells (Fig. 4).

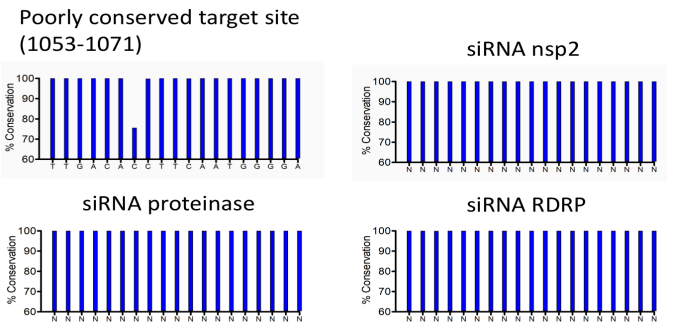

Figure 2. Sequence conservation of partial SARS-CoV-2 genome compared to candidate siRNAs. Percent conservation is shown on the vertical axis, while each nucleotide of the 19-nucleotide siRNA candidate sequence is shown on the horizontal axis. Real sequences are not shown for proprietary reasons. The upper left-hand panel provides an example of a poorly conserved target site, while the remaining three panels represent the targets site within the RNA coding for nsp2, proteinase, and RDRP, respectively.

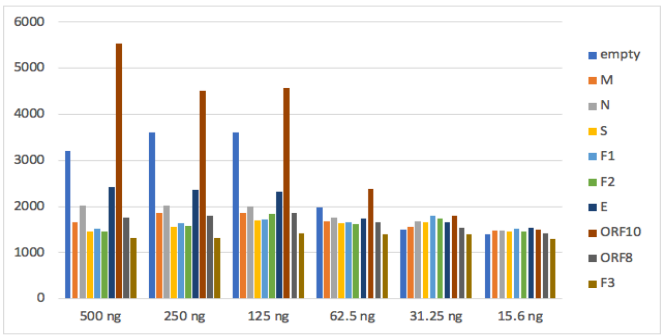

Figure 3. Graphical representation of GFP fluorescence readout in VeroE6 cells. GFP test showing RFUs in VeroE6 cells obtained with BioTek Synergy 4 plate reader (Excitation: 485 nm; Emission: 515 nm) after transfection of each GFP construct, cloned at decreasing doses.

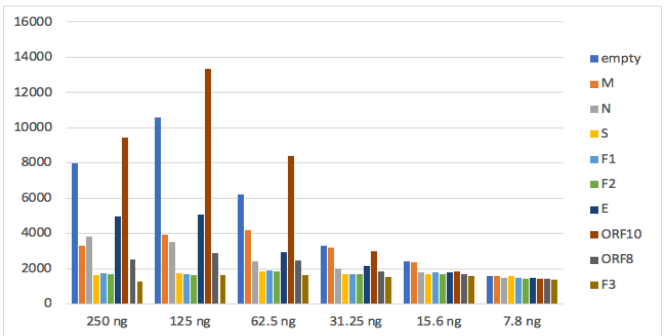

Figure 4. Graphical representation of GFP fluorescence readout in HEK293T cells. GFP test showing RFUs in HEK293T cells obtained with BioTek Synergy 4 plate reader (Excitation: 485 nm; Emission: 515 nm) after transfection of each GFP construct, cloned at decreasing doses.

Preliminary reverse transfection of HEK293T cells shows no toxicity to transfection reagent or to non-targeting siRNAs

To confirm that an siRNA did not produce toxic effects on the cells, we performed reverse transfection using negative-control siRNAs in HEK293T cells (Fig. 5). As show in Fig. 5, no conclusive differences in the viability or morphology of the cells were detected in the four transfection conditions: 1) no treatment, 2) treated with only the RNA transfection reagent, 3) treated with the RNA transfection reagent and the first non-targeting siRNA (siRNA1), and 4) treated with the RNA transfection reagent and the second non-targeting siRNA (siRNA2).

However, a few rounded cells and flat cells were found from cultures treated with RNAi max + siRNA1&2, compared to cells given no treatment. These results might indicate stress or an alternative effect on the cells.

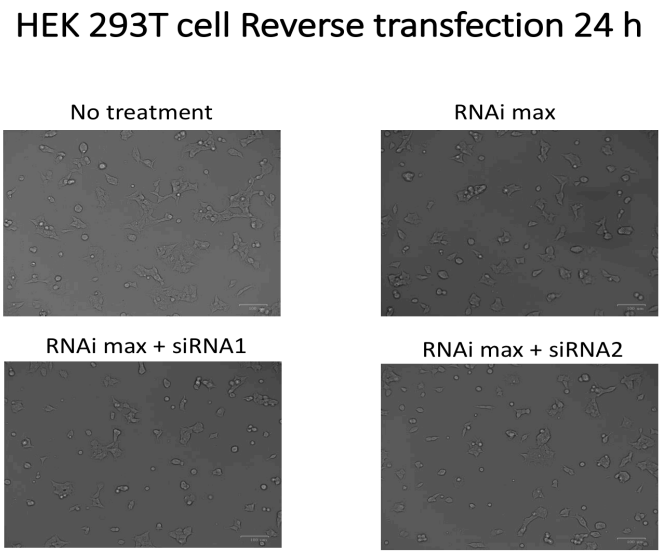

Figure 5. HEK 293T cells reverse transfected with non-targeting siRNAs after 24 h. Four reverse transfection conditions tested in HEK293T cells: no treatment, treated only with the RNAi MAX transfection reagent (RNAi max), treated with the RNA transfection reagent and scrambled siRNA1 (RNAi max + siRNA1), and treated with the RNA transfection reagent and scrambled siRNA2 (RNAi max + siRNA2).

Preliminary reverse transfection of HEK293T cells with targeting siRNAs identifies some efficacious siRNAs against the M, N, and E open reading frames

To identify effective siRNAs and confirm that our GFP assay can be used for siRNAs screening, we performed reverse transfection of siRNAs targeting the M, N, and E open reading frames and transfected the respective GFP-tagged open reading frames (Fig 6.). In subsequent experiments, all the other siRNAs will be screened once every construct expresses significant GFP signal.

Discussion

This research has the potential to create a safe and effective treatment against COVID-19. siRNAs targeting viruses have been studied preclinically for strains of Ebola and Marburg viruses in monkeys. (19-21) Additionally, three siRNAs (ARB-1740) were effective against Hepatitis B virus in human cells and are currently in clinical trials for the cure of chronic HBV infection. (22) To identify optimal siRNA target sites in coronavirus genomes, siRNAs against SARS-CoV-2 in particular, we examined the

conservation of all available sequences to evaluate homology and compared it to a limited number of candidate siRNAs. We cultured and plated two cell lines (VeroE6 andHEK293T) to test for siRNA efficacy and safety. Through this study, it was found that the target sites of all chosen siRNAs targeting the first half of the of the SARS-CoV-2 genome were conserved across all available circulating strains (examples shown in Fig 2). Confirming that the 19 nucleotides of the designed siRNAs were highly conserved within the target sequence in the SARS-CoV-2 reference genome was critical because siRNA activity relies on successful base pairing. Our study also supported that VeroE6 cells and HEK293T cells can be transfected with GFP-tagged SARS-CoV-2 RNA constructs. Measuring GFP fluorescence readouts informed the optimal concentration of GFP mRNA for screening so that, the chosen concentration produces a strong GFP fluorescence signal without saturating the potential inhibitory effects of siRNAs. In preparation for reverse transfection, HEK293T cells were reverse transfected with non-targeting siRNAs, although the results surrounding toxicity is still inconclusive. Reverse transfection with VeroE6 cells was not performed because the GFP fluorescence was not as strong. Lastly, we conducted reverse transfection of HEK293T cells with targeting siRNAs.

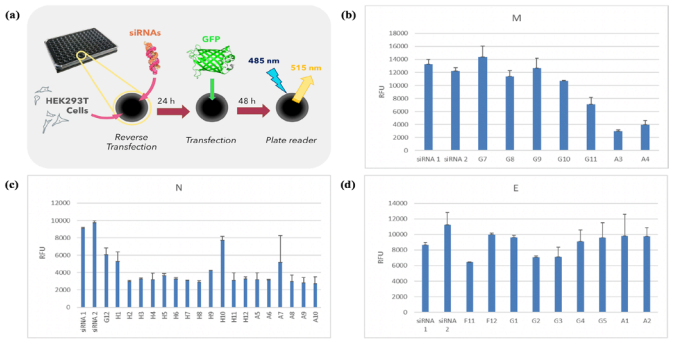

Figure 6. HEK 293T cell reverse transfected for targeting siRNAs followed by transfection of respective GFP constructs. HEK293T cells were plated onto siRNAs with RNAi Max transfection reagent (reverse transfection). Twenty-four hours later, we transfected cells with GFP constructs, and the plates on a fluorometer (excitation 485 nm; emission 515 nm) forty eight hours later. A schematic of the experimental procedures is depicted in (a). siRNAs targeting the (b) M open reading frame, (c) N open reading frame, and (d) E open reading frame are named according to their position in the 96-well plates. Two siRNA negative controls (siRNA1 and siRNA2) which do not target SARS-CoV2 are included for each GFP construct as a reference for the baseline GFP expression. Efficacious siRNAs decrease the GFP signal relative to controls. Data are expressed in relative fluorescent units (RFU) and represent the mean ± SD (standard deviation) of one experiment in duplicate (n=2).

We compared the conservation of siRNA candidate target sites using methods developed to calculate sequence conservation. As the pandemic progresses, this method can be updated with emerging sequences to verify that all siRNA target sites remain highly conserved in circulating strains of SARS-CoV-2. This data can also be used to identify new target sites, given that poorly conserved target sites can be easily excluded based on percent homology characteristics (Fig. 2). A recent study by Gilead Sciences used over 90,000 SARS-CoV-2 sequences isolated from clinics worldwide to analyze genetic diversity in the RNA replication complex in the context of potential SARS-CoV-2 genetic diversification impacting Remdesivir (RDV) efficacy as the virus spreads over time. (23) The researchers observed low genetic sequence variation; the high genetic stability of certain parts of the SARS-CoV-2 genome over time supports the prediction and hope for a minimal global risk of SARS-CoV-2 resistance to RDV. We employed the same idea to test for the entire first half of the SARS-CoV-2 genome in the context of siRNAs rather than RDV. While evidence suggests that the SARS-CoV-2 virus has remained genetically stable between January 12 and October 23 of 2020 (period for which NCBI Virus sequences were taken), there have been reports about the SARS-CoV-2 B.1.1.7 variant carrying deletions (69-70del) and mutations (N501Y, P681H) in the spike protein, resulting in increased virus infectivity and yield in human lung epithelial cells and primary airway tissue.(24) This enhanced transmissibility may imply that preventive measures against the original Wuhan-Hu-1 coronavirus reference genome may only be partly effective against new strains. Nevertheless, we have calculated that the UK B.1.1.7 lineage shared over 99.8% nucleotide identity with the original Wuhan-Hu-1 reference genome, and only three of our 192 siRNA target sites are altered in this lineage. More SARS-CoV-2 whole genome sequencing, genomic epidemiology, and collaboration for global surveillance will contribute to a better understanding of the speed and extent of mutations. (25) Our sequence conservation analysis is limited because only the first half of the SARS-CoV-2 genome was analysed due to the number of columns which can be created in Microsoft Excel. Another point worth mentioning is that two sequences did not align at the same nucleotide; coming from the same source, these two CoV-2 sequences were missing four nucleotides at the start of the sequence compared to the reference genome. We have now identified a method to analyze the second half of the genome independently and are calculating sequence conservation for the whole genome.

We performed two GFP tests, in VeroE6 cells (African Green Monkey kidney epithelial cell line) and HEK293T cells (Human embryonic kidney cell line). While the fluorescence readouts are similar in both cell lines, only HEK293T cells were used in subsequent reverse transfection experiments because there was little detectable signal obtained with the plate reader for some of the constructs in VeroE6 cells (Fig. 3). In both cell lines, the S, F1, F2 and F3 constructs did not produce a sufficiently strong GFP signal comparing to the background (Fig. 4). This weak signal can be caused by the large size of the segments (S, F1–F3). In future experiments, these constructs will be cloned into smaller fragments. The inserts (S, F1–F3) were also Sanger sequenced to confirm that the RNA is in frame with the GFP, eliminating out of frame cloning as a source of error. We hope to determine the lowest GFP dose that relays a good fluorescent signal. If the dose is above the GFP saturation limit, then it is harder for an introduced siRNA to decrease the signal from the overly abundant GFP mRNA. Hence, our goal was to determine the GFP doses which would eventually be used to screen siRNAs. The fact that only one independent experiment with two replicates was performed in each cell line presents a limitation and this experiment will be replicated to achieve a greater accuracy of results. One potential disadvantage of this technique is that no amplification of fluorescent signal using GFP occurs. Alternative reporter assays can also be used: the SARS-CoV-2 gene fragments can be fused with a luciferase reporter gene to produce better detection via the luciferase enzymatic reaction, which has been used recently in siRNAs silencing SARS-CoV-2 reporter constructs. (26)

Lastly, we performed early reverse transfection experiments. The first set of experiments provided data on HEK293T cells twenty-four hours after setting four conditions for negative control screening (Fig. 5). Two non-targeting siRNAs (scrambled siRNAs that do not target the SARS-CoV-2 genome) were used to reverse transfect HEK293T cells to evaluate whether the siRNAs exhibited any toxicity. Given that there are few cells to observe in Figure 5, it is difficult to determine toxicity visually or qualitatively. Thus, toxicity will be measured quantitatively in the future with a WST-1 assay. Hydrogen peroxide or Poly-I:C (a long, double-stranded RNA) will be used as a positive control to show cells death. Still, the absence of conclusive visual differences among cells in each condition steers us towards the cautious conclusion that there were no dramatic effects from the transfection reagent, nor from the transfection reagent with the siRNA negative controls. Given that transfection reagents and foreign RNAs can have toxic effects on cells via hybridization-dependent off-target effects, it is important to ensure that added concentrations are optimal before further screening. (16) We will also screen all efficacious test siRNAs for potential toxicity with the WST-1 metabolism assay. This will confirm that any decrease in GFP expression originates from siRNA targeting of the construct, as opposed to cell toxicity, which would also lead to a loss of GFP expression. The preliminary readouts for the test siRNAs targeting the M, N, and E constructs showed that some siRNAs appear to be active, although more replications are needed to determine accuracy of the observed effects. We will also need to confirm that there is no sequence-dependent toxicity caused by these siRNAs.

For future research, alignments of the second half of the SARS-CoV-2 genome will be made to calculate sequence conservation for the entire genome. For the constructs that did not produce adequate GFP signals in either VeroE6 cells or HEK293T cells, we will collect fluorometer readings in the near future after cloning the S and F1–F3 inserts into smaller fragments. If GFP fluorescence levels are significantly higher than the background, test siRNAs will be evaluated against the aforementioned constructs at varying concentrations. Inhibition of GFP signal will be monitored, with the expectation of observing a GFP signal decrease by some of the siRNAs. Following the optimization of GFP readout, the efficacy and safety can be tested. Cell metabolism assays can be used to eliminate siRNAs with cytotoxic effects in mammalian lung epithelial cell culture; this assay has been used in RNA therapies against HIV-1. (27) The efficacy and toxicity of the generated siRNAs can also be measured by their ability to target SARS-CoV-2 replication, inhibit SARS-CoV-2-induced cell death in a WST-1 cell metabolism assay, and independently affect cell metabolism. Specific constructs expressing viral mRNAs under a CMV promoter can also be created to verify the inhibition of the CoV-2 mRNA by qRT-PCR, which was previously performed for Zika Virus RNAs. (28) Inhibition of coronavirus protein production can also be confirmed using polyclonal antibodies that are anti-Capsid and anti-Spike. Thus, the next arm of this project is to screen the siRNAs for activities against SARS-CoV-2 production. There has been a great need for the development of therapies against the SARS-CoV-2 virus, and siRNAs are attractive candidates due to the simplicity in design and administration. Here, we used sequence conservation to confirm that our siRNAs target viral sequences have remained highly conserved throughout the course of the pandemic and began testing the binding of these siRNAs targets within SARS-CoV-2. This study aims to give health services an upper hand on the current pandemic as well as for future outbreaks of related coronaviruses.

Acknowledgements

I thank Dr. Robert Scarborough for his laboratory guidance and continued supervision throughout this project; it is my pleasure to be learning from you. Also, I thank Aïcha Daher for her work and patience in the creation of SARS-CoV-2 GFP constructs. Lastly, my work is made possible by Dr. Anne Gatignol, whose lab I am thankful to have been able to join despite difficulties in participating in student research activities during the pandemic. I acknowledge the McGill department of Microbiology and Immunology for promoting research experience through the Microbiology Advanced Research Project course. This work was supported by the grant VR3-172642 from Canadian Institutes of Health Research (to R.J.S and A.G.).

References

1. Human coronavirus types Centers for Disease Control and Prevention: U.S. Department of Health & Human Services; 2020 [Available from: https://www.cdc.gov/coronavirus/types.html.

2. Petersen E, Koopmans M, Go U, Hamer DH, Petrosillo N, Castelli F, et al. Comparing SARS-CoV-2 with SARS-CoV and influenza pandemics. Lancet Infect Dis. 2020;20(9):e238-e44.

3. Coronavirus World Health Organization: World Health Organization; 2020 [Available from: https://www.who.int/health-topics/coronavirus#tab=tab_1.

4. Li F. Structure, Function, and Evolution of Coronavirus Spike Proteins. Annu Rev Virol. 2016;3(1):237-61.

5. Song Z, Xu Y, Bao L, Zhang L, Yu P, Qu Y, et al. From SARS to MERS, Thrusting Coronaviruses into the Spotlight. Viruses. 2019;11(1).

6. Ge XY, Li JL, Yang XL, Chmura AA, Zhu G, Epstein JH, et al. Isolation and characterization of a bat SARS-like coronavirus that uses the ACE2 receptor. Nature. 2013;503(7477):535-8.

7. Jeffers SA, Tusell SM, Gillim-Ross L, Hemmila EM, Achenbach JE, Babcock GJ, et al. CD209L (L-SIGN) is a receptor for severe acute respiratory syndrome coronavirus. Proc Natl Acad Sci U S A. 2004;101(44):15748-53.

8. Kim DH, Rossi JJ. RNAi mechanisms and applications. BioTechniques. 2008;44(5):613-6.

9. Zhang H, Kolb FA, Jaskiewicz L, Westhof E, Filipowicz W. Single processing center models for human Dicer and bacterial RNase III. Cell. 2004;118(1):57-68.

10. Meister G, Landthaler M, Patkaniowska A, Dorsett Y, Teng G, Tuschl T. Human Argonaute2 mediates RNA cleavage targeted by miRNAs and siRNAs. Mol Cell. 2004;15(2):185-97.

11. Tang G. siRNA and miRNA: an insight into RISCs. Trends Biochem Sci. 2005;30(2):106-14.

12. Barik S, Lu P. Therapy of respiratory viral infections with intranasal siRNAs. Methods Mol Biol. 2015;1218:251-62.

13. DeVincenzo J, Lambkin-Williams R, Wilkinson T, Cehelsky J, Nochur S, Walsh E, et al. A randomized, double-blind, placebo-controlled study of an RNAi-based therapy directed against respiratory syncytial virus. Proc Natl Acad Sci U S A. 2010;107(19):8800-5.

14. Tang Q, Li B, Woodle M, Lu PY. Application of siRNA against SARS in the rhesus macaque model. Methods Mol Biol. 2008;442:139-58.

15. Scarborough RJ, Lévesque MV, Perreault J-P, Gatignol A. Design of Anti-HIV SOFA-HDV Ribozymes. Lafontaine D, Dubé A, editors: Springer Nature; 2014.

16. Yoshida T, Naito Y, Sasaki K, Uchida E, Sato Y, Naito M, et al. Estimated number of off-target candidate sites for antisense oligonucleotides in human mRNA sequences. Genes Cells. 2018;23(6):448-55.

17. Ichihara M, Murakumo Y, Masuda A, Matsuura T, Asai N, Jijiwa M, et al. Thermodynamic instability of siRNA duplex is a prerequisite for dependable prediction of siRNA activities. Nucleic Acids Res. 2007;35(18):e123.

18. Xie X, Muruato A, Lokugamage KG, Narayanan K, Zhang X, Zou J, et al. An Infectious cDNA Clone of SARS-CoV-2. Cell Host Microbe. 2020;27(5):841-8 e3.

19.Thi EP, Lee AC, Geisbert JB, Ursic-Bedoya R, Agans KN, Robbins M, et al. Rescue of non-human primates from advanced Sudan ebolavirus infection with lipid encapsulated siRNA. Nat Microbiol. 2016;1(10):16142.

20. Thi EP, Mire CE, Lee AC, Geisbert JB, Ursic-Bedoya R, Agans KN, et al. siRNA rescues nonhuman primates from advanced Marburg and Ravn virus disease. J Clin Invest. 2017;127(12):4437-48.

21. Thi EP, Mire CE, Lee AC, Geisbert JB, Zhou JZ, Agans KN, et al. Lipid nanoparticle siRNA treatment of Ebola-virus-Makona-infected nonhuman primates. Nature. 2015;521(7552):362-5.

22. Thi EP, Dhillon AP, Ardzinski A, Bidirici-Ertekin L, Cobarrubias KD, Cuconati A, et al. ARB-1740, a RNA Interference Therapeutic for Chronic Hepatitis B Infection. ACS Infect Dis. 2019;5(5):725-37.

23. Martin R, Li J, Parvangada A, Perry J, Cihlar T, Mo H, et al. Genetic conservation of SARS-CoV-2 RNA replication complex in globally circulating isolates and recently emerged variants from humans and minks suggests minimal pre-existing resistance to remdesivir. Antiviral Res. 2021;188:105033-.

24. Rambaut A, Loman N, Pybus O, Barclay W, Barrett J, Carabelli A, et al. Preliminary genomic characterisation of an emergent SARS-CoV-2 lineage in the UK defined by a novel set of spike mutations. COVID-19 Genomics Consortium UK 2020.

25. Cyranoski D. Alarming COVID variants show vital role of genomic surveillance. Nature. 2021;589(7842):337-8.

26. Khaitov M, Nikonova A, Shilovskiy I, Kozhikhova K, Kofiadi I, Vishnyakova L, et al. Silencing of SARS-CoV-2 with modified siRNA-peptide dendrimer formulation. Authorea. 2021.

27. Scarborough RJ, Adams KL, Del Corpo O, Daher A, Gatignol A. Evaluation of the Efficacy And Toxicity of RNAs Targeting HIV-1 Production for Use in Gene or Drug Therapy. J Vis Exp. 2016(115).

28. Alpuche-Lazcano SP, McCullogh CR, Del Corpo O, Rance E, Scarborough RJ, Mouland AJ, et al. Higher Cytopathic Effects of a Zika Virus Brazilian Isolate from Bahia Compared to a Canadian-Imported Thai Strain. Viruses. 2018;10(2).

Submitted: 11/11/2020

Review Article

[1]Department of Biology, McGill University, Montreal, QC, Canada

Keywords

Transposable elements, genomics, evolution, stress, molecular biology, epigenetic

Email Correspondence

oscar.dumoulin@mail.mcgill.ca

Oscar Dumoulin[1]

The Role of Stress in the Spread of Transposable Elements

Abstract

Background: Transposable elements (TEs) and genomes have been at war for millions of years. On one hand, genomes developed epigenetic systems to inactivate TEs. On the other hand, it appears that TEs can take advantage of stress to evade the genome's repressing systems and spread throughout the genome. However, until recently it was unclear how and why stress influences transposable elements' movement. In this review, we explore the mechanisms involved in TE stress-induced activation.

Methods: The first part of the review looks into epigenetic mechanisms, its 19 references were taken from Handbook of Epigenetics 2nd edition (1) and reviews (2) (3). The rest of the studies presented in this review were drawn from searches done on Web of Science with the terms: TS=((Transposable element* OR mobile genetic element*) AND (Stress or Evolution) AND (Activation)) with peer-reviewed articles and reviews written in English included only. The search yielded 401 results and 56 were estimated relevant and of sufficient quality to be selected.

Summary: The main conclusion reached by this review is that protection mechanisms against TEs movement, which are mostly epigenetic, are compromised by the presence of stress. Additionally, TEs themselves evolved diverse tools to promote their activation under certain stress conditions allowing them to evade the repression imposed by the genome. These two mechanisms provide opportunities for TEs to move around the genome and create genetic diversity during stress episodes. As such, TEs stress induced mobility certainly played a major role in the rapid adaption of populations and its impact can be witnessed across genomes.

Introduction

McClintock's discovery of transposable elements (TEs) in maize (4) unveiled the genome as a dynamic playground for mobile DNA sequences. TEs are ubiquitous, mostly repetitive, short DNA sequences that move from one location to another location in the genome, often creating a duplicate copy in the process. As sequencing techniques and our capacity to recognize transposable elements progressed, the genome appeared to be more of a battlefield, where TEs colonized a considerable part of eukaryote's genomes. In fact, biologists were startled to observe that TEs related sequences could constitute up to 85% of an organisms' genome. (5) It became necessary to understand the nature of TEs and explain their overwhelming presence in genomes. Dawkins and others (6, 7) hypothesized that TEs were selfish, self-replicating elements, serving no purpose to the genome. However, McClintock suggested that TEs were, instead, an important source of genetic variation, involved in regulatory networks and likely activated by stress. (8)

The observation of active TE families with transposition rates three orders superior to mutation rates have definitively established TEs as a source of variation and material for selection. (9, 10) Moreover, the discovery of TE families and individual insertions domesticated by genomes (11, 12), coupled to the discovery of TEs responding to stress and TEs involved in regulatory networks (13, 14) ruled out the view of TEs as junk DNA and proved McClintock right.

In addition to being a source of variation, TEs are themselves highly variable elements. The classification proposed by Wicker et al. (15) is the predominant system used in the literature to describe TEs. The classification divides TEs into two major classes, Class I (retrotransposons) replicating through an RNA intermediate and Class II (DNA transposons), which do not utilize an RNA intermediate to spread. Further sub-classification characterizes TEs as part of families and orders. (15)

For a long time, only the phenotypic consequences of TE activation -which describes the movement and spread of TEs- could be studied. Yet, it was enough to observe that organisms exposed to stress displayed increased TE activity. (8, 16, 17) The mechanisms underlying the activation of TEs remained elusive for a long time following TE's discovery until, as we will see, recent findings in the field of epigenetics have allowed us to discern the processes governing TE stress-induced activation.

In this review, we will first look at the known mechanisms involved in TE repression. Using our current understanding of repression mechanisms, we will, in a second part, study how stress affects silencing pathways and elicits TE activation. Finally, we will discuss how TE activation impacts organisms at the genetic, phenotypic and evolutionary level.

Genome's weapons against transposable elements activity

Under the threat of spreading transposable elements, the eukaryotic genome has developed a set of tools operating at multiple levels to turn mobile elements immobile. In fact, it has been hypothesized that epigenetic mechanisms involved in gene regulation such as DNA methylation and RNA interference (RNAi), first evolved as defense systems against TEs. (18) In this part, we will draw our attention towards the three main mechanisms developed by eukaryotes to repress TEs, namely RNAi, DNA methylation and histone modification. In addition, we will take a look at the Repeat-Induced Point (RIP) mutation system present in Neurospora.

RNAi

The main tool used by eukaryotic cells and genomes to counter TE activity is the RNAi system. RNAi uses RNA precursors to silence post-transcriptionally foreign DNA and TEs. Indeed, it is hypothesized that RNAi evolved as a defense against viruses and TEs. (19) Among vertebrates, the RNAi system is differentiated between the germinal and somatic cells.

In germinal cell lines, the piwi-interacting RNA (piRNA) pathway is involved, while in somatic cells it is the small-interfering and micro-interfering RNA (si- & miRNA). The repressing mechanisms employed by PIWI/piRNA and, siRNA & miRNA are similar, and only differ in the proteins involved, type of RNA used and their targets. (20) The PIWI/piRNA pathway represses TEs in germinal cells and prevents the uncontrolled spread of TEs in the next generation. (21-23) Indeed, mutations in genes associated with the PIWI/piRNA pathway results in de-repression of TEs in the germline and leads to defects in development. (24)

The PIWI/piRNA pathway uses piRNA loaded on an argonaute protein called PIWI, to repress transcripts with repeats such as TEs. The pathway includes the loading of a single-stranded 26-30 nucleotides piRNA on a PIWI protein. (20) The loading requires the presence of the chaperone Hsp90 and of Shu a co-chaperone. (25, 26) Once the loading is completed, the piRNA and PIWI form the RNA-induced silencing complex (RISC). The RISC binds to target mRNA, creating a double stranded RNA between the target mRNA and piRNA. The formation of a double stranded RNA acts as a signal for the recruitment of various nucleases. The nucleases then proceed with the degradation of the target mRNA.

The PIWI/piRNA pathway does not only mediate degradation of TEs' transcripts but also promotes epigenetic silencing of TEs' coding sequence. (27) For instance, binding of the RISC complex to piRNA complementary DNA sequence, triggers epigenetic modifications such as histone acetylation and DNA methylation. Mechanisms involved in silencing of TEs similar to the PIWI/piRNA pathway, can be found in plants (28-30) and in yeasts. (31, 32) In plants it is called RNA directed methylation (RdDM) and in yeasts RNA-induced transcriptional silencing, both use siRNA instead of piRNA. Overall, RNAi mechanisms across organisms are responsible for degradation of TE transcripts and initiation of epigenetic silencing of TE sequences.

DNA Methylation

One of the epigenetic repression mechanisms triggered by RNAi is DNA methylation. DNA methylation is characterized by the addition of a methyl group on the 5th position of the cytosine ring (5-mC). The methylation of cytosine is widespread in CpG rich regions, which are prevalent in promoters and TEs. As a matter of fact, TEs constitute 40% of the CpGs in the human genome and are largely hypermethylated. (33) 5-mC is mostly associated with gene and TE repression by hindering the binding of transcription factors. (34) In the maize plant, DNA holo-methylation inhibits the Ac transposase binding to TEs. (35) Additionally, 5-mC initiates histone modification and heterochromatin formation through the binding of Methyl-DNA binding proteins (MBDs). (33) It is important to note that DNA methylation is not an invariable process across eukaryotes. For instance, DNA methylation in D.melanogaster is restricted to the embryonic development stage and is absent in the other life-stages. (36)

Histone Modification

Histones are the linking unit between DNA methylation and chromatin structure. Several types of histones exist (Histone, 1, 2A, 2B, 3, 4). Specific histones combine into octamers and form the nucleosome which is the fundamental unit of chromatin structure. (37) The state of the chromatin structure depends on the electric charge carried by the histones making up the nucleosome and on modified histone structures recognized by effector and reader proteins. (38) In their default state, histones are positively charged and interact tightly with DNA, forming a compact structure called heterochromatin, which often surrounds TEs sequences. However, histones and their electric charge can be altered in many different ways. For example, acetylation of histone tails neutralizes the positive charge and suppresses the electromagnetic interaction between histones and DNA, loosening the chromatin structure and releasing sequences from repression. Some histones, such as histone 1 (H1), are not part of the nucleosome. Yet, H1 is also involved in TE silencing. H1 interacts with methylated DNA sequences in active regions of the genome. (39) The interaction enhances the repression of TEs localized near genes, without promoting heterochromatin formation. (39)

We have now presented the principal eukaryotic systems tasked to silence TEs. Nevertheless, these basic defense systems did not prevent species to evolve additional silencing pathways to control TEs. Of particular interest, the repeat induced point (RIP) mutation system evolved by the fungi genus Neurospora, which in the case of N. crassa has led to the definitive silencing of all TEs. (40) RIP works by efficiently detecting and mutating both copies of a sequence duplication. Furthermore, RIP mutated sequences are also targeted for DNA methylation ensuring the complete silencing of TEs. (41)

How stress allows TEs to escape repressing pathways

It is now evident that genomes evolved an effective defense mechanism to prevent the spread of mobile elements. Yet, TE activity is regularly witnessed and appears to increase with stress. (16) In this part we will see that there are two ways TEs take advantage of stress to escape repressing mechanisms. The first one is the acquisition of stress responsive elements allowing them to be activated by stress related factors. The second is through the incapacitation of the silencing mechanism following stressful events. Although TE stress-induced activation is a widespread phenomenon it cannot be generalized to all transposons nor all organisms.

TEs with stress responsive elements

TEs equipped with responsive elements in their coding sequences have the ability to respond to the environment. For instance, ONSEN, a copia-like retrotransposon in Arabidopsis thaliana, possesses a heat-responsive element. (42, 43) Under heat stress conditions, the plant produces heat-stress defense factors (mostly transcription factors), which recognize and interact with the ONSEN heat responsive element. The interaction leads to the de-repression of ONSEN and favors its activation. (42) The presence of the heat-responsive element makes it impossible for the plant to respond to stress without losing control over ONSEN.

ONSEN is not the only known TE responding to variation in temperature. Tam3 is a TE present in snap dragons and is characterized by a transposase sensible to temperature, which is only activated under cold conditions. (44) Indeed, the transposase is only capable of binding a motif on the TE at temperatures around 15 degrees. The transposase binding on the motif causes Tam3 to be demethylated and is followed by its transposition. (44)

Temperature is not the only source of stress TEs can respond to. Tnt1 is a superfamily of LTR-retrotransposons, found throughout the Solanaceae plant family. It is activated by plant microbial factors ensuing a bacterial infection. (45) In the case of Tnt1, its activation allows it to spread both vertically through the host genome and horizontally through transposition in the bacterial genome. Some TEs such as Bare1 and FaRE1 in plants respond to Abscisic Acid (ABA), a hormone associated with stress response. (46, 47) This was elegantly shown by fusing a GUS protein to FaRE1 and monitoring GUS signal after administration of ABA. (47) Stress-responsive elements are diverse and common among TEs, it is hypothesized that they confer a competitive advantage against TEs lacking responsive elements in terms of transposition rate. (48)

Opportunistic TEs and impact of stress on silencing mechanisms

The possession of a regulatory element sensible to environmental cues is not the only way for TEs to be activated by stress. There is now evidence that TEs take advantage of silencing mechanisms downturn following stress. Indeed, it appears that cellular stress response and TE silencing mechanisms are antagonistic. This is illustrated with the dual role of Hsp90. We saw earlier that Hsp90 is required for the loading of piRNA on PIWI. (25) However, Hsp90 also plays an important role as a chaperone and in cellular physiological stress response. (49, 50) As such, when exposed to stress, Hsp90 prioritizes its role in cellular stress-response and

temporarily drops its activity in the piRNA/PIWI silencing pathway. (51) Hence, Hsp90 manifold roles are responsible for the downturn of the piRNA/PIWI pathway and the subsequent activation of TEs during stress.

Hsp90 is not the only protein impaired by its different roles in the presence of stress. KAP1 and SIRT6 are chromatin remodeling proteins involved in the formation of heterochromatin and silencing of TEs. (52) However, under stress conditions and during aging, SIRT6 and KAP1 are recruited to DNA breaks, which releases TEs from their repression. (53) In the absence of SIRT6 and KAP1 chromatin around TEs is no longer compacted, which facilitates TE activation. (52) Once more, it is the competing roles of a single protein that compromises TEs silencing mechanisms. The existence of competing roles for proteins often underlies the rapid re-purposing of an existing gene under an evolutionary pressure, where the duplication and emergence of a new gene fulfilling that advantageous function was not rapid enough. (54)

An alternative hypothesis is that a protein's competitive role evolved because TEs activation are beneficial to organisms under stress. Indeed, in some instances, it appears that cells are forced to impede repressing mechanisms enforced on TEs. Under stress conditions, Hsp70, an inducible chaperone, forms a complex with Hsp90 along with other factors involved in piRNA biogenesis. The complex is then targeted for degradation by the lysosome. (55) This results in the functional collapse of the piRNA/PIWI pathway and is followed by activation of TEs. (55) This study demonstrates that TE repression is loosened under stress conditions with the presence of Hsp70. Similarly, it is observed in plants, where demethylation of TE rich regions is naturally triggered by stress. (56) As such, it appears that loosening TE repression during stress episodes is an advantageous trait. The effect of these mechanisms occurring in germ cells, is to increase and generate genetic diversity, providing material for natural selection and evolution.

All organisms are regularly exposed to stress. Since stress appears to incapacitate repressing mechanisms, TEs should be proliferating in genomes. Yet, TE movement is overall low in most organisms. (57) One explanation is that relaxation of silencing mechanisms is insufficient for TE activation. This is the case with ONSEN, where stress-induced demethylation is not enough to induce its activation. (42) Another explanation is that stress does not activate all TEs, some are even repressed. (53) For example, in the rat's hippocampus, acute stress results in an increase of H3K9me3 (a histone mark associated with heterochromatin), which provokes a reduction in TE movement. (58) A strengthening of repressing mechanisms enforced on TEs is also witnessed in rice after phosphate starvation. (59) In rice, phosphate starvation results in an increase of 5mC around known TEs. (59) Thus, stress does not always incapacitate silencing pathways and does not always compromise germ cells integrity.

Finally, we have to keep in mind that TE activation is dependent on many factors such as location, type of TE, epigenetics, physiological state, cell type and cell cycle phase. For example, in a fungal pathogen, families of TEs show temporal variation in activation upon exposure to an identical stress. (60) Additionally, change in the fungal pathogen physiological state altered the TE activation pattern. Hence, TE stress-induced activation is hard to predict and cannot be generalized.

Outcomes of TE stress-induced activation

In this part, we will explore the wide range of consequences TE movement has on genomes. Additionally, we will investigate the impact TEs have on species' evolutionary history. As we will see, TE activation produces a lot of genetic variability. To the point, where they might be responsible for adaptive radiations. Finally, we will see that TEs are essential for populations' survival on the evolutionary timescale.

Repercussion of TE movement on genomes

Novel TE insertion near a gene leads to many outcomes (Figure 1.). A TE can modify a gene by disrupting its coding sequence. For instance, genes can be rendered non-functional with an insertion in the open reading frame (I.a) or by interfering with promoters/enhancers (I.c) However, new insertions may also be source of variability, with the incorporation of a new exon (a process called exonization) (I.e) (61), the modification of a transcription start site (I.g) (62), or the formation of a new polyadenylation site (I.b). (63) In addition to generating new exons, TEs can influence the splicing pattern of a gene (I.h). (64) This often happens with the addition of a splice site or by making two or more exons incompatible. We saw in the previous part, that TEs can be equipped with regulatory sequences. As a consequence, the novel insertion of a TE may introduce new cis-regulatory sites next to a gene and modify its expression pattern (I.d). For instance, a study demonstrated that ONSEN insertions resulted in up-regulation of downstream genes, contributing to the formation of an ABA insensitive phenotype. (65)

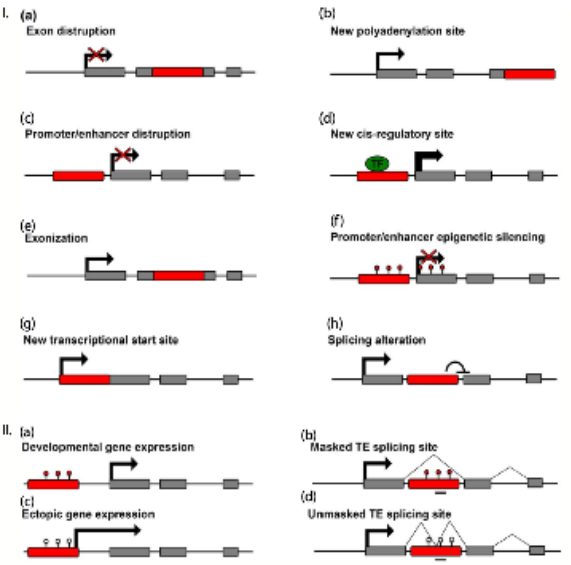

Figure 1. Schematic illustration of the various direct (I.) and indirect effects (II.) TEs have on genes. Red boxes represent newly inserted TE, grey boxes represent gene's open reading grame, red lollipops represent methylated DNA sites and white lollipops represent unmethylated sites. Black arrows represent transcription start site. a&b should write disruption. Figure from Pimpinelli, S and piacentini, L (92).

TEs do not necessarily have to be inserted in the coding region to affect gene expression. Indeed, TE insertion generating local epigenetic change is sufficient to impact gene expression. For example, TE insertion can result in local demethylation, unmasking cryptic promoters (II. C) and splice sites (II.d). Conversely, TE insertion can locally increase methylation, altering gene expression (II.a) and masking splice sites (II.b).

New TE insertions can influence the genome's architecture and chromatin state. Indeed, some TE families possess CTCF binding sites, which serve as anchor points for chromatin loops. (66) Hence, TEs introducing new CTCF binding sites induce divergent chromatin looping, re-shaping enhancer-promoter interactions and ultimately leading to altered gene expression. (67) There are other ways for TEs to influence the genome and gene expression. For instance, it is possible for TE to excise a complete gene and move it to a different genomic environment, resulting in a new gene expression profile. (68) Finally, the activation of Class II transposable elements, which generate a double strand break, is known to favor chromosomal rearrangements. (69) All in all, TEs have the power to modify the genome in a large number of ways and on different scales.

Sometimes, a TE produces a beneficial phenotype and the accountable insertion is conserved. This process is called TE exaptation. It describes the integration and conservation of TE insertions producing a beneficial phenotype. (70) Many genes originate from exapted TEs. For example, the

RAG genes, involved in the generation of antigen receptor repertoire in vertebrate's adaptive immune system, are derived from TEs. (71) Exapted elements are also embedded in regulatory networks. This is the case of FHY3 and FAR1, two transcription factors involved in the regulation of the photoreceptor phyA. (72) Interestingly, FAR1 emerged from a TE in the Mutator-like elements (MULEs) family. Elements in this family are periodically activated by stress. (73) It supports the hypothesis that stress facilitates and accelerates the creation of novel phenotypes. Recent studies showed that TEs insertions - called polymorphic mobile elements insertions (pMEIS) - were responsible for isoform diversity and differential gene regulation between human tissues. (74, 75)

TE activation is itself a source of stress that genomes have to face. As we saw previously some TE repression systems, such as RNAi, evolved under the threat of TE spread. (19) On one side, genomes and organisms are selected for their capacity to limit the stress imposed by transposable elements, which in turn forces TE to evolve systems to evade the silencing mechanisms. This could be compared to an evolutionary arms race between genomes and TEs. Yet, as we will see, it seems that TE activity is still required and needed to fuel genetic innovations on which populations are reliant on. Thus, in reality, genomes and TEs have reached a negotiated settlement, mutually depending on the others' existence.

TEs, a source of genetic diversity for populations

TE activity has the power to transform the genome on a small and large scale, but how important are TEs as a source of variation? For instance, could TE movement create enough genetic diversity to drive speciation? In diatoms, TEs are functionally involved in temperature stress response. The difference in TE insertions and families among diatom populations resulted into differential physiological response to stress. (76) In this case, TE movement could be the first step toward the speciation of diatom populations.

An emerging view called the TE-Thrust hypothesis (77), suggests that TE activation is responsible for adaptive radiations and evolution of lineages. (78) In fact, there is evidence to support that TE activity is linked to speciation events in mammals (79), angiosperms (80) and certain reptiles. (81) Moreover, primates adaptive radiation coincide with a burst in TE activity. (82) During such evolutionary events, stress might be responsible for triggering bursts in TE activity. For example, in the invasive species Cardiocondyla obscurior a large increase in TE movement is observed following founding events. (83) Founding events are known to put a lot of stress on the starting population as it needs to rapidly adapt to a new environment. TE burst could provide a molecular mechanism to Stress-Induced Evolutionary Innovation (SIEI), where sustained stress cues drive the formation of new group of cells - that characteristically exhibit more cellular stress - promoting the modelling and differentiation of new tissues. (84) Hence, there is increasing evidence to support the importance of TE stress-induced activation in the evolution of lineages and species. It would be interesting to monitor the rate of TE activity in endangered species to see if climate change related stress translates into higher TE activity and differential activation rate between populations.

Another argument advocates for the role of TEs in evolution. Can lineages persist on large timescales without TE activity? TEs are present in all eukaryotes and in most prokaryotes. Moreover, practically all studied organisms exhibit at least minimal TE activity. (85, 86) In fact, N. crassa is the only known living organism to have completely silenced TE activity with its RIP system. (40) It demonstrates that, first it is possible for evolution to produce systems that completely silence TEs and second, such systems are extremely rare and/or not conserved. Thus, suppression of TE activity appears to be an evolutionary dead-end. As a matter of fact, insufficient TE activity and lack of genetic variation might be responsible for extinctions among the sphenodontidae, a reptilian lineage. (78, 87) Hence, the conservation of TEs activity in almost all organisms indicates that TEs are essential for adaptation.

The TE-Thrust hypothesis only holds true if TE movement is not chaotic and completely uncontrolled. Indeed, TE movement is by itself a source of stress for genomes and organisms, illustrated by TEs implication in some human diseases such as monogenic disease allele, cancers and autoimmunity. (88, 89) If this source of stress becomes too intense under certain conditions, the affected population faces a risk of extinction. (90, 91) As such, the presence of repressing mechanisms and the idea of negotiated settlement is essential.

Conclusion

Genomes evolved a set of systems to prevent chaotic TE movement. However, the tools employed by genomes are not infallible. It appears that genomes and evolution tolerate and benefit from intrinsic flaws among silencing systems in order to facilitate TE activation when under stress. This is well illustrated with Hsp70 and the competing roles of silencing proteins. Moreover, some TEs borrowed stress-responsive elements to promote their own activation under stress. This widespread capacity to mobilize under stress indicates that TE stress-induced activation is necessary for populations to persist through time. As a matter of fact, increasing evidence supports the claim that TEs are important drivers of evolution and played a vital role in major adaptive radiations. All in all, TE stress-induced activation creates genetic variation, which fuels adaptation and speciation.

Acknowledgements

I would like to thank Professor Bureau for giving me the opportunity to write this review as a part of the BIOL 377 course. I also wish to express my gratitude to Nancy Nelson, who, through her invaluable advice, made my journey at McGill University a very pleasant and formative one. Overall, I wish to thank the professors that gave me the opportunity to hone my science, social and communication skills during my 3 years at McGill, thank you Prof. Hastings, Prof. Nepveu and Prof. Pavelka.

References

1. Index. In: Tollefsbol TO, editor. Handbook of Epigenetics (Second Edition): Academic Press; 2017. p. 653-68.

2. Handy DE, Castro R, Loscalzo J. Epigenetic modifications: basic mechanisms and role in cardiovascular disease. Circulation. 2011;123(19):2145-56.

3. Prakash V, Devendran R, Chakraborty S. Overview of plant RNA dependent RNA polymerases in antiviral defense and gene silencing. Indian Journal of Plant Physiology. 2017;22(4):493-505.

4. McClintock B. The origin and behavior of mutable loci in maize. Proc Natl Acad Sci U S A. 1950;36(6):344-55.

5. Wicker T, Gundlach H, Spannagl M, Uauy C, Borrill P, Ramírez-González RH, et al. Impact of transposable elements on genome structure and evolution in bread wheat. Genome Biology. 2018;19(1):103.

6. Yanchinski S. DNA - IGNORANT, SELFISH AND JUNK. New Sci. 1981;91(1262):154-5.

7. Dawkins R. The selfish gene: New edition. Oxford ; New York : Oxford University Press, 1989.; 1989.

8. McClintock B. The significance of responses of the genome to challenge. Science. 1984;226(4676):792.

9. Biemont C. A brief history of the status of transposable elements: from junk DNA to major players in evolution. Genetics. 2010;186(4):1085-93.

10. Wayne G. Rostant NW, David J. Hosken. Transposable elements and Insecticide Resistance. Advances in Genetecis. 2012;78:169-201.

11. Villasante A, Abad JP, Planelló R, Méndez-Lago M, Celniker SE, de Pablos B. Drosophila telomeric retrotransposons derived from an ancestral element that was recruited to replace telomerase. Genome Res. 2007;17(12):1909-18.

12. Jangam D, Feschotte C, Betrán E. Transposable Element Domestication As an Adaptation to Evolutionary Conflicts. Trends in Genetics. 2017;33(11):817-31.

13. Pimpinelli S, Piacentini L. Environmental change and the evolution of genomes: Transposable elements as translators of phenotypic plasticity into genotypic variability. Functional Ecology. 2020;34(2):428-41.

14. Chuong EB, Elde NC, Feschotte C. Regulatory activities of transposable elements: from conflicts to benefits. Nat Rev Genet. 2017;18(2):71-86.

15. Wicker T, Sabot F, Hua-Van A, Bennetzen JL, Capy P, Chalhoub B, et al. A unified classification system for eukaryotic transposable elements. Nature Reviews Genetics. 2007;8(12):973-82.

16. Liu B, Wendel JF. Retrotransposon activation followed by rapid repression in introgressed rice plants. Genome. 2000;43(5):874-80.

17. De Felice B, Wilson RR, Argenziano C, Kafantaris I, Conicella C. A transcriptionally active copia-like retroelement in Citrus limon. Cell Mol Biol Lett. 2009;14(2):289-304.

18. Hua-Van A, Le Rouzic A, Boutin TS, Filée J, Capy P. The struggle for life of the genome's selfish architects. Biol Direct. 2011;6:19-.

19. Obbard DJ, Gordon KHJ, Buck AH, Jiggins FM. The evolution of RNAi as a defence against viruses and transposable elements. Philosophical Transactions of the Royal Society B: Biological Sciences. 2009;364(1513):99-115.

20. Das PP, Bagijn MP, Goldstein LD, Woolford JR, Lehrbach NJ, Sapetschnig A, et al. Piwi and piRNAs Act Upstream of an Endogenous siRNA Pathway to Suppress Tc3 Transposon Mobility in the Caenorhabditis elegans Germline. Mol Cell. 2008;31(1):79-90.

21. Brennecke J, Aravin AA, Stark A, Dus M, Kellis M, Sachidanandam R, et al. Discrete small RNA-generating loci as master regulators of transposon activity in Drosophila. Cell. 2007;128(6):1089-103.

22. Aravin AA, Sachidanandam R, Girard A, Fejes-Toth K, Hannon GJ. Developmentally Regulated piRNA Clusters Implicate MILI in Transposon Control. Science. 2007;316(5825):744.

23. Carmell MA, Girard A, van de Kant HJ, Bourc'his D, Bestor TH, de Rooij DG, et al. MIWI2 is essential for spermatogenesis and repression of transposons in the mouse male germline. Dev Cell. 2007;12(4):503-14.

24. Klattenhoff C, Theurkauf W. Biogenesis and germline functions of piRNAs. Development. 2008;135(1):3.

25. Izumi N, Kawaoka S, Yasuhara S, Suzuki Y, Sugano S, Katsuma S, et al. Hsp90 facilitates accurate loading of precursor piRNAs into PIWI proteins. Rna. 2013;19(7):896-901.

26. Olivieri D, Senti K-A, Subramanian S, Sachidanandam R, Brennecke J. The cochaperone shutdown defines a group of biogenesis factors essential for all piRNA populations in Drosophila. Mol Cell. 2012;47(6):954-69.

27. Huang XA, Yin H, Sweeney S, Raha D, Snyder M, Lin H. A major epigenetic programming mechanism guided by piRNAs. Dev Cell. 2013;24(5):502-16.

28. Wierzbicki AT, Haag JR, Pikaard CS. Noncoding Transcription by RNA Polymerase Pol IVb/Pol V Mediates Transcriptional Silencing of Overlapping and Adjacent Genes. Cell. 2008;135(4):635-48.

29. Gao Z, Liu H-L, Daxinger L, Pontes O, He X, Qian W, et al. An RNA polymerase II- and AGO4-associated protein acts in RNA-directed DNA methylation. Nature. 2010;465(7294):106-9.

30. Wendte JM, Pikaard CS. The RNAs of RNA-directed DNA methylation. Biochimica et Biophysica Acta (BBA) - Gene Regulatory Mechanisms. 2017;1860(1):140-8.

31. Grewal SI. RNAi-dependent formation of heterochromatin and its diverse functions. Curr Opin Genet Dev. 2010;20(2):134-41.

32. Zofall M, Grewal SI. RNAi-mediated heterochromatin assembly in fission yeast. Cold Spring Harb Symp Quant Biol. 2006;71:487-96.

33. Edwards JR, Yarychkivska O, Boulard M, Bestor TH. DNA methylation and DNA methyltransferases. Epigenetics Chromatin. 2017;10:23.

34. Choy M-K, Movassagh M, Goh H-G, Bennett MR, Down TA, Foo RSY. Genome-wide conserved consensus transcription factor binding motifs are hyper-methylated. BMC Genomics. 2010;11:519-.

35. Ros F, Kunze R. Regulation of activator/dissociation transposition by replication and DNA methylation. Genetics. 2001;157(4):1723-33.

36. Lyko F, Ramsahoye BH, Jaenisch R. DNA methylation in Drosophila melanogaster. Nature. 2000;408(6812):538-40.

37. White CL, Suto RK, Luger K. Structure of the yeast nucleosome core particle reveals fundamental changes in internucleosome interactions. The EMBO Journal. 2001;20(18):5207-18.

38. Allshire RC, Madhani HD. Ten principles of heterochromatin formation and function. Nat Rev Mol Cell Biol. 2018;19(4):229-44.

39. Choi J, Lyons DB, Kim MY, Moore JD, Zilberman D. DNA Methylation and Histone H1 Jointly Repress Transposable Elements and Aberrant Intragenic Transcripts. Mol Cell. 2020;77(2):310-+.

40. Galagan JE, Calvo SE, Borkovich KA, Selker EU, Read ND, Jaffe D, et al. The genome sequence of the filamentous fungus Neurospora crassa. Nature. 2003;422(6934):859-68.

41. Gladyshev E. Repeat-Induced Point Mutation and Other Genome Defense Mechanisms in Fungi. Microbiol Spectr. 2017;5(4).

42. Cavrak VV, Lettner N, Jamge S, Kosarewicz A, Bayer LM, Mittelsten Scheid O. How a Retrotransposon Exploits the Plant's Heat Stress Response for Its Activation. PLOS Genetics. 2014;10(1):e1004115.

43. Matsunaga W, Kobayashi A, Kato A, Ito H. The effects of heat induction and the siRNA biogenesis pathway on the transgenerational transposition of ONSEN, a copia-like retrotransposon in Arabidopsis thaliana. Plant and Cell Physiology. 2011;53(5):824-33.

44. Hashida S-N, Uchiyama T, Martin C, Kishima Y, Sano Y, Mikami T. The temperature-dependent change in methylation of the Antirrhinum transposon Tam3 is controlled by the activity of its transposase. Plant Cell. 2006;18(1):104-18.

45. Grandbastien MA, Audeon C, Bonnivard E, Casacuberta JM, Chalhoub B, Costa AP, et al. Stress activation and genomic impact of Tnt1 retrotransposons in Solanaceae. Cytogenet Genome Res. 2005;110(1-4):229-41.

46. Vicient CM, Jääskeläinen MJ, Kalendar R, Schulman AH. Active retrotransposons are a common feature of grass genomes. Plant Physiol. 2001;125(3):1283-92.

47. He P, Ma Y, Dai H, Li L, Liu Y, Li H, et al. Characterization of the Hormone and Stress-Induced Expression of FaRE1 Retrotransposon Promoter in Strawberry. Journal of Plant Biology. 2012;55(1):1-7.

48. Abrusan G, Krambeck HJ. Competition may determine the diversity of transposable elements. Theor Popul Biol. 2006;70(3):364-75.

49. Erlejman AG, Lagadari M, Toneatto J, Piwien-Pilipuk G, Galigniana MD. Regulatory role of the 90-kDa-heat-shock protein (Hsp90) and associated factors on gene expression. Biochim Biophys Acta. 2014;1839(2):71-87.

50. Sangster TA, Lindquist S, Queitsch C. Under cover: causes, effects and implications of Hsp90-mediated genetic capacitance. Bioessays. 2004;26(4):348-62.

51. Ryan CP, Brownlie JC, Whyard S. Hsp90 and physiological stress are linked to autonomous transposon mobility and heritable genetic change in nematodes. Genome Biology and Evolution. 2016;8(12):3794-805.

52. Van Meter M, Kashyap M, Rezazadeh S, Geneva AJ, Morello TD, Seluanov A, et al. SIRT6 represses LINE1 retrotransposons by ribosylating KAP1 but this repression fails with stress and age. Nat Commun. 2014;5:5011.

53. Horváth V, Merenciano M, González J. Revisiting the Relationship between Transposable Elements and the Eukaryotic Stress Response. Trends in Genetics. 2017;33(11):832-41.

54. Copley SD. An evolutionary perspective on protein moonlighting. Biochem Soc Trans. 2014;42(6):1684-91.

55. Cappucci U, Noro F, Casale AM, Fanti L, Berloco M, Alagia AA, et al. The Hsp70 chaperone is a major player in stress-induced transposable element activation. Proceedings of the National Academy of Sciences. 2019;116(36):17943.

56. Liu R, Lang Z. The mechanism and function of active DNA demethylation in plants. Journal of Integrative Plant Biology. 2020;62(1):148-59.

57. Laricchia KM, Zdraljevic S, Cook DE, Andersen EC. Natural Variation in the Distribution and Abundance of Transposable Elements Across the Caenorhabditis elegans Species. Mol Biol Evol. 2017;34(9):2187-202.

58. Hunter RG, Murakami G, Dewell S, Seligsohn Ma, Baker MER, Datson NA, et al. Acute stress and hippocampal histone H3 lysine 9 trimethylation, a retrotransposon silencing response. Proceedings of the National Academy of Sciences. 2012;109(43):17657.

59. Secco D, Wang C, Shou H, Schultz MD, Chiarenza S, Nussaume L, et al. Stress induced gene expression drives transient DNA methylation changes at adjacent repetitive elements. eLife. 2015;4:e09343.

60. Fouche S, Badet T, Oggenfuss U, Plissonneau C, Francisco CS, Croll D. Stress-Driven Transposable Element De-repression Dynamics and Virulence Evolution in a Fungal Pathogen. Mol Biol Evol. 2020;37(1):221-39.

61. Schmitz J, Brosius J. Exonization of transposed elements: A challenge and opportunity for evolution. Biochimie. 2011;93(11):1928-34.

62. Feschotte C. Transposable elements and the evolution of regulatory networks. Nat Rev Genet. 2008;9(5):397-405.

63. Lee JY, Ji Z, Tian B. Phylogenetic analysis of mRNA polyadenylation sites reveals a role of transposable elements in evolution of the 3'-end of genes. Nucleic Acids Res. 2008;36(17):5581-90.

64. Abascal F, Tress ML, Valencia A. Alternative splicing and co-option of transposable elements: the case of TMPO/LAP2α and ZNF451 in mammals. Bioinformatics. 2015;31(14):2257-61.

65. Ito H, Kim J-M, Matsunaga W, Saze H, Matsui A, Endo TA, et al. A Stress-Activated Transposon in Arabidopsis Induces Transgenerational Abscisic Acid Insensitivity. Scientific Reports. 2016;6(1):23181.

66. Holwerda SJB, de Laat W. CTCF: the protein, the binding partners, the binding sites and their chromatin loops. Philos Trans R Soc Lond B Biol Sci. 2013;368(1620):20120369-.

67. Diehl AG, Ouyang N, Boyle AP. Transposable elements contribute to cell and species-specific chromatin looping and gene regulation in mammalian genomes. Nature Communications. 2020;11(1):1796.

68. Berrada S, Fournier D. Transposition-mediated transcriptional overexpression as a mechanism of insecticide resistance. Molecular and General Genetics MGG. 1997;256(4):348-54.

69. Zhang J, Yu C, Krishnaswamy L, Peterson T. Transposable Elements as Catalysts for Chromosome Rearrangements. In: Birchler JA, editor. Plant Chromosome Engineering: Methods and Protocols. Totowa, NJ: Humana Press; 2011. p. 315-26.

70. Joly-Lopez Z, Bureau TE. Exaptation of transposable element coding sequences. Current Opinion in Genetics & Development. 2018;49:34-42.

71. Fugmann SD. The origins of the Rag genes--from transposition to V(D)J recombination. Semin Immunol. 2010;22(1):10-6.

72. Lin R, Ding L, Casola C, Ripoll DR, Feschotte C, Wang H. Transposase-derived transcription factors regulate light signaling in Arabidopsis. Science (New York, NY). 2007;318(5854):1302-5.

73. Tittel-Elmer M, Bucher E, Broger L, Mathieu O, Paszkowski J, Vaillant I. Stress-induced activation of heterochromatic transcription. PLoS genetics. 2010;6(10):e1001175-e.

74. Cao X, Zhang Y, Payer LM, Lords H, Steranka JP, Burns KH, et al. Polymorphic mobile element insertions contribute to gene expression and alternative splicing in human tissues. Genome Biol. 2020;21(1):185.

75. Goubert C, Zevallos NA, Feschotte C. Contribution of unfixed transposable element insertions to human regulatory variation. Philosophical Transactions of the Royal Society B: Biological Sciences. 2020;375(1795):20190331.

76. Pargana A, Musacchia F, Sanges R, Russo MT, Ferrante MI, Bowler C, et al. Intraspecific Diversity in the Cold Stress Response of Transposable Elements in the Diatom Leptocylindrus aporus. Genes. 2020;11(1):25.

77. Oliver KR, Greene WK. Transposable elements and viruses as factors in adaptation and evolution: an expansion and strengthening of the TE-Thrust hypothesis. Ecology and Evolution. 2012;2(11):2912-33.

78. Oliver KR, Greene WK. Transposable elements: powerful facilitators of evolution. BioEssays. 2009;31(7):703-14.

79. Ricci M, Peona V, Guichard E, Taccioli C, Boattini A. Transposable Elements Activity is Positively Related to Rate of Speciation in Mammals. J Mol Evol. 2018;86(5):303-10.

80. Oliver KR, McComb JA, Greene WK. Transposable Elements: Powerful Contributors to Angiosperm Evolution and Diversity. Genome Biology and Evolution. 2013;5(10):1886-901.

81. Feiner N. Accumulation of transposable elements in Hox gene clusters during adaptive radiation of Anolis lizards. Proc Biol Sci. 2016;283(1840):20161555.

82. Oliver KR, Greene WK. Mobile DNA and the TE-Thrust hypothesis: supporting evidence from the primates. Mobile DNA. 2011;2(1):8.

83. Schrader L, Kim JW, Ence D, Zimin A, Klein A, Wyschetzki K, et al. Transposable element islands facilitate adaptation to novel environments in an invasive species. Nature Communications. 2014;5(1):5495.

84. Wagner GP, Erkenbrack EM, Love AC. Stress-Induced Evolutionary Innovation: A Mechanism for the Origin of Cell Types. Bioessays. 2019;41(4):e1800188.

85. Vangelisti A, Mascagni F, Usai G, Natali L, Giordani T, Cavallini A. Low

Long Terminal Repeat (LTR)-Retrotransposon Expression in Leaves of the Marine Phanerogam Posidonia Oceanica L. Life-Basel. 2020;10(3):12.
86. Pace JK, 2nd, Feschotte C. The evolutionary history of human DNA transposons: evidence for intense activity in the primate lineage. Genome Res. 2007;17(4):422-32.

87. Wang Z, Miyake T, Edwards SV, Amemiya CT. Tuatara (Sphenodon) genomics: BAC library construction, sequence survey, and application to the DMRT gene family. J Hered. 2006;97(6):541-8.

88. Burns KH. Our Conflict with Transposable Elements and Its Implications for Human Disease. In: Abbas AK, Aster JC, Feany MB, editors. Annual Review of Pathology: Mechanisms of Disease, Vol 15, 2020. Annual Review of Pathology-Mechanisms of Disease. 15. Palo Alto: Annual Reviews; 2020. p. 51-70.

89. Lynch-Sutherland CF, Chatterjee A, Stockwell PA, Eccles MR, Macaulay EC. Reawakening the Developmental Origins of Cancer Through Transposable Elements. Front Oncol. 2020;10:15.

90. Rankin DJ, Bichsel M, Wagner A. Mobile DNA can drive lineage extinction in prokaryotic populations. J Evol Biol. 2010;23(11):2422-31.

91. Abascal F, Corvelo A, Cruz F, Villanueva-Canas JL, Vlasova A, Marcet-Houben M, et al. Extreme genomic erosion after recurrent demographic bottlenecks in the highly endangered Iberian lynx. Genome Biology. 2016;17:18.

92. Pimpinelli S, Piacentini L. Environmental change and the evolution of genomes: Transposable elements as translators of phenotypic plasticity into genotypic variability. Functional Ecology. 2020;34(2):428-41.

Submitted: 01/16/21

Review Article

Department of Physics, McGill University, Montreal QC H3A 2T8, Canada

Keywords

EPR paradox, Einstein-Rosen bridges, quantum teleportation, general relativity

Email Correspondence

florian.seefeld@mail.mcgill.ca

Florian Seefeld[1]

The EPR Paradox, Einstein-Rosen bridges and teleportation

Abstract

In this review, we go over the bases of quantum teleportation, ER bridges in General relativity, and the foundational work on the hypothesis ER=EPR and summarize the resulting wormhole teleportation protocol. We then discuss that – resulting from ER=EPR – certain wormholes have to be either traversable or at the very least let information permeate, resulting in the exploration of the possibility that incoming matter might change the metric outside of wormhole throats. In this study, made in the Schwarzschild metric with the original coordinate system, we managed to find a non-zero energy-momentum tensor produced by a particular solution of the electromagnetic wave equation in curved spacetime, implying a change in the overall metric by Einstein's Equation.

1 Introduction

Quantum mechanics and general relativity have both led to the discovery of phenomena that seem to connect two arbitrarily distant entities: for quantum mechanics the EPR Paradox formulated by its namesakes Einstein, Podolski, and Rosen [1] connects two distant systems, through what is commonly called a quantum entanglement, such that the measurements on one instantaneously affects the other; for General Relativity, two black holes can be connected by a wormhole, or Einstein Rosen bridge, first described by extending the Schwarzschild solution to Einstein's equations [2]. In more recent years, several papers have linked both phenomena together, culminating in the elaboration of the hypothesis ER=EPR [3], that is that quantum entanglements and wormholes represent the same object. It is thus logical that, since Quantum Teleportation is possible [4] according to ER=EPR, teleportation using wormholes is also possible [5]. However, the hypothesis ER=EPR leads to interesting implications on the possibility of traversability or at least information permeability of wormholes, which we will elaborate on. We chose in this paper to explore the possibility, contrary to the no-hair theorem, that incoming information in one end of the wormhole changes the metric on the other end.

Firstly, this paper will review the relevant concepts surrounding the EPR Paradox and ER bridges in order to understand ER=EPR. Then, we will summarize the claim ER=EPR, as well as the wormhole teleportation protocol. We will then start with the author's contributions by quickly advancing and explaining the claim that certain wormholes have to be either traversable or permeable if ER=EPR, and by trying to see how an incoming photon might change the metric of a Schwarzschild black hole. To do this, we will find a particular solution of the electromagnetic wave equation in curved spacetime and deduce the energy-momentum tensor from it. Due to a lack of time for this project, the author only managed to derive the altered energy-momentum tensor, which by being non-zero is sufficient to prove a change in the metric. They also weren't able to solve Einstein's equation for more specific results, nor to study this phenomenon in the more general Kruskal-Szekeres coordinates for more decisive results.

2 The EPR paradox, quantum teleportation and Einstein-Rosen bridges

Before diving directly into ER=EPR, we first want to review some useful concepts, namely the EPR Paradox and ER Bridges. As we also want to study the wormhole teleportation protocol, we will also have to review the (very similar) quantum teleportation protocol. But first, we might want a little refresher on how quantum mechanics work by using the example of multiple SG devices in a row. You can skip directly to subsection 2.2.

2.1 Reminder on quantum mechanics: multiple SG devices in a row

A Stern-Gerlach device oriented in the $\vec{n}$ direction, in short an SG_n device, is composed of two magnets creating a magnetic field pointing in the $\vec{n}$ direction. This device can perform spin measurements on particles with quantum behaviours. Let's consider the following exercise: A particle with spin s passes through an SG_z device and is found to have spin value $S_z = s\hbar$. It now travels through an SG_x device. What are the possible values of S_x and what is their probability of appearing? We will solve this for $s = 1/2$.

We know that the possible values of S_x are $\frac{\hbar}{2}$ and $-\frac{\hbar}{2}$. We also know that the eigenstates of $\hat{S}_x$ are:

$$\left|\frac{1}{2},\frac{1}{2}\right\rangle_x = \frac{1}{\sqrt{2}}\left(\left|\frac{1}{2},\frac{1}{2}\right\rangle + \left|\frac{1}{2},-\frac{1}{2}\right\rangle\right)$$
$$\left|\frac{1}{2},-\frac{1}{2}\right\rangle_x = \frac{1}{\sqrt{2}}\left(\left|\frac{1}{2},\frac{1}{2}\right\rangle - \left|\frac{1}{2},-\frac{1}{2}\right\rangle\right).$$

Since $S_z = \frac{\hbar}{2}$, the particle is initially in state $\left|\frac{1}{2},\frac{1}{2}\right\rangle$, hence:

$$P\left(S_x = \frac{\hbar}{2}\right) = \left|{}_x\left\langle\frac{1}{2},\frac{1}{2}\right| \left.\frac{1}{2},\frac{1}{2}\right\rangle_z\right|^2 = \frac{1}{2}$$
$$P\left(S_x = -\frac{\hbar}{2}\right) = \left|{}_x\left\langle\frac{1}{2},\frac{1}{2}\right| \left.\frac{1}{2},\frac{1}{2}\right\rangle_z\right|^2 = \frac{1}{2}.$$

Now we can finally start reviewing the EPR Paradox.

2.2 The EPR Paradox and the Bell Inequality

The EPR Paradox was first formulated by Einstein, Podolski and Rosen [1] and concerned the two observables position and momentum. The following version of the paradox was proposed by Bohm [6]:

Suppose a particle in spin state $|0,0\rangle$ decays into 2 spin-$\frac{1}{2}$ particles. Due to conservation of linear and angular momentum, they move in opposite directions and their spin along any given direction must be opposite. Suppose now that two observers with SG devices, which we call A and B, will measure the spin of their respective particle along the axes $\overrightarrow{n_A}$ and $\overrightarrow{n_B}$. Since

we know that:

$$|0,0\rangle = \frac{1}{\sqrt{2}}|+z,-z\rangle - \frac{1}{\sqrt{2}}|-z,+z\rangle \tag{2.1}$$

$$= \frac{1}{\sqrt{2}}|+x,-x\rangle - \frac{1}{\sqrt{2}}|-x,+x\rangle \tag{2.2}$$

then we can conclude that, if $\overrightarrow{n_A} = \overrightarrow{n_B} = \overrightarrow{k}$, if A measures $S_{1z} = \frac{\hbar}{2}$, then B measures $S_{2z} = -\frac{\hbar}{2}$, and if A measures $S_{1z} = -\frac{\hbar}{2}$, then B measures $S_{2z} = \frac{\hbar}{2}$. But likewise, if if $\overrightarrow{n_A} = \overrightarrow{n_B} = \overrightarrow{i}$, then if $S_{1x} = \frac{\hbar}{2}$, then $S_{2x} = -\frac{\hbar}{2}$, and if $S_{1x} = -\frac{\hbar}{2}$, then $S_{2x} = \frac{\hbar}{2}$.

Yet, if $\overrightarrow{n_A} = \overrightarrow{k}, \overrightarrow{n_B} = \overrightarrow{i}$, if $S_{1z} = \frac{\hbar}{2}$, then there is a 50% chance that $S_{2x} = \frac{\hbar}{2}$ and a 50% chance that $S_{2x} = -\frac{\hbar}{2}$. We can only determine the value of S_{2x} by measuring it.

This would mean that we can determine with no uncertainty both the S_z and S_x values of the second particle, which violates the uncertainty principle if local realism, i.e. the assumption that the spin of each particle has an intrinsic and defined value, holds.

To prove that local realism does not hold, we use the Bell Inequality[7]:

Theorem 1 (Bell Inequality)**.** *Suppose local realism holds. Suppose also that a collection of particles in spin state $|0,0\rangle$ decay into pairs of spin-$\frac{1}{2}$ particles, with possibles values of spin $\left\{\frac{\hbar}{2}, -\frac{\hbar}{2}\right\}$ along 3 possible directions $\overrightarrow{a}$, $\overrightarrow{b}$ and $\overrightarrow{c}$. If the particles of each pair pass the SG devices A and B, respectively, oriented independently along $\overrightarrow{a}$, $\overrightarrow{b}$ or $\overrightarrow{c}$, and the event $(\pm n_1; \pm n_2)$ describes the situation in which the particle measured by A has spin value $\pm\frac{\hbar}{2}$ along $\overrightarrow{n_1}$ and the particle measured by B has spin value $\pm\frac{\hbar}{2}$ along $\overrightarrow{n_2}$, then:*

$$P(+a;+b) = P(+a;+c) + P(+c;+b). \tag{2.3}$$

Using this, then, if $\overrightarrow{c}$ bisects $\overrightarrow{a}$ and $\overrightarrow{b}$ by an angle $\theta/2$, then, by the predictions of quantum mechanics and (2.3), one finds

$$\sin^2\theta \leq 2\sin^2(\theta/2) \tag{2.4}$$

for all $\theta \in \mathbb{R}$, yet (2.4) only holds for $0 < \theta < \frac{\pi}{2}$. Thus local realism and quantum mechanics fundamentally yield different results. Experiments measuring the polarization states of pairs of photons yield results in accordance with QM, but violating Bell's inequality. Hence Bell's inequality disproves local realism and the existence of local hidden variables.

The EPR Paradox, under the form of quantum entanglement, can be used for teleportation, as we will now see.

2.3 Quantum Teleportation

A protocol to teleport quantum states was first elaborated in 1993 [4], derived directly from the EPR Paradox. The following discussion is based on it.

Suppose Alice has a particle in state $|\phi_1\rangle$. She wishes to send Bob enough information to make a copy of the state. Unless $|\phi_1\rangle$ is an already known eigenstate, Alice cannot determine $|\phi_1\rangle$ through measurement. Alice could solve the given task in different ways: either by trivially sending Bob the particle directly, or through a spin-exchange measurement. A spin-exchange measurement consists of making the particle in state $|\phi_1\rangle$ interact with another one, called ancilla, in state $|a_0\rangle$ through a unitary operation, thus leaving the initial particle in a new state $|\phi_0\rangle$. The ancilla, now in state $|a_1\rangle$, contains all the information necessary for Bob to reverse the steps and obtain $|\phi_1\rangle$. This example demonstrates the no-cloning principle of quantum information, stating that no quantum state $|\psi\rangle$ can be copied without being destroyed.

It is possible for Alice to divide the information needed to recreate $|\phi_1\rangle$ into a classical part and a quantum part, and upon reception of both, Bob can reconstruct $|\phi_1\rangle$, destroying Alice's $|\phi_1\rangle$ in the process. This process is called quantum teleportation, and, because of the need of a classical information channel, the "teleportation" is not instantaneous. The full process for the teleportation of $|\phi_1\rangle$ for a spin-$\frac{1}{2}$ particle is the following:

Two spin-$\frac{1}{2}$ particles, numbered 2 and 3, pertaining to an EPR singlet are in the overall state

$$\left|\psi_{23}^{(-)}\right\rangle = \frac{1}{\sqrt{2}}\left(|\uparrow_2\rangle|\downarrow_3\rangle - |\downarrow_2\rangle|\uparrow_3\rangle\right) \tag{2.5}$$

as in (2.1). Alice's particle shall be numbered 1. Particle 2 is received by Alice, while particle 3 is received by Bob. As the systems (1) and (23) are uncorrelated, we get that the overall system is given by

$$|\psi_{123}\rangle = |\phi_1\rangle\left|\psi_{23}^{(-)}\right\rangle. \tag{2.6}$$

Alice now entangles particles 1 and 2 by measuring an observable of the system (12), i.e performing a von Neumann measurement, in the Bell basis:

$$\left|\psi_{12}^{(\pm)}\right\rangle = \frac{1}{\sqrt{2}}\left(|\uparrow_1\rangle|\downarrow_2\rangle \pm |\downarrow_1\rangle|\uparrow_2\rangle\right) \tag{2.7}$$

$$\left|\phi_{12}^{(\pm)}\right\rangle = \frac{1}{\sqrt{2}}\left(|\uparrow_1\rangle|\uparrow_2\rangle \pm |\downarrow_1\rangle|\downarrow_2\rangle\right) \tag{2.8}$$

which is orthonormal. Hence:

$$|\uparrow_1\rangle|\downarrow_2\rangle = \frac{1}{\sqrt{2}}\left(\left|\psi_{12}^{(+)}\right\rangle + \left|\psi_{12}^{(-)}\right\rangle\right) \tag{2.9}$$

$$|\downarrow_1\rangle|\uparrow_2\rangle = \frac{1}{\sqrt{2}}\left(\left|\psi_{12}^{(+)}\right\rangle - \left|\psi_{12}^{(-)}\right\rangle\right) \tag{2.10}$$

$$|\uparrow_1\rangle|\uparrow_2\rangle = \frac{1}{\sqrt{2}}\left(\left|\phi_{12}^{(+)}\right\rangle + \left|\phi_{12}^{(-)}\right\rangle\right) \tag{2.11}$$

$$|\downarrow_1\rangle|\downarrow_2\rangle = \frac{1}{\sqrt{2}}\left(\left|\phi_{12}^{(+)}\right\rangle - \left|\phi_{12}^{(-)}\right\rangle\right) \tag{2.12}$$

If we write, for convenience,

$$|\phi_1\rangle = a|\uparrow_1\rangle + b|\downarrow_1\rangle \tag{2.13}$$

with $|a|^2 + |b|^2 = 1$, we get:

$$\begin{aligned}|\psi_{123}\rangle &= |\phi_1\rangle\left|\psi_{23}^{(-)}\right\rangle \\ &= (a|\uparrow_1\rangle + b|\downarrow_1\rangle)\left(\frac{1}{\sqrt{2}}\left(|\uparrow_2\rangle|\downarrow_3\rangle - |\downarrow_2\rangle|\uparrow_3\rangle\right)\right) \\ &= \frac{a}{\sqrt{2}}\left(|\uparrow_1\rangle|\uparrow_2\rangle|\downarrow_3\rangle - |\uparrow_1\rangle|\downarrow_2\rangle|\uparrow_3\rangle\right) \\ &\quad + \frac{b}{\sqrt{2}}\left(|\downarrow_1\rangle|\uparrow_2\rangle|\downarrow_3\rangle - |\downarrow_1\rangle|\downarrow_2\rangle|\uparrow_3\rangle\right)\end{aligned} \tag{2.14}$$

hence, by (2.9)-(2.12):

$$\begin{aligned}|\psi_{123}\rangle = \frac{1}{2}&\left[\left|\psi_{12}^{(-)}\right\rangle(-a|\uparrow_3\rangle - b|\downarrow_3\rangle) + \left|\psi_{12}^{(+)}\right\rangle(-a|\uparrow_3\rangle + b|\downarrow_3\rangle)\right] \\ + \frac{1}{2}&\left[\left|\phi_{12}^{(-)}\right\rangle(a|\downarrow_3\rangle + b|\uparrow_3\rangle) + \left|\phi_{12}^{(+)}\right\rangle(a|\downarrow_3\rangle - b|\uparrow_3\rangle)\right].\end{aligned} \tag{2.15}$$

Therefore, all 4 outcomes are equally likely with probability $1/4$. After Alice's measurement, Bob's particle 3 will take one of the following states:

$$\begin{aligned}|\phi_3\rangle \equiv &-\begin{pmatrix} a \\ b \end{pmatrix}, \begin{pmatrix} -1 & 0 \\ 0 & 1 \end{pmatrix}|\phi_3\rangle \\ &\begin{pmatrix} 0 & 1 \\ 1 & 0 \end{pmatrix}|\phi_3\rangle, \begin{pmatrix} 0 & -1 \\ 1 & 0 \end{pmatrix}|\phi_3\rangle.\end{aligned} \tag{2.16}$$

Each of these can be obtained by applying a unitary operation on $|\phi_1\rangle$: $|\phi_3\rangle$ is just $|\phi_1\rangle$ times a phase, whilst the other operations are clockwise rotations of 180° around the z, x and y axes, respectively, hence Bob just needs to rotate them anti-clockwise to obtain $|\phi_1\rangle$ again. All Bob needs to replicate $|\phi_1\rangle$ is the information, sent by Alice, of which of the four states $\left|\psi_{12}^{(\pm)}\right\rangle$

and $\left|\phi_{12}^{(\pm)}\right\rangle$ she obtained. No trace of $|\phi_1\rangle$ is left in her results, and she just needs to send the information to Bob. At the end of the process, two bits of information, uncorrelated to $|\phi_1\rangle$, are left behind.

Quantum teleportation also works for mixed or entangled states. If, taking the same example, we start with particle 1 already forming an EPR singlet with a fourth particle, which we call 0, i.e.

$$\left|\psi_{01}^{(-)}\right\rangle = \frac{1}{\sqrt{2}}\left(|\uparrow_0\rangle|\downarrow_1\rangle - |\downarrow_0\rangle|\uparrow_1\rangle\right), \tag{2.17}$$

then

$$\begin{aligned}|\psi_{0123}\rangle &= \left|\psi_{01}^{(-)}\right\rangle\left|\psi_{23}^{(-)}\right\rangle \\ &= \frac{1}{2}\big[\,|\uparrow_0\rangle|\downarrow_1\rangle|\uparrow_2\rangle|\downarrow_3\rangle - |\uparrow_0\rangle|\downarrow_1\rangle|\downarrow_2\rangle|\uparrow_3\rangle \\ &\quad - |\downarrow_0\rangle|\uparrow_1\rangle|\uparrow_2\rangle|\downarrow_3\rangle + |\downarrow_0\rangle|\uparrow_1\rangle|\downarrow_2\rangle|\uparrow_3\rangle\,\big] \\ &= \frac{1}{2}\Big[\left|\psi_{12}^{(-)}\right\rangle\left|\psi_{03}^{(-)}\right\rangle + \left|\psi_{12}^{(+)}\right\rangle\left|\psi_{03}^{(+)}\right\rangle + \left|\phi_{12}^{(-)}\right\rangle\left|\phi_{03}^{(-)}\right\rangle \\ &\quad + \left|\phi_{12}^{(+)}\right\rangle\left|\phi_{03}^{(+)}\right\rangle\Big]\end{aligned} \tag{2.18}$$

hence 0 and 3 form a singlet after the measurement on system (12).

All these results can be generalized to systems having N>2 orthogonal states. Alice would use the pair (23) of N-state particles in a completely entangled state, which can be written as:

$$\sum_j \frac{1}{\sqrt{N}}|j\rangle \otimes |j\rangle \tag{2.19}$$

where $j = 0, 1, ..., N-1$ are the N states. Let the state of particle 1 which we want to teleport be:

$$|\phi\rangle = \sum_j \rho_j |j\rangle, \tag{2.20}$$

with $\sum_j |\rho_j|^2 = 1$. Alice then performs her measurement on the system (12), yielding one of the following:

$$|\psi_{nm}\rangle = \sum_j \frac{1}{\sqrt{N}} e^{\frac{2\pi i j n}{N}} |j\rangle \otimes |(j+m) \bmod N\rangle, \tag{2.21}$$

where $n, m \in \{0, 1, ..., N-1\}$, the state of the total system being:

$$|\psi\rangle = \frac{1}{\sqrt{N}} \sum_j \rho_j \sum_k |j\rangle \otimes |k\rangle \otimes |k\rangle \tag{2.22}$$

Again, after performing a measurement on her particle and one of the two entangled particles, Alice sends classical information to Bob. This time, her information is of at least 2^N bits. Bob then performs the unitary transformation:

$$U_{nm} = \sum_k e^{\frac{2\pi i k n}{N}} |k\rangle\langle(k+m) \bmod N| \tag{2.23}$$

on his particle to obtain $|\phi\rangle$ again.

The message sent by Alice is crucial. If Bob were to guess her outcome, the sate $|\phi\rangle$ would be reconstructed (in the spin-$\frac{1}{2}$ case) as a superposition of the 4 states from 2.16, all having the same probability. Hence Bob would not be able to deduce from this any information about $|\phi\rangle$, which makes sense since otherwise the signal would travel faster than light.

It would be interesting to see if other states than an EPR singlet could be used for teleportation. In fact, it can be shown that the most effective configuration for teleportation is a state of two maximally entangled particles (i.e they form an EPR singlet). Indeed, we have the following property:

Proposition 2. *Consider a state $|\Upsilon_{23}\rangle$. Then Bob's particle 3 will be related to $|\phi_1\rangle$ by 4 fixed unitary operations if and only if*

$$|\Upsilon_{23}\rangle = \frac{1}{\sqrt{2}}\left(|u_2\rangle|p_2\rangle + |v_2\rangle|q_3\rangle\right), \tag{2.24}$$

where $\{|u\rangle, |v\rangle\}$ and $\{|p\rangle, |q\rangle\}$ are two pairs of orthonormal bases.

Hence 2 and 3 must be maximally entangled. Less entangled states will be less effective at teleportation, either limiting the accuracy of the teleportation or the range of possible $|\phi_1\rangle$ that can be teleported.

It can also be proven that a classical channel of two bits of information is necessary for teleportation. To do so, we study a 4-way coding scheme: B receives two bits of information and one particle of an EPR pair, sending out a particle in state $|\phi\rangle$ and an uncorrelated two bits, while A receives the other particle of the pair and the particle in state $|\phi\rangle$, sending out two bits of information. This is one way to transmit physically the 2 bits of information.

We can thus build a setup where B and A perform a 4-way coding, but in between the particle in state $|\phi\rangle$ gets intercepted and teleported by A' and B'. Suppose now that A' and B' use a channel of capacity C<2 bits, but is still capable of teleporting $|\phi\rangle$, hence also the 2 bit message that B sends to A. If B' were to guess the message superluminally, his probability 2^{-C} of guessing right would be bigger than $\frac{1}{4}$, resulting in a probability bigger than $\frac{1}{4}$ of sending the message superluminally from B to A. Hence there exist two distinct two-bit messages r and s, such that $P(r \mid s) < \frac{1}{4}$, probability of receiving superluminally r if s was sent, and $P(r \mid r) > \frac{1}{4}$, probability of receiving superluminally r if r was sent. It would thus be possible to reliably send messages superluminally, which thus, by contradiction, supposes that $C \geq 2$. By the same argument, teleportation of an N-state particle needs a classical channel of $2\log_2(N)$ bits.

After studying the EPR Paradox and Quantum Teleportation, in order to understand ER=EPR, we now need to direct our attention to ER Bridges.

2.4 Einstein equation, Penrose diagrams and the Schwarzschild black hole

We now shift our focus to general relativity. We will see in section 3 that general relativity and quantum mechanics share a connection, in the form of wormholes. wormholes, or ER bridges, are a theoretical result of general relativity. We first start with the fundamental part of general relativity, Einstein's equation. From there, we will obtain Schwarzschild's solution to Einstein's equation, which directly leads to the Schwarzschild black hole and to the easiest wormhole to describe. This section is based on [8].

Einstein's equation

Einstein's equation determines the local spacetime geometry, given by the metric $g_{\mu\nu}$[9]. It can be derivated from the Hilbert action, given by:

$$S_H = \int \sqrt{-g} R \, d^n x, \tag{2.25}$$

where $g = |g_{\mu\nu}|$, and R is the Ricci constant [10]. We now need to introduce a few objects, presented in chapters 2 and 3 of [8]. The derivation of Einstein's equation will be based on chapter 4. We use tensorial summation notation, also known as Einstein notation: the expression is ummed over all indices that appear as both subscripts and superscripts.

We will use the Christoffel symbol

$$\Gamma^{\lambda}_{\mu\nu} = \frac{1}{2} g^{\lambda\sigma}\left(\partial_\mu g_{\nu\sigma} + \partial_\nu g_{\sigma\mu} - \partial_\sigma g_{\mu\nu}\right), \tag{2.26}$$

which enables us to define the covariant derivative of a tensor $T^{\mu_1\cdots\mu_k}_{\nu_1\cdots\nu_l}$ as

$$\begin{aligned}\nabla_\mu T^{\mu_1\cdots\mu_k}{}_{\nu_1\cdots\nu_l} &= \partial_\mu T^{\mu_1\cdots\mu_k}{}_{\nu_1\cdots\nu_l} \\ &\quad + \sum_{i=1}^{k} \Gamma^{\mu_i}_{\sigma\lambda} T^{\mu_1\cdots\mu_{i-1}\lambda\mu_{i+1}\cdots\mu_k}{}_{\nu_1\cdots\nu_l} \\ &\quad + \sum_{i=1}^{l} \Gamma^{\lambda_i}_{\sigma\nu_i} T^{\mu_1\cdots\mu_k}{}_{\nu_1\cdots\nu_{i-1}\lambda\nu_{i+1}\cdots\nu_l},\end{aligned} \tag{2.27}$$

and the Riemann tensor

$$R^{\rho}_{\sigma\mu\nu} = \partial_\mu \Gamma^{\rho}_{\nu\sigma} - \partial_\nu \Gamma^{\rho}_{\mu\sigma} + \Gamma^{\rho}_{\mu\lambda}\Gamma^{\lambda}_{\nu\sigma} - \Gamma^{\rho}_{\nu\lambda}\Gamma^{\lambda}_{\mu\sigma}. \tag{2.28}$$

From this, we can get the Ricci tensor:

$$R_{\mu\nu} = R^{\lambda}{}_{\mu\lambda\nu} \tag{2.29}$$

and finally the Ricci constant given by

$$R = g^{\mu\nu} R_{\mu\nu}. \tag{2.30}$$

We will also make use of Stoke's theorem:

Theorem 3 (Stokes Theorem)**.** *Let M be an n-dimensional region with boundary δM. Suppose we use coordinates x^i in M, which has metric g_{ij}, and coordinates y^i on δM which has metric γ_{ij}, and suppose that n^μ is the unit normal to δM. Then, for a vector V^μ:*

$$\int_M d^n x \, \sqrt{|g|} \nabla_\mu V^\mu = \int_{\delta M} d^{n-1} y \, \sqrt{|\gamma|} n_\mu V^\mu \tag{2.31}$$

One can find, using this result and following the derivation from [8], that

$$\delta S_H = \int d^n x \, \sqrt{-g} \left[R_{\mu\nu} - \frac{1}{2} R g_{\mu\nu} \right] \delta g^{\mu\nu}. \tag{2.32}$$

Since the action is given by

$$S = \int \sum_i \left(\frac{\delta S}{\delta \phi^i} \delta \phi^i \right) d^n x, \tag{2.33}$$

hence

$$\frac{1}{\sqrt{-g}} \frac{\delta S_H}{\delta g_{\mu\nu}} = R_{\mu\nu} - \frac{1}{2} R g_{\mu\nu}. \tag{2.34}$$

The Hilbert action is the action exerted by gravity alone. To get the total action, we need to add the action due to matter fields as well. The total action is given by:

$$S = \frac{1}{16\pi G} S_H + S_M, \tag{2.35}$$

S_M being the action due to matter fields. By the principle of least action, we get that:

$$\frac{1}{\sqrt{-g}} \frac{\delta S}{\delta g_{\mu\nu}} = \frac{1}{16\pi G} \left(R_{\mu\nu} - \frac{1}{2} R g_{\mu\nu} \right) + \frac{1}{\sqrt{-g}} \frac{\delta S_M}{\delta g_{\mu\nu}} = 0. \tag{2.36}$$

If we define the energy-momentum tensor as

$$T_{\mu\nu} = -2 \frac{1}{\sqrt{-g}} \frac{\delta S_M}{\delta g_{\mu\nu}}, \tag{2.37}$$

we then get the Einstein equation:

$$R_{\mu\nu} - \frac{1}{2} R g_{\mu\nu} = 8\pi G T_{\mu\nu}. \tag{2.38}$$

Before continuing, let us introduce Penrose diagrams.

Penrose Diagrams

Like a Minkowski diagram, which represents flat spacetime in special relativity, a Penrose diagram allows us to represent causality in an understandable way. But in contrast to Minkowski diagrams, Penrose diagrams are conformally equivalent to the actual metric of spacetime, and allow us to represent all of spacetime on a finite diagram.

Figure 1 is a good example of a Penrose diagram. Every point on the diagram is a 2-sphere, and each hyperbola that is drawn represents a curve of either constant time (if horizontal) or constant space coordinate (if vertical). i^0 represents spatial infinity (note that the diagram is left-right symmetric), i^+ is the future timelike infinity and i^- is the past timelike infinity.

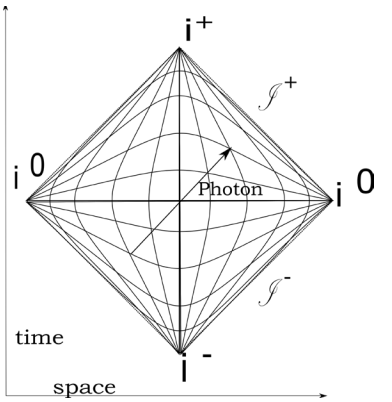

Figure 1. Penrose diagram of spacetime

We say that $\mathscr{I}^+$ is the future null infinity and $\mathscr{I}^-$ the past null infinity. On such a diagram, light moves at a 45° angle with the time and space axes (as shown by the photon), hence, as all events B that another event A can influence lie within the light cone of A, all such B lie within a 45° angle with the time axis from A. Also, all timelike curves start at i^- and end at i^+, all spacelike curves start and end at each i^0, and lightlike curves start on $\mathscr{I}^-$ and end on $\mathscr{I}^+$.

Penrose diagrams are useful for representing black holes and wormholes. We will now work out one of the solutions of Einstein's equation which describes a black hole.

Schwarzschild Solution

The Schwarzschild solution is one solution to (2.38), and the earliest example of a black hole and, as a matter of fact, of a wormhole. We will derive it here as an exercise.

In GR, the unique static spherically symmetric vacuum solution to (2.38) is the Schwarzschild metric [11][12]. A breakdown of all the terms:

- "static" means that the components of $g_{\mu\nu}$ do not depend on t, and that there are no cross terms of type $dtdx^i$ or $dx^i dt$ in the metric.
- "spherically symmetric" means that, in spherical coordinates (t, r, θ, ϕ), the metric depends on

$$d\Omega^2 = d\theta^2 + \sin^2\theta \, d\phi^2. \tag{2.39}$$

- "vacuum solution" means that 2.38 reduces to

$$R_{\mu\nu} - \frac{1}{2} R g_{\mu\nu} = 0 \Rightarrow R_{\mu\nu} = 0. \tag{2.40}$$

We can thus try to construct such a metric. It will be of the type

$$ds^2 = -e^{2\alpha(r)} dt^2 + e^{2\beta(r)} dr^2 + e^{2\gamma(r)} r^2 d\Omega^2. \tag{2.41}$$

Performing a change of variables

$$\bar{r} = e^{\gamma(r)} r$$
$$\text{with } d\bar{r} = e^{\gamma} dr + e^{\gamma} r d\gamma = \left(1 + r \frac{d\gamma}{dr} \right) e^{\gamma} dr, \tag{2.42}$$

we get

$$ds^2 = -e^{2\alpha(r)} dt^2 + \left(1 + r \frac{d\gamma}{dr} \right)^{-2} e^{2\beta(r) - 2\gamma(r)} d\bar{r}^2 + \bar{r}^2 d\Omega^2, \tag{2.43}$$

and we can now relabel $\bar{r} \to r$ and

$$\left(1 + r \frac{d\gamma}{dr} \right)^{-2} e^{2\beta(r) - 2\gamma(r)} \to e^{2\beta}, \tag{2.44}$$

giving the metric

$$ds^2 = -e^{2\alpha(r)}dt^2 + e^{2\beta(r)}dr^2 + r^2 d\Omega^2. \tag{2.45}$$

Let us now use Einstein's equation to solve for α, β. The Christoffel symbols are given by:

$$\begin{array}{ccc} \Gamma^t_{tr} = \partial_r \alpha & \Gamma^r_{tt} = e^{2(\alpha-\beta)}\partial_r\alpha & \Gamma^r_{rr} = \partial_r \beta \\ \Gamma^\theta_{r\theta} = \frac{1}{r} & \Gamma^r_{\theta\theta} = -re^{-2\beta} & \Gamma^\phi_{r\phi} = \frac{1}{r} \\ \Gamma^r_{\phi\phi} = -re^{-2\beta}\sin^2\theta & \Gamma^\theta_{\phi\phi} = -\sin\theta\cos\theta & \Gamma^\phi_{\theta\phi} = \frac{\cos\theta}{\sin\theta} \end{array} \tag{2.46}$$

bearing in mind that all other elements are either 0 or related by symmetry to those indicated. We thus get the Riemann tensor elements:

$$\begin{aligned} R^t{}_{rtr} &= \partial_r\alpha\partial_r\beta - \partial_r^2\alpha - (\partial_r\alpha)^2 \\ R^t{}_{\theta t\theta} &= -re^{-2\beta}\partial_r\alpha \\ R^t{}_{\phi t\phi} &= -re^{-2\beta}\sin^2\theta\partial_r\alpha \\ R^r{}_{\theta r\theta} &= re^{-2\beta}\partial_r\beta \\ R^r{}_{\phi r\phi} &= re^{-2\beta}\sin^2\theta\partial_r\beta \\ R^\theta{}_{\phi\theta\phi} &= \left(1 - e^{-2\beta}\right)\sin^2\theta \end{aligned} \tag{2.47}$$

giving us the elements of the Ricci tensor:

$$\begin{aligned} R_{tt} &= e^{2(\alpha-\beta)}\left[\frac{2}{r}\partial_r\alpha - \partial_r\alpha\partial_r\beta + \partial_r^2\alpha + (\partial_r\alpha)^2\right] \\ R_{rr} &= \frac{2}{r}\partial_r\beta + \partial_r\alpha\partial_r\beta - \partial_r^2\alpha - (\partial_r\alpha)^2 \\ R_{\theta\theta} &= e^{-2\beta}\left[r\left(\partial_r\beta - \partial_r\alpha\right) - 1\right] + 1 \\ R_{\phi\phi} &= \sin^2\theta R_{\theta\theta}. \end{aligned} \tag{2.48}$$

Since $R_{\mu\nu} = 0$, and since R_{tt} and R_{rr} vanish independently, we can set:

$$0 = e^{2(\alpha-\beta)}R_{tt} + R_{rr} = \frac{2}{r}\left(\partial_r\alpha + \partial_r\beta\right)$$

giving us $\alpha = -\beta + c,\ c \in \mathbb{R}$. Rescaling $t \to e^{-c}t$ gives

$$\alpha = -\beta. \tag{2.49}$$

We also set $R_{\theta\theta} = 0$, yielding

$$\begin{aligned} e^{2\alpha}\left(2r\partial_r\alpha + 1\right) &= 1 \\ \Rightarrow \partial_r\left(re^{2\alpha}\right) &= 1 \\ \Rightarrow e^{2\alpha} &= 1 - \frac{R_S}{r}, \end{aligned}$$

where R_S is a constant called the Schwarzschild radius. Since we have $g_{tt} = -e^{2\alpha} = -\left(1 - \frac{R_S}{r}\right)$ and in the weak-field limit it satisfies $g_{tt} = -\left(1 - \frac{2GM}{r}\right)$ around a point mass, we obtain that

$$R_S = 2GM, \tag{2.50}$$

and

$$ds^2 = -\left(1 - \frac{2GM}{r}\right)dt^2 + \left(1 - \frac{2GM}{r}\right)^{-1}dr^2 + r^2 d\Omega^2 \tag{2.51}$$

is the Scharzschild metric. We can think of (2.50) as the definition of M.

The metric diverges for $r = 0$ and $r = 2GM$. Since $R^{\mu\nu\rho\sigma}R_{\mu\nu\rho\sigma} = \frac{48G^2M^2}{r^6}$ diverges for $r = 0$, it is a singularity of the metric.

The behavior of matter outside $r = 2GM$ can be nicely described, but the interesting part comes from analyzing the Schwarzschild solution at $r < 2GM$.

Schwarzschild black holes

Let us now, in an attempt to understand causality in the Schwarzschild metric, study radial null curves, for which θ and ϕ are constant. By definition, $ds^2 = 0$ on null/lightlike curves. As a quick reminder we have $ds^2 < 0$ for timelike curves and $ds^2 > 0$ for spacelike curves:

$$ds^2 = 0 = -\left(1 - \frac{2GM}{r}\right)dt^2 + \left(1 - \frac{2GM}{r}\right)^{-1}dr^2,$$

implying

$$\frac{dt}{dr} = \pm\left(1 - \frac{2GM}{r}\right)^{-1}, \tag{2.52}$$

which is the slope of the light cones on a spacetime diagram of the $t - r$ plane. We have $\lim_{r\to+\infty}\frac{dt}{dr} = \pm 1$, and $\lim_{r\to 2GM}\frac{dt}{dr} = \pm\infty$. It thus seems that the light rays never reach $r = 2GM$,but that is just an illusion caused by our coordinate system (hence an outside observer will never see the light rays reach that point). In order to see what really happens, we need to find a more suitable coordinate system. First, let us take $t \to \pm r^* + \text{const}$, where $r^* = r + 2GM\ln\left(\frac{r}{2GM} - 1\right)$. Our metric thus becomes well behaved at $r = 2GM$ (meaning that it is not a singularity after all). Now, define

$$\begin{aligned} v &= t + r^* \\ u &= t - r^* \end{aligned} \tag{2.53}$$

and use the coordinate system (v, r, θ, ϕ), known as the Eddington-Finkelstein coordinates. The metric now becomes:

$$ds^2 = -\left(1 - \frac{2GM}{r}\right)dv^2 + (dv\,dr + dr\,dv) + r^2 d\Omega^2 \tag{2.54}$$

and the determinant of the metric is $g = -r^4\sin^2\theta$, well-behaved at $r = 2GM$. The condition for radial null-curves is solved by:

$$\frac{dv}{dr} = \begin{cases} 0, & \text{(infalling)} \\ 2\left(1 - \frac{2GM}{r}\right)^{-1}. & \text{(outgoing)} \end{cases} \tag{2.55}$$

This result is interesting. The light cones remain well-behaved, but for $r < 2GM$, they close up ($\frac{dv}{dr} < 0$ for outgoing curves for $r < 2GM$), hence all future-directed paths are in the direction of decreasing r. Hence, $r = 2GM$ is a point of no return: this is the event horizon. Since nothing can escape it, the whole region lying within $r < 2GM$ is called a black hole.

We can extend the Schwarzschild solution even further to include even more regions.

Indeed, in the (v, r) coordinates, we can cross the event horizon on future-directed, but not on past-directed paths. If we now choose to replace v by u from (2.53), our metric becomes

$$ds^2 = -\left(1 - \frac{2GM}{r}\right)du^2 - (du\,dr + dr\,du) + r^2 d\Omega^2 \tag{2.56}$$

for which we get

$$\frac{du}{dr} = \begin{cases} -2\left(1 - \frac{2GM}{r}\right)^{-1}, & \text{(infalling)} \\ 0. & \text{(outgoing)} \end{cases} \tag{2.57}$$

The event horizon can only be crossed on past-directed paths. Where the coordinatees (v, r, θ, ϕ) extended spacetime to the future, the coordinates (u, r, θ, ϕ) extended it to the past. We call that region of spacetime a white hole (a region from which things can escape to us, while we cannot get there).

Following spacelike geodesics uncovers even another region. Using the coordinates

$$\begin{aligned} v' &= e^{v/4GM} \\ u' &= e^{-u/4GM} \end{aligned} \tag{2.58}$$

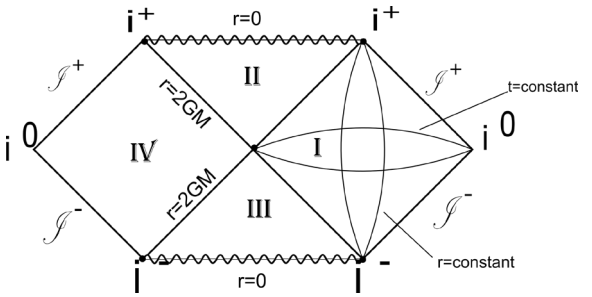

Figure 2. Penrose diagram of the Schwarzschild metric. Region I is our asymptotically flat region outside $r = 2GM$, Region II is the black hole, Region III the white hole and Region IV the other asymptotically flat region. $r = 0$ represents the singularity. Note that only spacelike curves connect regions I and IV, and that all timelike curves on II end at $r = 0$ and on III start at $r = 0$.

which can be expressed as

$$\begin{aligned} v' &= \left(\frac{r}{2GM} - 1\right)^{\frac{1}{2}} e^{(r+t)/4GM} \\ u' &= -\left(\frac{r}{2GM} - 1\right)^{\frac{1}{2}} e^{(r-t)/4GM}, \end{aligned} \tag{2.59}$$

we can create the new set of coordinates (T, R, θ, ϕ), where T and R are defined as

$$\begin{aligned} T &= \frac{1}{2}(v' + u') = \left(\frac{r}{2GM} - 1\right)^{\frac{1}{2}} e^{r/4GM} \sinh\left(\frac{t}{4GM}\right) \\ R &= \frac{1}{2}(v' - u') = \left(\frac{r}{2GM} - 1\right)^{\frac{1}{2}} e^{r/4GM} \cosh\left(\frac{t}{4GM}\right). \end{aligned} \tag{2.60}$$

Thus, using $T^2 - R^2 = \left(1 - \frac{r}{2GM}\right) e^{r/2GM}$, the metric becomes

$$ds^2 = \frac{32G^3M^3}{r} e^{-r/2GM}(-dT^2 + dR^2) + r^2 d\Omega^2. \tag{2.61}$$

With these coordinates, the metric covers all of spacetime for which $-\infty \leq R \leq +\infty, T^2 < R^2 + 1$. We can thus uncover a fourth region: another asymptotically flat spacetime which can only be reached from the other regions by spacelike curves. That is we can not reach it, nor can anything from it reach us. We can think of it as a region connected to the region $r > 2GM$ by an ER bridge. The entirety of spacetime covered by the Schwarzschild metric can be represented by Figure 2.

We can think of the non-traversable ER-bridge, if we were to slice the diagram into spacelike slices of constant time, as the two regions I and IV reaching for each other, join together through a wormhole for a while, then disconnect. The wormhole closes too quickly for anyone to traverse it.

Now that we have seen both the EPR Paradox and ER Bridges, we can start reviewing ER=EPR.

3 ER=EPR, wormhole teleportation and wormhole dynamics.

We can now finally make a connection between general relativity and quantum mechanics, by connecting ER Bridges and the EPR Paradox through the statement ER=EPR. It is a quite recent hypothesis[3], with certain implications on the feasibility of teleportation using wormholes. We will thus review both concepts here, before diving into our own deductions and contributions.

3.1 ER=EPR

Maldacena and Susskind present in their paper "Cool horizons for entangled black holes" [3] a conjecture on Einstein Rosen bridges (ER) and quantum entanglement (EPR), claiming that both phenomena are the same.

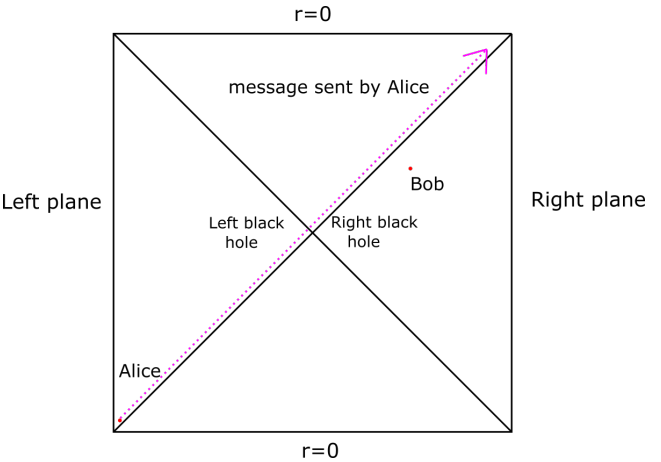

Figure 3. Penrose diagram of the situation described: Alice sends a message through her black hole, which can only be intercepted by Bob if he enters his. If Alice sends it early enough, and her message is a deadly set of quanta, then this situation represents a firewall from Bob's perspective.

Firstly, they present different ER bridges, like the AdS black hole or the Schwarzschild black hole as presented here in section 2.4. It is shown that the ER bridge onnecting each of the two black holes in each case can be described at $t = 0$ as an entangled state $|\psi\rangle = \sum_n e^{-\beta \frac{E_n}{2}} |n, n\rangle$, and that, if we consider the time evolution of $|\psi\rangle$ to be

$$|\psi_t\rangle = \sum_n e^{-\beta \frac{E_n}{2}} e^{-2iE_n t} |n, n\rangle , \tag{3.1}$$

each $|\psi_t\rangle$ can also represent a different state. They thus claim that black holes represented in such a way do not have firewalls, and that we can instead consider Figure 3.

They also describe a way of creating an ER bridge by using quantum entanglement, and how the wormhole geometry varies with time.

After that, the authors present their main claim: that an ER bridge and an EPR entanglement are the same thing (hence ER=EPR). They base this on the numerous similarities between the two phenomena (i.e. that both phenomena do not violate locality and that both forms of connection between two shares either need a pre-existing connection or direct contact of the two connected shares to be created, that is they cannot be created by local operations or classical communication). They therefore claim that every instance of an ER bridge is also an instance of quantum entanglement, and vice versa. The paper also explores the possibility of Einstein-Rosen bridges which, instead of connecting two black holes, connect a whole set of particles together. That way, every two subsystems are maximally entangled and thus connected by the ER bridge. They also study how such a system would behave, and how Hawking radiation is such a cloud entangled with a black hole.

3.2 Using wormholes for teleportation

Assuming ER=EPR, it should be possible to teleport information through a wormhole exactly like one can teleport information using an entangled pair of particles. This idea is presented in the paper "Teleportation through the wormhole" [5] , of which we present now a summary, as well as some further implications of ER=EPR:

Some prerequisites

A black hole of entropy N will be represented by N qubits, and the Hamiltonian by $H = \sum_{i,j} h_{ij}$, h depending on the Pauli operators. The

time-evolution $U(t) = e^{-iHt}$ is used to express precursor operators $U^\dagger(t) AU(t)$, where A is an operator that adds or subtracts particles to the system, which represent a system to which A is applied at time t. Note that $U(t)$ and $U^\dagger(t)$ act on a different number of qubits.

As such a system needs a time $t_* = \log N$ to scramble, the corresponding time-evolution operator for an N qubit system until scrambling is denoted by $V_N = e^{-iHt_*}$. The complexity of V_N $N \log N$, hence that of $V^\dagger W V$ for a simple two qubit operator W is, by the switchback effect, N.

The actual protocol

Let us now assume that Alice and Bob each have one throat of the wormhole, each portion labeled **A** and **B** respectively, which is modeled by a system of $2N$ maximally entangled qubits, such that its entropy is N. Suppose that Alice wants to teleport a system of n particles in the state $|\phi\rangle$denoted by **T**. We need to take into account that $n \leq N$ and that Alice needs to send a classical message of size $2n$ for this to work. We consider the example case $n = 1$.

We assume that the initial state of the system is the thermofield-double state

$$|\text{TFD}\rangle = \sum_I |I\rangle_A |I\rangle_B , \tag{3.2}$$

where $|I\rangle_{A,B}$ is the complete set of states in the chosen bases of **A** and **B**'s systems. If k is a complete set of states in the Hilbert space of **T**, i.e. $|0\rangle, |1\rangle$, then **T**'s state is

$$|\phi\rangle_T = \sum_k \phi(k) |k\rangle_T . \tag{3.3}$$

The initial state of the whole system is thus

$$|\text{initial}\rangle = \sum_{I,k} \phi(k) |k\rangle_T |I\rangle_A |I\rangle_B . \tag{3.4}$$

Before the teleportation, the qubit of **T** is absorbed by the black hole **A** and scrambled. This is represented by applying the operator V on the initial state:

$$V |\text{initial}\rangle = \sum_{I,k} \phi(k) V |kI\rangle_{AT} |I\rangle_B . \tag{3.5}$$

Picking now any two qubits from (**AT**), and labeling them as θ, in the state $|\theta\rangle$, and all the other particles from that system as α, our system is thus in the state:

$$\sum_{I,k,\theta,\alpha} \phi(k) |\theta,\alpha\rangle \langle\theta,\alpha| V |kI\rangle_{AT} |I\rangle_B . \tag{3.6}$$

Defining now $V_{kI}^{\theta,\alpha} \equiv \langle\theta,\alpha| V |kI\rangle$, (3.6) becomes

$$\sum_{I,k,\theta,\alpha} \phi(k) V_{kI}^{\theta,\alpha} |I\rangle_B |\theta,\alpha\rangle . \tag{3.7}$$

Alice then measures θ, obtaining a specific result which she then sends to Bob, who then acts on **B** with a unitary operator Z^θ, which bijectively depends on θ, obtaining $|\phi\rangle$ as a result. The paper studies how to choose Z^θ in order to minimize the time between sending and receiving $|\phi\rangle$, but here we will just focus on the protocol. We therefore jump directly to the necessary operator Z^θ, which minimizes the time complexity:

$$Z^\theta = U^\dagger(t_*) \left(\sum_\gamma V_{I,j}^{\theta,\gamma} V_{\gamma\beta}^\dagger \right) U(t_*) . \tag{3.8}$$

3.3 Consequences of ER=EPR, wormhole dynamics, electromagnetic wave equation and photon energy-momentum tensor

Even if a wormhole teleportation protocol exists, it is still necessary for a wormhole connecting two particles as a quantum entanglement (and thus serving as a bridge for information from one particle to affect the other as claimed in [5]) to either be traversable or to allow information in its interior to affect its exterior. We prove this qualitatively:

Claim 1. A wormhole connecting two particles that are entangled is either traversable or lets information permeate, supposing ER=EPR holds.

Proof. If we suppose that every quantum entanglement is an instance of a wormhole, and that the influence of the measurement of one of the connected systems on the value taken by the other is in fact just an information transfer through that wormhole connecting both systems, then this would either mean that such a wormhole is traversable, or that the information inside a wormhole can have observable influences on the outside of the wormhole, in order for the information to affect the second particle. ■

We explore here and in Appendices A and B the possibility that the incoming information changes the metric if ER=EPR is valid, which raises the question about the validity of the no-hair development. To this end, we will study the particular case of an incoming photon moving towards a Schwarzschild black hole in the original (t, r, θ, ϕ) coordinate system, calculating the energy-momentum produced by a particular solution to the electromagnetic wave-equation in curved spacetime.

Finding the energy-momentum tensor

By Appendices A and B, in which we determine how to calculate the energy momentum tensor of our metric from the Faraday tensor for Appendix A and how to obtain the Faraday tensor by solving the electromagnetic wave equation in curved spacetime for Apendix B, we can determine the Faraday tensor from the metric and the electromagnetic potential A_μ:

$$F_{\mu\nu} = \nabla_\mu A_\nu - \nabla_\nu A_\mu = \partial_\mu A_\nu - \Gamma^\lambda_{\mu\nu} A_\lambda - \partial_\nu A_\mu + \Gamma^\lambda_{\nu\mu} A_\lambda \tag{3.9}$$

and since $A_\mu = g_{\mu\lambda} A^\lambda$, we can determine that all elements of $F_{\mu\nu}$ are 0 except for:

$$\begin{aligned} F_{tr} &= -F_{rt} = \partial_t A_r - \Gamma^t_{tr} A_t - \partial_r A_t + \Gamma^t_{rt} A_t = \partial_t A_r - \partial_r A_t \\ &= \partial_t \left(g_{rr} A^r \right) - \partial_r \left(g_{tt} A^t \right) \\ &= g_{rr} \partial_t A^r - \partial_r g_{tt} A^t - g_{tt} \partial_r A^t . \end{aligned} \tag{3.10}$$

After solving the wave equation, we get a spherically symmetric wave. Indeed, using (**??**), setting

$$f_3 = \left(\frac{\left(\partial_r f_1 f_2 + f_1 \partial_r f_2\right)(r - 2GM) + 2 f_2 f_1 (r - 2GM) - \frac{8G^2M^2\omega^2}{r^3}}{\left(f_2 f_1 (r - 2GM)^2 + \frac{4G^2M^2\omega^2}{r^2} \right)^2} + \frac{i\omega}{f_2 + \frac{4G^2M^2\omega^2}{f_1 (r-2GM)^2 r^2}} \right),$$

we get

$$\begin{aligned} F_{tr} = \int \Bigg[&- \frac{i\omega}{f_2 (r - 2GM) + \frac{4G^2M^2\omega^2}{f_1 (r-2GM) r^3}} \\ &+ \frac{i\omega 4G^2M^2}{f_2 f_1 r^2 (r - 2GM)^2 + 4G^2M^2\omega^2} \\ &+ i\omega 2GM \left(1 - \frac{2GM}{r}\right) f_3 \Bigg] \tilde{J}^r e^{i(kr - \omega t)} \mathrm{d}k \, \mathrm{d}\omega . \end{aligned} \tag{3.11}$$

We can see that F_{tr} is non-zero.

From this, we get, with $F^{\mu\nu} = g^{\mu\alpha} g^{\nu\beta} F_{\alpha\beta}$, the energy-momentum tensor generated by the particular photon producing the electromagnetic potential **??** in the Schwarzschild metric:

$$T_{\mu\nu} = \begin{pmatrix} -\frac{3}{2}\left(1 - \frac{2GM}{r}\right) F_{tr}^2 & 0 & 0 & 0 \\ 0 & \frac{3}{2} \frac{1}{\left(1 - \frac{2GM}{r}\right)} F_{tr}^2 & 0 & 0 \\ 0 & 0 & \frac{1}{2} r^2 F_{tr}^2 & 0 \\ 0 & 0 & 0 & \frac{1}{2} r^2 \sin^2\theta F_{tr}^2 \end{pmatrix}, \tag{3.12}$$

which has elements that are non-zero. Therefore, we can conclude that the incoming photon indeed has an effect on the metric.

We must stress that this result is interesting, as this seems to help substantiate the claim that an object entering a wormhole changes its metric. The case with a photon is very particular as it does not directly contradict the no-hair theorem, which states that the only parameters affecting the metric of a black hole are its mass, angular momentum and charge. As the photon carries angular momentum, this should be what affects the metric. More work is needed to see if, for photons or massive objects, the change in the metric can be directly related to the mass, charge and angular momentum of the incoming object, or if there is other information affecting it. We could even go a bit further and imagine that the change in the metric is uniquely determined by the information of the infalling object, which would lead to another protocol for wormhole teleportation than that of [5]. And even if the metric remains unaffected by the information, with Claim 1, we have established that certain wormholes are either traversable or let information permeate if ER=EPR holds, meaning that that can also be used for teleporting information (say the spin of a particle).

Further Developments

Although we did not solve Einstein's equation in order to see how exactly the metric changes, we think that the result might be worth studying. We expect the metric of the wormhole to change uniquely with respect to the information sent in, but to do this we would need to solve Einstein's equation using (3.12) as the energy-momentum tensor to determine the new metric. We also want to point out that we have used here the Schwarzschild metric in the original coordinate system, which only properly describe the metric outside the black hole. This is probably useful to determine how a photon inside might affect the metric outside, but we also think that studying this in the Kruskal-Szekeres coordinates is probably better. Additionally, the Schwarzschild black hole is not a good contender for a wormhole connecting two entangled particles, hence we would need to study different types of black holes/wormholes for better results.

It is also worth noting that a change in the metric is not the only possible explanation for information permeability. black hole complementarity might be a good candidate, or maybe even Hawking radiation. Traversable wormholes would also let information permeate for obvious reasons. Finally, we must also consider the possibility that ER=EPR does not hold.

4 Conclusion

We have reviewed the basics of quantum teleportation and of wormholes, and subsequently one of the implications of the claim ER=EPR, that is that a wormhole and a quantum entanglement are the same object, namely how, analogously to quantum teleportation, wormholes could be used to teleport information. We have also determined that certain wormholes have to be either traversable or at the very least let the information stored inside somehow affect the outside in an observable way. We have advanced the claim that the information might change the metric at the receiving end of the wormhole, and have started to explore this path. Unfortunately, we were only able to obtain the energy-momentum tensor, without being able to either solve Einstein's equation or obtaining it in the Kruskal-Szekeres coordinate system.

We have only started exploring one of the possible ways information swallowed by one throat of a wormhole might affect the other end in an observable way. Other ways that could be explored would be black hole complementarity [13] for example. Several papers, such as [14] and [15] have established theoretical frameworks in which traversable wormholes are possible, and it would be interesting to examine if such a wormhole might be a good candidate for the usual quantum entanglement.

Acknowledgments

I would like to thank my supervisor, Prof. Keshav Dasgupta, without whose supervision and support this work would not have been possible.

References

1. Einstein A, Podolsky B, Rosen N. Can Quantum-Mechanical Description of Physical Reality be Considered Complete? Physical Review. 1935 may;47(10):777–780. DOI: 10.1103/physrev.47.777.

2. Ludwig Flamm. Republication of: Contributions to Einstein's theory of gravitation. General Relativity and Gravitation. 2015 may;47(6). DOI: 10.1007/s10714-015-1908-2.

3. Maldacena J, Susskind L. Cool horizons for entangled black holes. Fortschritte der Physik. 2013 aug;61(9):781–811. DOI: 10.1002/prop.201300020.

4. Charles H Bennett, Gilles Brassard, Claude Crépeau, Richard Jozsa, Asher Peres, William K Wootters. Teleporting an unknown quantum state via dual classical and Einstein-Podolsky-Rosen channels. Physical Review Letters. 1993 mar;70(13):1895–1899. DOI: 10.1103/physrevlett.70.1895.

5. Susskind L, Zhao Y. Teleportation through the wormhole. Physical Review D. 2018 aug;98(4). DOI: 10.1103/PhysRevD.98.046016.

6. Bohm D, Aharonov Y. Discussion of Experimental Proof for the Paradox of Einstein, Rosen, and Podolsky. Physical Review. 1957 nov;108(4):1070–1076. DOI: 10.1103/physrev.108.1070.

7. Bell JS. On the Einstein Podolsky Rosen paradox. Physics Physique. 1964 nov;1(3):195–200. DOI: 10.1103/physicsphysiquefizika.1.195.

8. Carroll S. Spacetime and geometry : an introduction to general relativity. San Francisco: Addison Wesley; 2004.

9. Einstein A. Die Grundlage der allgemeinen Relativitaetstheorie. Annalen der Physik. 1916;354(7):769–822. DOI: 10.1002/andp.19163540702.

10. Hilbert D. Die Grundlagen der Physik. Nachrichten von der Gesellschaft der Wissenschaften zu Goettingen a Mathematisch-Physikalische Klasse. 1915;1915:395–408.

11. Schwarzschild K. Über das gravitationsfeld eines massenpunk-tes nach der einsteinschen theorie. Sitzungsberichte der Königlich Preußischen Akademie der Wissenschaften (Berlin. 1916:189–196.

12. George David Birkhoff REL. Relativity and Modern Physics. Harvard University Press; 1927. Available from: https://www.ebook.de/de/product/21911011/george_david_birkhoff_rudolph_ernest_langer_relativity_and_modern_physics.html.

13. Susskind L, Thorlacius L, Uglum J. The stretched horizon and black hole complementarity. Physical Review D. 1993 oct;48(8):3743–3761.

14. Maldacena J, Stanford D, Yang Z. Diving into traversable wormholes. Fortschritte der Physik. 2017 may;65(5):1700034. DOI: 10.1002/prop.201700034.

15. Maldacena J, Milekhin A. Humanly traversable wormholes. Physical Review D. 2021 Mar;103(6). Available from: http://dx.doi.org/10.1103/PhysRevD.103.066007.

Submitted: 01/13/2021

Research Article

[1]Department of Bioengineering, McGill University, Montreal, QC, Canada

Keywords

Mesenchymal stem cell; Liver disease; Cell delivery, Critical literature review

Email Correspondence

zhiyue.zhu@mail.mcgill.ca

Zhiyue Zhu[1]

Comparative analysis of delivery methods for stem cell therapy in liver diseases

Abstract

Background: Mesenchymal stem cell transplantation is an emerging therapy for treating acute and chronic liver diseases as an alternative for patients who are not transplant candidates. The potential of this treatment depends on its therapeutic efficiency and safety, which have been investigated and evaluated in both preclinical and clinical settings. However, there are still some risks associated with the delivery methods, such as low long-term retention rate and the possibility of arousing cancer or rejection.

Methods: During the review process, previous papers mentioning "stem cell treatment" and "liver diseases" were searched. We described different up-to-date approaches for stem cells from various origins to be delivered to the liver and compared respectively their pros and cons for clinical applications. We also proposed several potential techniques for future studies.

Summary: An efficient and safe stem cell delivery could be enabled via Alginate-Polylysine-Alginate (APA) microencapsulation, lipid-conjugated coating or the use of nanoparticles. Their efficacy will be improved through tissue engineering and microrobots as the delivery is sustained and targeted with fewer rejection responses.

Introduction

Acute and chronic liver injury, such as that arising from viral infection, alcohol abuse, metabolic disorders and toxins, can lead to liver cirrhosis or failure (1). Liver transplantation has been deemed the gold standard therapy for liver failure. However, the procedure still carries considerable risks and limitations. Donor organ supply shortage, graft failure, and severe transplant rejections make this an impractical option for many patients (2, 3).

Alternative approaches other than organ transplant have been pursued for decades before the advent of liver stem cells therapy. Regenerative therapy with granulocyte colony-stimulating factor (G-CSF) has become a lucrative option for improving transplant-free short-term survival by stimulating the proliferation and migration of bone marrow stem cells (4, 5). However, most clinical trials on G-CSF have been conducted without adequate knowledge on the pathway that promotes quantity and durable restoration of existing healthy hepatocytes or regeneration and formation of new liver cells (4). Thus, the potential risks regarding the utility of G-CSF in treating patients with liver diseases remain unclear. On the other hand, prosperous studies on transplantation of engineered mesenchymal stem cells have shown promising results in preclinical and clinical experiments, which could offer a potentially unlimited source of cells for hepatocytes (6). MSC therapy for liver has been shown to be effective via their immunomodulation, differentiation, and anti-fibrosis properties. Though, it is noticeable that stem cell therapy in liver failure is not yet standardized, as every laboratory has their own methods, in terms of the type of cells and delivery mechanisms.

In this review, we highlight the current findings from peer-reviewed journals on various stem cell delivery methods, which have ensured an efficient stem cell accumulation in liver for clinical treatments according to previous studies (1-3, 6). Some possible modifications could further increase the safety of liver pathology therapy by lowering immune rejection or inflammation.

Available Approaches

We summarized and examined currently available approaches for liver stem cell therapy published in precious academic journals.

Artificial Cell Microencapsulation

In 1957, Chang invented artificial cells which are ultra-thin polymer membrane microcapsules that can encapsulate various materials (7). The team showed that microencapsulation can immobilize stem cells to provide a favorable microenvironment for stem cells survival and functioning, as well as make the stem cells immuno-isolated after transplantation (8-10). Bone marrow stem cells (BMCs) were flushed out from the femurs of Wistar rats; hepatocytes were isolated and collected from the rat's liver (8-10). Alginate-Polylysine-Alginate (APA) encapsulation method was used to encapsulate the BMCs and hepatocytes (9, 10). This method led to cross-linking of anionic alginate with cationic poly-L-lysine (PLL) which allows a more controlled pore size of the microcapsules (11). This enables the controlled release of cell secretions from the microcapsule.

The microbeads of microscopic dimensions (less than 2 mm in diameter) can provide a high surface-to-volume ratio, which allows for good mass transfer of oxygen and nutrients as the theoretical diffusion across a membrane is proportional to the total surface area and inversely proportional to its membrane thickness (12). This ensures cell viability, while also acting to protect the cells from immune-rejection (7). In particular, hepatocytes have been shown to maintain 65% viability at Day 28 when co-cultured or co-encapsulated with bone marrow cells compared to 18% viability at Day 28 for hepatocyte in single encapsulation (8). Chang et al. and Zhang et al. proposed that the preservation of hepatocyte functions seemed to be dependent on cell-cell contact interactions. Transplanted stem cells will produce cytokine and secrete several potentially beneficial growth factors, such as the hepatocyte growth factor (HGF). HGF is an important factor in liver regeneration and stimulating the transdifferentation of BMCs into hepatocytes (13, 14). Hepatic stimulatory substance (HSS) released from free or microencapsulated hepatocytes can pass through the APA membrane to stimulate the remnant liver to regenerate (10, 15, 16). The most promising application of this technique is in acute liver failure such as hepatic coma, as it can provide immediate liver support (17). These bioencapulated BMCs could be retained in the peritoneal cavity such that secreted HGF is drained into the portal circulation to reach the liver, compared to free BMCs which will be rapidly removed from the peritoneal cavity; this may contribute to the higher efficiency of microencapsuled BMCs than the free ones (10).

The application of stem cell encapsulation is promising from these preliminary results. However, some challenges stop the technology to deliver its promise. The first contact of the capsule with the host could elicit

host immune response and cells in capsules might produce proteins that can provoke inflammatory responses in immune cells (7, 18). Research shows that this is because the thin and poorly formed membrane in the standard method allowed cells to be protruded and entrapped within the micro-capsular membrane matrix (19). These cells might activate rejection from body and degradation enzymes might be released from activated leukocytes of lysing cells, which can further accelerate the erosion of micro-capsular membrane (19, 20). These problems have now been solved by the use of a novel two step method of preparation resulting in membrane that does not allow the entrapment or protrusion of cells across the membrane (20).

Lipid-conjugated Heparin Coating

For acute liver failure (ALF) arising from acetaminophen (APAP) overdose, Hwang et al. investigated on the therapeutic effects of human adipose-derived stem cells (hADSCs), which could recover the metabolic rates of the liver cells to over 60% after one-day treatment (21). An enhanced delivery and longer retention of the cells was enabled by applying coating of lipid-conjugated heparin; the coating of lipid-conjugated heparin on hADSCs also enhanced the anti-inflammatory effects on the damaged liver to increase the recovery efficiency (21-23).

Many ALF patients with APAP overdose develop infectious complications with inflammatory response that can progress to multi-organ failure (24). hADSCs are a promising candidate to treat APAP liver injury as their secretomes have therapeutic effects by enhancing hepatocyte regeneration and inhibiting liver stress and inflammatory signaling (21-23). To increase the delivery and engraftment efficiency of the administered cells to the target tissue, cell surface engineering that decorates a target-oriented ligand on the cell surface, has been employed (25-27). It was reported by Tae et al. that the cell surface of hADSCs can be engineered with lipid-conjugated heparin (28). Heparin is an anionic glycosaminoglycan which has many distinct bioactivities including anticoagulant activity, immune suppression activity, and strong binding affinity hADSCs (29). Therefore, the interaction between heparin and cell membrane will contribute to the coating of it across the cell surface. However, free heparin itself did not induce stable coating on hADSCs (28). Thus, lipid-conjugation to heparin was necessary to induce the effective presence of heparin on the cell membrane. Sinusoid capillary structures within the liver are abundant with heparin receptors Stabilin on cell membrane, and this increases the amount of trapped heparin-coated ADSCs on the capillary wall, which might provide more chances for the cells to migrate into the parenchyma parts of liver from bloodstream (30-32).

For the synthesis of lipid-conjugated heparin, carboxyl-group activated heparin dissolved in deionized water (DIW) was mixed with the 1, 2-Dipalmitoyl-sn-glycero-3-phosphoethanolamine (DPPE) lipid solution at 65 °C, and the mixture was then incubated for 20 h. Heparin was modified using its carboxylate group to ensure sufficient contact of the heparin (hydrophilic with a highly negative charge from sulfate groups) with the hydrophobic lipid (33). The obtained lipid-conjugated heparin was then added into human ADSCs (with 100% confluency) seeded one day prior to heparin coating at 250 μg/ml in 1% (v/v) fetal bovine serum (FBS). The harvested heparin-coated cells were intravenously injected to mice through the tail vein. Distinct changes in biodistribution by heparin coating could be seen with an increased accumulation of ADSCs in the liver (1.8 times more) and a reduced accumulation of the cells in the lung (59% less) compared to the control group with uncoated ADSCs (28). A 2.4-fold increase in heparin-coated ADSCs was also observed in the spleen of the mice. As spleen has been used as alternative cell transplantation site to treat acute and chronic liver diseases, this accumulation of ADSCs in spleen could also provide better therapeutic effects (28).

Therefore, lipid-conjugated heparin coating on hADSCs might function to enhance the therapeutic effect of intravenously administered stem cells on liver diseases as cytokines or growth factors are secreted from the delivered hADSCs. This helps to recover the liver injury by improving liver tissue regeneration (21). The coating of lipid-conjugated heparin on hADSCs also enhanced the anti-inflammatory effects on the damaged liver (34). Despite the advantages of heparin-coated ADSCs to treat ALF, their benefits might not be applied successfully to other chronic liver diseases due to the relatively low retention rate (50% remaining after four days) of the stem cells (21). This might result from the lack of supporting matrix after hADSCs are trapped in liver (35). In addition, ALF might cause high oxidative stress (36), leading to an alteration or loss of stem cell functions (37). Unfortunately, heparin coating might not be efficient enough for antioxidant effects, which probably requires genetic modification of the stem cells such as overexpressing miR-210 (37, 38). From the work of Xu et al., MSCs transfected with agomiR-210 were exposed to H2O2 in vitro, which induces MSC apoptosis via oxidative stress, but miR-210 overexpression could attenuate the c-Met activity repression induced by H2O2, alleviate accumulation of ROS, as well as decrease the apoptosis rate of MSCs in H2O2 (41.52% less than non-modified MSCs (37). This indicated their antioxidant effects. However, in vivo research has not been continued, and thus the antioxidant effects of miR-210 mutations in liver disease environments may require further investigation.

Nanoparticles

Nanoparticles are nanosized structures in which at least one of its phases has a dimension ranging from 1 to 100 nm. Magnetic nanoparticles with paramagnetic characterization because of the unpaired electrons have been used in stem cell therapy for stem cell homing and tracking in the attempts of treating liver diseases (39).

MSCs homing is the delivery process of the cells to the site of injury, but its mechanism is not totally understood yet (40). There are different factors that are thought to affect this process, such as the expression of homing regulating molecules C-X-C chemokine receptor 4 (CXCR4) and Stromal cell-derived factor 1 (SDF1) (41). Yu Meng and his team showed that MSCs labelled with super-paramagnetic iron oxide nanoparticles (SPIONs) lead to efficient homing in vivo when exposed to an external magnetic field (EMF) generated by permanent magnets (42). In Yu Meng's experiment, Wharton's Jelly-derived MSCs (WJ-MSCs) were transfected using SPIONs with a final concentration of 25 μg/mL, and the labelled MSCs were hypodermically injected (hypodermis) in mice. By applying an external magnetic field (0.5 T, 1.5 cm away from the tissue, 6h/day), the direct movement of magnetized cells to the target tissues was accelerated with a significant reduction in displacement, area and signal-to-noise ratio (SNR) parameters by more than 50% (42). Yun et al. suggested that these SPIONs would not affect MSCs properties such as viability, proliferation and differentiation in vitro and in vivo in short-term experiments. Via the internalization of rhodamine B (IRBs) in SPIONs, it also showed an increase in CXCR4 as the nanoparticles stimulated the signaling receptor of CXCR4-SDF1 axis, which is essential in MSCs' homing (43).

In vivo stem cell tracking and visualization of the transplanted stem cell is an essential means for monitoring their tissue localization (39). MRI has the utility to track the homing and trajectory of SPION-labelled MSCs in the liver (44). This can help to predict the therapeutic potential of certain treatment since the success of cell therapy will depend on the local availability of stem cells for tissue. The combination of iron oxide nanoparticle along with MRI provides a means to deliver cells and immediately verify whether the cells have indeed grafted within the target organ (45).

Beyond the application of magnetic nanoparticles for MSC homing and tracking, there is also administration of other nanoparticles to increase the efficiency of stem cell delivery by lowering the possible inflammation. IL-1-induced intracellular signaling pathway could be blocked by IL-1Ra, and this will exhibit an anti-inflammatory effect. As shown previously, MSCs are promising in treating ALF by transdifferentiating into hepatocytes. Consequently, the co-administration of IL-1Ra with MSC transplantation has great potential of effectively treating ALF, as well as maintaining MSCs' functions against oxidative stress (36, 46). However, due to the high cost and short biological half-life of IL-1Ra, its clinical application is seriously restricted (47). Xiao et al. proposed the use of IL-1Ra loaded in lactosylated chitosan nanoparticles instead of using large dose of IL-1Ra directly. FITC-1L-1Ra lactosylated chitosan nanoparticles were prepared by dissolving lactose acyl chitosan in diluted acetic acid solution (0.3 mg FITC and a small amount of polyethylene oxide [PEO]) (46). Lactose acyl group on chitosan surface could specifically target the nanoparticles to hepato-

cytes, and this could be observed as concentration of IL-1Ra in liver tissue (147.15 pg/ml) was significantly higher than that in serum (25.65 ± 9.59 pg/ml), kidney (42.65 ± 9.79 pg/ml), and heart (46.58 ± 10.18 pg/ml). IL-1Ra will be released from biocompatible and biodegradable chitosan through self-diffusion, therefore, the time of drug release and effect will be significantly extended (48). IL-1Ra chitosan nanoparticles thus can not only lower the cost using IL-1Ra via controlled drug release but also show significant liver targeting ability via employing lactose acyl on chitosan surface. Combined therapy with IL-1Ra chitosan nanoparticles and MCS transplantation exhibited great synergistic effects for ALF treatment through suppression of inflammation for a period of time with 200% extension, and this can significantly improve the survival rate of transplanted cells. In addition, this therapeutic strategy can promote hepatocyte proliferation (46).

The implementation of nanoparticles in stem cell therapy has a great effect in enhancing the efficiency of stem cell-based liver diseases treatment, however, the relatively short duration of investigation might not be sufficient to conclude the long-term effects of magnetic field and nanoparticles on the viability and differentiation potential of the labelled MSCs (42). Nevertheless, experimental settings as the concentration of nanoparticles and the strength of the applied EMF are not standardized, which requires further research to allow the optical therapy effects.

Comparison and Summary

The basic principle, method, advantages and disadvantages of each aforementioned approach is compared and summarized in **Table 1**.

efficiency and safety, as well as solve some risks associated with using stem cell treatments. For example, tissue engineering and microrobots allowed a more sustained and targeted cell delivery to liver.

Tissue Engineering

Tissue engineering has been a promising technique to promote stem cell homing by providing a bioactive material scaffold and include some necessary biochemical signals within the structure. Hydrogels could serve the purpose of extracellular matrices (ECMs) which assist in cell adhesion, proliferation, and differentiation.

Das et al. developed a 3D bioprinting tissue analog using silk fibroin-gelatin (SF-G) bioink encapsulating tissue-derived mesenchymal progenitor cells (50). The hydrophobic interaction of silk fibroin macromolecules could be altered by tyrosinase and sonication, which changes the crosslinking of the hydrogel. The effect of optimized rheology and other printing parameters were assessed to achieve maximum cell viability and multilineage differentiation of the encapsulated hMSCs. Lee et al. and his team showed that by including hepatocytes within the bioink, the survivability and functionality of HCs could also help with the transdifferentiation of stem cells (51).

Xu et al. transplanted mouse ADSC-seeded and BMSC-seeded regenerated silk firoin (RSF) electrospun matrix on the injured liver surface of a mice (35). RSF scaffolds were excellent in biological effect and biocompatibility; the degradation products of RSF are amino acids that could be conducive to cell growth, which make RSF an effective biomaterial for liver regenera-

Table 1 Liver diseases that can be treated with stem cell therapy and the applied delivery technique

Method	Role	Disease	Advantages	Disadvantages	Author
APA membrane microencapsulation	APA encapsulation for BMCs and hepatocytes to maintain a longer viability of hepatocytes. BMCs secrete HGF for liver regeneration and transdifferentiate into hepatocytes within the capsule	Acute liver failure Ex: Hepatic coma	a. Provide a favorable environment for stem cells survival and function b. Recovered easily c. Prevent immuno-rejection	Applicable for liver regeneration especially for short-term uses	Chang et al. (7-10, 12, 15-17, 19, 20, 49)
Lipid-conjugated heparin coating	Lipid-conjugated heparin can interact with hACSCs' cell membrane and be recognized by liver capillary receptor to ensure efficient stem cell delivery	APAP-induced acute liver failure	a. Could be recognized by Stabilin receptors on the liver capillary to ensure a higher distribution of stem cells in liver b. Heparin also has anti-inflammatory effects, which enhance the liver disease treatment	a. Low retention rate for long-term treatment due to lack of support matrix b. Cannot withstand oxidative stress	Hwang et al. (21, 33) Kim et al. (28, 29)
Nanoparticles	Magnetic SPIONs used for stem cell homing by applying external magnetic field and tracking by using MRI	Diverse liver diseases Ex: liver fibrosis, liver cirrhosis and liver cancer	a. SPIONs with EMF can enhance homing b. MRI and nanoparticle can monitor stem cell trajectory to target	a. Unknown long-term effects of magnetic fields and SPIONs on MSCs b. Design setting not optimized	Meng et al. (42) Bos et al. (45)
	IL-1Ra chitosan nanoparticles used to exhibit extra anti-inflammatory effects and protect MSCs from oxidative stress	Acute liver failure	a. Cost efficient for controlled release of IL-1Ra, which also helps with ALF treatment b. Lactosylated chitosan could specifically target the NPs to target	Unsure long-term effects of IL-1Ra and chitosan on MSCs' viability and functions	Xiao et al. (46)

Perspectives

In this section, we propose some intriguing techniques that have the potential to be incorporated with stem cell therapy to improve the delivery

tion. MSCs also exhibited good interaction with RSF and differentiated to hepatocyte-like cells in vitro. The transplanted stem cells could remain in tissue for up to 30 days and have been proved to lead to an improved recovery of the liver (35). This technique could enhance the retention rate of stem cells at the target for long-term treatments, but the requirement of an

open surgery renders it less attractive than minimally invasive treatment.

Microrobots

Magnetically actuated microrobots could facilitate cell/drug delivery in fluidic environments; due to their small size and wireless control, microrobots undergo littler distortion or attenuation in the body. Thus, they have several advantages as medical treatments, such as reduced pain, risk of infection, and trauma (52). If stem cells are transported via microrobots, cell function could be preserved by the devices; these cell-loaded microrobots can be guided toward some hard-to-reach tissue or human cavities, making various medical treatments possible (53). Therefore, fewer cells are needed, which lower the possible host immune response due to cytokine production.

Jeon et al. developed a biocompatible porous 3D microrobots and assessed their feasibility for delivery of stem cells in 3D culture using magnetic locomotion (52). With different shape designs, the microrobots exhibited different motions upon application of a rotating magnetic field: for spherical microrobot, it would be a rolling motion; for a helical microrobot, it would be a corkscrew motion. These designs showed higher propulsion efficiencies for a precise targeting of the transplanted stem cells. The porosity of the 3D scaffold could be customized by laser lithography; pore size of 15 μm was chosen to fit the size of stem cell, and nickel and titanium layers were deposited to increase the model's biocompatibility. Human stem cells could then be cultured within the microrobots. By applying an external magnetic field (EMF), the devices have shown precise movements along the direction of the applied magnetic field gradient. Real-time visualization and localization are required for a more accurate in vivo manipulation of the microrobots. In addition, the recycle of microrobots is another problem as this might arouse rejection response from body.

To reduce the potential immune activation and thrombi formation, degradable materials PEG diacrylate (PEGDA) were used to fabricate the microrobots (54). The degradation and swelling of the microrobot will help the cells to passively detach from the device surface. PA imaging was used to visualize the microrobots with a penetration depth reaching 2 cm to achieve a precise delivery of therapeutic cells. The penetration depth may not be optimal for stem cell transplantation in deep tissue; therefore, alternative tracking systems should be investigated. Similar to the use of magnetic nanoparticles, the effects of EMF on the functions of these stem cells need further research.

Comparison and Summary

The basic principle, advantages and disadvantages of each promising technique is compared and summarized in **Table 2**.

Conclusion

Many studies have been conducted to ensure an efficient and safe delivery of stem cells, including microencapsulation with APA membrane, lipid-conjugated heparin coating and administration of nanoparticles. They have shown promising results to treat both acute and chronic liver diseases. However, several concerns remain, regarding the poor long-term cell retention rate, and the risk of host rejection. We proposed several techniques to enhance the delivery efficacy. By including a 3D matrix, we could enhance cell homing and support long-term treatment. Tracking and targeted delivery could be achieved with degradable magnetic microrobots when applying external magnetic fields and MRI.

MSCs delivery should be easy to perform, less invasive, with limited side effects and high stem cell survival. It should also be capable of having a live tracking of the delivery process. Among the various potential modalities for stem cell delivery in liver disease as discussed in this review, each approach has its own peculiarities, so the choice of the modality should be based on the clinical settings. When the corresponding issues for those methods have been addressed, an optimal approach integrating stem cell biology, gene therapy, tissue engineering, and transplant medical devices can be pursued. This will lead to better treatment for liver diseases like ACLF, HBV reactivation with immunosuppression and alcoholic hepatitis, especially for patients who are in liver failure but are not transplant candidates.

References

1. Sharma A, Nagalli S. Chronic Liver Disease. StatPearls. Treasure Island (FL): StatPearls Publishing Copyright © 2020, StatPearls Publishing LLC.; 2020.

2. Burki TK. Liver disease in Canada: the scale of the problem. The Lancet Gastroenterology & Hepatology. 2020;5(2):114-5.

3. Liu C-L, Soong R-S, Lee W-C, Chen D-H, Hsu S-H. A predictive model for acute allograft rejection of liver transplantation. Expert Systems with Applications. 2018;94:228-36.

4. Philips CA, Augustine P, Ahamed R, Rajesh S, George T, Valiathan GC, et al. Role of Granulocyte Colony-stimulating Factor Therapy in Cirrhosis, 'Inside Any Deep Asking Is the Answering'. J Clin Transl Hepatol. 2019;7(4):371-83.

5. Meng F, Francis H, Glaser S, Han Y, DeMorrow S, Stokes A, et al. Role of stem cell factor and granulocyte colony-stimulating factor in remodeling during liver regeneration. Hepatology. 2012;55(1):209-21.

6. Dahlke MH, Popp FC, Larsen S, Schlitt HJ, Rasko JE. Stem cell therapy of the liver--fusion or fiction? Liver Transpl. 2004;10(4):471-9.

Table 2 Promising techniques to enhance stem cells delivery efficiency and safety

Method	Role	Advantages	Disadvantages	Author
Tissue engineering	Promote stem cell homing by providing a scaffold and include some biochemical signals Generate a matrix to be transplanted in tissue where stems cells are seeded	a. Increase differentiation efficiency with the mechanical support from the biomaterials and inclusion of certain growth factors b. Increase stem cell retention rate for long-term treatment	May require an open surgery to transplant the scaffold or tissue	Das et al. (50) Xu et al. (35)
Microrobots	Magnetic SPIONs used for stem cell homing by applying external magnetic field and tracking by using MRI	a. Ensure a target transport of stem cells with externally applied magnetic fields b. Could monitor the cell movements by MRI and other visualization techniques c. Lower the number of stem cells required to reach therapeutic effects, and this decreases the potential of host rejection response	The effects of the microrobots materials and applied external fields on stem cell viability are unknown	Jeon et al. (52) Wei et al. (54)

7. Chang TM. Therapeutic applications of polymeric artificial cells. Nat Rev Drug Discov. 2005;4(3):221-35.

8. Liu Z, Chang TM. Effects of bone marrow cells on hepatocytes: when co-cultured or co-encapsulated together. Artif Cells Blood Substit Immobil Biotechnol. 2000;28(4):365-74.

9. Wong H, Chang TM. Bioartificial liver: implanted artificial cells microencapsulated living hepatocytes increases survival of liver failure rats. Int J Artif Organs. 1986;9(5):335-6.

10. Liu ZC, Chang TMS. Transdifferentiation of bioencapsulated bone marrow cells into hepatocyte-like cells in the 90% hepatectomized rat model. Liver Transplantation. 2006;12(4):566-72.

11. Orive G, Tam SK, Pedraz JL, Hallé JP. Biocompatibility of alginate-poly-L-lysine microcapsules for cell therapy. Biomaterials. 2006;27(20):3691-700.

12. Chang TMS. ARTIFICIAL CELL evolves into nanomedicine, biotherapeutics, blood substitutes, drug delivery, enzyme/gene therapy, cancer therapy, cell/stem cell therapy, nanoparticles, liposomes, bioencapsulation, replicating synthetic cells, cell encapsulation/scaffold, biosorbent/immunosorbent haemoperfusion/plasmapheresis, regenerative medicine, encapsulated microbe, nanobiotechnology, nanotechnology. Artificial Cells, Nanomedicine, and Biotechnology. 2019;47(1):997-1013.

13. Zhang Y, Chen X-M, Sun D-L. Effects of coencapsulation of hepatocytes with adipose-derived stem cells in the treatment of rats with acute-on-chronic liver failure. The International journal of artificial organs. 2014;37(2):133-41.

14. Banas A, Teratani T, Yamamoto Y, Tokuhara M, Takeshita F, Osaki M, et al. IFATS collection: in vivo therapeutic potential of human adipose tissue mesenchymal stem cells after transplantation into mice with liver injury. Stem Cells. 2008;26(10):2705-12.

15. Kashani SA, Chang TMS. Release of Hepatic Stimulatory Substance from Cultures of Free and Microencapsulated Hepatocytes: Preliminary Report. Biomaterials, Artificial Cells and Artificial Organs. 1988; 16(4):741-6.

16. Kashani SA, Chang TMS. Effects of Hepatic Stimulatory Factor Released from Free or Microencapsulated Hepatocytes on Galactosamine Induced Fulminant Hepatic Failure Animal Model. Biomaterials, Artificial Cells and Immobilization Biotechnology. 1991;19(3):565-77.

17. Chang TM. Haemoperfusions over microencapsulated adsorbent in a patient with hepatic coma. Lancet. 1972;2(7791):1371-2.

18. Paredes Juárez GA, Spasojevic M, Faas MM, de Vos P. Immunological and Technical Considerations in Application of Alginate-Based Microencapsulation Systems. Frontiers in Bioengineering and Biotechnology. 2014;2(26).

19. Wong H, Chang T. The Microencapsulation of Cells Within Alginate Poly-L-Lysine Microcapsules Prepared with the Standard Single Step Drop Technique: Histologically Identified Membrane Imperfections and the Associated Graft Rejection. Biomaterials, Artificial Cells and Immobilization Biotechnology. 1991;19(4):675-86.

20. Wong H, Chang T. A Novel two Step Procedure for Immobilizing Living Cells in Microcapsules for Improving Xenograft Survival. Biomaterials, Artificial Cells and Immobilization Biotechnology. 1991;19(4):687-97.

21. Hwang Y, Kim JC, Tae G. Significantly enhanced recovery of acute liver failure by liver targeted delivery of stem cells via heparin functionalization. Biomaterials. 2019;209:67-78.

22. Kapur SK, Katz AJ. Review of the adipose derived stem cell secretome. Biochimie. 2013;95(12):2222-8.

23. Salomone F, Barbagallo I, Puzzo L, Piazza C, Li Volti G. Efficacy of adipos tissue-mesenchymal stem cell transplantation in rats with acetaminophen liver injury. Stem Cell Res. 2013;11(3):1037-44.

24. Fontana RJ. Acute liver failure including acetaminophen overdose. Med Clin North Am. 2008;92(4):761-viii.

25. Stephan MT, Irvine DJ. Enhancing Cell therapies from the Outside In: Cell Surface Engineering Using Synthetic Nanomaterials. Nano Today. 2011;6(3):309-25.

26. Abbina S, Mohtaram NK, Kizhakkedathu JN. Cell Surface Engineering. In: Jafar Mazumder MA, Sheardown H, Al-Ahmed A, editors. Functional Biopolymers. Cham: Springer International Publishing; 2018. p. 1-42.

27. Lee JK, Choi IS, Oh TI, Lee E. Cell-Surface Engineering for Advanced Cell Therapy. Chemistry – A European Journal. 2018;24(59):15725-43.

28. Kim JC, Tae G. The modulation of biodistribution of stem cells by anchoring lipid-conjugated heparin on the cell surface. Journal of Controlled Release. 2015;217:128-37.

29. Kim M, Kim YH, Tae G. Human mesenchymal stem cell culture on heparin-based hydrogels and the modulation of interactions by gel elasticity and heparin amount. Acta Biomaterialia. 2013;9(8):7833-44.

30. Harris EN, Baggenstoss BA, Weigel PH. Rat and human HARE/stabilin-2 are clearance receptors for high- and low-molecular-weight heparins. Am J Physiol Gastrointest Liver Physiol. 2009;296(6):G1191-9.

31. Mishima Y, Lotz M. Chemotaxis of human articular chondrocytes and mesenchymal stem cells. J Orthop Res. 2008;26(10):1407-12.

32. Ross MH, Pawlina W. Histology : a text and atlas : with correlated cell and molecular biology. 6th ed. ed: Philadelphia : Wolters Kluwer/Lippincott Williams & Wilkins Health; 2011.

33. Hwang SR, Seo D-H, Al-Hilal TA, Jeon O-C, Kang JH, Kim S-H, et al. Orally active desulfated low molecular weight heparin and deoxycholic acid conjugate, 6ODS-LHbD, suppresses neovascularization and bone destruction in arthritis. Journal of Controlled Release. 2012;163(3):374-84.

34. Mousavi S, Moradi M, Khorshidahmad T, Motamedi M. Anti-Inflammatory Effects of Heparin and Its Derivatives: A Systematic Review. Adv Pharmacol Sci. 2015;2015:507151-.

35. Xu L, Wang S, Sui X, Wang Y, Su Y, Huang L, et al. Mesenchymal Stem Cell-Seeded Regenerated Silk Fibroin Complex Matrices for Liver Regeneration in an Animal Model of Acute Liver Failure. ACS Applied Materials & Interfaces. 2017;9(17):14716-23.

36. McGill MR, Jaeschke H. Oxidative Stress in Acute Liver Failure. In: Albano E, Parola M, editors. Studies on Hepatic Disorders. Cham: Springer International Publishing; 2015. p. 199-214.

37. Xu J, Huang Z, Lin L, Fu M, Gao Y, Shen Y, et al. miR-210 over-expression enhances mesenchymal stem cell survival in an oxidative stress environment through antioxidation and c-Met pathway activation. Science China Life Sciences. 2014;57(10):989-97.

38. Lapenna D, Mezzetti A, de Gioia S, Ciofani G, Marzio L, Di Ilio C, et al. Heparin: does it act as an antioxidant in vivo? Biochem Pharmacol. 1992;44(1):188-91.

39. Fahmy HM, Abd El-Daim TM, Mohamed H, Mahmoud E, Abdallah EAS, Mahmoud Hassan FE, et al. Multifunctional nanoparticles in stem cell therapy for cellular treating of kidney and liver diseases. Tissue Cell. 2020;65:101371.

40. Sohni A, Verfaillie CM. Mesenchymal Stem Cells Migration Homing and Tracking. Stem Cells International. 2013;2013:130763.

41. Wynn RF, Hart CA, Corradi-Perini C, O'Neill L, Evans CA, Wraith

JE, et al. A small proportion of mesenchymal stem cells strongly expresses functionally active CXCR4 receptor capable of promoting migration to bone marrow. Blood. 2004;104(9):2643-5.
42. Meng Y, Shi C, Hu B, Gong J, Zhong X, Lin X, et al. External magnetic field promotes homing of magnetized stem cells following subcutaneous injection. BMC Cell Biol. 2017;18(1):24.

43. Yun WS, Choi JS, Ju HM, Kim MH, Choi SJ, Oh ES, et al. Enhanced Homing Technique of Mesenchymal Stem Cells Using Iron Oxide Nanoparticles by Magnetic Attraction in Olfactory-Injured Mouse Models. International Journal of Molecular Sciences. 2018;19(5):1376.

44. Faidah M, Noorwali A, atta H, Ahmed N, Habib H, Damiati L, et al. Mesenchymal stem cell therapy of hepatocellular carcinoma in rats: Detection of cell homing and tumor mass by magnetic resonance imaging using iron oxide nanoparticles. Advances in Clinical and Experimental Medicine. 2017;26:1171-8.

45. Bos C, Delmas Y, Desmoulière A, Solanilla A, Hauger O, Grosset C, et al. In vivo MR imaging of intravascularly injected magnetically labeled mesenchymal stem cells in rat kidney and liver. Radiology. 2004;233(3):781-9.

46. Xiao J-q, Shi X-l, Ma H-c, Tan J-j, Lin z, Xu Q, et al. Administration of IL-1Ra Chitosan Nanoparticles Enhances the Therapeutic Efficacy of Mesenchymal Stem Cell Transplantation in Acute Liver Failure. Archives of Medical Research. 2013;44(5):370-9.

47. Granowitz EV, Porat R, Mier JW, Pribble JP, Stiles DM, Bloedow DC, et al. Pharmacokinetics, safety and immunomodulatory effects of human recombinant interleukin-1 receptor antagonist in healthy humans. Cytokine. 1992;4(5):353-60.

48. Nishikawa M, Miyazaki C, Yamashita F, Takakura Y, Hashida M. Galactosylated proteins are recognized by the liver according to the surface density of galactose moieties. Am J Physiol. 1995;268(5 Pt 1):G849-56.
49. Liu ZC, Chang TMS. Artificial cell microencapsulated stem cells in regenerative medicine, tissue engineering and cell therapy. Adv Exp Med Biol. 2010;670:68-79.

50. Das S, Pati F, Choi Y-J, Rijal G, Shim J-H, Kim SW, et al. Bioprintable, cell-laden silk fibroin–gelatin hydrogel supporting multilineage differentiation of stem cells for fabrication of three-dimensional tissue constructs. Acta Biomaterialia. 2015;11:233-46.

51. Lee JW, Choi YJ, Yong WJ, Pati F, Shim JH, Kang KS, et al. Development of a 3D cell printed construct considering angiogenesis for liver tissue engineering. Biofabrication. 2016;8(1):015007.

52. Jeon S, Kim S, Ha S, Lee S, Kim E, Kim SY, et al. Magnetically actuated microrobots as a platform for stem cell transplantation. Science Robotics. 2019;4(30):eaav4317.

53. Li J, Esteban-Fernández de Ávila B, Gao W, Zhang L, Wang J. Micro/nanorobots for biomedicine: Delivery, surgery, sensing, and detoxification. Science Robotics. 2017;2(4):eaam6431.

54. Wei T, Liu J, Li D, Chen S, Zhang Y, Li J, et al. Development of Magnet-Driven and Image-Guided Degradable Microrobots for the Precise Delivery of Engineered Stem Cells for Cancer Therapy. Small. 2020;16(41):e1906908.

Born from a passion for science communication, the McGill Scientific Writing Initiative (MSWI) aims to help students navigate the intricacies of scientific texts in order to effectively convey scientific material to a variety of audiences. They strive to make science communication accessible to McGill students with efforts such as the SciComm Case Competition where teams of 2-4 students were tasked to research a creative topic pertaining to this year's theme of environment. The teams completed three writing prompts based on their research topic and were challenged to tailor their writing to target diverse audiences. The teams first wrote news articles, and then the top 11 finalists were asked to write children's books and literature reviews.

MSURJ is proud to collaborate with MSWI by publishing the following review from the 2021 SciComm Case Competition Symposium winning team.

Maya Willard-Stepan[1], Allie Fong[1], Yehia Sabaa[2]

Changing Climate Change: Examining efficacy of community based initiatives and micro-scale climate action

Review Article

[1]Faculty of Science, McGill University, Montreal, QC, Canada
[2]Department of Mathematics and Statistics, McGill University, Montreal, QC, Canada

Keywords

Community supported agriculture, local climate action plans, climate indicators

Email Correspondence

maya.willard-stepan@mail.mcgill.ca
alexandra.fong@mail.mcgill.ca
yehia.sabaa@mail.mcgill.ca

Abstract

It is well established that global warming surpassing 1.5-2°C above pre-industrial levels will cause irreversible damage to our world. The adverse rise in global temperatures is accelerated by anthropogenic activity such as greenhouse gas emissions and environmental degradation. While certain scenarios have been projected to significantly lower global warming rates, most of these developments will require immediate global top-down policy shifts. Several international treaties and agreements have been created to combat climate change. Nonetheless, these remain ineffective at creating meaningful progress and cast doubt on how realizable a positive climate scenario is.

In this review, we analyze how regional policies and actions combat the climate crisis by examining how specific community initiatives impact climate indicators such as reforestation, greenhouse gas emissions reduction, and sustainable agriculture. Our findings conclude that local initiatives have shown more immediate success compared to their global counterparts. Thus, additional locally led climate initiatives is warranted.

Introduction

Climate change is a crisis associated with ocean acidification, ice field melting, mass extinction, desertification, and ecosystem collapse. Each of these effects will severely impact civilization and global ecosystems. While the impacts of the climate crisis are well established, understanding and implementing effective actions to prevent these events has proven challenging. The standard classical analysis of Rayleigh-Bénard convection uses the Boussinesq approximation, (9) in which variations in the density of the fluid are only accounted for in the buoyancy term, and thus the fluid is consider to be incompressible. This approximation requires low Mach-number and neglects acoustic frequencies. Work has been done to study the validity of the Boussinesq approximation in a compressible fluid in the context of the onset of convection, (10) which shows that it is only valid when the vertical dimension of the fluid is much less than any scale height. This implies that, in this context, the Boussinesq approximation will not hold at the spatial scales of the atmosphere.

For decades, scientists, philosophers, and economists have called upon decision makers to take action, but the response has been at best inconsistent and at worst regressive. Progressive results have could result from heavily sanctioning global emissions; however little guidance or motivation is present for policymakers below the international level. (1)

To mitigate climate change, nations have attempted to create legally binding policies that reduce environmentally harmful anthropogenic activities. In 2015, the United Nations drafted the first treaty calling to ratify international parties accounting for at least 55% of the world's annual greenhouse gas emissions. (2) The treaty's goal to avoid global warming of 1.5-2 °C above pe-industrial levels has made insufficient progress. (3) Although intergovernmental action is has led to little success, there are climate solutions which do not exist within the traditional climate scenario models.

Recently, small-scale actions intended to provide solutions to local effects have formed. Because the effects of climate change are most quickly felt by the individuals which live on land being impacted, these communities have two options: wait for national and international treaties to take effect, or choose to take action that incorporates knowledge of the local issue.

With the emergence of social movements and grass-root organizations, there is much debate as to whether small actions have a meaningful effect. If these actions are in fact effective, the first accessible and realizable climate scenario which avoids climate collapse appears. The following literature examines the efficacy of these movements by considering the effect of community-based initiatives on deforestation, CO2 emission policy, and sustainable agriculture.

Examining Impact

Community Initiatives and Combating Deforestation

Over the past several hundred years, the concentration of forested area across the globe has decreased dramatically. (4) A large portion of this loss can be attributed to increased human habitation and natural resource extraction. It has been demonstrated that large-scale deforestation directly impacts ecosystems through biodiversity loss, decrease in soil cycling, and pollution of freshwater systems. (5) Additionally, deforestation contributes significantly to the negative impacts of climate change; tropical deforestation accounted for up to 40% of global CO2 emissions annually in the 1980s. (6) Particularly, in biodiverse, tropical climates, the removal of forested regions leads to elevated levels of CO2 in the atmosphere caused by the decrease in greenery which can absorb greenhouse gases. This phenomenon creates a feedback loop known as the Greenhouse Gas Effect, leading to an increase in temperatures. (5)

Given the impacts of large-scale deforestation, communities which have

felt these effects directly have become increasingly invested in reforestation: the process of replanting and restoring forests on land that was traditionally forested. The act of reforestation has proven to be an effective method in combating the climate crisis. (7) Reforestation promotes biodiversity which decreases the susceptibility of species and ecosystems to climate change (8) and has the potential to directly combat the effects of global warming through increasing carbon sequestration, reducing the amount of CO2 in the atmosphere. (9)

There is evidence that reforestation at the local level confers environmental benefits. In north Queensland, Australia, the Community Rainforest Reforestation Project (CRRP) occurred between 1993 and 2000. Its goals were to create a sustainable lumber source, ensureland protection, enhance water quality, and train a workforce to aid with rainforest. (10) Though this program was initiated at the federal level, planning was aided by local governments and the program was implemented at the community level through local landholders. (10) A report that estimated both the economic and environmental impacts of theprogram predicted that it would lead to increased water quality, conservation, and would havecarbon sequestration benefits. (11) The amount of carbon sequestration was estimated by modelling the above-ground and below-ground biomass of the trees. In this model, the quantity of carbon was equated to 45% of the tree biomass. Using this model, the report estimated that, after all the tree harvesting had been completed, 146,885 tons of carbon wouldhave been sequestered over 1142 hectares. (11) In terms of water quality, a study predicted that available water volume would increase because of the CRRP (11), and another report found that water quality in areas with CRRP plantings increased. (12) Surveys of CRRP participants revealed that 70% noticed an increase of wildlife (particularly in terms of birds and small mammals), with 30% noticing a large increase. (10) However, the lack of systematic scientific reports and the reliance on layman observations make it difficult to quantify the impact of the CRRP on biodiversity. Overall, the CRRP demonstrates that community-based reforestation projects can strike a balance between economic gain and environmental benefits in sustainable forestry.

Another example of a community reforestation initiative is the organization called Trees of Life, located in Scotland. Since their inception 25 years ago, Trees for Life has planted almost 2 million trees to restore the Scottish Highlands. (13) This organization focuses on planting native and endangered tree species such as the 'dwarf birch' to restore traditional Scottish ecosystems. The Trees for Life project hopes reforestation will provide support for ecosystems, reduce soil erosion, increase rainfall, sustain local water sources, and help fight climate change through carbon sequestration. (13) There is also an emphasis on sustainability and efforts have been taken to ensure that the restored forests are able to survive and proliferate on their own, enforced primarily through creating sustainable seed sources. The planting of these trees has yielded approximately 40,000 acres of reforested area. This may seem insignificant in comparison to the total 36 billion acres of land area globally, however an acre of forested area can absorb up to 2.5 tonnes of CO2 annually, meaning the region of reforested land has nontrivial carbon capture and storage capacity. (14)

Local Climate Action Plans for Reducing CO2 Emissions

A powerful way that local initiatives can impact the climate crisis is through environmental policy implemented by local governments. While climate change is undoubtedly a global issue, its profound impact on communities demands that each unique circumstance be addressed through appropriate and individualized policy.

Local governments may be in a unique position to fight the climate crisis from the bottom-up as they can impact local emissions, can implement catered climate initiatives, and are able to contribute to larger emission and progress tracking. (15) The efficacy of local climate action plans (CAPs) across the world have been assessed through various case studiesin the literature, however this section will focus specifically on progress made through this avenue in Copenhagen, Denmark.

Copenhagen has long been considered a leader in forming environmentally consciouscities and a role model for how municipalities are able to nurture a green economy. (17) The City's progress in these environmental indicators and objectives of its CAPs over the years have reflected this. Copenhagen aims to be carbon neutral, with net zero carbon emissions, by 2025 and has been planning green initiatives for nearly 20 years, adopting its first CAP in 2002. (16) In 2017, an extensive case study examined the implementation of a local climate action plan in Copenhagen and assessed the adherence to and success of the plan. (16) The authors of the study assessed the effectiveness of the implementation of the CAPs through analysis of the Copenhagen 2002, 2009, and 2012 CAPs, which involved compiling municipal Climate Action Plans, greenhouse gas accounts, municipal waste plans and more, as well as conducting interviews with key stakeholders. (16)

The study found that for the 2012 CAP, 6 of the 19 milestones were on target with an additional 6 underway, and 7 remaining with significant difficulties. (16) It was also reported that the majority of the 66 proposed initiatives had begun. This is in stunning contrast with the markers created to analyse progress of the Paris Agreement, none of which have experienced significant progress - in fact many the progress on many of the goals has worsened since the document was ratified in 2015.

Noteworthy initiatives from Copenhagen's CAPs each year include increasing investment in wind power, encouraging use of biomass as opposed to coal in power plants, and incineration of waste. With respect to the reduction of greenhouse gas emissions, the emission target specified in the CAP was not met in 2010, but in 2015, emissions were belowtarget by an equivalent of 480,902 CO2, which bodes well for the goal of 2025 net carbon neutrality. In Summary, Damso, Kjaer and Christensen (16) conclude that the Copenhagen climate action plans have been effectively implemented and have shown tangible results in terms of emission reduction. These findings indicate an ability for local CAPs to make important contributions to climate change mitigation.

Community Supported Agriculture (CSA)

CSA is a model that offers an alternative method to farming, consuming, and distributing agricultural produce. (18) The Term 'Community Supported Agriculture' was coined and formulated by the Swiss farmer, Jan VanderTuin in 1984, but the concept behind it has existed in Europe since the 1960s. (19) The primary function of CSA is to create agricultural systems which remove the steps between farmers and consumers. Some of the environmental benefits of this method of food distribution include decreased CO2 emissions from transportation and refrigeration, both of which occur in higher volumes when a farmer supplies their goods to the global market.

Most CSA farms follow a similar structure: near the beginning of each growing season, individuals pay the farmers an agreed upon fee. This allows farmers to avoid relying on conventional funding such as loans or waiting for supermarkets to purchase their produce in bulk. In return, members of the community receive weekly baskets filled with fresh and local produce.

CSA models are not without inconveniences. (20) For individuals and families, much of the customization of choosing what produce is purchased weekly is lost. As a result, there is potential for food waste if the produce delivered is not familiar or preferred. Additionally, CSA is often more expensive than conventional grocery shopping, fortunately some communities can make these sacrifices to reap the social and environmental benefits of CSA.Those issues did not prevent the number of CSA farms from increasing throughout the United States in the past two decades. It was also shown that when more farms adopt the CSA mode, the issues mentioned above begin to resolve themselves organically. This is due to collaborative efforts among neighbouring farms attempting to avoid the shortcomings of the model.

This text focuses primarily on the environmental benefits of CSA, but it should be mentioned that this model has social and economic benefits as well. (20) An example of such economic benefits is the creation of jobs within the community. One of the key characteristics of a CSA farm is that it uses agro-ecological methods, including diverse crop cycling, natural manures and fertilizers, rainwater harvesting, and more to grow produce.

(18) Through a survey in 2003, it was found that 96% of CSA farmers used organic farming methods which have been shown to have fewer negative impacts on the surrounding ecosystems. (21) In a study done on CSAs in China, it was proposed that the new agricultural method offers a solution to China's environmental concerns such as soil pollution (22) because of the ecologically mindful methods followed by the CSA farming methodology.

A strong case for the development of CSA farms can be found in Hungary. The first Hungarian CSA farm was established in 1998, by Mathew Hayes. (23) The first few CSA farms faced some challenges due to the novelty of the model. In 2011, there was a new surge in CSA farms in Hungary. After learning from the mistakes of the programs which Hayesstarted, new CSA farms were far better equipped to manage the diverse challenges of themarket and better compete with conventional agriculture farms. By 2016, CSA farms composed nearly 20% of all farms in the country. Furthermore, due to pressure of communities where this model has been hugely successful, the Hungarian government adopted new policies that support existing CSA farms and encourage conventional farms to adopt this new model. These policies range from exempting CSA farms from following certain regulations, to the allocation of higher national aids relative to conventional farms. This showcases that generating food locally has excellent social, environmental, and economic benefits, and can become the model for a country's farming practices moving forward.

Discussion

The examples discussed above highlight the promise that small scale actions show increating new solutions to solve existing climate change challenges such as deforestation, the increase of CO2 emissions, and – the environmentally detrimental – conventional agriculture.

Deforestation is clearly a global issue, but it has dramatic effects on the communities closest to the affected forests. In Scotland, deforestation of the highlands has been a problem for decades, but it wasn't until local groups like Trees for Life chose to take action that a solution was realized. This indicates that the people most likely to offer meaningful contributions to solving specific climate change related challenges are the people in the communities most affected by these issues. For local communities, the issue goes beyond statistics; it is a meaningful challenge to their way of life. The direct impacts of the climatecrisis are experienced daily, from mass drought to extreme weather. When sitting in a UN summit debating, it can be difficult to understand the sense of urgency required for climateaction, but when you are watching a forest fire creep dangerously close to your home, thegravity of inaction could not be clearer.

Grassroot organizations are so effective simply because the members are personal stakeholders and will be most directly affected. The actions communities take towards reforestation is closely tied to the effects of CO2 on the environment.

For decades now national governments and international organizations have made pledges and composed treaties promising to lower global CO2 emissions. A prominent barrier to success with this approach is that it assumes homogeneity in solutions. We live in ahighly diverse world composed of unique ecosystems, cultures, and economies; it is unlikely that there is one climate solution that is always relevant. In order to implement meaningful action that will generate positive change, climate policies must come from local governments alongside international movements. Small municipalities and governments are the most aware of their constituents' needs and the challenges their communities face. This places more importance on the voices of individuals and responsibility on the choices of decision makers, as the effect of these policies are immediate, and profoundly evident. The instance of Copenhagen is a clear success, indicating that small government policy has a meaningful effect on the combating extent of Anthropogenic forcing through CO2 emissions. Through implementing local policies to create CAPs catered to the needs of the community, Copenhagen managed to set an example of what cities can achieve by choosing to create local methods to combat climate change.

A main driver for success in Copenhagen was the city's ability to take charge of its own emissions policies. Every region faces unique barriers to creating sustainable systems, by allowing municipalities to create individualized climate plans, they gain the power to choose the methods that will best suit the needs of their citizens and environment.

City emissions are not the only anthropogenic force that has a major impact on the climate crisis. A large portion of emissions and environmental degradation comes from large-scale agricultural systems. These must change as well. In recent years, the major stakeholdersin the agricultural industry have been scaling production and distribution to increase profit without regard for environmental or social consequences. This upscale has created a disconnect between consumers and growers, amongst many ecological issues. Farming is bedrock of a strong community, and just as the argument for reforestation, the individuals most impacted have the potential to create the fastest change. This is why Community Supported Agriculture offers a great alternative to the practices of large farming companies. In Hungary, CAS farms began through communities looking to create a support system for local farms while ensuring they received fresh produce harvested using environmentally conscious methods. Due to the success of this model, regions around the nation chose to incorporate this method of sustainable farming, which ultimately influenced government funding and policy change. This is an excellent instance of inspiring other regions to create successful local systems rather than scaling a system to fit mass demand, losing individuality in the process. With more communities taking similar initiatives, the effects of local action can be noticed throughout the world.

The notion of local initiatives as a method of combating the climate crisis was firstproposed by Bennett et al. in 'Bright spots: seeds of a good Anthropocene' (24), where researchers argued that bottom-up initiatives are our best hope for a safe future. This project chose to examine micro-scale climate scenarios as opposed to the standard global analysis. This was done by selecting 100 projects similar to those mentioned above, with the following criteria:

(i) The three initiatives are attempting to solve highly specific challenges rather thanattacking a general vague problem.

(ii) The three initiatives stem from small communities rather than large organizations.

(iii) The three initiatives were relatively successful in achieving meaningful change, not only at the local level, but on a larger scale as well.

When examined individually, each movement appears insignificant, but when considered in tandem with one another, a pattern of success begins to form. This is the power of collective action, and it is precisely the method of success for this climate scenario.

Conclusion

Current climate models focus on macro-scale scale solutions to climate change. We have shown, however, that grassroots initiatives have significant benefits, and can be an effective strategy in the fight against climate change. Community driven initiatives have the added value of being led by the people most affected by the issues they decide to tackle. Creative, local, and successful ideas already exist all around us. The main challenge is to encourage more communities all over the world to act and to fill the world with hope.

References

1. IPCC Working Group III. IPCC Special Report: Emissions Scenarios [Internet].IPCC. 2000. Available from: https://www.ipcc.ch/site/assets/uploads/2018/03/sres-en.pdf

2. UNCC. Paris Agreement - Status of Ratification [Internet]. unfccc.int. 2015 [cited 2021Mar7]. Available from: https://unfccc.int/process/the-paris-agreement/status-of-ratification

3. Cornwall W. The Paris climate pact is 5 years old. Is it working? Science Magazine[Internet].AAAS;2020;Availablefrom:https://www.sciencemag.org/news/2020/12/paris-climate-pact-5-years-old-it-working

4. Ramankutty N, Foley J. Estimating historical changes in global land cover: Croplands from 1700 to 1992. Global Biogeochemical Cycles. 1999;13(4):997-1027.

5. Bala G, Caldeira K, Wickett M, Phillips T, Lobell D, Delire C et al. Combined climate and carbon-cycle effects of large-scale deforestation. Proceedings of the National Academy of Sciences. 2007;104(16):6550-6555.12

6. Bäckstrand K, Lövbrand E. Planting Trees to Mitigate Climate Change: Contested Discourses of Ecological Modernization, Green Governmentality and Civic Environmentalism. Global Environmental Politics. 2006;6(1):50-75.

7. Griscom B, Adams J, Ellis P, Houghton R, Lomax G, Miteva D et al. Natural climate solutions. Proceedings of the National Academy of Sciences.2017;114(44):11645-11650.

8. Hooper D, Chapin F, Ewel J, Hector A, Inchausti P, Lavorel S et al. EFFECTS OF BIODIVERSITY ON ECOSYSTEM FUNCTIONING: A CONSENSUS OF CURRENT KNOWLEDGE. Ecological Monographs. 2005;75(1):3-35.

9. Cunningham S, Mac Nally R, Baker P, Cavagnaro T, Beringer J, Thomson J et al.Balancing the environmental benefits of reforestation in agricultural regions.Perspectives in Plant Ecology, Evolution and Systematics. 2015;17(4):301-317.

10. Harrison R, Harrison S, Herbohn J. Evaluation of the performance of the community rainforest reforestation program in North Queensland, Australia. Small-scale Forest Economics, Management and Policy. 2004;3(3):411-429.

11. Eono J, Harrison S. Estimation of Costs and Benefits of the CommunityRainforest Reforestation Program in North Queensland. Economic Analysis andPolicy. 2002;32(2):69-89.

12. Harrison S. Sustainable farm forestry in the tropics. Cheltenham: Elgar; 2001.

13. Why Plant Trees? [Internet]. Trees for Life. 2021 [cited 6 March 2021]. Availablefrom: https://treesforlife.org.uk/support/plant-a-tree/

14. Urban Forestry Network. (n.d.). Trees improve our air quality. Retrieved March 05, 2021, from http://urbanforestrynetwork.org/benefits/air%20quality.htm

15. Tang Z, Brody S, Quinn C, Chang L, Wei T. Moving from agenda to action:evaluating local climate change action plans. Journal of Environmental Planning and Management. 2010;53(1):41-62.13

16. Damsø T, Kjær T, Christensen T. Implementation of local climate action plans:Copenhagen – Towards a carbon-neutral capital. Journal of Cleaner Production.2017;167:406-415.

17. Floater G, Rode P, Zenghelis D. Copenhagen: green economy leader report. 2014.

18. Paul M. Community-supported agriculture in the United States: Social, ecological,and economic benefits to farming. Journal of Agrarian Change. 2018;19(1):162-180.

19. Schnell S. Food With a Farmer's Face: Community-Supported Agriculture in the United States. Geographical Review. 2007;97(4):131-148.

20. Thompson C, Coskuner-Balli G. Enchanting Ethical Consumerism. Journal of Consumer Culture. 2007;7(3):275-303.

21. Brown C, Miller S. The Impacts of Local Markets: A Review of Research on Farmers Markets and Community Supported Agriculture (CSA). American Journal ofAgricultural Economics. 2008;90(5):1298-1302.

22. Krul K, Ho P. Alternative Approaches to Food: Community Supported Agriculture in Urban China. Sustainability. 2017;9(5):844.

23. Balázs B, Pataki G, Lazányi O. Prospects for the future: Community supported agriculture in Hungary. Futures. 2016;83:100-111.

24. Bennett EM, Solan M, Biggs R, McPhearson T, Norström AV, Olsson P, et al. Bright spots: seeds of a good Anthropocene. Frontiers in Ecology and the Environment. 2016;14(8):441–8.